AFWAL-TR-82-4097
Volume I
ADA 122890

STRUCTURAL INVESTIGATIONS OF FIBERS AND FILMS OF POLY (P-PHENYLENEBENZOBISTHIAZOLE)

J. R. Minter

Polymer Science and Engineering Department
The University of Massachusetts
Amherst, MA 01003

May 1982
Interim Report for Period September 1978 - May 1982

Approved for Public Release - Distribution Unlimited

MATERIALS LABORATORY
AIR FORCE WRIGHT AERONAUTICAL LABORATORIES
AIR FORCE SYSTEMS COMMAND
WRIGHT-PATTERSON AIR FORCE BASE, OHIO 45433

BEST AVAILABLE COPY

Best Available Copy 20040223061

NOTICE

When Government drawings, specifications, or other data are used for any purpose other than in connection with a definitely related Government procurement operation, the United States Government thereby incurs no responsibility nor any obligation whatsoever; and the fact that the government may have formulated, furnished, or in any way supplied the said drawings, specifications, or other data, is not to be regarded by implication or otherwise as in any manner licensing the holder or any other person or corporation, or conveying any rights or permission to manufacture use, or sell any patented invention that may in any way be related thereto.

This report has been reviewed by the Office of Public Affairs (ASD/PA) and is releasable to the National Technical Information Service (NTIS). At NTIS, it will be available to the general public, including foreign nations.

THADDEUS E. HELMINIAK
Project Scientist

R. L. VAN DEUSEN, Chief
Polymer Branch
Nonmetallic Materials Division

FOR THE COMMANDER:

F. D. CHERRY, Chief
Nonmetallic Materials Division

"If your address has changed, if you wish to be removed from our mailing list, or if the addressee is no longer employed by your organization please notify AFWAL/MLBP *, W-PAFB, OH 45433 to help us maintain a current mailing list".*

Copies of this report should not be returned unless return is required by security considerations, contractual obligations, or notice on a specific document.

SECURITY CLASSIFICATION OF THIS PAGE (When Data Entered)

REPORT DOCUMENTATION PAGE

READ INSTRUCTIONS BEFORE COMPLETING FORM

1. REPORT NUMBER: AFWAL-TR-82-4097, Vol I

2. GOVT ACCESSION NO.

3. RECIPIENT'S CATALOG NUMBER

4. TITLE (and Subtitle): Structural Investigations of Fibers and Films of Poly(p-phenylenebenzobisthiazole)

5. TYPE OF REPORT & PERIOD COVERED: Interim Report 1 Sep 78 - 1 May 82

6. PERFORMING ORG. REPORT NUMBER

7. AUTHOR(s): J.R. Minter

8. CONTRACT OR GRANT NUMBER(s): F33615-78-C-5175

9. PERFORMING ORGANIZATION NAME AND ADDRESS: Polymer Science and Engineering Department, The University of Massachusetts, Amherst, MA 01003

10. PROGRAM ELEMENT, PROJECT, TASK AREA & WORK UNIT NUMBERS: P.E. 62102F, Project 24190407

11. CONTROLLING OFFICE NAME AND ADDRESS: Materials Laboratory (AFWAL/MLBP), Air Force Wright Aeronautical Laboratories, Air Force Systems Command, Wright-Patterson AFB, OH 45433

12. REPORT DATE: May 1982

13. NUMBER OF PAGES: 238

14. MONITORING AGENCY NAME & ADDRESS (if different from Controlling Office)

15. SECURITY CLASS. (of this report): Unclassified

15a. DECLASSIFICATION/DOWNGRADING SCHEDULE

16. DISTRIBUTION STATEMENT (of this Report): Approved for public release; distribution unlimited.

17. DISTRIBUTION STATEMENT (of the abstract entered in Block 20, if different from Report)

18. SUPPLEMENTARY NOTES: Volume II of AFWAL-TR-82-4097 contains computer software. Distribution is limited to DOD components only. Non-DoD requests for the volume must be referred to AFWAL/MLBP, WPAFB, OH 45433 and must include the statement of terms and conditions contained in Atch 21 to AFR 300-6.

19. KEY WORDS (Continue on reverse side if necessary and identify by block number)

Rod-like Polymers	X-Ray Scattering
Heterocyclic Polymers	Electron Microscopy
High Modulus	Optical Microscopy
High Strength	Structure Analysis

20. ABSTRACT (Continue on reverse side if necessary and identify by block number)

Dry-jet-wet spun poly(p-phenylene benzobisthiazole) (PBT) fibers and films were studied to determine how such wholly aromatic molecules are arranged in the solid state. The effect of processing variables on microstructure was also investigated.

Fragments obtained by detachment replication of bulk samples were quite resistant to electron beam damage compared to aliphatic polymers. A characteristic dose of 1.6 Coul cm^{-2} decreases the intensity of the (010) reflection to 37% of its initial value. Artefact-free dark field images could then be obtained

(CONTINUED)

DD FORM 1 JAN 73 1473 EDITION OF 1 NOV 65 IS OBSOLETE

SECURITY CLASSIFICATION OF THIS PAGE (When Data Entered)

at magnifications of up to 40,000X. High resolution (010) dark field (DF) images of fibers and films processed from methane sulfonic acid (MSA) and polyphosphoric acid (PPA) solutions have coherently scattering regions less than 2 nm in size. Tension heat treatment above 475°C results in growth of the coherently scattering regions to 10 nm perpendicular to the extrusion direction and 15 nm parallel to the extrusion direction.

The lack of prominent diffraction contrast in (00ℓ) DF images is caused by axial translational disorder of the chains along the orientation direction. Microvoids in PBT fibers and films were analyzed using the ORNL 10 m small angle x-ray scattering apparatus. Average microvoid size was measured parallel and perpendicular to the extrusion direction.

The effects of atomic coordinates, cylindrical averaging and preferred chain orientation and the phenyl-bisthiazole conformational angle on the calculated single chain scattering (molecular transform) were examined. Electron and x-ray diffraction patterns may be explained by a model with chains packed in 2-dimensional monoclinic nets with axial translational disorder along the chain axis. The $\underset{\sim}{c}$ axis in as-spun films is modestly oriented in the extrusion direction since the orientation factors for the (100) and (010) reflections average -0.3, a value of -0.5 corresponding to perfect orientation.

FOREWORD

This report covers work performed by the University of Massachusetts, Amherst, Massachusetts 01003, on "Mechanical Properties versus Morphology of Ordered Polymers". The work was conducted under contract F33615-78-C-5175 for the Materials Laboratory. The performance period was from 1 September 1978 to 1 May 1982. This report was submitted in May 1982.

The work was performed in the Polymer Science and Engineering Department with Dr. Edwin L. Thomas acting as principal investigator. Author of this report is Dr. John R. Minter. The project engineer was Dr. Thaddeus E. Helminiak, AFWAL/MLBP, Materials Laboratory, Wright-Patterson Air Force Base, Ohio.

The author wishes to thank Professors Roger S. Porter, Julio M. Ottino and Marion B. Rhodes for helpful constructive criticism. The author is indebted to the students and staff of the Polymer Science and Engineering Department, who gave me valuable advice and assistance. Special thanks go to Cam Murray and Ron Tabar for assistance in computer programming and Wade Adams and Dale Handlin for many late evening discussions, and especially Mrs. Judith Allardice for typing the manuscript.

Best Available Copy

TABLE OF CONTENTS

Chapter

I. INTRODUCTION..... 1

1.1 Historical Perspective..... 1
1.2 The Dissertation Problem..... 1
1.3 Organization of the Dissertation..... 3

II. SURVEY OF THE RELEVANT LITERATURE..... 5

2.1 Synthesis of PBT..... 5
2.2 Solution Properties..... 8
2.3 Fiber Spinning..... 16
2.3.1 Fiber Spinning of PBO and PBT..... 16
2.4 Formation of Tapes of Rigid Macromolecules..... 19
2.5 Mechanical Properties..... 21

III. SAMPLE PREPARATION AND EXPERIMENTAL TECHNIQUES..... 27

3.1 Preparation of Liquid Crystalline Solutions for for Characterization..... 27
3.2 Sample Preparation for Polarized Light and Differential Interference Microscopy..... 28
3.3 Sample Preparation for Transmission Electron Microscopy..... 29
3.4 Transmission Electron Microscopy..... 29
3.5 Microdensitometry of Electron Diffraction Patterns..... 40
3.6 Sample Preparation for X-ray Diffraction..... 42
3.7 Wide Angle Diffraction Measurements..... 42
3.8 Small Angle X-ray Scattering..... 42
3.9 Snall Angle Neutron Scattering..... 44
3.10 Fiber and Film Nomenclature..... 45

IV. POLARIZED LIGHT AND INTERFERENCE MICROSCOPY OF PBT SOLUTIONS, FIBERS AND FILMS..... 52

4.1 Light Microscopy of PBT Solutions..... 52
4.2 Light Microscopy of PBT Fibers..... 57
4.3 Polarized Light Microscopy of PBT Films..... 67

TABLE OF CONTENTS (cont'd.)

Chapter
V. MICROVOID ANALYSIS BY SMALL ANGLE X-RAY SCATTERING..... 73

5.1 Introduction..... 73
5.2 The Intensity of Small Angle Scattering..... 75
5.3 Isotropic Systems..... 78
5.3.1 Guinier's Law..... 78
5.3.2 Debye-Bueche Theory..... 79
5.4 Extension to Anisotropic Systems..... 80
5.4.1 The Projected Correlation Function..... 81
5.4.2 Extension to Uniaxial Systems Using Spherical Coordinates..... 82
5.4.3 Guinier Analysis of Anisotropic Systems..... 84
5.4.4 Extension to Uniaxial Systems Using Cylindrical Coordinates..... 86
5.4.5 Analysis of Diffuse SAXS from Selected Fibers and Films..... 88
5.4.6 Comparison of the Models for Data Analysis.. 99
5.5 Correlation of Void Size with Processing Conditions..... 99
5.6 Suggestions for Future Experiments..... 100

VI MEASUREMENT OF FINE STRUCTURE BY TRANSMISSION ELECTRON MICROSCOPY..... 104
6.1 Measurement of the Electron Irradiation Lifetime of PBT..... 104
6.2 Dark Field Imaging of PBT Fibers and Films..... 111
6.3 PBT LAttice Imaging..... 126

VII STRUCTURAL ANALYSIS BY X-RAY AND ELECTRON DIFFRACTION... 133

7.1 Review of Prior Structure Analysis of PBT and PPTA..... 133
7.1.1 PBT..... 133
7.1.2 PPTA..... 144
7.2 Calculation of Single Chain Scattering..... 147
7.2.1 Cylindrically Averaged Single Chain Scattering..... 151
7.2.2 Chains with Preferred Orientation..... 157
7.2.3 Comparison with Experiments..... 157
7.3 Packing Analysis in the PBT Unit Cell..... 169
7.4 Diffraction Line Broadening: A Preliminary Study..... 175
7.5 Orientation: A Preliminary Study..... 179

TABLE OF CONTENTS (cont'd.)

Chapter
VIII SMALL ANGLE NEUTRON SCATTERING..... 188

IX CONCLUSIONS AND POSSIBLE EXTENSIONS..... 200

9.1 Recapitulation..... 200
9.1.1 Observation of PBT Fine Structure by High Resolution Transmission Electron Microscopy..... 200
9.1.2 Structural Analysis by Diffraction Methods..... 202
9.1.3 Void Analysis in PBT..... 204
9.2 Generalizations and Suggestions for Future Work..... 206
9.2.1 The Molecular Transform..... 206
9.2.2 Structural Analysis of PBT..... 207
9.2.3 Microvoid Analysis..... 207
9.2.4 Study of Lyotropic Helical Polypeptides..... 208

REFERENCES..... 210

APPENDIX I MOLECULAR TRANSFORM COMPUTER PROGRAMS..... Volume II

APPENDIX II PACKING ANALYSIS PROGRAMS..... Volume II

LIST OF FIGURES

Figure

1 Rigid Rodlike Macromolecules for High Modulus/High Strength Fibers and Films 2
2 The synthesis of PBT 6
3 The synthesis of PBO 7
4 Viscometric data on a PPTA polymer in CSA containing selected concentrations of lithium chlorosulfonate as indicated. The crosses are calculated with the one-point limiting viscosity number formula:
$$[\eta] = \{ 2 (\eta_{sp} - \ln \eta_{rel})/c^2 \}^{1/2}$$
Extrapolations of the logarithmic viscosity number, $\ln \eta_{rel}/c$, and the viscosity number, η_{sp}/c, to zero concentration are also shown. From reference [9] 9
5 Molecular weight distribution of PBO of DP ~ 30. Points show experimental curve. Line shows value for $M_w/M_n = 2$ at comparable M_n. From Reference [5]..... 11
6 Viscosity of PBO in H_2SO_4 as a function of concentration. $[\eta]$ PBO = 2.1. From reference [6]..... 13
7 Phase diagram for PBT of selected limiting viscosity numbers in selected solvents. Arrows indicate the biphasic region. From Reference [15]..... 14
8 Viscosity versus strain rate for PBT solutions in MSA. Closed circles: PBT $[\eta] = 31$ dL g^{-1}, 23°C, 10 wt% Open circles: PBT $[\eta] = 18$ dL g^{-1}, 25°C, 9.5 wt% Open circles, pip down: PBT $[\eta] = 18$ dL g^{-1}, 12°C, 9.5 wt% From Reference [15]..... 15
9 Apparatus used to spin PBO and PBT fibers. From Reference [12]..... 18
10 Apparatus used to prepare films of PBT. From Reference [12,13]..... 20
11 SEM micrographs of typical PBT fiber and film..... 22
12 Stress-strain curves for PBT fibers. HT - heat treated..... 23
13 Optics for Zeiss-Nomarski differential interference contrast equipment. From Reference [21]..... 30
14 Kink bands observed in PBT fibers prepared by sonication. From Reference [25]..... 32
15 Transverse section of a PBT fiber. Notice the deformation caused by the microtome knife. From Reference [26]..... 33
16 Detachment replication procedure I with polyacrylic acid (PPA). After Geil [28]..... 34
17 Detachment replication procedure II with collodion. From Reference [29]..... 35

LIST OF FIGURES (cont'd.)

Figure

18 Image formation in the TEM. S_0-incident beam S'-scattered beam..... 38

19 Electron microscopy with minimum electron irradiation damage. Square - area to be photographed. Small circle - auxillary viewing screen. Shaded area - electron beam. From Reference [65]..... 39

20 Direct measurement of electron current incident upon viewing screen..... 41

21 Schlieren texture in 9% PBT in MSA after 48 hours relaxation..... 53

22 Inversion wall in 9% PBT in MSA as a function of orientation. Polarizer vertical, analyser horizontal..... 54

23 Nematic texture in H_2SO_4 solutions of PPTA. Micrograph courtesy of Benoit and Stazielle [36]. No magnification value supplied..... 56

24 Anisotropic PBT/MSA domains in an isotropic matrix as viewed by interference and polarized light microscopy. Top: interference Bottom: crossed polars..... 58

25 (a) HTF-23 475°C heat treatment (b) ASF-13 typical 'as-spun' fiber..... 64

26 Typical circumferential banding defect in PBT fiber.... 66

27 Polarized light micrograph of ASR-9 (a) Film oriented at 45° to polarizer; (b) Film oriented at 5° to polarizer..... 68

28 Polarized light micrograph of ASR-7 (a) Film oriented at 45° to polarizer; (b) Film oriented at 0° to polarizer..... 69

29 Schematic of the model and coorinates used to study SAXS from PBT fibers and films..... 76

30 Typical isointensity contour plots of as-spun and heat treated fibers..... 89

31 Typical Guinier plot from the intensity along s_2 from PBT fibers and films. Sample is HTF-42..... 93

32 Typical Debye type plot for data along s_2 from PBT fibers and films. Sample is HTF-42..... 95

33 Typical plot of SAXS data from PBT fibers and films assuming a cylindrical exponential correlation function. Sample is HTF-42..... 97

34 Projected correlation function along R_2 for HTF-42..... 98

35 Decrease of scattered intensity from (010), ($\bar{1}$10) and (100) reflections from HTR-5..... 107
36 Determination of D^* for HTR-5..... 108
37 BF/DF pair from HTR-5 (tension-heat treated at 475°C) prepared by detachment replication..... 112
38 Successive DF images from (110) and the (010),($\bar{1}$10) and (110) reflections DF HTR-4 tension heat treated at 465°C. A. 100 DF; B. (010),(110) and ($\bar{1}$10) DF..... 114
39 Successive dark field images from the (010), ($\bar{1}$10) and (110) reflections from HTR-4. A. Objective aperture centered on reflection B. Objective aperture displaced to accept only the off axis component of reflection..... 116
40 Schematic of experiment similar to that in Figure 38 on PPTA. From Reference [67]..... 118
41 Schematic of pleated sheet model for PPTA fibers. From Reference [67]. The PPTA molecules are assumed to undergo tilt from one pleated region to the next.... 119
42 DF micrograph of PBT fragment suspended over a gold decorated, perforated support film (S). "K" denotes tilted area. Extrusion direction is horizontal. Instrumental Magnification = 33,000X. Top: Enlargement of boxed area at bottom. B denotes probable twisted regions..... 121
43 Schematic of scattering from a uniformly bent crystal. s is the deviation parameter..... 122
44 Rocking curve for 1.68 nm^{-1} (100) reflection. Assumed crystal thickness 10 nm..... 124
45 Rocking curve for 2.76 nm^{-1} (010) reflection. Assumed crystal thickness 10 nm..... 125
46 Two regions of an axial bright field lattice image(100,000X instrumentalmagnification) of a tension heat treated fiber. From Reference [66]..... 127
47 (a) Optical transform of micrograph used to obtain Figure 45. (b) Schematic of Figure 46a. Sharp spots are due to .59 nm E fringes and diffuse streaks to 1.24 nm M fringes..... 128
48 Schematic of model with condensed chain ends. From Reference [72]..... 132
49 Packing of PBT chains in the solid..... 135
50 Projection down $\underset{\sim}{c}^*$ of $\underset{\sim}{a}^*$ $\underset{\sim}{b}^*$ plane viewed along $\underset{\sim}{c}^*$ in PBT. Circles represent equatorial reflections for uniaxial symmetry..... 139

LIST OF FIGURES (cont'd.)

Figure

51 Cylindrically averaged molecular transform of a single PBT repeat unit. From Reference [75]..... 140

52 Cylindrically averaged molecular transform of a single PBT chain of 8 repeat units. Numbers on the right side are layer line numbers. From Reference [75]..... 141

53 Comparison between the cylindrically averaged molecular transform of 8 repeat units and electron diffration from HTF-23A. Transform from Reference [75], diffraction pattern from this work..... 142

54 Comparison between PBT and cells proposed by Roche [74] and Odell et al. [75]..... 143

55 Crystal structure of PPTA proposed by Northolt [76-78]..... 145

56 Cylindrically averaged intensity profiles for the first eight layer lines for a PBT chain of 8 units generated assuming the coordinates of Odell et al. [75]. Temperature factor (0.06, 0.06 nm^2) (parallel, perpendicular) to the chain axis. Numbers on the right are the layer line numbers..... 152

57 Cylindrically averaged intensity profiles for the first eight layer lines for an H_6PBT chain of 8 units generated assuming the coordinates of Wellman et al. [83]. Temperature factor (0.06, 0.06 nm^2) (parallel, perpendicular) to the chain axis. Numbers on the right are the layer line numbers. Notice splitting of ℓ=6..... 154

58 Cylindrically averaged intensity profiles for the first eight layer lines for an H_6PBT chain of 8 units generated assuming the coordinates of Wellman et al. [83]. Temperature factor (0.005, 0.025 nm^2) (parallel, perpendicular) to the chain axis. Numbers on the right are the layer line numbers. Notice splitting of ℓ=6..... 155

59 Cylindrically averaged intensity profiles for the first eight layer lines for an H_6PBT chain of 8 units generated assuming the coordinates of Wellman et al. [83]. Center profile is for sixth layer line. Numbers at the right indicate the displacement along s_1 from ℓ=6. Temperature factor (0.005, 0.025 nm^2) (parallel, perpendicular) to the chain axis..... 156

60a Intensity profiles for the first eight layer lines for an H_6PBT chain of 8 units generated assuming the coordinates of Wellman et al. [83]. ϕ = 35°, α = 0°. Temperature factor (0.005, 0.025 nm^2) (parallel, perpendicular) to the chain axis. Numbers on the right are layer line numbers..... 158

LIST OF FIGURES (cont'd.)

Figure

60b Intensity profiles for the first eight layer lines for an H_6PBT chain of 8 units generated assuming the coordinates of Wellman et al. [83]. $\phi = 35°$, $\alpha = 35°$. Temperature factor (0.005, 0.025 nm^2) (parallel, perpendicular) to the chain axis. Numbers on the right are layer line numbers..... 159

60c Intensity profiles for the first eight layer lines for an H_6PBT chain of 8 units generated assuming the coordinates of Wellman et al. [83]. $\phi = 35°$, $\alpha = 45°$. Temperature factor (0.005, 0.025 nm^2) (parallel, perpendicular) to the chain axis. Numbers on the right are layer line numbers..... 160

60d Intensity profiles for the first eight layer lines for an H_6PBT chain of 8 units generated assuming the coordinates of Wellman et al. [83]. $\phi = 35°$, $\alpha = 60°$. Temperature factor (0.005, 0.025 nm^2) (parallel, perpendicular) to the chain axis. Numbers on the right are layer line numbers 161

60e Intensity profiles for the first eight layer lines for an H_6PBT chain of 8 units generated assuming the coordinates of Wellman et al. [83]. $\phi = 35°$, $\alpha = 90°$. Temperature factor (0.005, 0.025 nm^2) (parallel, perpendicular) to the chain axis. Numbers on the right are layer line numbers..... 162

61a Intensity profiles for the first eight layer lines for an H_6PBT chain of 8 units generated assuming the coordinates of Wellman et al. [83]. $\phi = 0°$, $\alpha = 0°$. Temperature factor (0.005, 0.025 nm^2) (parallel, perpendicular) to the chain axis. Numbers on the right are layer line numbers..... 163

61b Intensity profiles for the first eight layer lines for an H_6PBT chain of 8 units generated assuming the coordinates of Wellman et al. [83]. $\phi = 25°$, $\alpha = 0°$. Temperature factor (0.005, 0.025 nm^2) (parallel, perpendicular) to the chain axis. Numbers on the right are layer line numbers..... 164

61c Intensity profiles for the first eight layer lines for an H_6PBT chain of 8 units generated assuming the coordinates of Wellman et al. [83]. $\phi = 45°$, $\alpha = 0°$. Temperature factor (0.005, 0.025 nm^2) (parallel, perpendicular) to the chain axis. Numbers on the right are layer line numbers..... 165

62 Two-dimensional contour plot of diffracted intensity. Microdensitometry of electron diffraction from HTR..... 166

LIST OF FIGURES (concluded)

Figures

63 Zero layer precession photograph from HTF-23A. Ni filtered CuKα radiation was used..... 167

64 Comparison of the calculated intensity of the sixth layer line (cylindrically averaged) with experimentally determined curve. Calc 1: coordinates from Odell et al. [75] Calc 2: coordinated from Wellman et al. [83]..... 168

65 Cylindrically averaged intensity profiles for the first eight units generated assuming the coordinates of Northolt et al. [77]. Temperature factor (0.005, 0.025 nm^2) (parallel, perpendicular) to the chain axis. Numbers on the right are layer line numbers..... 170

66 Configuration of packing calculation..... 172

67 Potential energy surface of the H_6PBT unit cell. Contours represent 0.5, 1, 2, 4, 8, 16, 32, 54, 128 Kcal/9 monomer units from the minimum..... 174

68 Typical diffracometer traces of as-spun and heat-treated fibers: (a) ASF-39 (b) HTF-39..... 178

69 Wide angle x-ray diffraction from PBT film from MSA solution along 3-directions..... 180

70 Wide angle x-ray diffraction from a PBT film from PPA solution along 3-direction..... 181

71 Hermans-Stein orientation factors, f, and average square direction cosines, $\langle\cos^2\phi\rangle$, for the (100) and (010) reflections with respect to the three film axes..... 183

72 Comparison between WAXS and SAED in PBT films.
(a) WAXS: ASR-5 (b) WAXS: HTR-5
(c) SAED: ASR-5 (d) SAED: HTR-5..... 184

73 Single chain scattering function, S(q), for a rod and a sphere. R is the radius of the sphere and 1/2 the length of the rod. From Reference [95]..... 194

74 Guinier plot for SANS intensity from precipitated PBT. 10% D_4H_2PBT, 90% H_6PBT..... 198

LIST OF TABLES

Table		
I	Modulus and Strength of PBT Fibers. From Reference [18]	25
II	Mechanical Properties for Comparison to PBT. From Reference [18]	25
III	Processing History of Samples Used in This Study	46
IV	Typical Physical-Chemical Data for Samples Used in This Study	51
V	Defect Analysis of PBT Fibers from MSA Solutions	60
VI	Orientation by Dichroism	72
VII	Void Size Measurements Along Selected Direction	91
VIII	Processing Parameters for Samples for SAXS	92
IX	Calculated and Observed Equatorial Structure Factors for PBT and d-spacings for Electrons and X-rays	137
X	Structural Parameters for Selected Aromatic Polymers	146
XI	Apparent "Crystal Size" by Line Broadening	177
XII	Observed Structure Factors by Electron Diffraction	186
XIII	Scattering parameters of Atoms Useful for PBT SANS	189
XIV	Parameters for Contrast Factor and Signal to Noise Calculations for SANS	190
XV	Optimum Matrix Thickness of SANS of PBT	192
XVI	Contrast Factor and Signal to Noise Ratio for Selected Pairs of Species 1 (LABEL) in Species 2 (MATRIX) for Small Angle Neutron Scattering Assuming $W_1 = 0.01$ and $DP_1 = 50$	196
XVII	Mark-Howink Constants for PBG in Selected Solvents From Reference [113]	208

CHAPTER I

INTRODUCTION

1.1 Historical Perspective

The development of high modulus, high strength fibers from semi-rigid macromolecules such as poly(p-phenylene terephthalamide) (PPTA) has encouraged workers to look to aromatic heterocyclic, rigid macromolecules in anticipation of producing fibers and films with higher modulus and strength as well as superior thermal stability. Two candidate materials developed through the Air Force Materials Laboratory Ordered Polymers Program [1] are poly(p-phenylene benzobisoxazole) (PBO), and poly(p-phenylene benzobisthiazole) (PBT). These are shown in Figure 1. PBT has been spun into fibers with 250 GPa modulus and 2.5 GPa tensile strength [2] and has aroused a great deal of interest.

The purpose of this dissertation was to investigate the structure of fibers and films from PBT and attempt to correlate the observed structure with processing history. The work reported herein represents a part of a program sponsored by the Air Force Materials Laboratory underway at the University of Massachusetts and several other institutions designed to produce PBT fibers and films with optimum mechanical properties.

1.2 The Dissertation Problem

The dissertation problem is to understand how the rodlike PBT

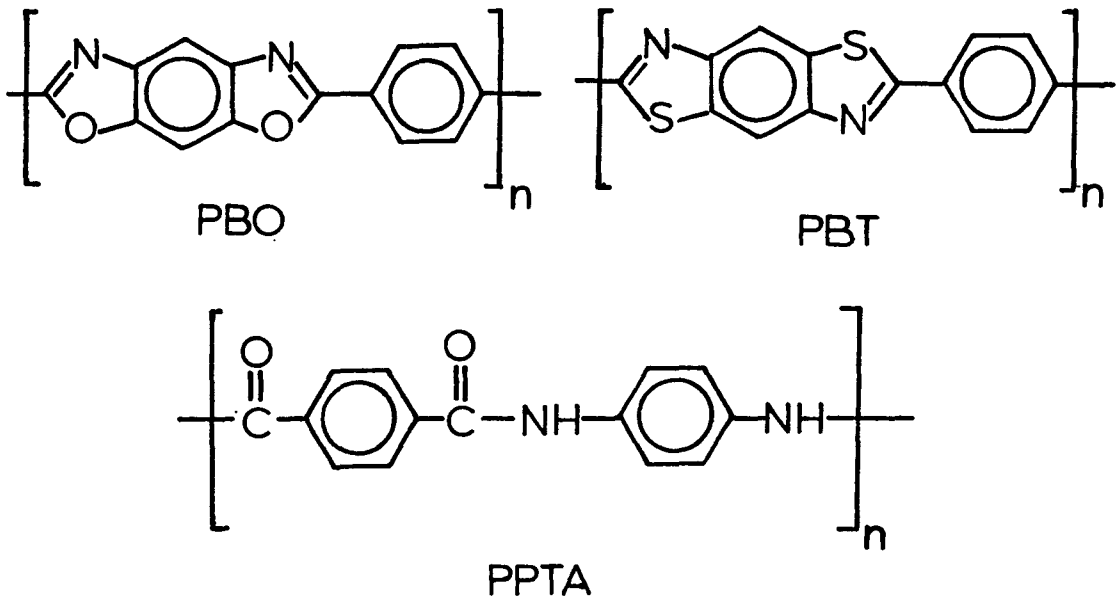

Figure 1. Rigid Rodlike Macromolecules for High Modulus/High Strength Fibers and Films

molecule is arranged in the solid state and how changes in processing history affect this arrangement. The macrostructure of fibers and films has been investigated by polarized light and interference microscopy. Small angle x-ray scattering has been used to determine the size of microvoids present in such materials. Packing of chains in the solid state has been studied by electron and wide-angle x-ray diffraction and high resolution dark field electron microscopy. Diffraction results have been compared to those predicted by a relatively simple model of chains packed in a two-dimensional net with translational disorder along the chain axis.

1.3 Organization of the Dissertation

This dissertation is organized as follows: Chapter II surveys the synthesis, solution behavior, processing and mechanical properties of PBT. Chapter III contains a synopsis of the experimental techniques used in this investigation. The next six chapters represent the experimental results obtained from structural investigations of PBT. Chapter IV presents the results of polarized light and interference microscopy of PBT solutions, fibers and films. Chapter V presents the analysis of the diffuse small angle x-ray scattered intensity to determine the size of the microvoids present. Chapter VI contains the results of high resolution dark field electron microscopy on thin fragments from PBT fibers and films obtained by detachment replication. Chapter VII presents the results of wide angle x-ray diffraction and selected area electron diffraction from PBT fibers

and films and a comparison to values predicted on the basis of a two-dimensional structure with axial translational disorder along the chain axis. Chapter VIII presents the theory and results of a brief excursion into small angle neutron scattering. Chapter IX recapitulates the conclusions of the dissertation, summarizes the microstructure of PBT fibers and films and contains suggestions for future work. The computer programs developed in this work are in Volume II.

CHAPTER II

SURVEY OF THE RELEVANT LITERATURE

This chapter presents a survey of prior work on the synthesis, solution properties, processing and mechanical properties of PBT fibers and films. The purpose of this section is not to be an exhaustive review of the literature concerning high modulus aromatic fibers. Since PBT is a new material, the purpose of this section is to provide the reader with a foundation and a perspective from which to view the later chapters and to place structural investigations in the proper context. Whenever useful for comparison, or when data from PBT is unavailable, data from PBO and PPTA will be presented. The discussion of previous structural studies of PBT and other high modulus fibers is delayed until later chapters.

2.1 Synthesis of PBT

PBT was first polymerized by Wolfe *et al*. [3]. The basic synthetic scheme involves step growth condensation polymerization from 2,5 diamino-1,4 benzenedithiol hydrochloride (DABDT) and phthalic acid (TA) as shown in Figure 2. Polmerization with this isomer of DABBT results in a polymer which is loosely termed a "trans" isomer. The polymerization is conducted in poly (phosphoric acid) solution (PPA) at temperatures up to 200°C. This may be contrasted with PBO which is normally prepared by polymerization of 4,6 diamino-1,3 benzenediol and TA as shown in Figure 3 [4,5,6].

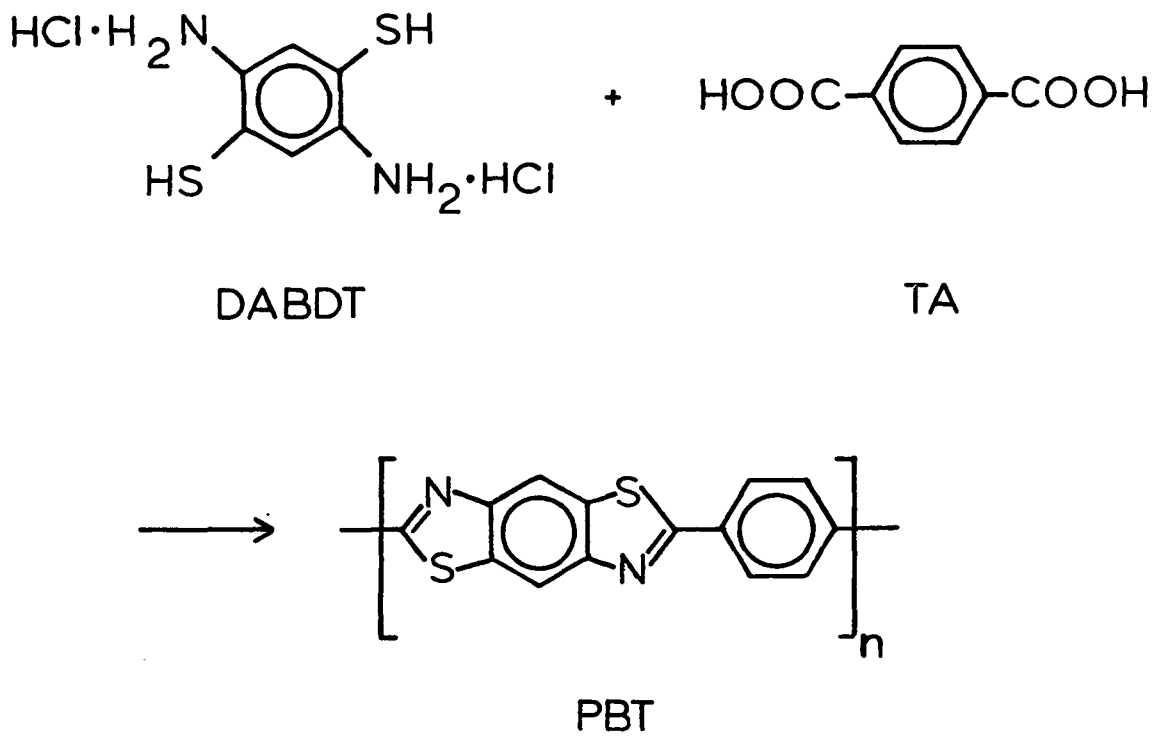

Figure 2. The synthesis of PBT

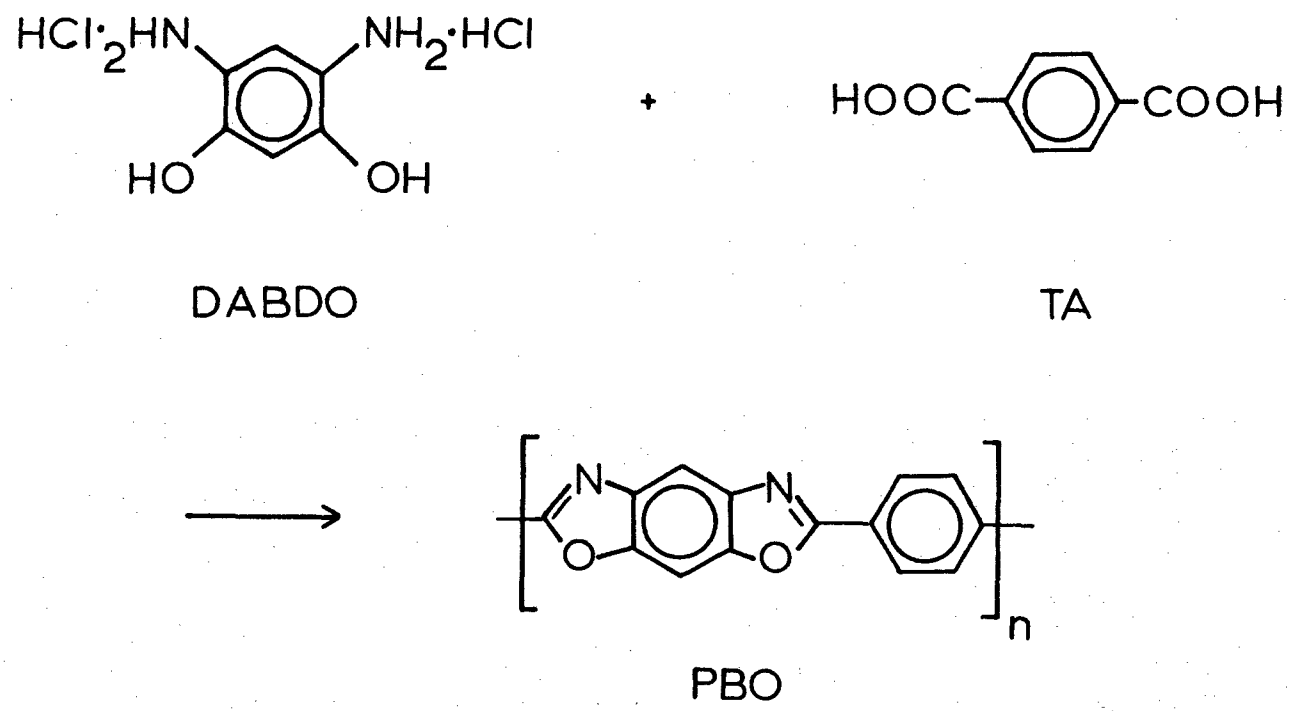

Figure 3. The synthesis of PBO

This produces what is loosely termed a "cis" isomer. Presumably due to difficulties in monomer purification PBO was never prepared at high molecular weight while PBT has been polymerized to high degrees of polymerization [5]. In subsequent sections we will see the deliterious effect of low molecular weight on fiber spinning. High molecular weight, coupled with the increased thermal-oxidative stability of PBT lead to the development of PBT over PBO.

2.2 Solution Properties

PBO and PBT are only soluble in strong acids such as concentrated sulfuric acid, methane sulfonic acid (MSA), chlorosulfonic acid (CSA) and PPA. PBT solutions have been studied less extensively than PBO and PPTA solutions, so much of the data presented here will be for PBO. When dissolved in strong acids, PBO and PBT are reported to be highly protonated [7,8].

The limiting viscosity number of PBO polymerized as above, ranges from 1.4 to 9.3 dL g^{-1} in MSA [4,5,6]. However, PBT has limiting viscosity of numbers up to 30 dL g^{-1} [3]. These correspond to a degree of polymerization up to about 100 ($M_W \approx 34,000$).

Berry [9,10] reports that irreversibiliy protonated parallel aggregates of molecules are present in PBO and PPTA solutions and result in a higher weight average molecular weight, but a lower limiting viscosity number [η]. This aggregation has been shown to be dependent upon ionic strength as shown in Figure 4. Unfortunately,

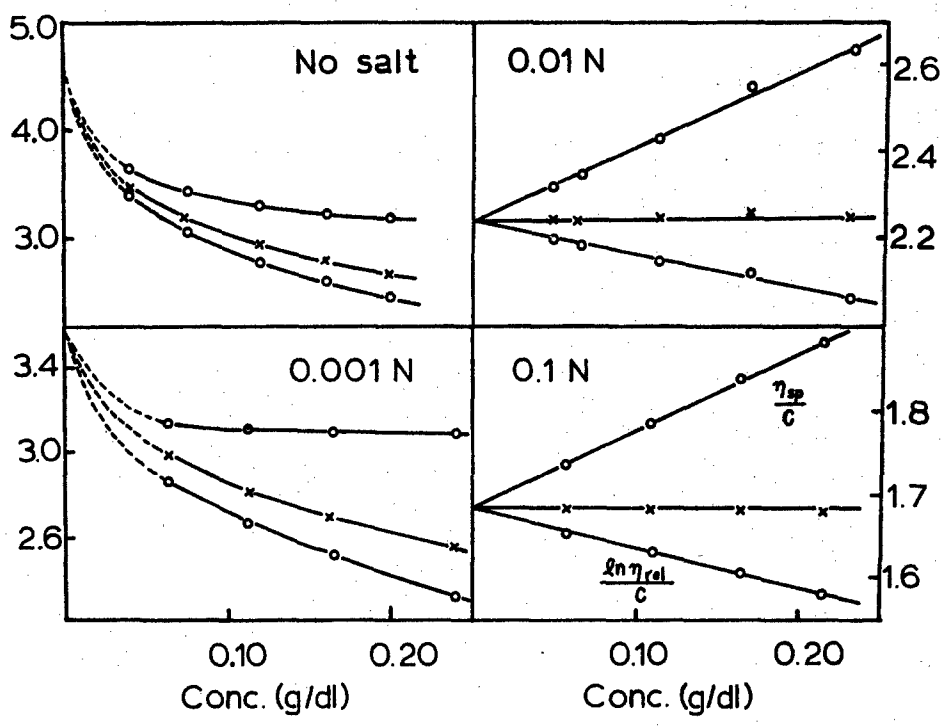

Figure 4. Viscometric data on a PPTA polymer in CSA containing selected concentrations of lithium chlorosulfonate as indicated. The crosses are calculated with the one-point limiting viscosity number formula:

$$[\eta] = \{ 2 (\eta_{sp} - \ln \eta_{rel})/c^2 \}^{1/2}$$

Extrapolations of the logarithmic viscosity number, $\ln \eta_{rel}/c$, and the viscosity number, η_{sp}/c, to zero concentration are also shown. From reference [9].

similar data have not been reported for PBT. Therefore, the Mark-Howink relationship [9] does not give a reliable measure of the molecular weight unless ionic strength is carefully accounted for. Berry et al. [9] report the Mark-Howink exponent of PBO to be 1.85, very close to the value of 1.80 expected for a rodlike polymer. Schaefgen et al. [11] found the Mark-Howink exponent to be 1.7 for low molecular weight PPTA and poly(p-benzamide) ($M_W \sim 12,000$) but to decrease to 1.08 for higher molecular weight. These data suggest that high molecular weight PPTA is semi-rigid. Crosby et al. [104] have measured the persistance length (a measure of rigidity) of PBT in CSA and compared this value to that of PPTA in H_2SO_4. PBT samples with $\overline{M}_W$ ranging from 15,000 - 18,000 had a persistance length of 64 $\pm$ 9 nm compared to a value of 15 nm for PPTA of comparable molecular weight. Thus, PBT is more rigid than PPTA. There is insufficient data to assess the effect of higher molecular weight on chain rigidity in PBO and PBT.

Size exclusion chromatography results [7,9] suggests that the molecular weight distribution of PBO is broad. The ratio of the weight to number average molecular weight, M_W/M_n, for PBO was found to reach the value of 2.0 expected for a 'most probable distribution' only at high conversions. The distribution was found to be consistently skewed toward higher molecular weights than a distribution with an equivalent Mn and Mw/Mn of 2. A distribution for a PBO sample with a degree of polymerization of about 30 is shown in Figure 5. For a similar PBT sample an Mw/Mn of 1.3 has been reported [8] but the data analagous to those in Figure 5 have not been published.

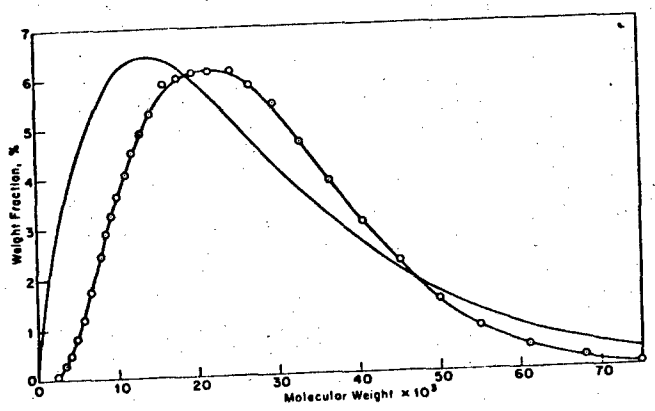

Figure 5. Molecular weight distribution of PBO of DP ≈ 30. Points show experimental curve. Line shows value for $M_w/M_n = 2$ at comparable M_n. From Reference [5].

At room temperature, when the concentration of PBO or PBT is increased to greater than 2.5 wt % in CSA, 5 wt % in H_2SO_4 or MSA, or 3 wt % in PPA, the solutions exhibit stir opalescence [3,6]. As the polymer concentration is increased beyond this critical value, the solution viscosity passes through a maximum. A typical example is shown in Figure 6 for a PBO sample of limiting viscosity number of 2.1 in MSA at 20°C [6]. Thus, these solutions form lyotropic liquid crystalline phases at moderate concentrations in acid solutions.

Berry et al. [12] have studied the phase equilibria of PBT solutions. The extent of the biphasic (isotropic and anisotropic phases) region as a function of temperature and volume fraction is shown in Figure 7 for PBT of selected limiting viscosity numbers and solvents. There is a need for more in-depth studies since these authors found that the variation of the data with concentration is not explained by athermal mixing models and must indicate intermolecular interaction.

Berry [12] has measured the shear viscosity of PBO and PBT solutions in MSA and PPA on a gold coated cone and plate rheometer. Typical results for PBT solutions in MSA are shown in Figure 8 and demonstrate that the solutions are only modestly shear thinning at moderate shear rates. At a given molecular weight, concentration and shear rate, the viscosity of PBT in PPA is roughly two orders of magnitude greater than PBT in MSA with a concomitant increase in relaxation time. Therefore PPA solutions of PBT will maintain the orientation induced during elongation longer but will require higher

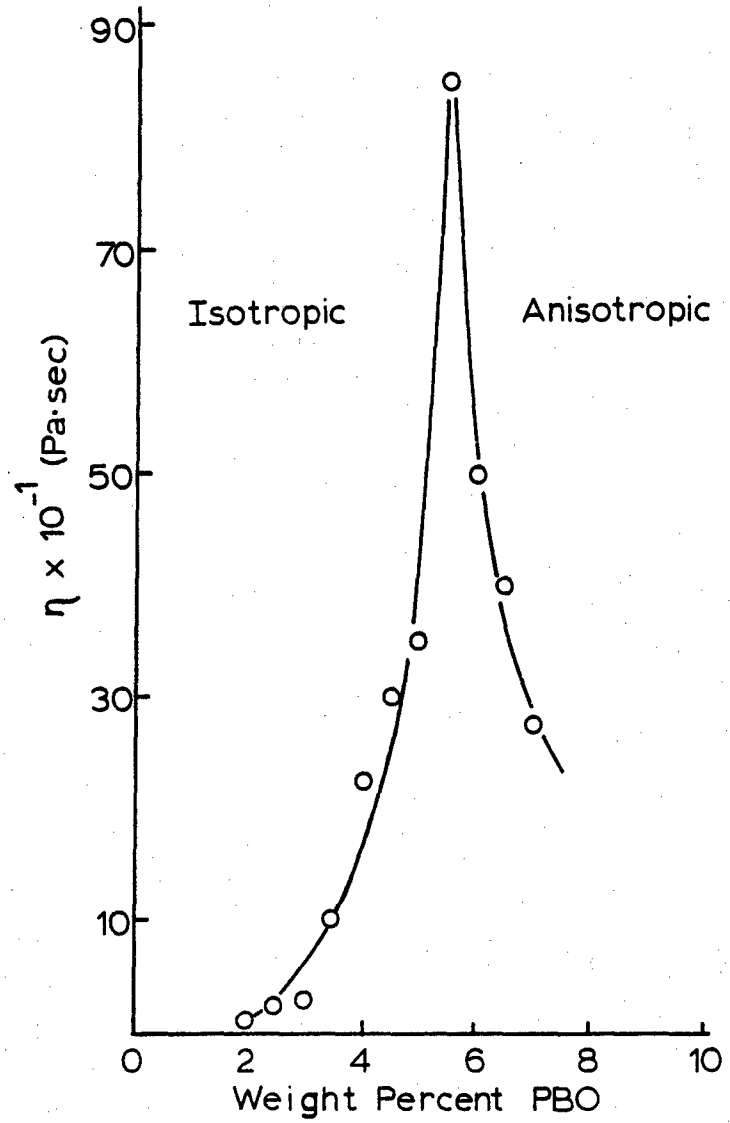

Figure 6. Viscosity of PBO in H_2SO_4 as a function of concentration. [η] PBO = 2.1. From reference [6].

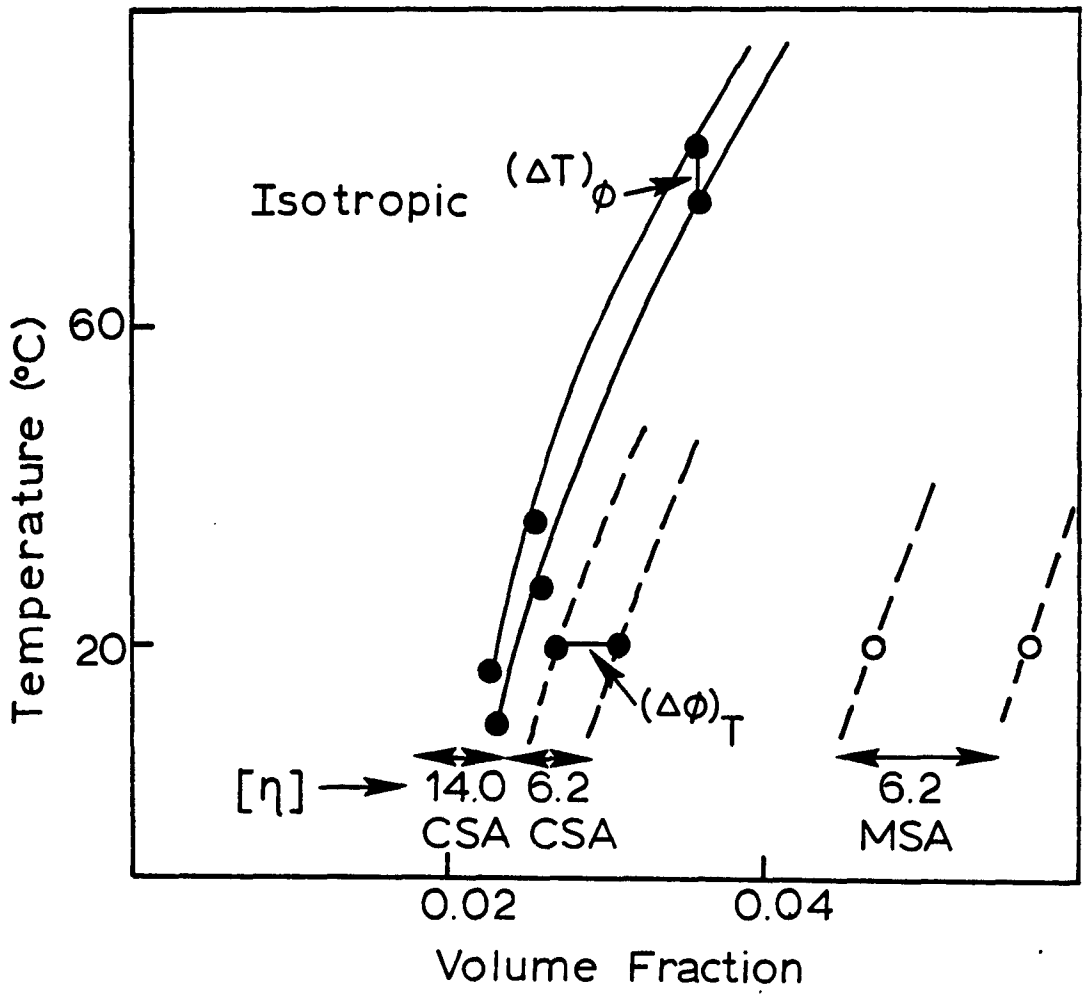

Figure 7. Phase diagram for PBT of selected limiting viscosity numbers in selected solvents. Arrows indicate the biphasic region. From Reference [15].

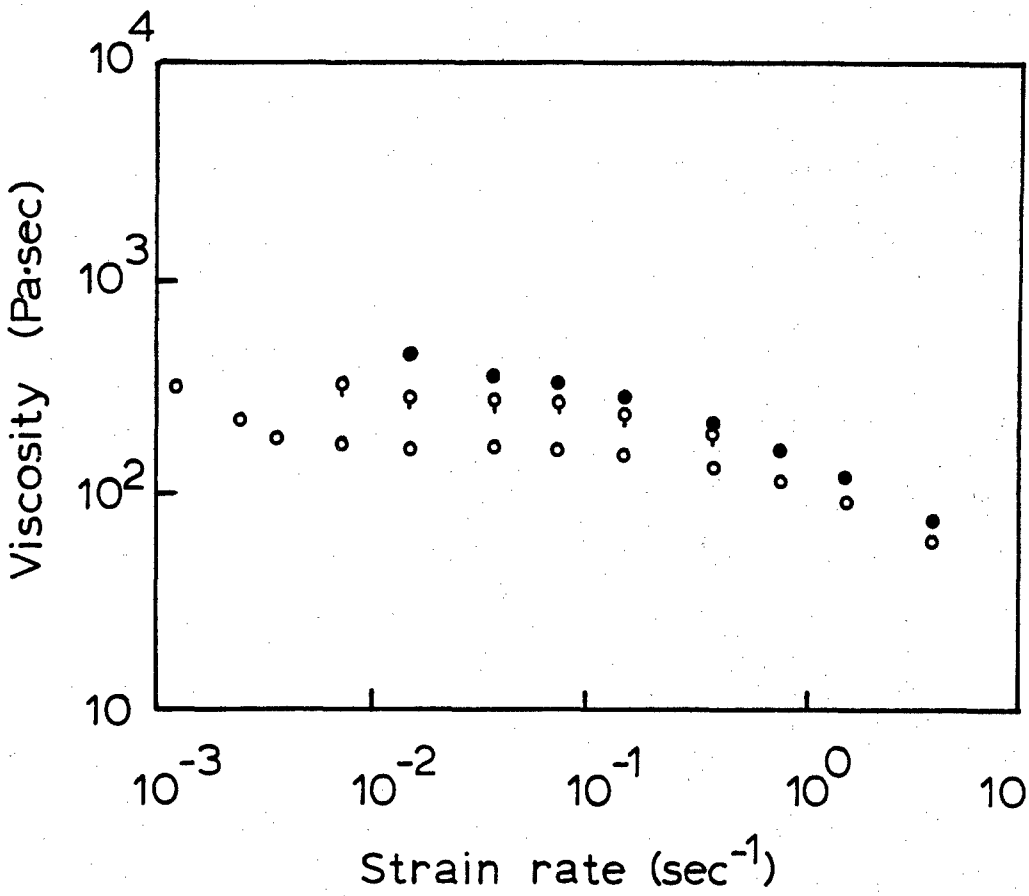

Figure 8. Viscosity versus strain rate for PBT solutions in MSA.
Closed circles: PBT [η] = 31 dL g^{-1}, 23°C, 10 wt%
Open circles: PBT [η] = 18 dL g^{-1}, 25°C, 9.5 wt%
Open circles, pip down: PBT [η] = 18 dL g^{-1}, 12°C, 9.5 wt%
From Reference [15].

extrusion pressures than comparable MSA solutions of PBT.

2.3 Fiber Spinning

Solids of rigid macromolecules tend to degrade before forming a melt which could be spun into fibers as is commonly done with polyesters and aliphatic polyamides. Instead, these polymers must be spun from solution. The solvents for rigid molecules are usually not sufficiently volatile to allow dry spinning and so one must employ techniques such as wet spinning or dry-jet-wet spinning.

In wet spinning, the polymer solution is extruded through a capillary, i.e. spinneret, directly into a coagulation bath containing a non-solvent for the polymer. After precipitation occurs, the resulting fiber is wound onto a take-up bobbin. Dry-jet-wet spinning is a variation of wet spinning described by Blades [119] for PPTA in which there is a "dry gap" between the spinneret and coagulation bath allowing the polymer solution to elongate and orient prior to coagulation.

2.3.1 Fiber spinning of PBO and PBT. Berry's group [10] has constructed a gas driven system to force dope through a glass spinneret to spin fibers of PBO and PBT. This system was plagued by instabilities which were attributed to pressure fluctuations which propagated in a capillary wave resulting in breakage of the fluid jet. Ziabicki [14] lists this as one of two mechanisms for jet breakage, the other being cohesive failure. Since the surface tension

of the solution-air interface is appreciable in dry spinning and presumably in the dry-jet-wet spinning, the capillary wave mechanism may be correct. However, Ziabicki [120] pointed out that capillary wave failure has never been reported in technical wet spinning where interfacial tension is less important.

Chenevey [12,13] and Choe and Kim [6] have spun PBO and PBT solutions of a wide range of inherent viscosities from 97.5% MSA/2.5% CSA and PPA solutions while varying coagulant composition, temperature, and dope concentration. Their apparatus is shown in Figure 9.

The polymer solutions are extruded through a spinneret (typically 5 holes, 100 μm diameter) through a variable air gap and into a coagulation bath containing 50 to 100% H_2O, the remainder being solvent. The fibers were then pulled through a wash bath by a driven roll and taken up on a bobbin. Constant tension was maintained in the spin line by a dancer. The spin-draw ratio (SDR) is defined as the ratio of the take-up speed of the fiber to the extrusion speed of the spinning solution. For solutions of PBT in MSA this typically ranged from 1 -4. For PBT solutions in PPA, recent fibers have been extruded with SDRs as high as 14. PBO was found to be of insufficient molecular weight to allow the formation of solutions with sufficient cohesive strength to allow dry-jet-wet spinning, so consequently PBO was wet spun. On the other hand, PBT solutions had sufficient cohesive strength for dry-jet-wet spinning and therefore resulted in fibers with better orientation and mechanical properties. The detailed microstructure of some of these fibers will be discussed in this

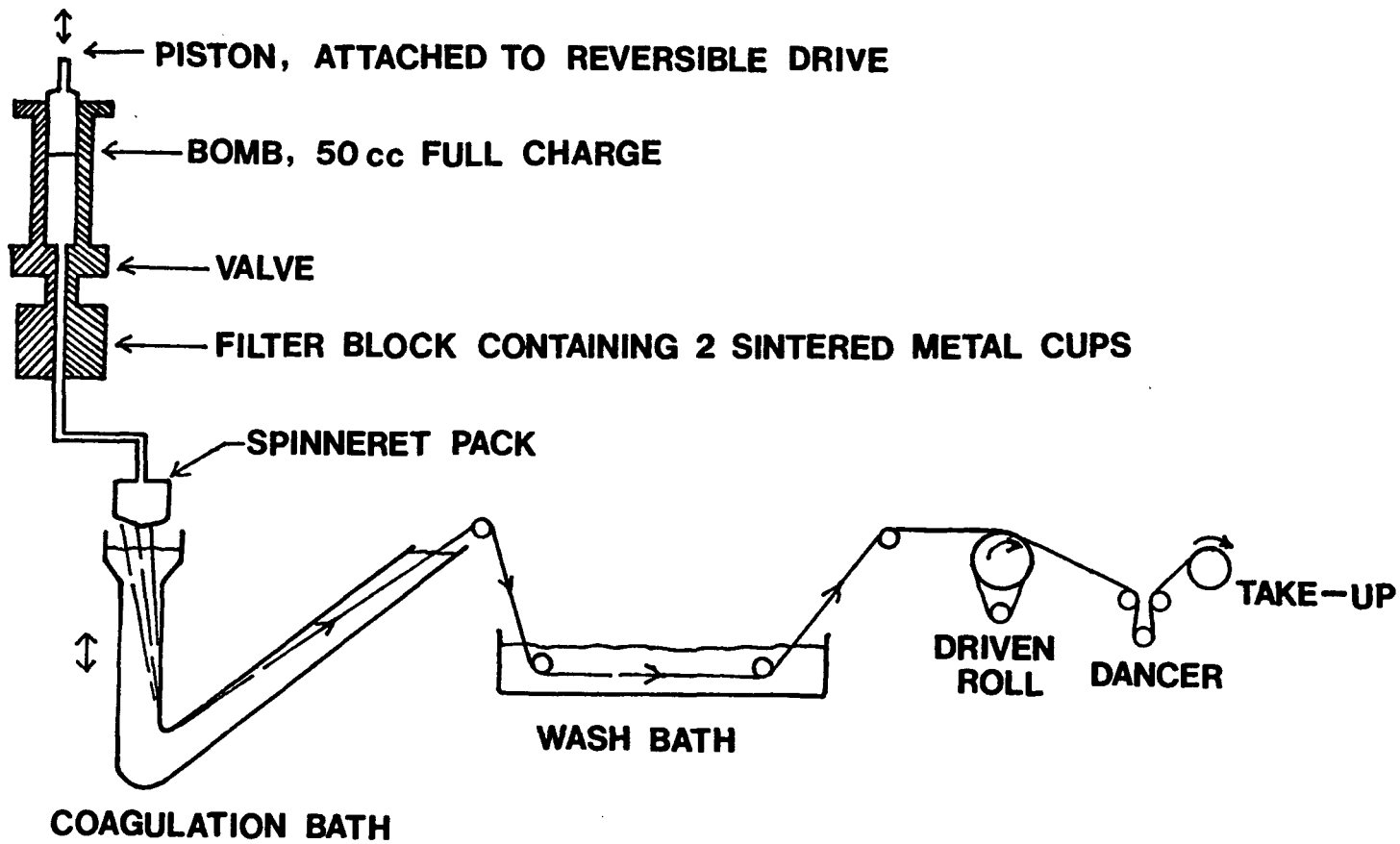

Figure 9. Apparatus used to spin PBO and PBT fibers. From Reference [12].

dissertation.

2.4 Formation of Tapes of Rigid Macromolecules

There is considerable interest in the formation of films of rigid macromolecules. It is desirable to utilize the information gained from fiber spinning, which only uses a small amount of material per unit length of sample and is attractive for expensive materials with limited availability. To study oriented films it is often advantageous to exchange the circular spinneret for a slit and produce films, or more descriptively, tapes on the equipment used for fiber spinning with only minor modifications. Chenevey [12,13] has done this and prepared PBO and PBT films in a flow field with elongational components (see Figure 10).

The PBT solutions were extruded out of thin rectangular die (typically 12 mm wide x 1.7 mm long x 0.2 mm thick) through an air gap onto the rotating surface of a casting drum. The ribbon was then removed from the drum, washed and taken up on movie film reels. Tensioning rolls maintained constant tension in the film line. The use of a casting drum introduces the possibility of morphological differences between the two sides of the ribbon due to different coagulation boundary conditions. According to Chenevey [12] the casting drum was dried by a wiper and film extrusion was sufficiently slow, such that the drum surface contacting the extruded ribbon remained dry. Typical SDRs range from 1 to 4, although Chenevey recently reported a value of 21.

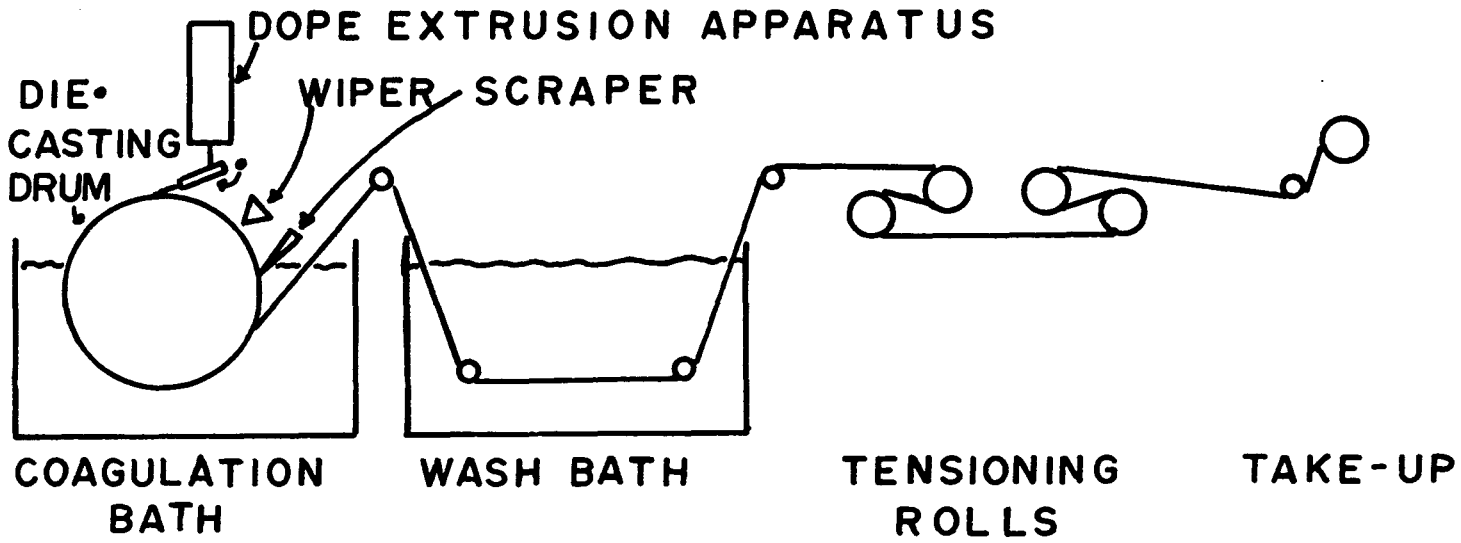

Figure 10. Apparatus used to prepare films of PBT. From Reference [12,13].

Berry et al. [15] have taken a slightly different approach by drawing a Mylar® tape coated with PBT/MSA dope through a shear gap and into a coagulation bath. Berry [10] modeled the flow of a rod-like molecule in solution using Bird's model [16] of two beads connected by a rigid connector. The angular distribution of rods was calculated as a function of $\tau \langle \dot{\varepsilon} \rangle$, where τ is the time constant (the product of the zero shear viscosity and the recoverable compliances, as measured in a cone and plate viscometer) and $\langle \dot{\varepsilon} \rangle$ is the average elongation rate. As expected, this model predicted much greater orientation in an elongational flow than in a shear flow. Thus, there should be significant differences in properties of ribbons prepared under similar coagulation conditions by the Celanese [13] or the King and Berry [15] method. Low magnification SEM micrographs of typical PBT fiber and film are shown in Figure 11.

Aoki et al. [14] studied tapes and blown film of PPTA but did not report the effect of processing conditions on morphology. These authors only reported out-of-focus scanning electron micrographs and, therefore, did not adequately characterize their films.

2.5 Mechanical Properties

The impetus to study PBT comes from the high modulus and strength of this material and the retention of modulus and strength at high temperatures. The purpose of this section is to review the latest mechanical properties of fibers and films. PBT fibers and films processed as described in previous sections are mechanically highly

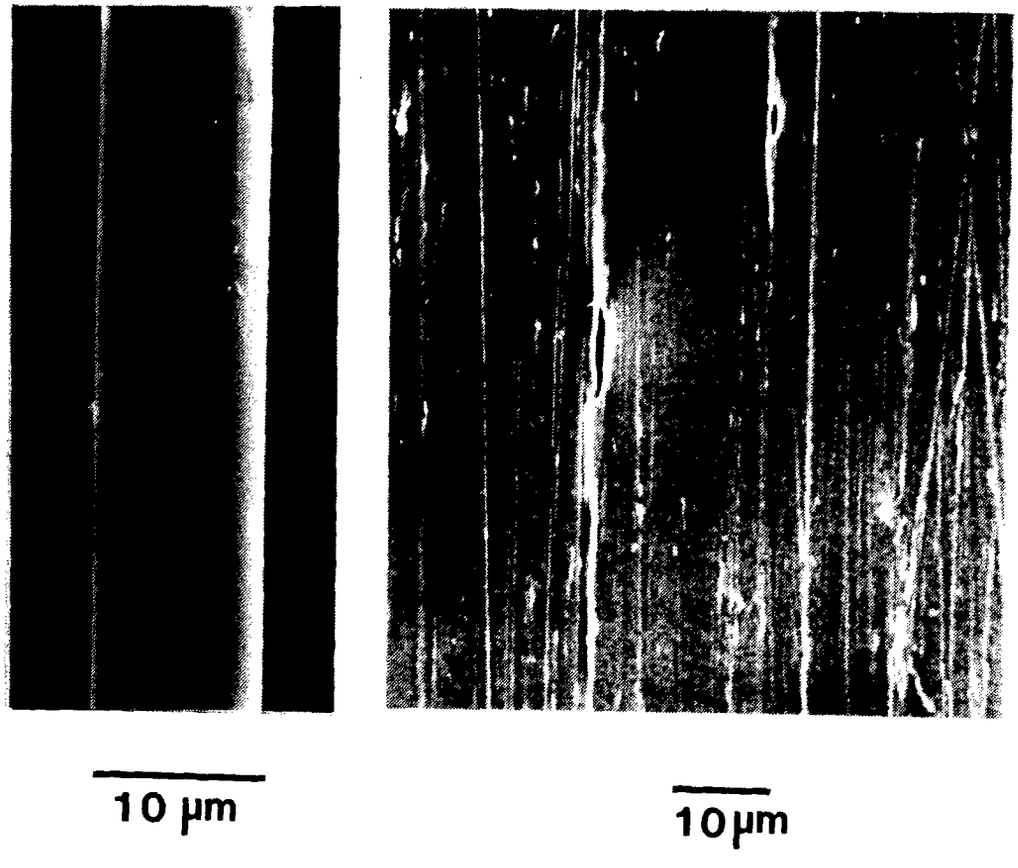

Figure 11. SEM micrographs of typical PBT fiber and film.

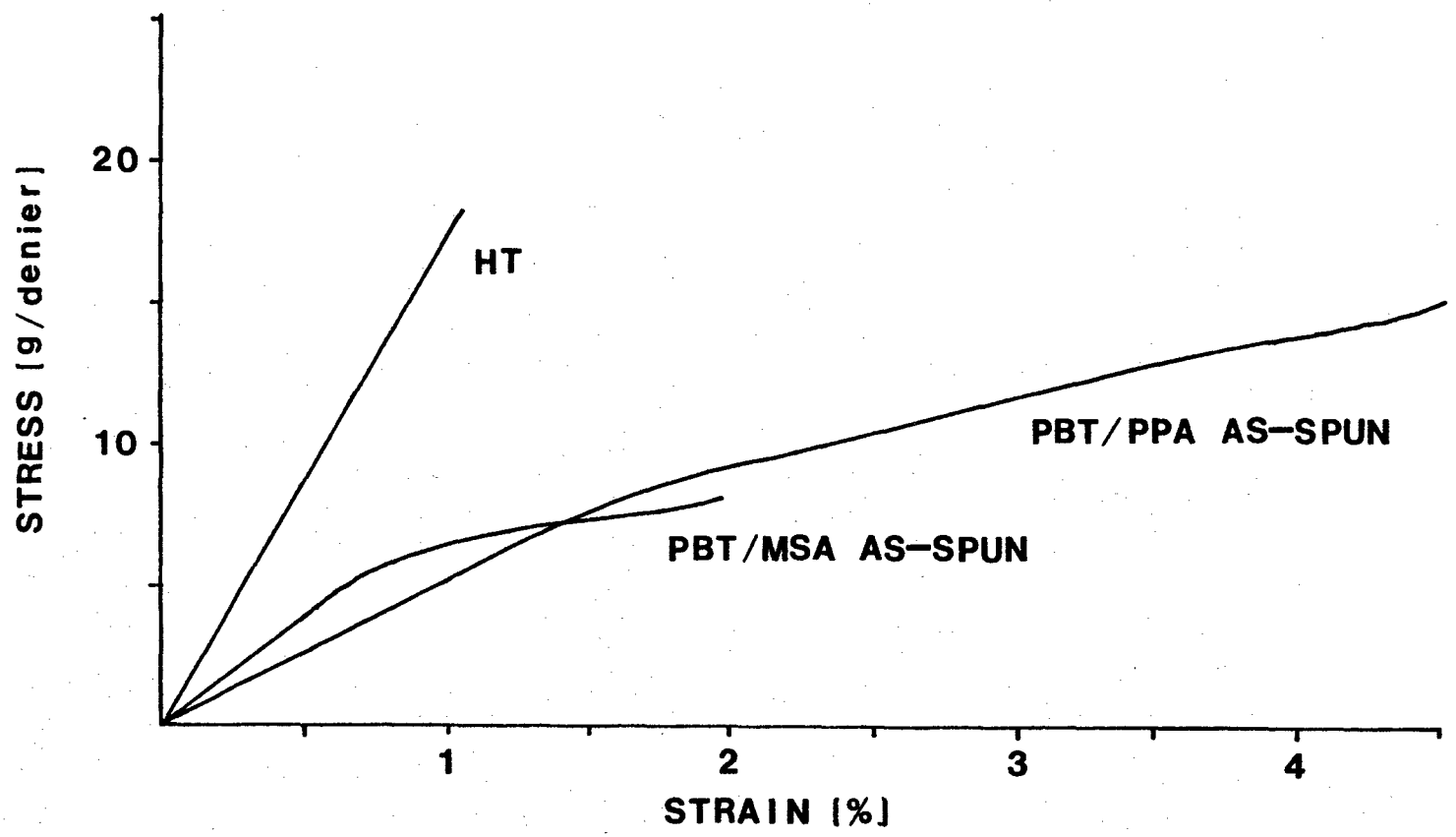

Figure 12. Stress-strain curves for PBT fibers. HT - heat treated.

anisotropic.

PBT fibers spun from MSA solutions contain voids and fracture has been observed to occur at these flaws [17], thus limiting the tensile strength. The effect of processing variables on these flaws will be discussed in Chapter IV. The stress-strain behavior of as-spun PBT fibers is decidedly non-linear while heat treated fibers show a linear stress-strain behavior (see Figure 12). The nonlinear behavior in as-spun fibers has been attributed to residual stresses occurring due to coagulation [17]. When the skin of the fiber solidifies, the core is still approximately 90% solvent and a 90% volume change is required to form the solid polymer. As this solvent diffuses out, the core attempts to contract and the skin resists further shape changes. Thus, the core develops a large component of axial tensile stress and compressive stresses are generated in the skin. Hoop stresses are also produced by the skrinkage. With loading at high temperature these residual stresses can be relieved. The modulus, strength, and elongation to break of PBT from selected processing histories are given in Table I. These data are compared for other commerical fibers in Table II. These data were taken from Reference [18]. Modulus and strength values are given in engineering units (GPa) and fiber units (g/denier). Note that one denier is the weight of 9,000 meters of fiber. Allen also found [18] that when tested at 200°C in the air after ten minutes, the PBT fibers retained 82% of modulus and 73% of strength. These values are similar to those reported for Kevlar® [18].

Table I

Modulus and Strength of PBT Fibers
From Reference 18

Spinning Dopes	Fiber Condition	Modulus (g/denier)	Strength (g/denier)
PBT-MSA	as-spun	350-1200	3-12
	heat treated	1000-2100	11-18
PBT-PPA	as-spun	400-600	4-18
	heat treated	600-2100	6-20

Table II

Mechanical Properties for Comparison to PBT
From Reference 18

Fiber	Modulus g/denier	Modulus GPa	Strength g/denier	Strength GPa	Elongation %	Density g/cm^3
PBT	2100	250	20	2.4	1.5	1.5
Kevlar®49	980	120	32	4.1	2.5	1.44
Glass	260	55	9	2	4	2.55
PET	50-110	5-12	6-9	1	10-16	1.38
Graphite	600-4000	100-700	6-25	1-4	0.6-1.6	1.8-2.1

PBT films extruded from MSA and PPA solution to date exhibit similar moduli to as-spun PBT fibers but only about 50% of the strength. Heat treatment of PBT films has produced strengths as high as those in PBT fibers, but only half the modulus. The PBT films are highly anisotropic and split easily.

Allen et al. [19] have studied PBT fibers in torsional pendulum experiments. Heat treated PBT fibers were found to have a shear modulus

of 1.3 GPa and a ratio of tensile to shear moduli of 150. This may be compared to a ratio of 80 for Kevlar 49® fibers calculated from data reported by Dobb et al. [67]. For isotropic materials the tensile to shear modulus ratio lies between 2.5 and 3. Thus PBT fibers are mechanically highly anisotropic.

CHAPTER III

SAMPLE PREPARATION AND EXPERIMENTAL TECHNIQUES

In this chapter we report the general methods used to prepare liquid crystalline solutions of PBT and techniques used to prepare samples of PBT fibers and films for observation by polarized light microscopy, transmission electron microscopy, wide and small angle x-ray scattering and small angle neutron scattering. PBT was supplied by J. Wolfe of Stanford Research Institute in the form of PPA reaction mixtures and precipitated powders. Fibers and films prepared under selected processing conditions described in Chapter II, were supplied by E.C. Chenevey [12,13] of Celanese Research Corporation.

3.1 Preparation of Liquid Crystalline Solutions for Characterization

Solutions were prepared from PBT powders which were previously dried in a vacuum oven at 110° to 120°C for at least three days. MSA was purified by vacuum distillation (105 - 107°C, 25 m torr) as suggested by Perrin *et al*. [19]. Following the suggestion of Berry *et al*. [10], the polymer, freshly distilled solvent, and a Teflon stir bar were placed in a 35 ml centrifuge tube sealed with a Teflon-lined cap and slowly rotated in a magnetic field while gently heated to 60°-90°C. Material transfers were performed in a glove bag purged with dry N_2. This procedure prevented contamination by atmospheric moisture. Solutions for optical microscopy (Chapter IV) and small-angle

neutron scattering (Chapter VIII) were prepared in this manner.

3.2 Sample Preparation of Polarized Light and Differential Interference Microscopy

In order to prepare samples of PBT solutions in MSA for observation, a small droplet of solution was transferred to a clean glass slide which had been dried in an oven at 110°C for 24 hours. This transfer was performed in a glove bag. After placing the droplet on a glass slide, a dry coverslip was placed on top of the droplet. The assembly was quickly removed from the glove bag and sealed with paraffin. Samples prepared in this manner were observed to remain free from coagulation for several weeks. The solutions were normally examined within 2-3 days after preparation on a Zeiss Standard WL microscope equipped with a rotating stage and rotating polarizer and analyzer. All observations were made with the microscope aligned for Köhler illumination [20].

Fibers and films were prepared for examination by removing a sample from the cardboard tube on which they were supplied exercising care to minimise deformation due to handling. Since these materials have low compressional and shear strength the fibers and films were easily kinked. Samples were mounted in Permount® [Fischer Scientific, n = 1.5]. Samples were examined under crossed polars and Zeiss-Normaski differential interference contrast with the microscope aligned for Kohler illumination [20]. Micrographs under polarized light were taken on Kodak Tri-X® Film and developed in D76 for 5 minutes at 20°C.

In Zeiss-Nomarski differential interference contrast (DIC) equipment [21], a plane polarized incident beam is split or "sheared" by a modified Wollaston prism (see Figure 13). For the 40X/0.65 numerical aperture objective used, this corresponds to 0.55 μm separation, about the limit of resolution of the objective. After passing through the object, the two beams are recombined with a second modified Wollaston prism. Contrast is generated by the phase difference between the two interferring wave fronts. The contrast is varied by adding a bias retardation by using a compensator or, more easily, by displacing one of the prisms [22]. Thus one may obtain maximum contrast by adjusting the interference colors from the path difference to the response of the film. For the present work we followed the suggestion of D. Thompson of the Royal Microscopical Society [23] and used KODAK SO115 film developed in HC110 developer diluted 1:9 with H_2O for 6 minutes. This provided a contrast index of 1.45 [24].

3.3 Sample Preparation and Transmission Electron Microscopy

One major difficulty in the application of transmission electron microscopy to bulk samples is the need to obtain ultrathin (100 nm or less) specimens which are representative of the bulk. There are three general methods to achieve this which are listed in the order of increasing difficulty:

1. Disruption by sonication
2. Detachment/extraction replication
3. Ultra microtomy

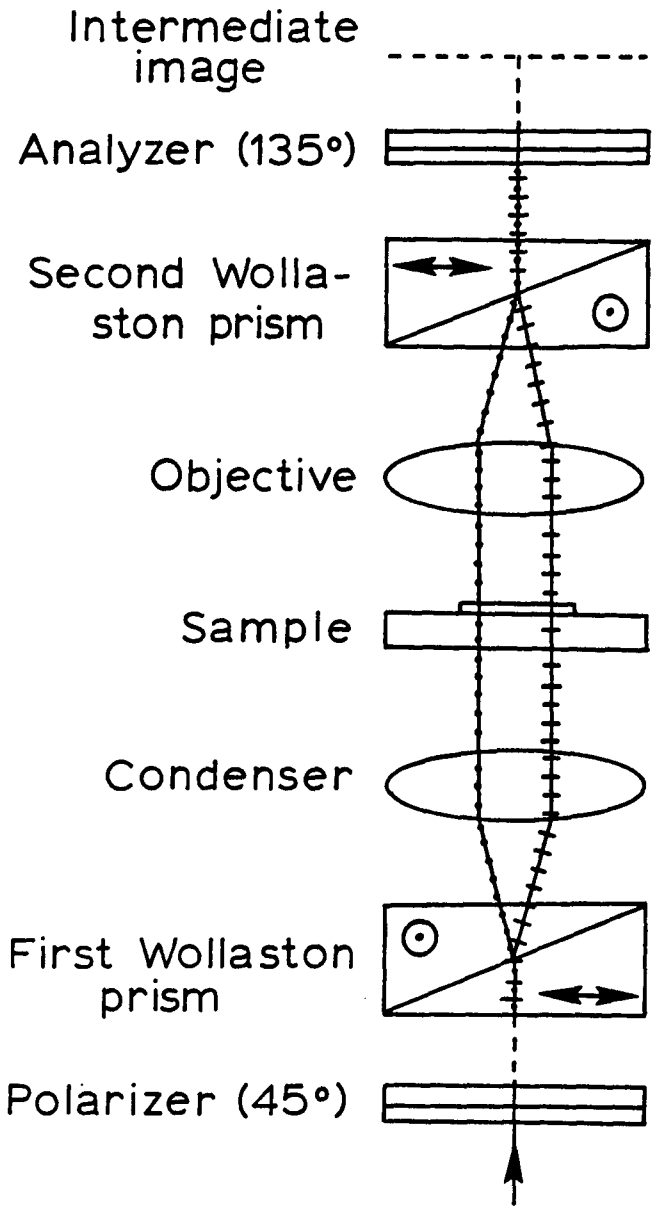

Figure 13. Optics for Zeiss-Nomarski differential interference contrast equipment. From Reference [21].

Sample preparation by ultrasonic disruption involves placing the sample into a fluid and dispersing with a tissue disruptor. Roche and Takahashi [25] used this method in early work on PBT and a typical bright field/dark field image pair obtained by transmission electron microscopy is shown in Figure 14. The kink bands denoted by arrows arise due to deformation during sample preparation and are artefacts.

Ultramicrotomy is tedious and involves embedding the material in a resin such as epoxy and sectioning with a glass or diamond knife. Shimamura [26] attempted to section PBT fibers and was unable to obtain transverse sections without inducing severe distortion of the PBT chains (see Figure 15). Similar difficulties have been encountered by Dobb et al. with PPTA fibers [27]. Some success was achieved by sectioning at 45° to the fiber axis and using a low viscosity Spurr® resin which penetrated into the microvoids in the fiber.

In this work, samples of fibers were prepared by detachment/extraction replication in which thin fragments were extracted from the surface of the fiber or film during the process of preparing a surface replica. Hereafter we will refer to this technique as detachment replication. Samples have been prepared using two variations of the technique. The first variation, shown in Figure 16, is that outlined by Geil [28]. A film is attached to a glass microscope slide with epoxy and allowed to dry for 24 hours. The surface of the film is then lightly shadowed at about 30° in a vacuum evaporator with C/Pt. The sample is then coated at about 90° with carbon to form the replica. Next, a thick (ca. 2-3 mm) of a concentrated aqueous

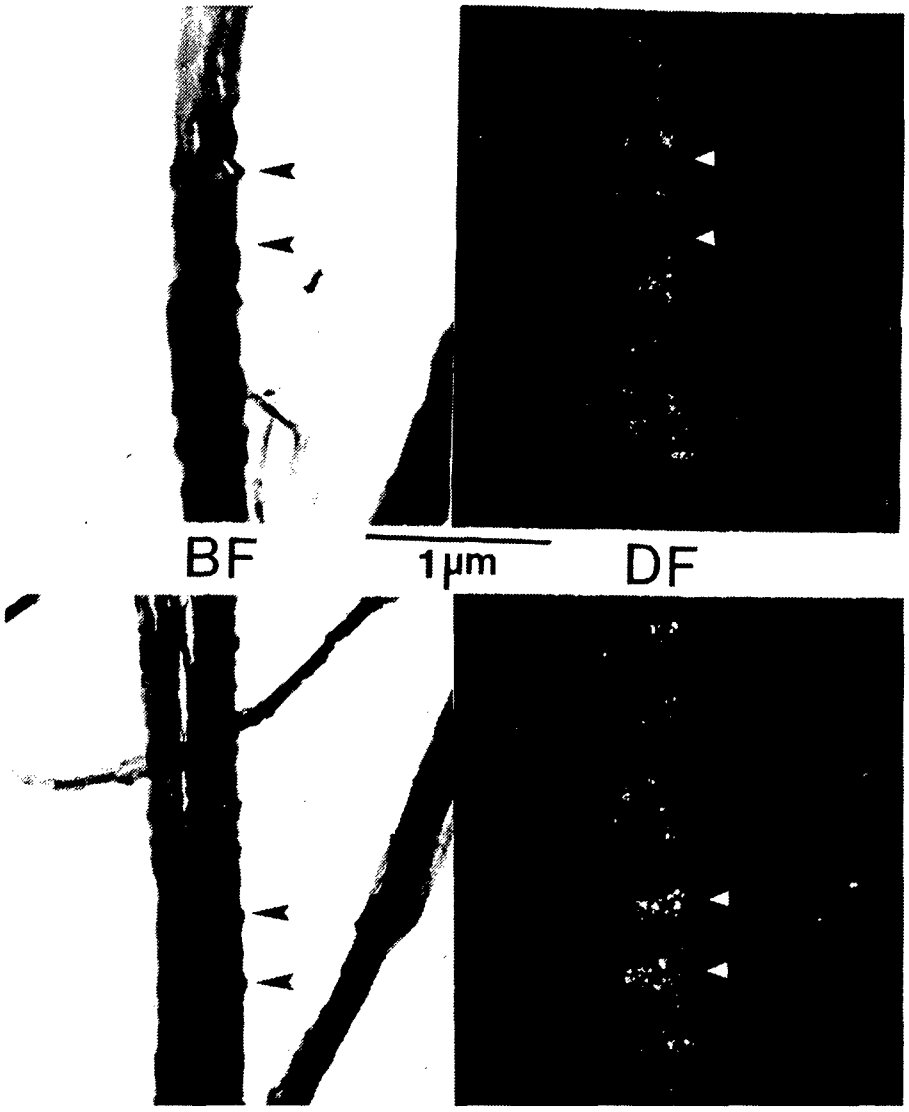

Figure 14. Kink bands observed in PBT fibers prepared by sonication. From Reference [25].

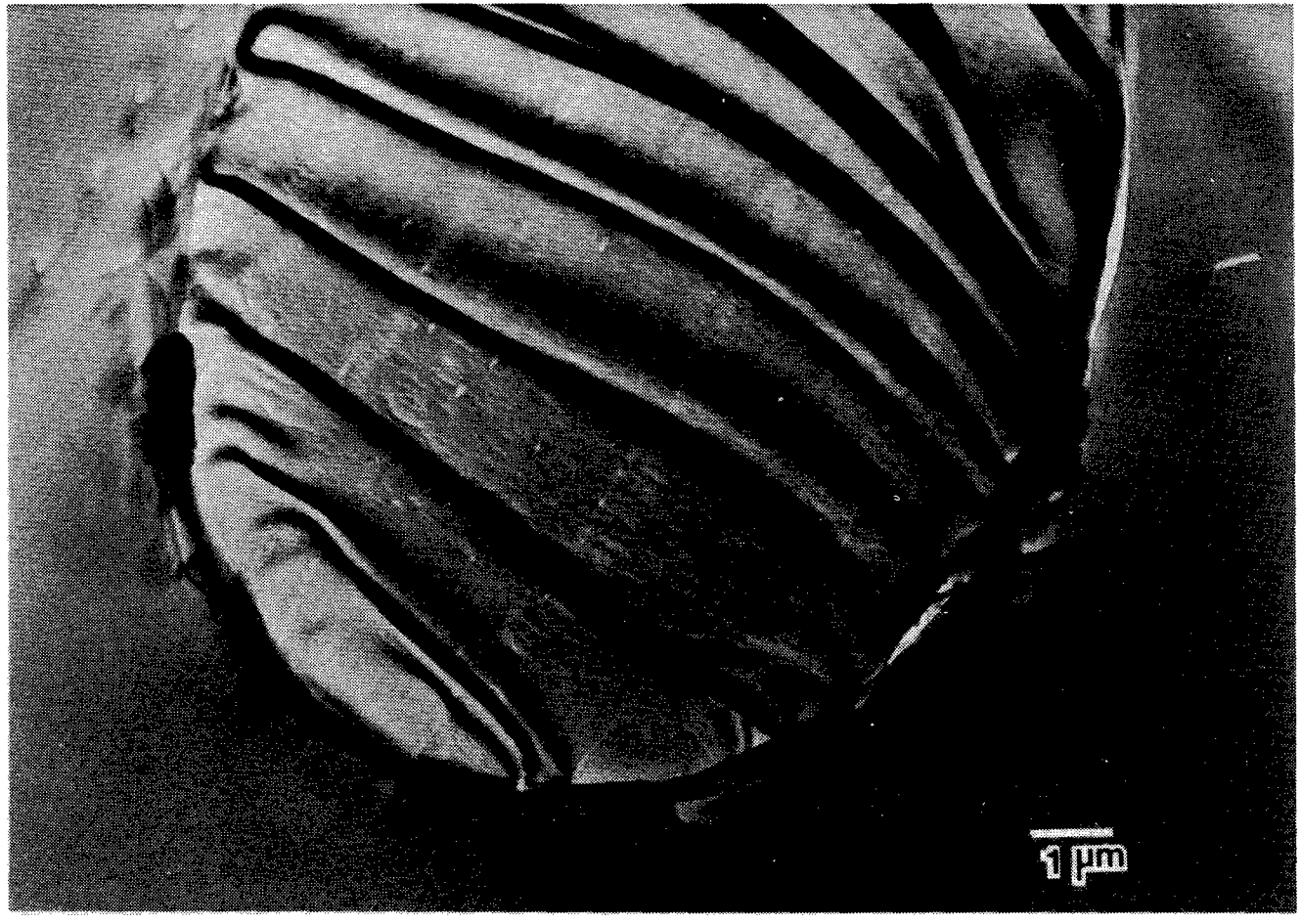

Figure 15. Transverse section of a PBT fiber. Notice the deformation caused by the microtome knife. From Reference [26].

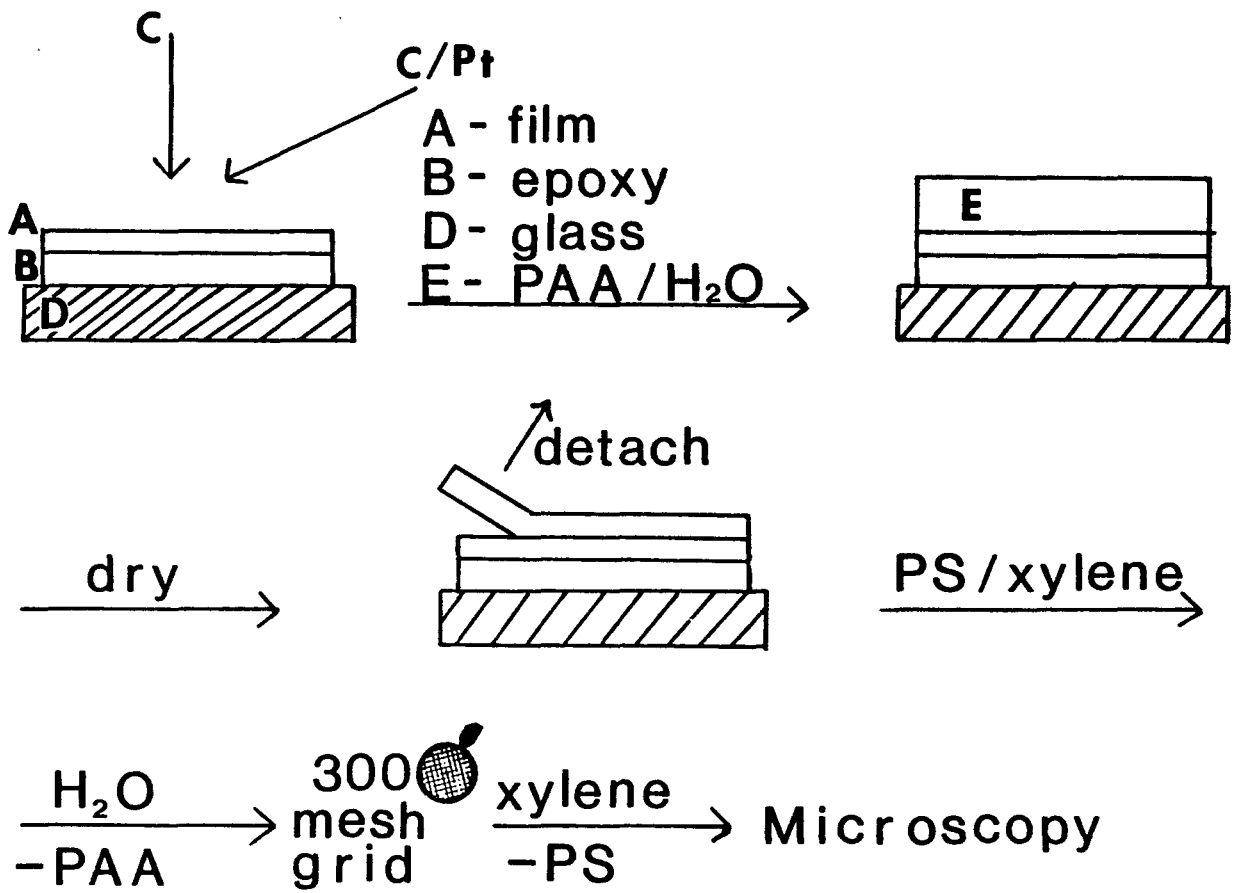

Figure 16. Detachment replication procedure I with polyacrylic acid (PPA). After Geil [28].

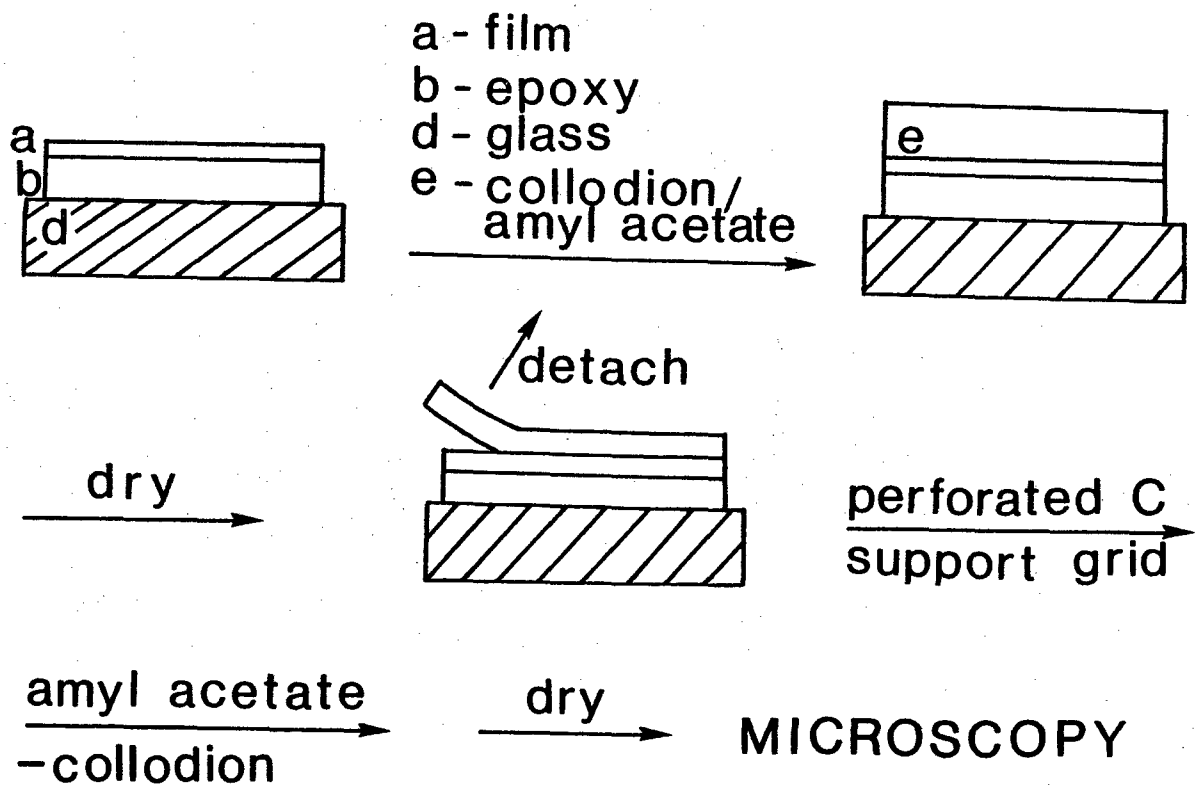

Figure 17. Detachment replication procedure II with collodion. From Reference [29].

solution of polyacrylic acid (PAA) is spread on the sample. After drying, the replica is detached also removing fibrillar fragments from the surface. At this stage the replica is lightly coated with dilute solution of polystyrene in xylene and the PAA is dissolved in H_2O. This last step prevents surface tension from breaking the carbon replica. Finally, the replica is placed on top of a 400 mesh grid and the polystyrene is dissolved with xylene. The advantage of this technique is that the detachment induces very little deformation of the material. This technique works well because of the fibrillar nature of the films and their poor transverse strength.

The second variation of this technique was amenable to the study of both fibers and films and was adapted from a procedure used at Kyoto University [29]. In this second version a concentrated solution of collodion (nitrocellulose) in amyl acetate was used in place of PAA. In the case of films the procedure shown in Figure 17 was used. The samples were only lightly coated (10 nm or less, as outlined by Dubochet [30]) with carbon for thermal stability or left uncoated and covered with collodion. The detached, extracted fragments were then suspended across 400 mesh grids covered with perforated carbon support films prepared as described by Baumeister and Hahn [31]. The advantage of this technique was the fast drying time of the collodion solution and the availability of substrate free areas for imaging. It was important to allow the collodion to dry thoroughly before detachment to avoid inducing kink bands in the fibrils. Fibers were detachment replicated by suspending them over a film of collodion/amyl acetate

dried such that the surface was tacky but the fiber was not embedded. The fibers were then detached using Scotch® tape, and the collodion dissolved with the replica suspended over 400 mesh grids previously coated with perforated carbon films.

3.4 Transmission Electron Microscopy

Samples prepared as outlined above were examined by transmission electron microscopy on a JEOL 100 CX operated at 100 KeV. Care was taken to minimize specimen beam heating by working at low electron dose rates, typically 2.8×10^{-3} Amp cm^{-2} or lower. Samples were examined in bright field (Figure 18) where only electrons scattered at angles less than the radius of the objective aperture were used to form the image and in tilted beam dark field (Figure 18) where the incident beam was tilted to allow only the desired scattered electrons to pass the objective aperture and form the image. This latter technique is discussed in detail in Chapter VI. Selected area diffraction patterns were formed by decreasing the strength of the intermediate lens in order to image the back focal plane of the objective lens.

The sample was searched in a systematic fashion in order to always move to areas undamaged by previous irradiation. To obtain minimum dose images, focussing was performed with the beam deflected so that the image was formed on an auxillary phosphorescent screen and sample adjacent to the are of interest was radiation damaged. This is shown in Figure 19. A plate was then loaded into the camera and the beam

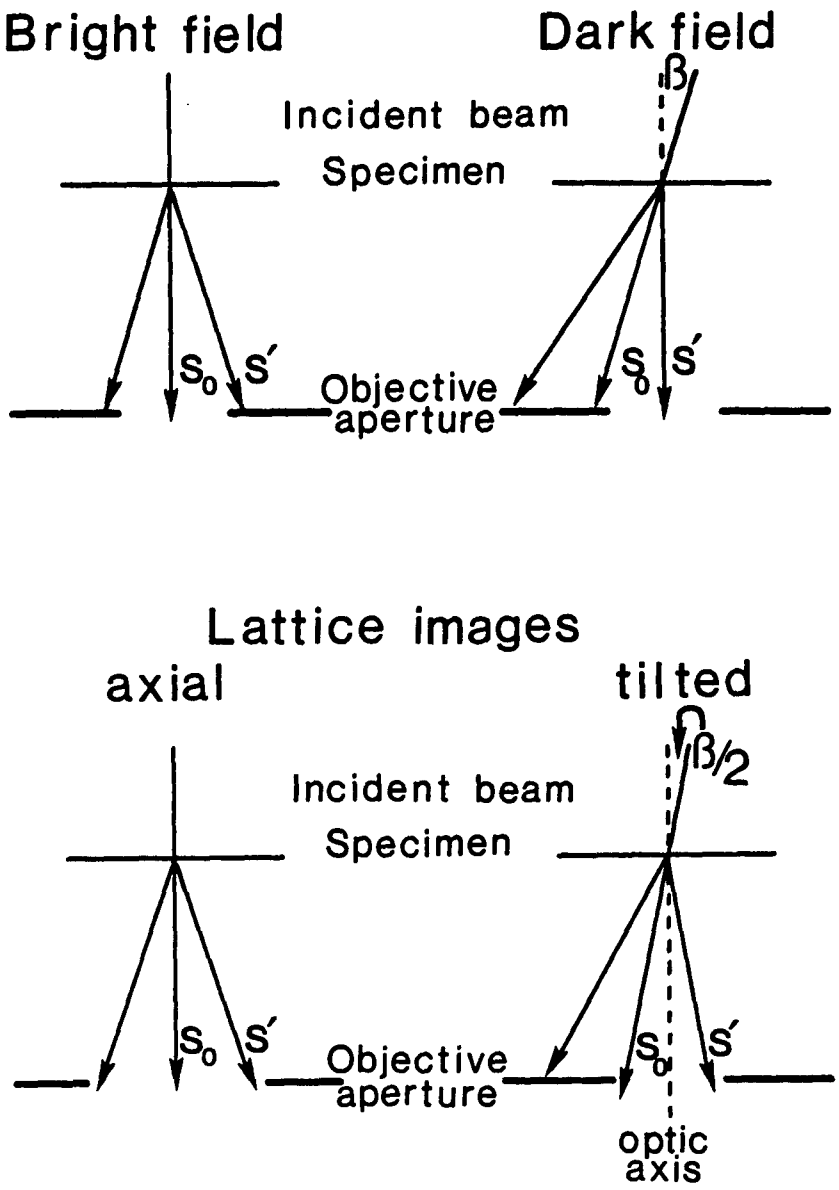

Figure 18. Image formation in the TEM. S_0-incident beam S'-scattered beam.

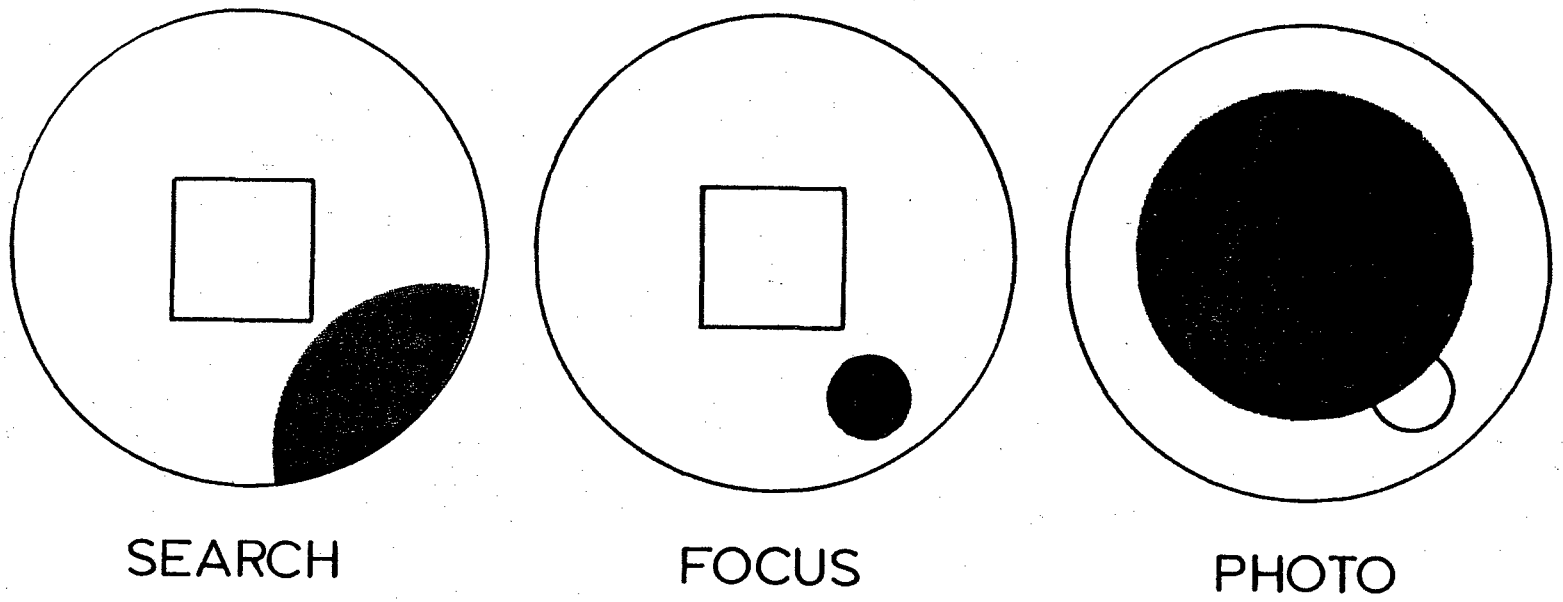

Figure 19. Electron microscopy with minimum electron irradiation damage. Square - area to be photographed. Small circle -auxillary viewing screen. Shaded area - electron beam. From Reference [65].

deflected back onto the optic axis and the image recorded. Kodak 4463 and 4489 films were used and developed for 4 minutes at 20°C in D19 diluted 1:2 in H_2O. The current produced by electrons incident on the viewing screen was measured with a Keithley electrometer (see Figure 20). The analysis of such measurements will be discussed in detail in Chapter VI.

3.5 Microdensitometry of Electron Diffraction Patterns

Intensity profiles of electron diffraction patterns were measured by microdensitometry. Radial 2θ, traces of equatorial reflections were obtained on a Joyce Loebl Model MK III CS kindly made available by Mr. R. White of Smith College. Diffraction patterns were scanned at 10:1 and 20:1 ratios using a 10 X objective. Typically, 20 - 40 μm primary slits were used with a slit height of 5 mm. The wedge used had a nominal optical density range of 0 to 2.52 although calibration with a step wedge revealed a practical upper limit of approximately 1.40 before the signal to noise ratio became intolerable at these slit settings. The exposure-density curve of the film used was observed to be linear up to a density of approximately 1. The microdensitometer response to the photographic step wedge revealed instrumental broadening to be negligible for the conditions used.

Intensity traces of non-equatorial layer lines in electron diffraction patterns were obtained form an Optronics Photoscan located at Wright Patterson Air Force Base with aid of software written by Mr. Dale Ford of the Air Force Materials Laboratory (AFML). Typically,

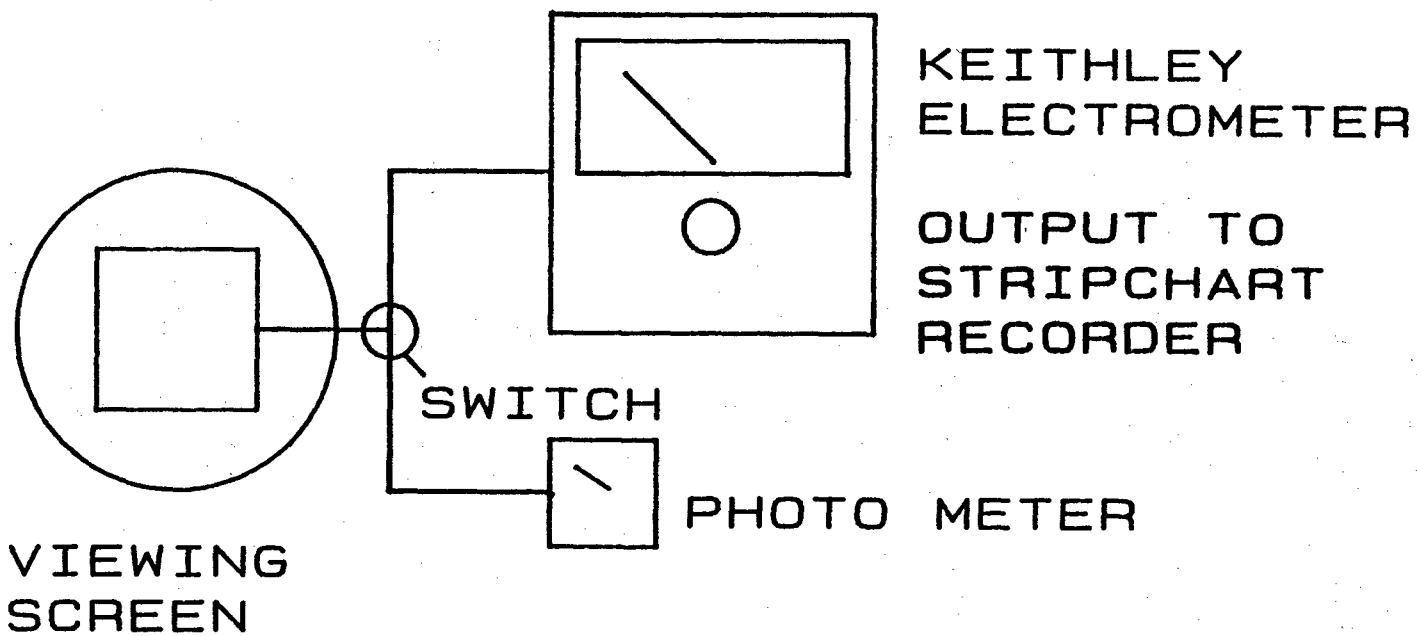

Figure 20. Direct measurement of electron current incident upon viewing screen.

electron diffraction patterns were scanned at 100 μm resolution and the data analyzed on the AFML's Prime Computer. This instrument was reported to respond linearly to optical density up to a value of 4.0 [32], well beyond the linear range of the film.

3.6 Sample Preparation for X-ray Diffraction

Fiber samples were prepared for x-ray diffraction by carefully winding the fibers around cardboard tabs with v-shaped notches and then tying the bundle together with cotton thread. Film samples were carefully prepared by stacking films. Final sample thickness was about 1 mm.

3.7 Wide Angle Diffraction Measurements

Equatorial intensity traces from selected fibers and films were obtained on the Siemens D-500 x-ray diffractometer with a Cu Kα tube and line focus collimation. Typically 0.3° (2θ) initial slits and a final slit of .018° (2θ) were used. The height of the initial slits was limited to about 3 mm by lead wedges. Samples were also measured on a Picker FACS 1 diffractometer with pinhole collimation through the courtesy of Dr. A. Viswanathan and Mr. W. W. Adams of the Air Force Materials Laboratory. Flat film photographs were also recorded on a Statton camera at the Air Force Materials Laboratory by Mr. Gary Price.

3.8 Small Angle X-ray Scattering

Small angle x-ray scattering measurements on selected fibers and

films were measured on the Oak Ridge National Laboratory 10-M SAXS apparatus with a 2-dimensional position sensitive detector. This facility is described in detail in reference [33]. Data was collected on each sample for 2000 sec corresponding to approximately 10^7 total counts (all elements) above background. The data were corrected by subtracting the intensity of parasitic scattering and for detector sensitivity by scaling by the intensity of the detector when evenly illuminated with a ^{55}Fe source. Unfortunately ^{55}Fe is not quite the optimum x-ray wavelength to correct for detector sensitivity because the 5.8 KeV x-rays from the ^{55}Fe source interact less strongly with the Al grid covering the detector than do the 8 KeV Cu Kα x-rays. PBT fibers swollen with H_2O were measured using liquid cells with thin Mylar® windows.

Transmission coefficients were measured by comparing the intensity of microvoid scattering from a glassy carbon standard with and without the sample in the beam. This method was found to result in values which were systematically 10% too large by comparison to a Kratky Lupolen (polyethylene) Standard. Thus, the transmission coefficients measured by this method were corrected by -10%. Therefore experimentally measured intensity at each of the 4096 detector elements, I_{exp}, was corrected to give

$$I_{COR} = \left[\left(I_{EXP} - \frac{I_{DC}S_m}{D_m}\right) - \frac{T_S S_m}{T_B B_m}\left(I_{BKG} - \frac{I_{DC}B_m}{D_m}\right)\right] \frac{SUM}{I_{SENS}} \qquad (3.1)$$

where I_{DC} = counts collected due to dark current

I_{BKG} = counts collected without the sample

I_{SENS} = counts collected with detector evenly illuminated with ^{55}Fe

$$SUM = \frac{1}{4096} \sum_{i=1}^{4096} I_{SENS}(i) \qquad (3.2)$$

B_m = primary beam monitor counts during background collection

D_m = primary beam monitor counts during dark current collection

S_m = primary beam monitor bounts during sample data collection

T_s = transmission coefficient of the sample

T_B = transmission coefficient of the sample cell, = 1 when samples were examined without cells

3.9 Small Angle Neutron Scattering

Liquid samples prepared as in section 3.1 were sealed in quartz cells of 2 mm path length. Blends of 10% D_4H_2PBT were mixed with 90% H_6PBT and a 10% solution in MSA was processed into oriented and unoriented films on an apparatus similar to that described by King and Berry [15]. These samples were stacked in 1 cm x 1 cm x 1 mm arrays. The ORNL 30-M small angle neutron scattering appartus with a 2-dimensional position sensitive detector was employed. Scattered intensity was corrected for dark current, detector sensitivity and parasitic scattering in a fashion identical to the x-ray work.

3.10 Fiber and Film Nomenclature

PBT fibers and films prepared with selected processing histories were supplied by Chenevey [12,13] using the apparatus described in Chapter II.

Samples are referred to by three letters and a numeral. The first two letters are either "AE", which specifies "as extruded", or "HT", which specifies "heat treated". The third letter is either "F" ("fiber") or "R" (film or "ribbon"). The number is an identifying index given in roughly chronological order. For clarity, the heat treated fiber of film has been given the same numerical index as the as-extruded precursor. The processing history of samples used are given in Table III. Typical physical-chemical data for the samples used in this study are summarized in Table IV.

Table III

Processing History of Samples Used in This Study

A. As Spun Fibers

Sample I.D.	L.V.N.	Solvent	% Polymer	SDR	Air Gap (mm)	% Solvent in C.B.	C.B. Temp. (°C)	T GPa	E %	M GPa	Ref
ASF-1	14	MSA	9.5	2.0	13	37.5	23	1.27	3.9	84	40
ASF-2	14	MSA	9.5	2.0	13	37.5	23	1.25	3.8	80	40
ASF-3	14	MSA	9.5	2.0	13	50	23	1.41	3.2	133	40
ASF-4	18	MSA	9.5	2.0	13	50	23	1.28	3.7	106	40
ASF-5	18	MSA	9.5	2.0	6	50	23	1.20	3.3	102	40
ASF-6	18	MSA	9.5	3.9	13	50	23	1.31	2.9	143	40
ASF-7	18	MSA	9.5	2.0	13	37.5	23	1.13	3.5	83	40
ASF-8	18	MSA	9.5	2.0	13	37.5	23	1.16	3.4	91	40
ASF-9	18	MSA	9.5	2.0	13	25	23	0.99	2.7	83	40
ASF-10	18	MSA	9.5	2.0	13	25	23	1.04	3.0	78	40
ASF-11	18	MSA	9.5	3.9	15	50	23	1.37	2.8	116	12
ASF-12	18	MSA	9.5	4.8	15	50	8	--	---	--	12
ASF-13	18	MSA	9.5	3.5	15	50	8	1.53	2.9	142	12
ASF-14	18	MSA	9.5	2.0	15	50/50	8/24	1.50	3.0	131	12
ASF-15	18	MSA	9.5	2.0	15	50	-10	1.33	2.0	147	12
ASF-16	18	MSA	9.5	2.0	15	50	- 5	1.23	1.7	134	12
ASF-17	18	MSA	9.5	2.0	15	50	19	0.71	3.1	62	12
ASF-18	18	MSA	9.5	2.0	15	50/50	12-19/23	1.24	2.4	132	12
ASF-19	18	MSA	9.5	2.0	15	50/50	4-0/23	0.74	2.5	76	12
ASF-20	18	MSA	9.5	2.0	15	50/50	-1/23	0.78	2.1	77	12
ASF-21	18	MSA	9.5	2.0	15	50	0	1.30	2.4	125	12
ASF-22	18	MSA	11	3.8	15	50	24	1.33	1.9	144	12
ASF-23	18	MSA	11	4.9	15	60	1.37	1.3	150	12	
ASF-24	31	MSA	8	0.3	15	50	23	0.10	9.4	8	12
ASF-25	31	MSA	8	1.0	15	50	23	0.45	8.4	21	12

Table III (cont'd.)

A. As Spun Fibers

Sample I.D.	L.V.N.	Solvent	% Polymer	SDR	Air Gap (mm)	% Solvent in C.B.	C.B. Temp. (°C)	T GPa	E %	M GPa	Ref
ASF-26	31	MSA	8	1.9	15	50	23	1.16	3.8	98	12
ASF-27	31	MSA	8	2.9	15	50	23	1.20	3.4	88	12
ASF-28	31	MSA	8	3.8	15	50	23	1.07	1.9	119	12
ASF-29	31	MSA	8	0.5	15	8	23	0.24	21.5	10	12
ASF-30	31	MSA	8	1.1	15	8	23	0.93	4.9	52	12
ASF-31	31	MSA	8	1.6	15	8	23	1.27	4.2	59	12
ASF-32	31	MSA	8	2.1	15	8	23	1.46	3.7	76	12
ASF-33	31	MSA	8	2.6	15	8	23	1.50	2.7	127	12
ASF-34	31	MSA	8	2.1	15	8	23	1.44	3.5	112	12
ASF-35	31	MSA	8	2.1	15	8	23	1.48	3.4	116	12
ASF-36	31	MSA	8	1.1	15	8	23	1.22	4.3	86	12
ASF-37	31	MSA	8	2.1	15	8	23	1.41	2.7	128	12
ASF-38	31	MSA	12	2.6	15	12	23	1.54	2.0	156	12
ASF-39	31	PPA[1]	5.6	3.7	159	9	23	2.30	7.5	54	12
ASF-40	31	PPA[2]	5.6	3.6	75	0	23	2.39	5.4	80	12
ASF-41	31	PPA[3]	5.6	3.7	75	9	23	2.54	6.9	68	12
ASF-42	31	PPA[4]	5.6	3.8	75	0	23	2.36	6.6	73	12

Extrusion temperatures [1] 66°C, [2] 50°C, [3] 57-62°C, [4] 50°C.

Table III (cont'd.)

B. Heat Treated Fibers

Sample I.D.	Temperature °C	Time (sec)	Stretch (1%)	T GPa	E_B %	M GPa	Ref
HTF-23A	475	32	1.0	1.91	1.1	183	12
HTF-38	525	32	1.4	2.30	0.9	287	12
HTF-41A	475	64	4.0	2.91	1.2	270	12
HTF-41B	475	64	1.1	1.29	6.2	86	12
HTF-40	475	30	0.8	2.47	1.8	177	12
HTF-42	475	30	0.8	2.40	2.4	144	12

L.V.N. = Limiting viscosity number
SDR = Spin draw ratio
C.B. = Coagulation bath
T = Tenacity
E = Elongation to break
M = Modulus

Table III (cont'd.)

A. As Spun Films

Sample I.D.	L.V.N.	Solvent	% Polymer	SDR	Air Gap (mm)	% Solvent in C.B.	C.B. Temp. (°C)	T GPa	E %	M GPa	Ref
ASR-1	26	PPA	10	26+	---	0	23	---	---	---	A
ASR-2	26	PPA	10	67+	---	0	23	---	---	---	A
ASR-3	18	MSA	9	160+	---	0	23	---	---	---	A
ASR-4	20	MSA	12	1.4	1.5	50	20	.415	4.2	25	12
ASR-5	30	MSA	12	1.4	1.5	50	20	.435	4.5	26	12
ASR-6	30	MSA	12	1.4	1.5	50	20	.316	6.1	13	12
ASR-7	30	PPA	12	1.4	1.5	50	20	.372	7.9	13	12
ASR-8	14	PPA	9.2	5.3	0.5	0	19	---	---	---	13
ASR-9	14	PPA	9.2	5.3	0.5	0	19	1.16	2.4	93	13
ASR-10	14	PPA	9.2	3.5	4.0	0	19	1.06	1.9	99	13
ASR-11	14	PPA	9.2	5.3	0.5	0	19	1.19	2.6	92	13
ASR-12	14	PPA	9.2	5.3	0.5	0	19	1.16	2.3	93	13
ASR-13	14	PPA	9.2	1.3	1.5	0	19	1.20	2.1	109	13
ASR-14	14	PPA	9.2	7.1	6.5	0	23	1.24	4.0	66	
ASR-15	14	PPA	9.2	21.7	7.0	0	23	1.16	2.3	78	

+ shear rate (sec^{-1})

A - This work, with J. Odell on apparatus in Reference [40]

Table III (cont'd.)

B. Heat Treated Fibers

Sample I.D.	Temperature °C	Time (sec)	% Stretch	Load g	T GPa	E_B %	M GPa	Ref
HTR-4	475	32	---	~ 25	.190	1.8	13	12
HTR-5	475	32	---	~ 25	.255	1.6	19	12
HTR-6	475	32	---	~ 25	.207	4.1	7	12
HTR-7	475	32	---	~ 25	.155	2.8	7	12
HTR-9	400	3600	---	25	---	---	---	B
HTR-13A	475	32	---	500	1.58	2.0	123	13
HTR-13B	525	32	0.6	---	0.92	1.1	116	13

(GPa = 0.141 g/den)

B - This work

Table IV

Typical Physical-Chemical Data for Samples Used in This Study

Polymer MW ≈ 15,000

Mer MW ≈ 266

DP ≈ 50

C_{repeat} = 1.245 nm

L_{chain} = 70 nm

Persistance Length = 45 nm

Nematic > 3-5 wt% at 25°C

Methanesulfonic Acid

Chlorosulfonic Acid

Polyphosphoric Acid

CHAPTER IV

POLARIZED LIGHT AND INTERFERENCE MICROSCOPY OF PBT SOLUTIONS, FIBERS AND FILMS

In this chapter concentrated solutions, fibers and films of PBT are examined by polarized light and inteference microscopy. Solutions were examined to determine whether the features present in low molecular weight nematic liquid crystals were present in PBT solutions. Fibers and films were examined for the presence of macroscopic defects and evidence of orientation.

4.1 Light Microscopy of PBT Solutions

An MSA solution of 9% PBT of limiting viscosity number 18 was examined by polarized light and interference microscopy. This concentration was typical of that used to spin fibers and exhibited stir opalescence. Immediately after a droplet was sandwiched between a clean dry glass slide and coverslip, the sample was sealed with molten paraffin. Initial examination in cross polars revealed a large number of very small defects. After the sample had relaxed for 48 hours, one could observe the classical Schlieren texture (see Figure 21) similar to that observed in low molecular weight nematic compounds [34,35]. Upon rotation of the stage (see Figure 22), one observes that the "threads" exhibit maximum extinction at different rotation angles than for the background.

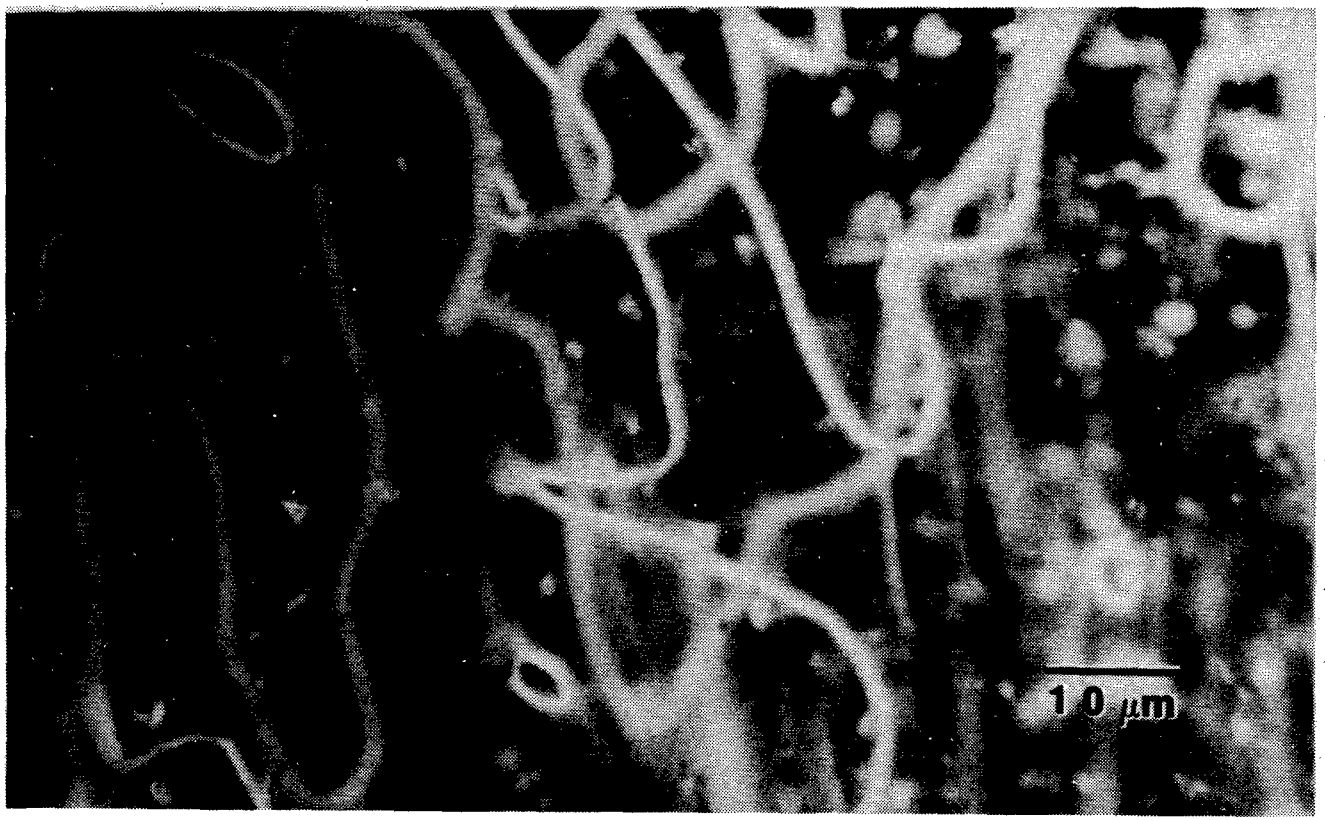

Figure 21: Schlieren texture in 9% PBT in MSA after 48 hours relaxation.

Figure 22 Inversion wall in 9% PBT in MSA as a function of orientation. Polarizer vertical, analyser horizontal.

According to Chandrasekhar [34] such textures arise from inversion walls perpendicular to the fluid layer. The alignment of the molecules is parallel to the surfaces of the slide and coverslip except near the wall. This represents the correct identification of classical nematic texture in PBT solutions. Chenevey [13] has observed texture similar to Figure 21 but did not correctly identify the defect structure. Similar results have been observed in solutions of PPTA and its derivatives in H_2SO_4 by Benoit and Strazielle [36] and Morgan [37] and an example is shown in Figure 23. It is important to reiterate that 48 hours at room temperature were required for the defect structure seen in Figures 21 and 22 to develop to the scale of several microns. At early times there appears to be a high density of much smaller defects perhaps induced during fluid deformation during sample preparation. An important question to ask is how these defects affect the solidification process during fiber and film formation. These may in part account for the low degree of lateral strength which was observed in 'as-spun' fibers and films which is discussed in detail in Chapters VI and VII.

When small, isolated droplets of PBT in MSA are examined under polarized light, their extinction pattern frequently appears similar to that expected from spherulites. However, closer examination indicates that the extinctions are due to molecular alignment around point defects termed disclinations [34,35]. Disclinations represent singularities in the molecular orientation and are well known features in low molecular weight liquid crystals. Several authors, for example

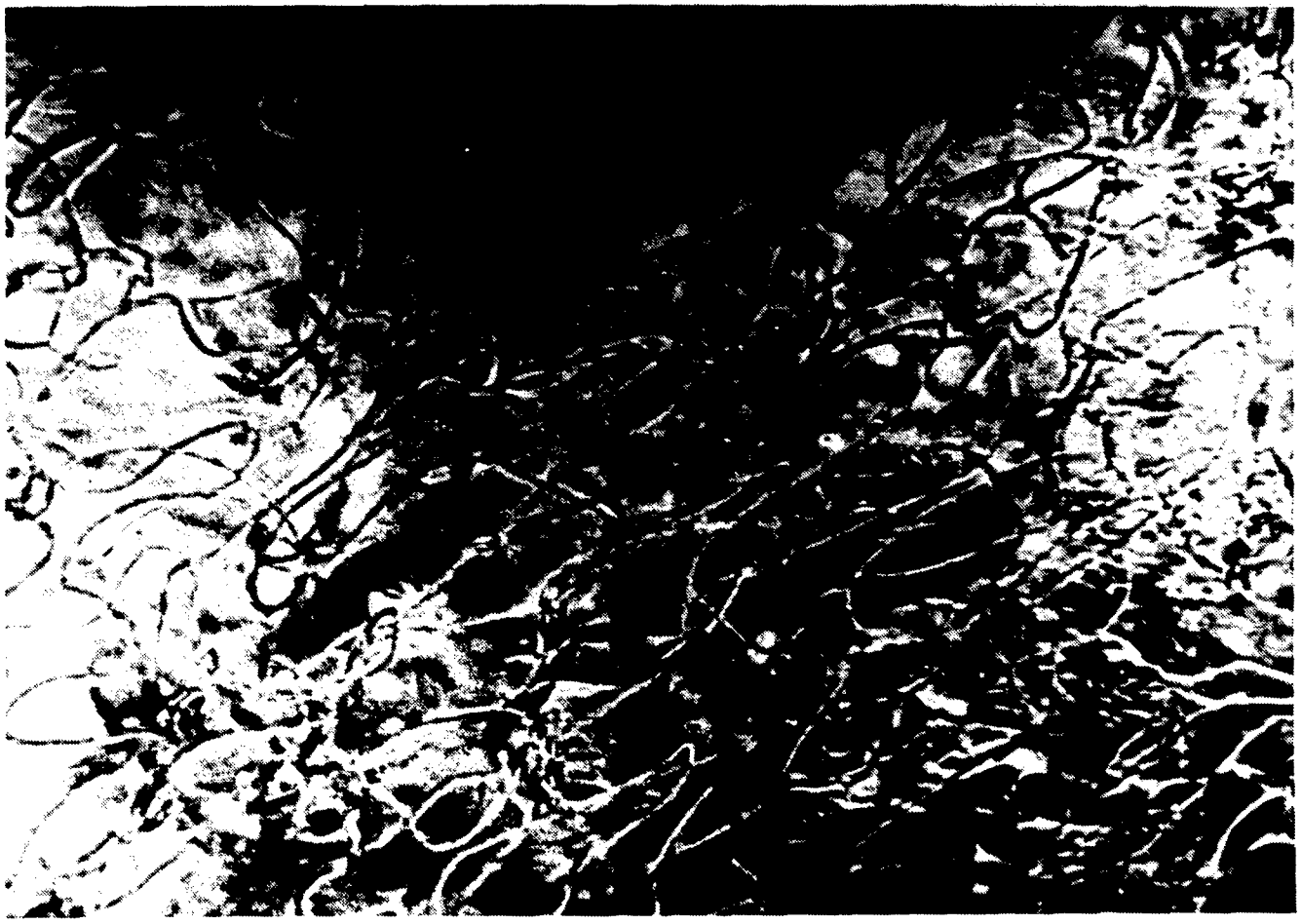

Figure 23. Nematic texture in H_2SO_4 solutions of PPTA. Micrograph courtesy of Benoit and Stazielle [36]. No magnification value supplied.

Onogi et al. [38], have mistakenly termed such texture as in Figure 24 spherulites. This is a misnomer, since the supramolecular alignment of a polymer spherulite is radial and only one type of disclination has such an arrangement [34].

To summarize, classical nematic textures have been correctly identified for the first time in PBT solutions. These textures reveal the presence of defects, the size and density of which are strongly dependent on previous flow history and on the time and temperature at which the solution is in a given configuration. These defects also have important ramifications for processing. This work indicates the need for further studies of the effect of such defects on coagulated films. For instance, one could study well annealed solutions containing only a few defects oriented in a shear field until coagulated. Measurement of mechanical properties of such films should reveal if these defects act as failure initiation sites.

4.2 Light Microscopy of PBT Fibers

A series of PBT fibers prepared under varying processing conditions were examined with the optical microscope using crossed polars and Zeiss-Nomarki differential interference illumination. Both techniques revealed that the fibers contain two principal types of defects which have been categorized as:

1. Voids
2. Circumfrential bands

The linear number density (voids/mm fiber) of voids from a series

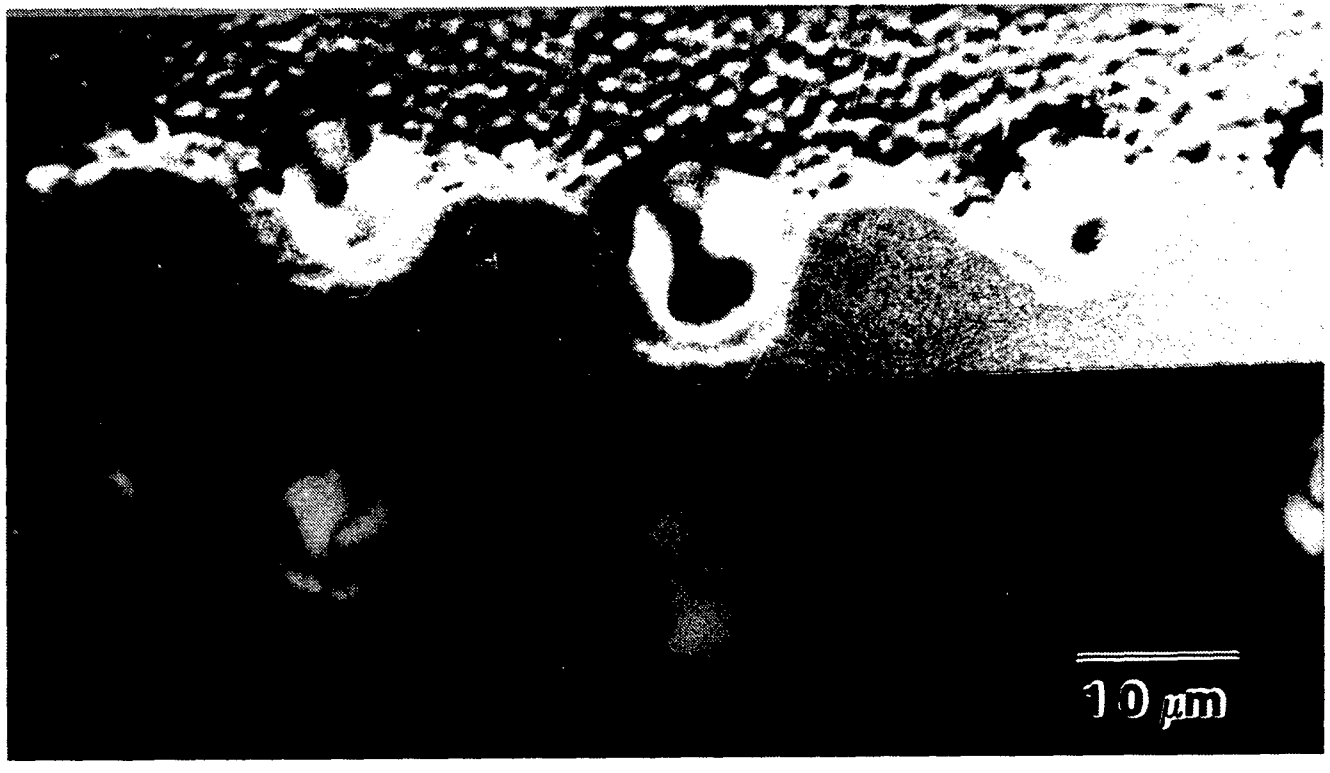

Figure 24. Anisotropic PBT/MSA domains in an isotropic matrix as viewed by interference and polarized light microscopy. Top: interference Bottom: crossed polars.

of fibers spun from MSA solutions using selected draw ratios, coagulation bath compositions and coagulation bath temperatures is given in Table V. The most significant correlation of void content with processing history is with coagulation bath composition.

In the coagulation process, the extruded polymer solution is forced to undergo a large change in composition. To form a homogeneous fiber requires a decrease in volume of approximately 95%. The coagulation process is quite complicated and difficult to model since one must be concerned with mass and heat transfer with an accompanying phase change in a stretching flow. The modeling of this process is beyond the scope of this dissertation and the expertise of the author, and is an area of active interest of other investigators in this laboratory [39]. However, to understand how the structure is affected by changing coagulation parameters, a brief description of the process must be included.

After extrusion from the spinneret and drawing in the dry-jet region, the oriented polymer solution enters a coagulation bath containing an appreciable fraction of nonsolvent. In the case of PBT, this is typically water, although Berry and Wong [40] have considered other nonsolvents. The solvent begins diffusing out of the solution and the nonsolvent begins diffusing in. Because the solvents are acids, there is a substantial heat of mixing and heat transfer will be important. The rate at which coagulation occurs will generally increase with increasing nonsolvent concentration of the coagulation

TABLE V

Defect Analysis of PBT Fibers from MSA Solutions

#	L.V.N. Polymer	Total Voids per mm	dpf[1]	% MSA[4] Bath	Temp °C	SDR[3]	% Polymer in soln.	Tenacity[2] g/den
ASF-1	14	too thick	5.1	37.5	RT	2	9.5	9.0/8.0
ASF-2	14	15.6	4.2*	37.5	RT	2	9.5	8.9/11/0
ASF-3	14	15.6	3.1*	50	RT	2	9.5	10.0/16.5
ASF-4	18	.7	5.4*	50	RT	2	9.5	9.1/10.2
ASF-5	18	1.7	5.3*	50	RT	2	9.5	8.5/8.7
ASF-6	18	.56	3.3*	50	RT	3.9	9.5	9.3/8.3
ASF-7	18	3.9	6.5*	37.5	RT	2	9.5	8.0/8.6
ASF-8	18	5.1	5.2*	37.5	RT	2	9.5	8.2/7.9
ASF-9	18	7.3	5.3*	25	RT	2	9.5	7.0/8.5
ASF-10	18	3.5	6.3*	25	RT	2	9.5	7.4/8.4
ASF-11	18	2.3	1.6*	50	23	3.9	9.5	9.5
ASF-12	18	1.4		50	8	4.8	9.5	
ASF-13	18	1.9	1.9*	50	8	3.5	9.5	10.8
ASF-14	18	0.55	2.6*	50/50	8/24	2	9.5	10.2
ASF-15	18	unseparable	1.7*	50	-10	2	9.5	9.4
ASF-16	18	3.0	2.2*	50	- 5	2	9.5	8.7
ASF-17	18	2.3	3.8*	50	19	2	9.5	5.0
ASF-18	18	unseparable	1.9*	50/50	12-19/23	2	9.5	8.8
ASF-19	18	4.8	4.0*	50/50	4-0/23	2	9.5	5.2
ASF-20	18	4.4	3.7*	50/50	-1/23	2	9.5	5.5
ASF-21	18	2.1	1.8*	50	0	2	9.5	9.2
ASF-22	18	1.6		50	24	3.8	11	
ASF-23	18	1.6		50	24	4.9	11	
ASF-24	31	too thick	20-7@	50	RT	.26	8	.69
ASF-25	31	2.1	4.4@	50	RT	.96	8	3.2
ASF-26	31	2.6	2.2@	50	RT	1.9	8	8.2
ASF-27	31	4.2	1.6@	50	RT	2.9	8	8.5

TABLE V (cont'd.)

#	I.V. Polymer	Total Voids per mm	dpf[1]	% MSA[4] Bath	Temp °C	SDR[3]	% Polymer in soln.	Tenacity[2] g/den
ASF-28	31	2.5	1.3@	50	RT	3.8	8	7.6
ASF-29	31	too thick	9.4@	50	RT	.53	8	1.7
ASF-30	31	1.9	4.7@	50	RT	1.1	8	6.6
ASF-31	31	2.5	3.2@	50	RT	1.6	8	9.0
ASF-32	31	3.2	2.3@	50	RT	2.1	8	10.3
ASF-33	31	3.3	1.8@	50	RT	2.6	8	10.6
ASF-34	31	2.8	2.2@	50	RT	2.1	8	10.2
ASF-35	31	2.1	2.3@	50	RT	2.1	8	10.5
ASF-36	31	.52	4.6@	62.5	RT	1.1	8	8.6
ASF-37	31	.38	2.4@	62.5	RT	2.1	8	10.0

L.V.N. = Limiting viscosity number

[1]The deniers, supplied by Cheveney [12], were determined by two methods:
*denotes vibrascope @ denotes weight

The two measurements differed by 45% for the case of ASF-25, the vibrascope giving higher values in all cases where both were measured.

[2]Tenacity values are reported Chenevey [12] value Allen [41] value

[3]SDR - spin draw ratio

[4]Two numbers indicate two coagulation baths were used

bath and with increasing temperature. Since the filament is moving through the bath, the residence time in the coagulation bath should be sufficient to completely coagulate the filament before it proceeds to a wash bath (typically 100% water).

Generally, larger amounts of nonsolvent in the coagulation bath produced more macroscopic voids in the fiber, indicating that fast coagulation produces the most defects. The fewest fiber defects were observed for a +6 to +8°C coagulation bath. A 10°C bath yielded more defects - perhaps because the fiber did not have sufficient residence time to fully coagulate before entering a harsher (100% H_2O) wash bath.

These observations are in agreement with those of Epstein and Rosenthal [42] for nylons in sulfuric acid. These authors' results differ from Knudgen's [43] results for polyacrylonitrile fibers where coagulation bath temperature was the controlling factor. Epstein and Rosenthal [42] interpreted this phenomenon to indicate that, in nylons, coagulation from sulfuric acid occurred by deprotonation - an acid base reaction. This is also a plausible explanation in the present system based upon the work of Shen et al. [7] who showed by spectroscopic analysis that PBT model compounds were highly protonated in MSA solution. Thus, these data suggest that further experiments similar to those of Shen et al. [7] studying protonation of PBT in MSA with the addition of a weak base would be helpful in confirming this hypothesis. One could follow the Laser Raman spectra of PBT in MSA and PPA as a function of H_2O content and determine the minimum degree

of protonation before precipitation occurs.

Fibers spun from PPA dopes at room temperature and similar polymer concentration as MSA solutions were observed to have very few macroscopic voids, perhaps due to the higher viscosity of the spinning solution. This reduction in the number of voids in as-spun fibers is probably responsible for the concomitant increase in tensile strength of as-spun fibers from PPA (2.1GPa) as opposed to similar as-spun fibers from MSA solution (1.4 GPa). This would also be predicted from the tensile strengths in Table IV. Such increases in tensile strength for void free fibers are quite reasonable as Allen [17] has shown that fracture tends to occur at such voids which tend to reduce the load bearing area by 10 to 15%.

Heat treatment of fibers (typically at 475°C under load) tends to produce internal fibrillation of PBT fibers. Figure 25 shows interference micrographs of a heat-treated fiber and its as-spun precursor. Notice the fine structure in the heat treated fiber and the outline of the void. This fine structure is indicative of the internal fibrillation which has occurred.

The second type of defect, circumfrential banding, can arise in two ways, both related to the low compressional strength of the fiber. These bands are visible in polarized light and interference microscopy because the orientation in the band is different from that in the remainder of the fiber and therefore, exhibits different extinction positions upon stage rotation. Residual stresses arising from the solidification of the skin of the fiber before the core has been able

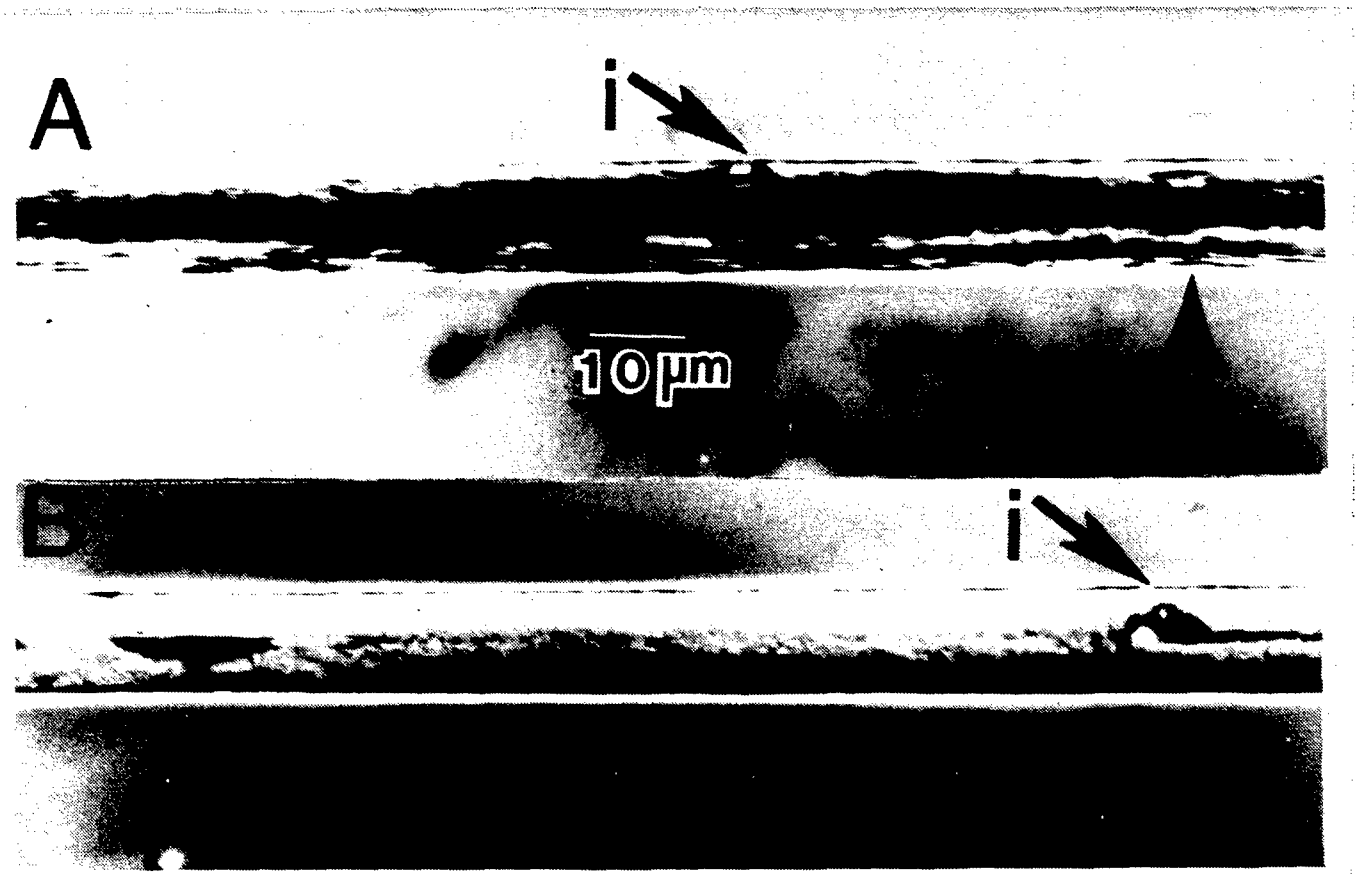

Figure 25. (a) HTF-23 475°C heat treatment (b) ASF-13 typical 'as-spun' fiber.

to contract can produce such defects [17]. The non-linear stress-strain behavior of as-spun fibers would tend to support this view [17]. Banding defects can also be induced during sample preparation due to mechanical damage from handlingA typical banding defect is shown in Figure 26.

PBT fibers from both MSA and PPA solutions are highly anisotropic and are quite birefringent when viewed under polarized light. The presence of a chromophore with an absorption maximum at λ = 440 nm causes these fibers to exhibit anomalous dispersion of light making refective index determination by the Becke Line technique fruitless. The high birefringence (Berry [10] predicts a value of $\Delta n = n_{\parallel} - n_{\perp} =$ 1.5 from light scattering data) was too large to be measured on the 10 m fibers with a compensator. However, complete extinction of all fibers when rotated so that the fiber axis coincided with the polarizer or analyzer axis suggests that the molecular orientation was quite high.

To summarize, PBT fibers from MSA solutions were found to contain macroscopic voids, the number of which was most strongly correlated with increasing nonsolvent content of the coagulation bath although lower temperatures also tended to favor fewer voids. Few voids were observed in PPA fibers, perhaps due to the higher viscosity of the solution (and hence slower coagulation). Based upon extinction of the image intensity when the fiber axis was rotated into coincidence with the polarizer or analyzer axis, the fibers are highly oriented.

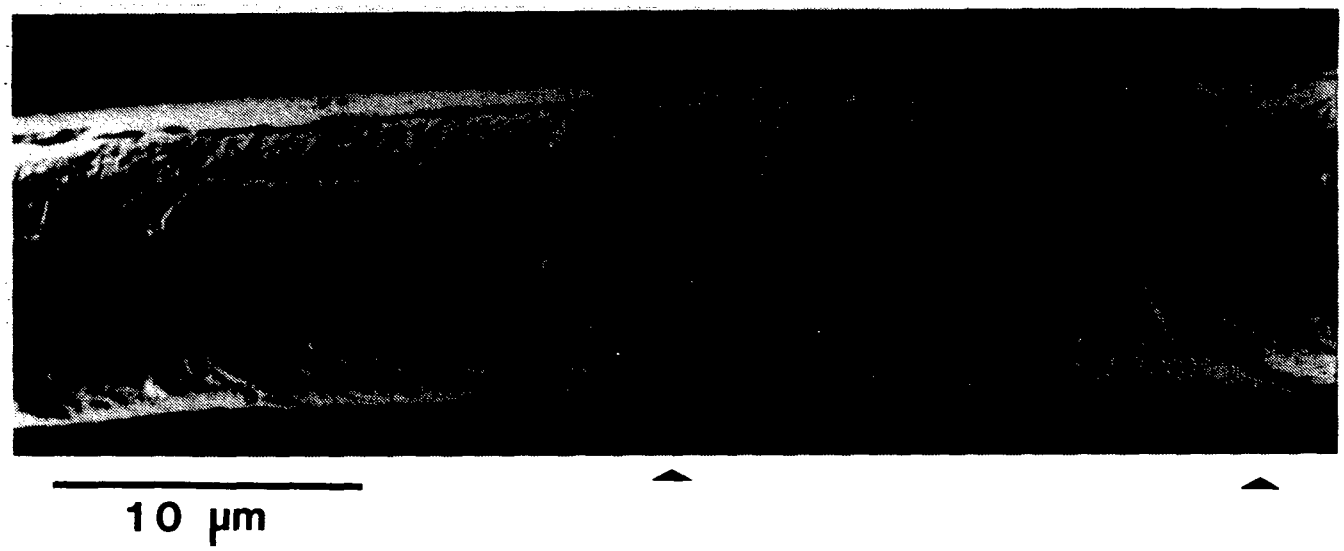

Figure 26. Typical circumferential banding defect in PBT fiber.

4.3 Polarized Light Microscopy of PBT Films

PBT films have been examined by incident and reflected polarized light microscopy. PBT films formed from MSA solutions were too thick to be examined in transmitted light and so were examined with reflected light and found to possess irregular surfaces and to exhibit blisters after heat treatment. The films also change color from maroon to gold upon heat treatment. Voids were also observed on both sides of the film, one of which was a "free surface" in the coagulation bath, the other was in contact with the casting drum.

Samples of PBT films from PPA solutions were examined by transmitted polarized light microscopy. All ribbons in the series were observed to contain voids, the size and number of which increased with increasing extrusion temperature. Figure 27 shows a sample of ASR-9 at two different orientations with respect to the polarizer. In Figure 27a, where the ribbon is oriented at about 45° to the polarizer, the dark areas are voids and are aligned in the extrusion direction. In Figure 27b, the ribbon is oriented at about 5° to the polarizer revealing that the voids are surrounded by misoriented regions. Complete extinction when the ribbon is oriented along the polarizer suggests that the average molecular orientation is high. Figure 28a shows ribbon ASR-7 oriented at 45° to the polarizer. Notice the increased size of the voids in this ribbon extruded at 90°C. In Figure 29b the same area is oriented at 0° to the polarizer, showing the increased misorientation around the voids.

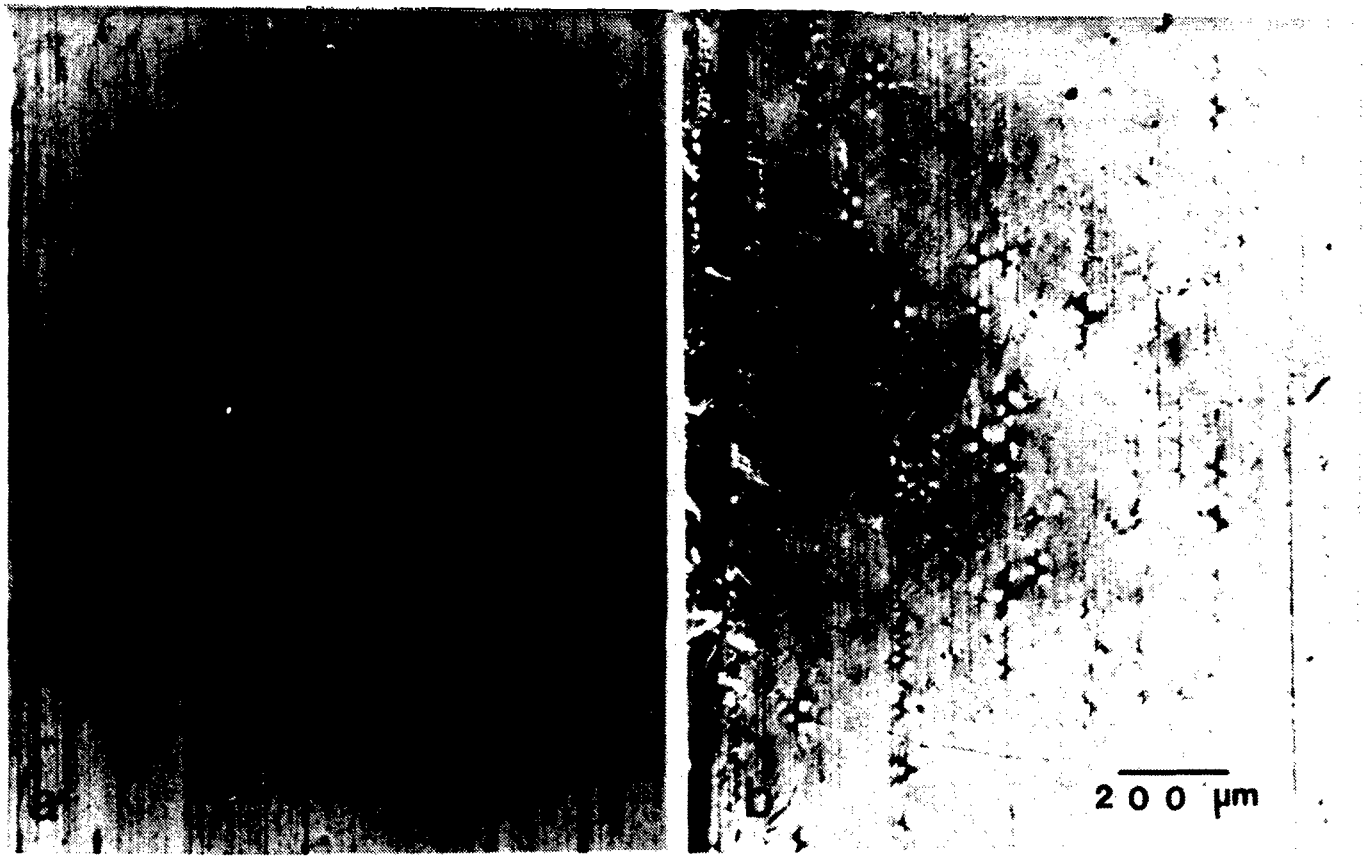

Figure 27. Polarized light micrograph of ASR-9 (a) Film oriented at 45° to polarizer; (b) Film oriented at 5° to polarizer.

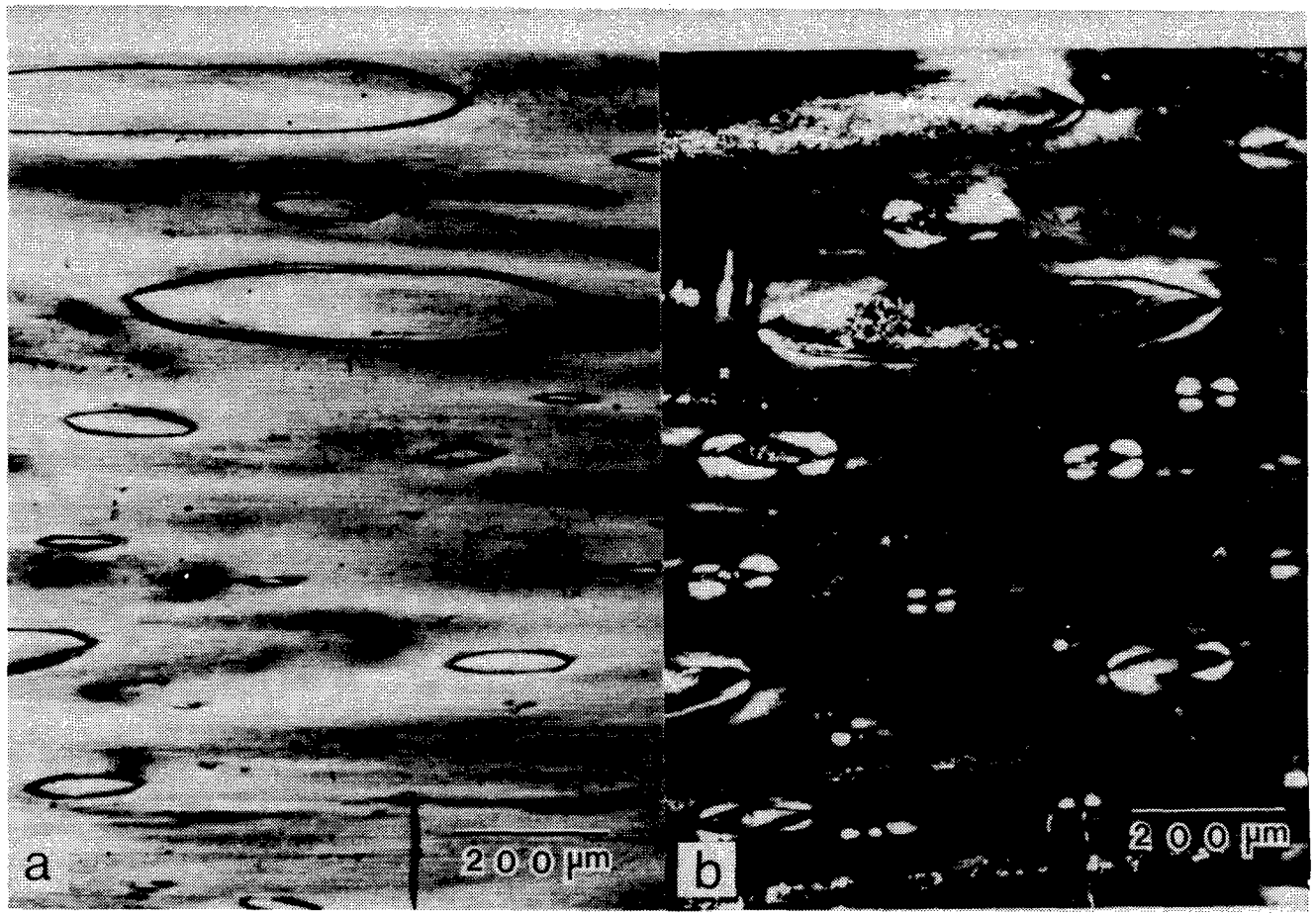

Figure 28. Polarized light micrograph of ASR-7 (a) Film oriented at 45° to polarizer; (b) Film oriented at 0° to polarizer.

Based on the limited number of samples received, the size and number of voids increases with increasing extrusion temperature. The latter explanation is supported by Celanese observation that frequently the uncoagulated films extruded at high temperatures tend to have a grainy appearance. Void formation may be attributed either to water evolved from the PPA at higher temperatures or coagulation inhomogeneities.

The dichroic ratio, D, of selected fibers and films was measured by outfitting a Zeiss microscope with a KODAK GBX safelight filter with the maximum transmittance at 660 nm and bandpass from 610-780 nm. Successive images were recorded with polarized light with the fiber or film oriented perpendicular and then parallel to the polarization direction. The optical density, σ, was measured from the negative with a spot microdensitometer. D was calculated as follows:

$$D = \frac{\log \frac{\sigma_{\parallel}}{\sigma_0}}{\log \frac{\sigma_{\perp}}{\sigma_0}} \tag{4.1}$$

where $\sigma_{\parallel}$ and $\sigma_{\perp}$ are the optical densities of the fiber or film oriented parallel or perpendicular to the polarization direction, respectively, and σ_0 is the optical density of the background which was considered to be non-absorbing. The orientation function of the transition moment f_{moment} was calculated as

$$f = \frac{D-1}{D+2} = \frac{3 \langle\cos^2\phi\rangle - 1}{2} \tag{4.2}$$

where ϕ is the angle between the transition moment and orientation direction. Measured values of sample orientation by this method (see Table VI) are low compared to WAXS and SAED and may be due to two effects. First, the transition moment may not be along the chain direction and, secondly, error is introduced into $\sigma_{\parallel}$ and $\sigma_{\perp}$ by the fog level of the film. Electron diffraction indicated a higher degree of orientation for these same samples (see Chapter VI). Also AR-2 was quite thick so the negative f is probably an artefact. This method might be useful if the microscope were outfitted with a photometer and the intensity measured electronically. However, this equipment is presently unavailable at the University of Massachusetts.

In summary, PBT films have been observed to be highly oriented and to contain macroscopic voids. In the case of voids observed in films from MSA solutions, their origin is analagous to those described earlier for fibers. PPA films on the other hand, exhibit macroscopic voids when extruded at high temperatures. This may be due either to coagulation inhomogeneities or to gas evolved from the solution at higher temperatures.

Table VI

Orientation by Dichroism

Sample	D	f	$\langle\cos^2\phi\rangle_{moment}$	$\langle\phi\rangle_{moment}(°)$
ASR-2	0.895	-0.362	0.309	56.2
ASR-14	1.62	0.171	0.447	48.0
HTF-23	2.60	0.348	0.565	41.3
ASF-13	6.23	0.635	0.757	29.5

CHAPTER V

MICROVOID ANALYSIS BY SMALL ANGLE X-RAY SCATTERING

5.1 Introduction

Wet spun fibers have long been known to exhibit a diffuse, continuous distribution of intensity of x-rays scattered at small angles [44]. This diffuse scattering has been attributed to the presence of microvoids which are small regions, generally 10 nm or less in size, that have lower electron density than the surroundings. Statton [61] envisioned microvoids as "the unfilled spaces around polymer segments, around segment bundles (fibrils), and between lamellae, if such exist." The degree of crystallinity, when measured by wide angle x-ray scattering and differential scanning calorimetry, is unrelated to the diffuse scattered intensity [45]. Cellulose acetate which is known to be noncrystalline exhibits a high intensity of diffuse scatter [44]. The scattering from rayon was also found to decrease in intensity when the fibers were swollen with water, thereby decreasing the difference in electron density between the void and the polymer matrix [44]. Thus, this diffuse SAXS intensity is not caused by crystalline regions of high electron density embedded in a noncrystalline polymer matrix as many early investigators postulated [44]. Heikens, Hermans and Weidinger [45] found the diffuse scattered intensity increased with decreasing density and therefore, increasing void fraction, in air swollen cellulose. Comparison of the volume

fraction of voids calculated from the SAXS integrated intensity with that calculated from density measurements indicated that only 20% of the total void volume consisted of sufficiently small voids to affect their accessable small angle scattering region.

Dobb et al. [47] have studied microvoids in Kevlar 29® and Kevlar 49® fibers by SAXS and electron microscopy. To visualize the microvoids by TEM and to increase the SAXS intensity, these authors stained the polymer with silver sulfide. The apparent microvoid size measured by SAXS in stained fibers was always smaller than the size measured in unstained fibers. They postulated that this occurred either by structural changes upon staining or a proportion of the voids were inaccessible to the stain. The former case is plausible since the staining procedure involved impregnation of the fibers with H_2S at a pressure of 2 MPa followed by impregnation with aqueous $AgNO_3$. The high pressure of impregnation could cause a collapse of some void space. The latter case implies that the surface of the fiber which solidified first during coagulation contained voids smaller than the voids in the center of the fiber which solidified later and tended to cavitate. Thus, diffusion controlled staining would selectively stain the smaller voids. One may distinguish between these two cases by varying the time of staining.

In the following sections we will examine how to measure microvoid size and the assumptions inherent in the measurement. The results of SAXS experiments on selected PBT and Kevlar® samples will then be presented. The data will be analyzed by several models to determine

which model(s) best represent this scattering system. We will then discuss how changes in processing history affect the average microvoid size.

5.2 The Intensity of Small Angle Scattering

The objective of this section is to relate the intensity of diffuse small angle x-ray scattering (SAXS) to the size and number of the fluctuations in electron density (voids in this case) which produce the scattering. One may approach this problem by two basic routes. The first option is to assume particulate scattering and, following Guinier and Fournet [97], to derive an equation for the scattered intensity in terms of the average squared radius of gyration of the particle, $\langle R_g^2 \rangle$. The second option uses a statistical approach patterned after Debye and Bueche [48]. We will consider each option and seek to determine which is most useful for analysis of the SAXS from PBT.

Let us consider an x-ray beam $\underset{\sim}{s}_0$ incident upon a sample which generates a scattered x-ray beam $\underset{\sim}{s}'$ that subtends an angle 2θ with $\underset{\sim}{s}_0$. The scattered intensity is expressed in terms of the difference between $\underset{\sim}{s}'$ and $\underset{\sim}{s}_0$ (see Figure 29).

$$\underset{\sim}{s} = \underset{\sim}{s}_0 - \underset{\sim}{s}' \tag{5.1}$$

$$|\underset{\sim}{s}| = \frac{2 \sin\theta}{\lambda} \quad . \tag{5.2}$$

Here λ is the wavelength of x-rays (0.154 nm for CuKα). If one assumes

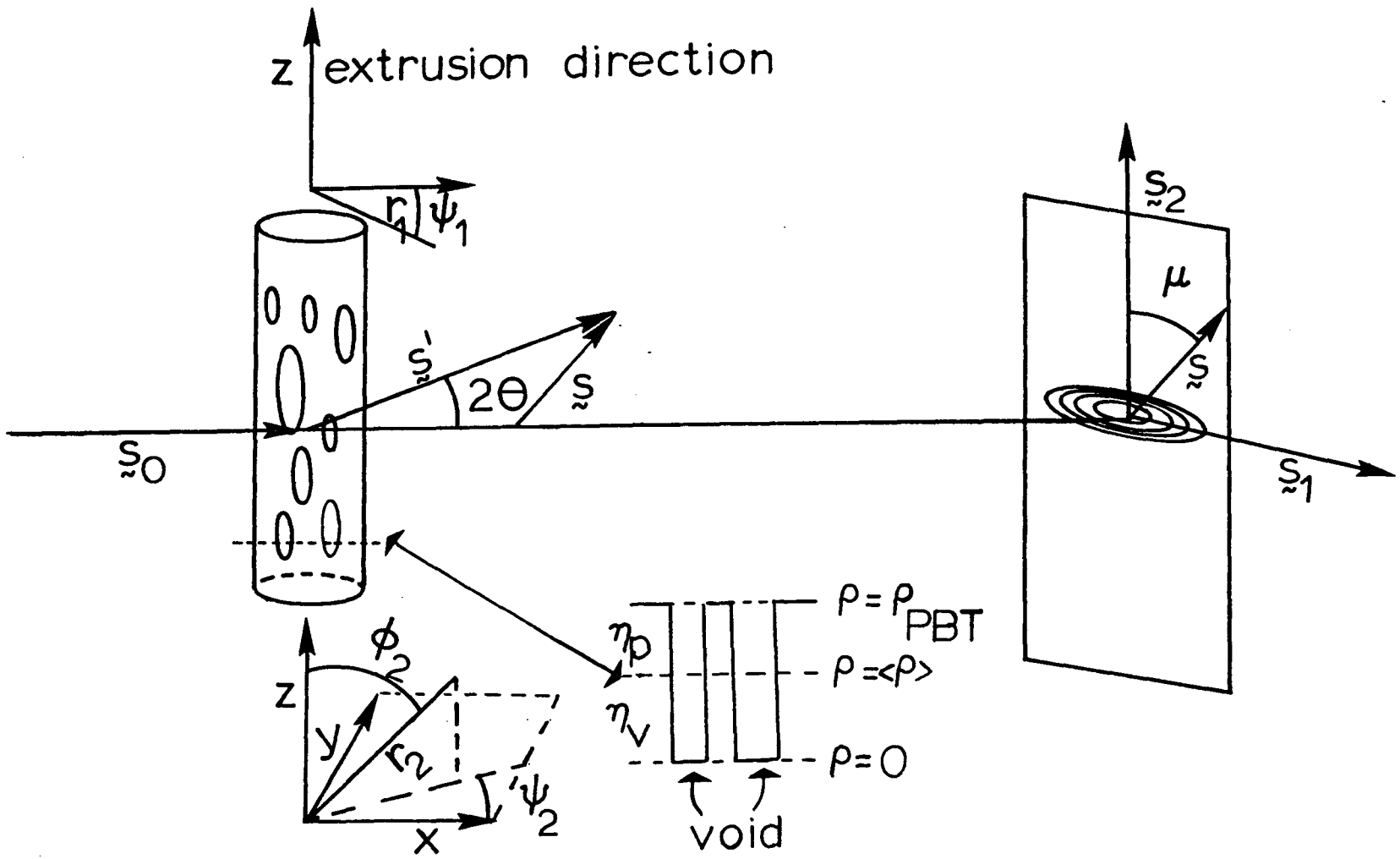

Figure 29 Schematic of the model and coorinates used to study SAXS from PBT fibers and films.

that the specimen consists of a dilute system of N particulate scatterers each of which may be subdivided into M scattering elements which have scattering amplitudes $f(\underset{\sim}{s})$, the scattered intensity, $I(\underset{\sim}{s})$, is given by [49]

$$I(\underset{\sim}{s}) = NI_e \sum_{i=1}^{M} \sum_{j=1}^{M} f_i(\underset{\sim}{s}) f_j(\underset{\sim}{s}) \cos(2\pi \underset{\sim}{s} \cdot \underset{\sim}{r}_{ij}) \tag{5.3}$$

where I_e is the scattered intensity from a single electron

$$I_e = P_0 \left(\frac{e^2}{mc^2}\right) \frac{1}{a^2} = 7.96 \times 10^{-26} \text{ cm}^2 \; P_0/a^2 \tag{5.4}$$

and

P_0 ≡ primary beam intensity (counts/sec^{-1})

a ≡ sample to detector distance (cm)

$\underset{\sim}{r}_{ij}$ ≡ vector between scattering elements i and j (nm) when $\underset{\sim}{s}$ has units nm^{-1}.

Alternately, one may assume that for SAXS the system may be considered as continuous distribution of electron density, $\rho(\underset{\sim}{r})$, which may be expressed in terms of fluctuations, $\eta(\underset{\sim}{r})$, from an average value, $\overline{\rho}$

$$\rho(\underset{\sim}{r}) = \overline{\rho} + \eta(\underset{\sim}{r}). \tag{5.5}$$

(see the insert in Figure 29). These fluctuations in electron density are described by the correlation function, $\gamma(\underset{\sim}{r})$ which is defined as

$$\gamma(r) \equiv \frac{\int \eta(\underset{\sim}{r}')\ \eta(\underset{\sim}{r}' + \underset{\sim}{r})\ dv_{\underset{\sim}{r}'}}{\int \eta(r')\ \eta(r') dv'_{\underset{\sim}{r}}} \tag{5.6}$$

or

$$\gamma(r) = \frac{\int \eta(\underset{\sim}{r}')\ \eta(\underset{\sim}{r}' + \underset{\sim}{r})\ dv_{r'}}{\langle \eta^2 \rangle\ v_x} \tag{5.7}$$

where $\langle \eta^2 \rangle$ is the mean squared electron density fluctuation ((moles electrons)^2 cm^{-3}) and v_x is the volume of the sample irradiated by the x-ray beam [49]. By definition $\gamma(\underset{\sim}{r})$ (equation 5.6) is normalized to unity at r = 0. For a two phase system such as that depicted in the inset in Figure 29, $\gamma(\underset{\sim}{r})$ represents the probability that a small volume element probe separated by the vector $\underset{\sim}{r}$ from a reference volume element in phase 1, is also in phase 1. In such a two phase system with randomly positioned voids, $\gamma(\underset{\sim}{r})$ reaches an asymptotic value of zero as $|\underset{\sim}{r}|$ reaches infinity.

For this model, $I(\underset{\sim}{s})$ is given by the three-dimensional Fourier transform of $\gamma(\underset{\sim}{r})$ [49]

$$I(\underset{\sim}{s}) = I_e\ v_x\ \langle \eta^2 \rangle \int\int\int \gamma(\underset{\sim}{r}) \exp\{-2\pi i\ \underset{\sim}{s} \cdot \underset{\sim}{r}\}\ dv_{\underset{\sim}{r}}. \tag{5.8}$$

5.3 Isotropic Systems

5.3.1 Guinier's Law. After averaging over all orientations of the particle, equation 5.3 becomes

$$I(|\underset{\sim}{s}|) = \sum_{i=1}^{M} \sum_{j=1}^{N} f_i(|\underset{\sim}{s}|) \frac{\sin 2\pi |\underset{\sim}{s}||\underset{\sim}{r}_{ij}|}{2\pi |\underset{\sim}{s}||\underset{\sim}{r}_{ij}|} . \tag{5.9}$$

Guinier [105] expanded the sine in equation 5.9 as a power series and found $I(\underset{\sim}{s})$ for a monodisperse system of spheres to be given by

$$I(|\underset{\sim}{s}|) = (\Sigma f_i(|\underset{\sim}{s}|))^2 \{ 1 - \frac{4\pi^2 |\underset{\sim}{s}|^2}{3} R_g^2 + \ldots \} \tag{5.10}$$

which, for $2\pi |\underset{\sim}{s}| R_g < 1$, may be written as

$$I(|\underset{\sim}{s}|) = I(0) \exp \{ - 4\pi^2 |\underset{\sim}{s}|^2 R_g^2/s \} \tag{5.11}$$

when this model is valid, a plot of $\ln I(|\underset{\sim}{s}|)$ versus $4\pi^2 |\underset{\sim}{s}|^2$ yields a straight line with a slope equal to $- R_g^2/3$.

5.3.2 Debye-Bueche Theory. For an isotropic system $\gamma(\underset{\sim}{r})$ is only a function of the magnitude of $\underset{\sim}{r}$ so that equation 5.8 becomes:

$$I(|s|) = I_e V_x \langle \eta^2 \rangle \int_{\phi_2=0}^{\pi} \int_{\psi_2=0}^{2\pi} \int_{r=0}^{\infty} r^2 \gamma(r) dr \exp \{-2\pi i s r \cos\psi_2 \} \times \sin \psi_2 \, d\psi_2 d\phi_2 \tag{5.12}$$

where ψ_2 and ϕ_2 are the two angles in spherical coordinates (see Figure 29). We have assumed the isotropic sample to be positioned in the x-ray beam such that $\underset{\sim}{s} \cdot \underset{\sim}{r} = sr \cos \psi_2$. Performing the integration over ϕ_2 and ψ_2 yields

$$I(|\underset{\sim}{s}|) = 4\pi I_e V_x \langle\eta^2\rangle \int_{r=0}^{\infty} \gamma(r)\, r^2 \frac{\sin(2\pi s r)}{2\pi s r}\, dr \tag{5.13}$$

Debye and Bueche [48] have shown that for many systems $\gamma(\underset{\sim}{r})$ may be approximated as exp $\{ - r/\ell_a\}$ where ℓ_a is termed the correlation length and is a measure of the size of voids. For a random 2 phase system of voids in a continuum, the exponential correlation function is rigorous. Physically, this indicates that the probability that two volume elements separated by a distance r are both in the same phase decreases exponentially with increasing values of r. Substituting this exponential correlation function into equation (5.7) and integrating leads to

$$I(s) = \frac{8\pi\ I_e V_x \ell_a^3}{(1 + 4\pi^2 s^2 \ell_a^2)^2} \tag{5.14}$$

Equation 28 may be rearranged to yield

$$I(s) = \frac{1 + 4\pi^2 s^2 \ell_a^2}{[8\pi I_e V_x \ell_a^3]^{1/2}} \tag{5.15}$$

Thus, for an exponential correlation function, a plot of $[I(s)]^{-1/2}$ vs $4\pi^2 s^2$ is linear and ℓ_a^2 is given by the ratio of the slope to y-intercept of the plot.

5.4 Extension to Anisotropic Systems

Four approaches to apply equation (5.3) to a system with uniaxial

symmetry will be discussed in detail below. We will postulate that the microvoids in PBT fibers and films are axially symmetric with respect to rotation about the extrusion direction. A schematic of the model is shown in Figure 29. Thus, following Crist [57], $\underset{\sim}{s}$ may be decomposed into components such that $\underset{\sim}{s}_1$ is the component along the extrusion direction and $\underset{\sim}{s}_2$ is the component normal to the extrusion direction lying in the detector plane. This is shown schematically in Figure 29. The vector $\underset{\sim}{s}$ may also be described in terms of its magnitude and the angle μ with respect to the $\underset{\sim}{s}_1$ axis in Figure 29.

In the following treatment we postulate that the microvoids are all perfectly oriented along the extrusion direction and that the scattered intensity is only determined by the shape, size and spatial arrangement of microvoids and not variation of their orientation. We also assume that, in addition to each microvoid being perfectly oriented along the extrusion direction, the microvoids are randomly positioned in a continuum of PBT.

5.4.1 The Projected Correlation Function. Considering equation (5.3) one finds that for any principal direction, s_i

$$I(s_i,0,0) = I_e V_x \langle \eta^2 \rangle \iiint \gamma(r) \exp\{-2\pi i (s_i,0,0)\cdot \underset{\sim}{r}\} \, \underset{\sim}{dv_r} \cdot \qquad (5.16)$$

For example, the intensity along s_1 may then be written as

$$I(s_1,0,0) = I_e V_x \langle \eta^2 \rangle \int \left[\iint \gamma(r_1,r_2,r_3)\, dr_2 dr_3\right] e^{-2\pi i s_1 r_1}\, dr_1 \qquad (5.17)$$

which may be written more compactly as

$$I(s_1,0,0) = I_e V_x \langle \eta^2 \rangle \int \gamma_{pp}(r_1)\, e^{-2\pi i s_1 r_1}\, dr_1 \tag{5.18}$$

where $\gamma_{pp}(r_1)$ is the projection of the correlation function onto the r_1 axis. By Fourier inversion one finds

$$\gamma_{pp}(r_1) = \frac{1}{I_e V_x \langle \eta^2 \rangle} \int_{-\infty}^{\infty} I(s_1,0,0)\, e^{2\pi i s_1 r_1}\, ds_1 \tag{5.19}$$

or

$$\gamma_{pp}(r_1) = \frac{1}{I_e V_x \langle \eta^2 \rangle} \mathfrak{F}^{-1} \left[I(s_1,0,0) \right] \tag{5.20}$$

where $\mathfrak{F}^{-1}$ denotes the inverse Fourier transformation. Thus, by using the Fast Fourier Transform algorithm [52] to perform a discrete inverse Fourier transformation on the measured I(s), one directly obtains the projection of the correlation function onto a given axis. This technique is the most general since it requires no assumptions about the form of the correlation function. However, because of the nature of the discrete transform algorithm, the data is forced to be periodic by flipping it about the last point [52]. One also must be careful to sample data over the correct interval [52]. Still, truncation of intensity data at high and low values of s causes error in the corelation function low and high values of r.

5.4.2 Extension to Uniaxial Systems Using Spherical Coordinates. Summerfield and Mildner [51] have modeled scattering from systems with scattering patterns that possess centrosymmetric azimuthal symmetry. These authors have chosen to approach the problem using spherical

coordinates and find that the scattered intensity at the limit of small angles is given by [51]:

$$I(|\underset{\sim}{s}|) = K\,[1 + 4\pi^2 |\underset{\sim}{s}|^2 (\ell_a^2 \cos^2 \mu + \ell_c^2 \sin^2 \mu)]^{-2} \tag{5.21}$$

where μ is the polar angle with respect to the axis of azimuthal symmetry of the pattern (see Figure 29). They have defined ℓ_a^2 and ℓ_c^2 as

$$\ell_a^2 = \pi N \int_0^\infty r^4\, dr \int_{-1}^{1} d(\cos\phi_1)\; g(r,\phi_1) \cos^2\phi_1 \tag{5.22}$$

$$\ell_c^2 = \frac{\pi N}{2} \int_0^\infty r^4\, dr \int_{-1}^{1} d(\cos\phi_1)\; g(r,\phi_1) \sin^2\phi_1 \tag{5.23}$$

where r and ϕ_1 are the polar coordinates of the scattering center and N is the number of scatterers (see Figure 29). The static pair correlation function, $g(\underset{\sim}{r})$, is defined by [51]

$$g(\underset{\sim}{r}) = \langle \sum_{i \neq j} \sum \delta\,(\underset{\sim}{r} - \underset{\sim}{r}_i + \underset{\sim}{r}_j) \rangle \cdot \frac{1}{N} \tag{5.24}$$

where $\underset{\sim}{r}_i$ and $\underset{\sim}{r}_j$ are the radius vectors to the ith and j^{th} scattering elements and N is the number of scatterers. For a two phase system of microvoids in a continuum of PBT, $\gamma(\underset{\sim}{r})$ is related to $g(\underset{\sim}{r})$ by equation 5.25 [106]

$$\langle \eta^2 \rangle\, \gamma(\underset{\sim}{r}) = \langle \rho \rangle \{ \delta(\underset{\sim}{r}) + \langle \rho \rangle [\, g(\underset{\sim}{r}) - 1] \} \,. \tag{5.25}$$

Thus ℓ_a^2 and ℓ_c^2 are projected correlation lengths and are a measure of the size of the inhomogeneities.

Summerfield and Mildner [51] have also related these parameters to the generalized Guinier approximation and therefore the radius of gyration of the inhomogeneities in the plane of the scattering vector. When the scattering plane includes the axis of symmetry, $(\underset{\sim}{s} \parallel \hat{\underset{\sim}{z}})$ then

$$\langle R_g^2 \rangle_{\parallel} = 2\,(\ell_a^2 \cos^2 \mu + \ell_c^2 \sin^2 \mu)\ . \tag{5.26}$$

<u>5.4.3 Guinier Analysis of Anisotropic Systems</u>. The third approach to this problem is due to Stein [53] and requires only the assumption that the correlation function is separable into components along the x, y and z direction (see Figure 29). Thus

$$\gamma(\underset{\sim}{r}) = \gamma(x)\ \gamma(y)\ \gamma(z)\ . \tag{5.27}$$

Assuming $\underset{\sim}{s}_0$ is along the x direction of the sample and $\underset{\sim}{s}'$ is at an angle 2θ to s_0 and makes an angle μ with the z axis (see Figure 29) one can calculate $I(|\underset{\sim}{s}|)$. The result was that at small angles

$$I\,(|\underset{\sim}{s}|) \simeq K \exp\{-4\pi^2 |\underset{\sim}{s}|^2 (R_y^2 \sin^2\mu + R_z^2 \cos^2\mu)\} \tag{5.28}$$

and so a Guinier plot of $\ell n I$ vs $4\pi^2 |\underset{\sim}{s}|^2$ at $\mu = 0°$ will have a limiting slope equal to $\langle R_z^2 \rangle$ and at $\mu = 90°$ will have a limiting slope equal to

$\langle R_y^2 \rangle$. Equation 5.28 reduces to the proper limit for isotropic samples since $R_x^2 = R_y^2 = R_z^2 = \langle R_g \rangle / 3$

$$I_{iso}(|\underset{\sim}{s}|) = K \exp\{-4\pi^2 |\underset{\sim}{s}|^2 \langle R_g^2 \rangle / 3\} . \tag{5.29}$$

Thus, when analyzing Guinier plots on anisotropic of data it is important <u>not</u> to divide the slope by 3 as one would do for an isotropic sample. It is important to note that, as for all Guinier plots, we are interested in the limiting slope at zero angle. This can be contrasted with the analysis of Jellinek <u>et al</u>. [54] who have attempted to resolve curved Guinier plots into components. This is equivalent to fitting the scattering curve with a number of Gaussians and often violates the small angle assumption ($2\pi s R_g < 1$) used in deriving Guinier's Law. The results of such analysis are not unique and moreover, without further information about the nature of the system one cannot differentiate between polydispersity of size or non-spherical shape of the scattering particles.

The treatment due to Stein [53] may be compared to the results for a single elliposoid of rotation with axes a, a, νa oriented along s_1 reported by Hosemann and Bagchi [55]

$$I_{el}(\underset{\sim}{s}) \sim \exp\{-\frac{4}{5}\pi^2 a^2 (\nu^2 s_1^2 + s_2^2 + s_3^2)\} . \tag{5.30}$$

This suggests that the projected $\langle R_g^2 \rangle$ measured from a Guinier plot

on anisotropic data is 1/5 of the average square of the radius of such an ellipsoid along the axis of projection. This is the model used by Dobb et al. [63] to interpret data from Kevlar 29® and Kevlar 49®. They reported an average ellipse diameter perpendicular to the extrusion direction of 10 nm in an unstained sample of Kevlar 49®.

5.4.4 Extension to Uniaxial Systems Using Cylindical Coordinates. The treatment described below was developed during the analysis of SAXS data for this dissertation. To follow Debye and Bueche [48], one must assume a form of correlation function to describe a uniaxial system. Two are considered here. First, one may follow the treatment of Stein and Hotta [50] for light scattering from oriented films and assume a uniaxial Gaussian correlation function

$$\gamma_1(\underset{\sim}{r}) = \exp\{-(\frac{x^2}{\ell_a^2} + \frac{y^2}{\ell_a^2} + \frac{z^2}{\ell_c^2})\} = \exp\{-(\frac{r_1^2}{\ell_a^2} + \frac{z^2}{\ell_c^2})\} \tag{5.31}$$

where the z axis has been chosen to be unique (see Figure 29). This is equivalent to saying that the probability that two volume elements are both in a void decreases exponentially with the square of the distance between them, and that this rate of decrease is different along z and perpendicular to z.

Alternately, one may generalize the Debye exponential correlation function to cylindrical coordinates

$$\gamma_2(\underset{\sim}{r}) = \exp\{-(\frac{|r_1|}{\ell_a} + \frac{|z|}{\ell_c})\}. \tag{5.32}$$

This is equivalent to postulating that the probability that two volume elements are both in a void decreases exponentially with the distance.

If one assumes a uniaxial Gaussian correlation function equation 5.8 reduces to

$$I(s_1,s_2) = 2\pi V_x I_e \langle\eta^2\rangle \int_{r=0}^{\infty} \int_{z=\infty}^{\infty} \exp\{-(\frac{r^2}{\ell_a^2} + \frac{z^2}{\ell_b^2})\} J_0(2\pi s_2 r) \quad (5.33)$$

$$\times \exp\{-2\pi i\, z\, s_1\}\, r\, dr\, dz\ .$$

For the intensity along s_1 this becomes

$$I(s_1,0) = 2\pi\ I_e V_x \langle\eta^2\rangle \int_{r=0}^{\infty} \exp(\frac{-r^2}{\ell_a^2})\, rdr \int_{z=-\infty}^{\infty} \exp(\frac{-z^2}{\ell_c^2}) \quad (5.34)$$

$$\times \exp\{-2\pi i z s_1\}\, dz\ .$$

After integration one obtains

$$I(s_1,0) = \pi^{3/2}\ I_e V_x \langle\eta^2\rangle \ell_c \exp\{-\pi^2 \ell^2 s_1^2\} \quad (5.35)$$

If a uniaxial Gaussian correlation function adequately describes the system, a Guinier type plot of $\ell n I(s_1,0)$ vs s_1^2 will be linear with a slope equal to $-\pi^2\ell_c^2$. Similarly for the intensity along s_2 one obtains by Hankel Transformation

$$I(0,s_2) = 2\pi^{3/2}\ I_e \langle\eta^2\rangle V_x \ell_c \ell_a^2 \exp\{-\ell_a^2 s_2^2\} \quad (5.36)$$

Thus, a plot of $\ell n I(0,s_2)$ vs s_2^2 will be linear with a slope equal to $-\ell_a^2$.

For the case of the cylindrical exponential function, equation 5.8 becomes

$$I(s_1,s_2) = 2\pi\ I_e V_x \langle\eta^2\rangle \int_{r=0}^{\infty} \exp\{-\frac{|r|}{\ell a}\}\ J_0(2\pi s_2 r)\ r dr \qquad (5.37)$$

$$\times \int_{-\infty}^{\infty} \exp\{-|z|/\ell_c\} \exp\{-2\pi i z s_1\}\ dz\ .$$

For the intensity along s_2 one obtains by Hankel Transformation

$$I(0,s_2) = \frac{8\pi^2 I_e V_x \langle\eta^2\rangle \ell_a^2\ \ell_c}{(4\pi^2 \ell^2 s^2 + 1)^{3/2}}\ . \qquad (5.38)$$

A plot of $[I(s_2)]^{-2/3}$ vs $4\pi^2 s_2^2$ will be linear with a ratio of slope to intercept equal to ℓ_a^2. For the case of a slice along s_2, one obtains

$$I(s_1,0) = \frac{4\pi I_e V_x \langle\eta^2\rangle \ell_a\ P_c}{1 + 4\pi^2\ \ell_c^2\ s_1^2}\ . \qquad (5.39)$$

A plot of $[I(s)]^{-1}$ vs $4\pi^2 s_1^2$ will be linear with a ratio of slope to intercept equal to ℓ_c^2.

5.4.5 Analysis of Diffuse SAXS from Selected Fibers and Films. SAXS patterns were recorded from PBT fiber bundles and stacked films using the 10 m ORNL SAXS Camera with a 64 x 64 element position sensitive detector. The data were corrected point-by-point for dark current, parasitic scatter, and detector sensitivity, as described in Chapter III. Typical isointensity contour plots for as-spun and heat-treated fibers are shown in Figure 30. Intensity profiles two channels wide were then extracted along the equator (s_2) and the meridion (s_1).

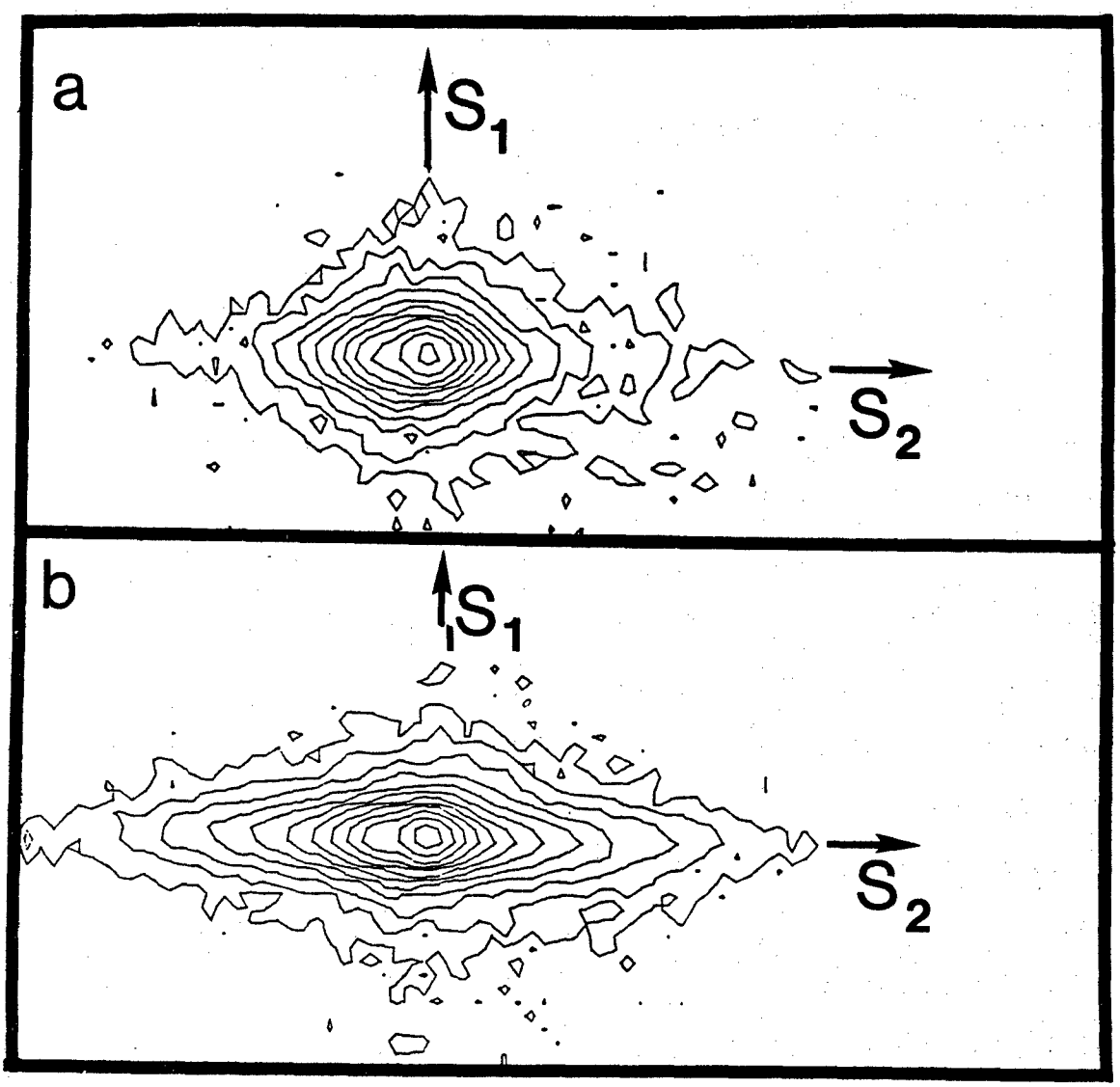

Figure 30: Typical isointensity contour plots of as-spun and heat treated fibers.

These intensity profiles were then analyzed for agreement with the models outlined in sections 5.4.1 - 5.4.4 and the numerical results are given in Table VII. For comparison purposes, the processing histories are given in Table VIII. These will be discussed in detail below.

A typical Guinier type plot along s_2 for PBT is shown in Figure 31. Such plots are always highly curved which implies that a cylindrical Gaussian correlation function is not a good model for this system. Nevertheless, the anisotropic Guinier analysis is still valid so the limiting slope at small angles ($2\pi sR_g < 1.5$) has been measured and the projected radii of gyration are given in Table VI. All the films examined were processed from PPA solutions and possess voids which have a radius of gyration of 10 - 12 nm perpendicular to the extrusion direction. With the exception of heat treatment, changes in processing variables appear to have no effect upon the average radius of gyration of the microvoids within experimental error. For example films ASR-9 and ASR-15 were both extruded from PPA dopes with substantially different SDRs and yet have essentially the same projected radius of gyration perpendicular to the extrusion direction. Although the extrapolation to zero angle for radius of gyration was difficult for HTF-38, this sample appeared to have voids three times as long as wide, in agreement with the results from the Kevlar sample measured.

The void radius in the Kevlar 49® sample calculated assuming ellipsoidal voids was about 3 times larger than reported by Dobb *et al*. [63]. This must be due to difference in commercial samples or

Table VII

Void Size Measurements Along Selected Direction Determined by SAXS

Polymer	Direction	$\langle R_g^2 \rangle^{1/2}$ (nm)	$\langle \ell^2 \rangle^{1/2}$ (nm) low s	$\langle \ell^2 \rangle^{1/2}$ (nm) high s	$\langle \ell^2_{cy\ell} \rangle^{1/2}$ (nm)
Fibers					
ASF-38	s_2	10.9 ± 0.6	21 ± 6	2.4 ± 0.1	7 ± 1
HTF-38	s_1	14.6 ± 0.6[1]	9.1 ± 0.2	4.8 ± 0.5	80 ± 120
	s_2	4.7 ± 0.1[1]	9 ± 1		negative intercept
ASF-41	s_2	12.3 ± 0.4	16 ± 2	2.5 ± 0.1	9 ± 2
HTF-41B	s_2	6.6 ± 0.3	11.0 ± 0.2	4.8 ± 0.3	26 ± 12
ASF-40	s_2	10.4 ± 0.4	9.1 ± 0.1	1.9 ± 0.3	6.6 ± 0.8
HTF-40	s_2	9.4 ± 0.5	8.5 ± 0.4	5.0 ± 0.5	negative intercept
HTF-42 wet	s_2	8.5 ± 0.3	8.1 ± 0.6	4.1 ± 0.3	29 ± 80
HTF-42	s_2			3.9 ± 0.3	
Kevlar 49®	s_1	17.8 ± 0.6	28 ± 3	1.9 ± 0.1	negative intercept
	s_2	7.3 ± 0.3	9.0 ± 0.7	1.9 ± 0.1	9 ± 2
Films					
ASR-9	s_2	12.6 ± 0.3	16 ± 1	1.6 ± 0.1	50 ± 30
HTR-13A	s_2	8.3 ± 0.5[1]	12 ± 2	5.2 ± 0.2	negative intercept
HTR-13B	s_2	10.9 ± 0.5	13 ± 1	5.2 ± 0.3	negative intercept
ASR-14	s_2	12.0 ± 0.5	11.9 ± 0.9	1.4 ± 0.1	negative intercept
ASR-15	s_2	12.2 ± 0.3	15 ± 1	2.0 ± 0.1	26 ± 7

[1] - difficulty with determination of limiting slope due to problems in background subtraction

Table VIII

Processing Parameters for Samples for SAXS

Polymer	Dope	Extrusion Temp. (°C)	SDR	Coagulant	Heat Treatment Time (Sec)	Heat Treatment Temp. (°C)	Heat Treatment Stretch (%)
Fibers							
ASF-38	B	23	2.6	E	--	---	---
HTF-38	B	23	2.6	E	32	527	1.4
ASF-41	A	66	3.7	D	--	---	---
HTF-41B	A	57-62	3.7	D	64	475	1.1
ASF-40	A	64	3.6	D	--	---	---
HTF-40	A	64	3.6	D	30	475	0.8
HTF-42	A	50	3.8	D	30	475	0.8
Films							
ASR-9	C	50	5.3	F	42	110	---
HTR-13A	C	23	1.3	F	32	475	500 g+
HTR-13B	C	23	1.3	F	32	525	0.6
ASR-14	C	29	7.1	F	--	109	---
ASR-15	C	23	21.7	F	90	167	---

A = 5.6% PBT ([η]=31) in PPA
B = 12% PBT ([η])=31 in MSA
C = 9.2% PBT ([η]=31) in PPA
D = 9% H_3PO_4, 91% H_2O, 23°C
E = 50% MSA, 50% H_2O, 3.5°C
F = 100% H_2O, 23°C
+ = heat treated under constant load

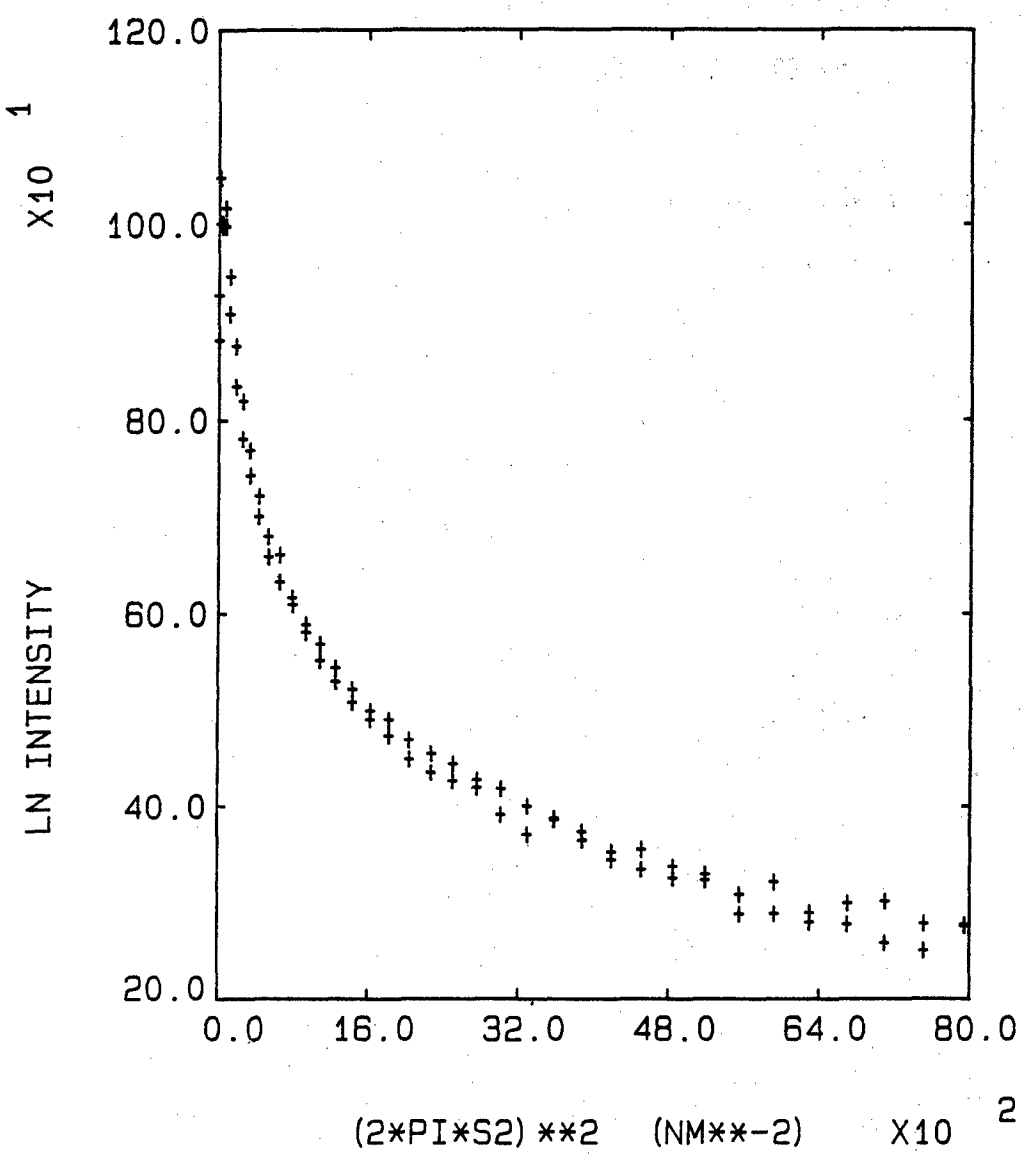

Figure 31. Typical Guinier plot from the intensity along s_2 from PBT fibers and films. Sample is HTF-42.

angular ranges used. Dobb's minimum value of $|\underset{\sim}{s}|$ was 2.9×10^{-2} nm^{-1} compared to 2.0×10^{-3} nm^{-1} in this work. Thus, larger voids could be measured on the ORNL apparatus, and this is reflected in the average value.

Guinier and Fournet [97] have shown that the average radius of gyration is given by

$$\langle R_g^2 \rangle = \frac{\sum_k P_k n_k^2 R_{gk}^2}{\sum_k P_k n_k^2} \tag{5.40}$$

where P_k are the number of particles of type k and n_k are the number of electrons in the particles of type k. Assuming that all particles are geometricaly similar and that n_k is proportional to the volume of the particles, then n_k is proportional to R^3. Substituting for n_k in equation 5.35,

$$\langle R_g^2 \rangle = \frac{\sum_k P_k R_{gk}^8}{\sum_k P_k R_{gk}^6} \quad . \tag{5.41}$$

Thus the average radius of gyration is strongly influenced by the larger voids. Since the largest voids scatter at the smallest angles, the average radius of gyration will be sensitive to the small angle limit.

A typical Debye type plot is shown in Figure 32. These curves tend to have linear asymptotes at low and high s. If one refers to the assumptions in the development of Summerfield and Mildner [51], one finds the low angle limit to be desired value. This low angle

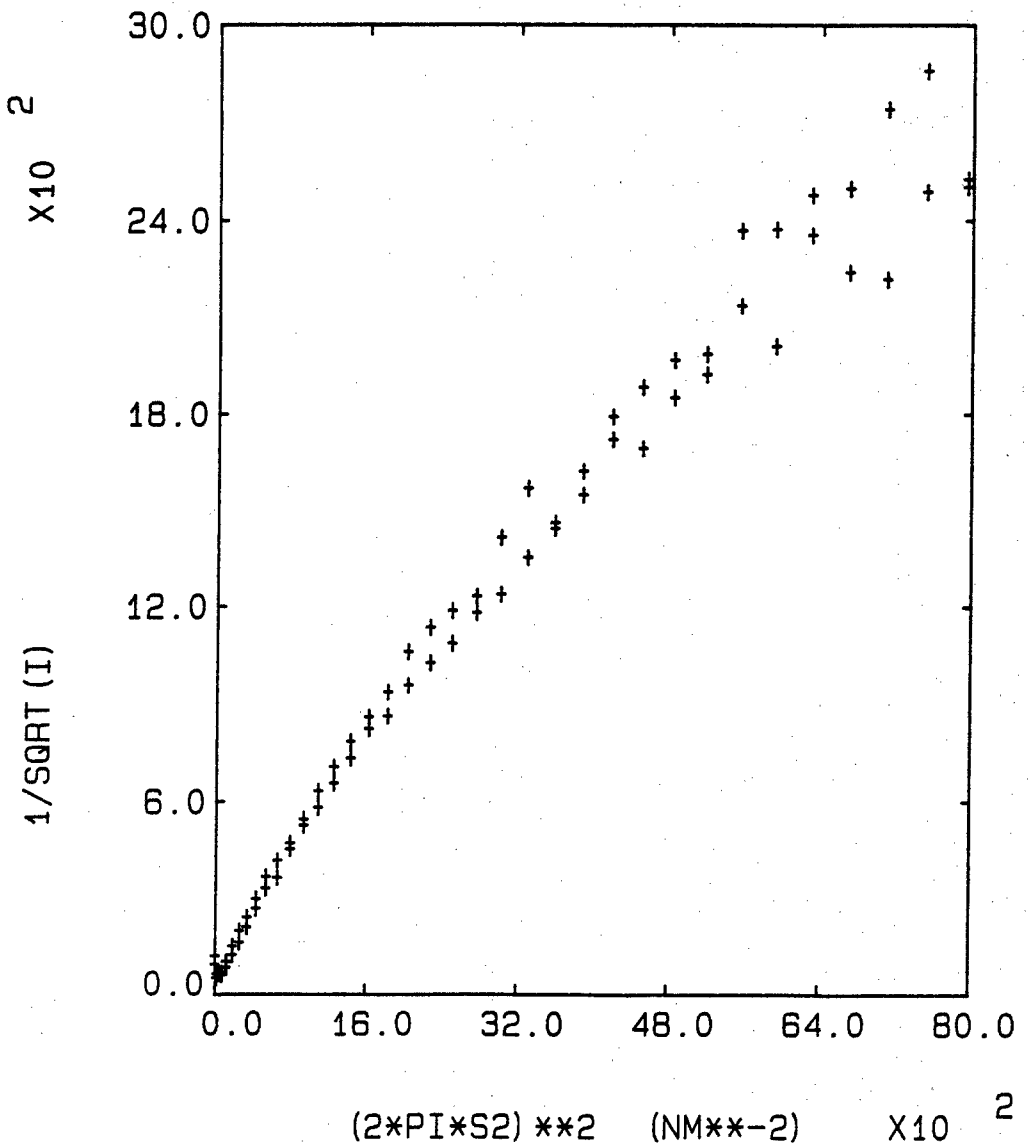

Figure 32. Typical Debye type plot for data along s_2 from PBT fibers and films. Sample is HTF-42.

limit should be 1/2 of $\langle R_g^2 \rangle$ suggesting that $\langle R_g^2 \rangle^{1/2}$ should equal 1.41 $\langle \ell^2 \rangle^{1/2}$.

Scruitiny of Table VII suggests that the low angle limit of $\langle \ell^2 \rangle^{1/2}$ is generally equal to $\langle R_g^2 \rangle^{1/2}$ which implies the approximation does not hold. The development of Guinier's law assumes a dilute suspension of particles. Guinier and Fournet [97] have shown that as the concentration of a suspension increases, the smallest angle scattering is decreased. This type of behavior would lead to a lower value of $\langle R_g^2 \rangle$ than predicted. Perhaps this type of behavior accounts for the discrepancy in the measured value of $\langle R_g^2 \rangle$ and that predicted from $\langle \ell_a^2 \rangle$.

A plot of the same data for a cylindrical exponential correlation function is shown in Figure 33. These plots generally exhibit positive deviation from linearity. Frequently the intercepts are so small that they are negative when a linear least squares regression analysis is performed. Even when the intercepts are positive, the error is sufficiently large to result in large errors in the cylindrical correlation length $\langle \ell_{cy\ell}^2 \rangle^{1/2}$. Therefore this model is not particularly useful for analysis of microvoids in PBT.

A plot of the projected correlation function obtained by Fast Fourier Transformation [52] of the data is given in Figure 34. The data up to $|\underset{\sim}{s}| \approx 2 \times 10^{-2}$ nm^{-1} were used and were flipped about the last point to make a periodic function for discrete transformation. If one tries to graphically estimate the first zero of the projected $\gamma(r_2)$ one obtains about 100 nm. For an isolated sphere of radius R,

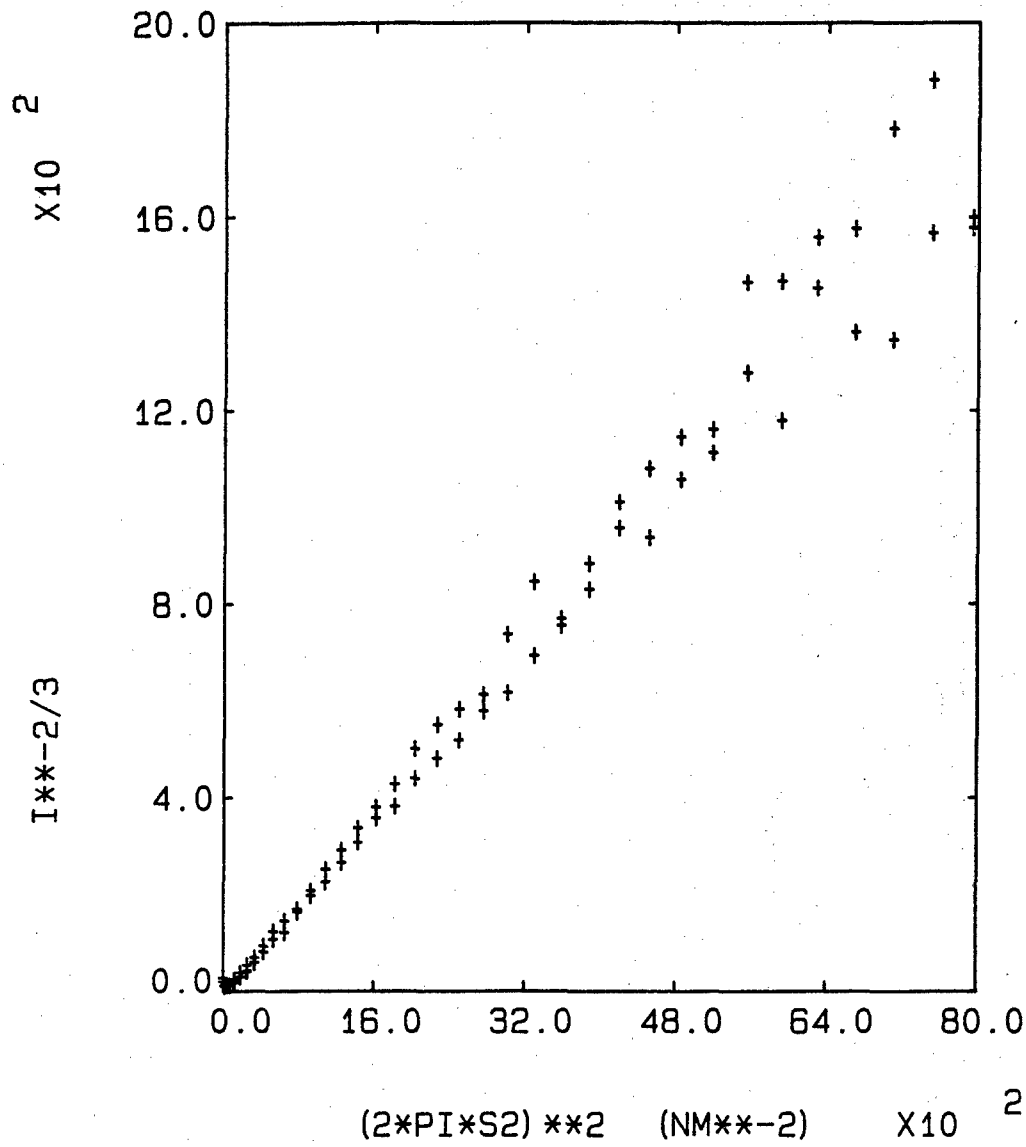

Figure 33. Typical plot of SAXS data from PBT fibers and films assuming a cylindrical exponential correlation function. Sample is HTF-42.

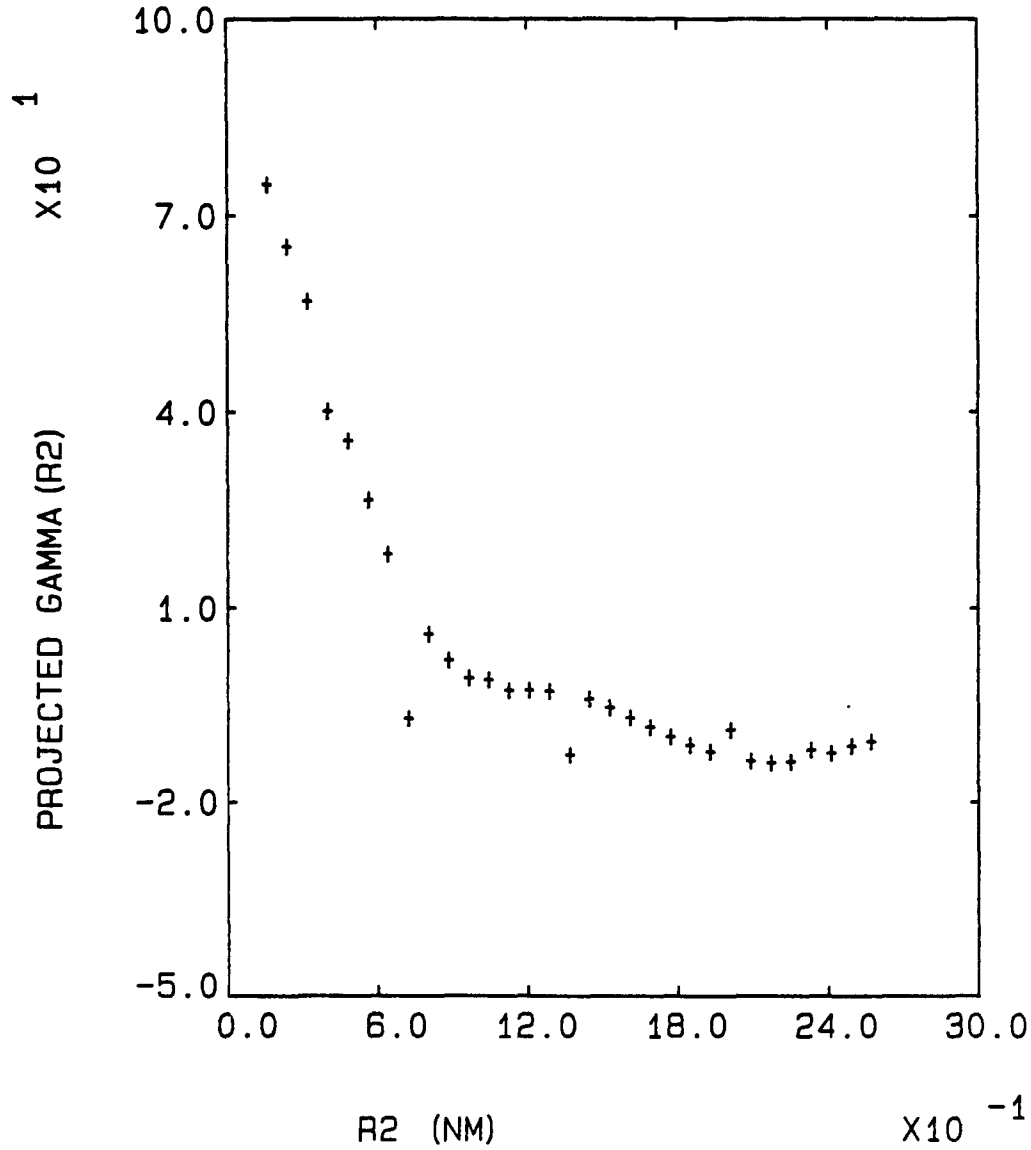

Figure 34. Projected correlation function along R_2 for HTF-42.

$\gamma(r)$ reaches zero for $r = 2R$ [55]. If we assume this to be true for the general case of non-spherical particles, this would imply a projected diameter of about 100 nm for this sample. This is roughly twice the size predicted if one assumes that the voids are ellipsoidal and derives the radius using the formula from Hosemann and Bagchi [55] and 10 times the size of the projected radius of gyration.

5.4.6 Comparison of the Models for Data Analysis. For comparison purposes, the best method is to directly examine the correlation function. Although it is difficult to relate the correlation function to physical dimensions in the sample, one can make relative statements. Examination of correlation lengths obtained from the Summerfield-Mildner [51] analysis and the projected radii of gyration from Summerfield *et al*. [51] and Stein [53] have thus far proved to be most useful. As long as one is careful to make comparisons on data from instruments with the same angular range and is careful to take the limiting slope at small angles, useful comparison of data may be made with these models.

5.5 Correlation of Void Size with Processing Conditions

Before proceeding further, it is worthwhile to discuss the results of an experiment in which HTF-42 was swollen with water and examined by SAXS while still wet. The total scattered intensity from the wet sample after correction for background was significantly smaller than the dry sample. However, the projected correlation length perpendicular to the fiber axis in the wet sample was identical, within experimtnal

error, to that from the dry sample. This confirms our model of voids within a matrix of PBT.

From Tables VII and VIII we see that the average microvoid size determined from the projected radius of gyration and projected correlation length in fibers from MSA solution (ASF-38/HTF-38) decreases upon heat treatment. A similar trend is seen in fibers from PPA solution (ASF-41/NTF-41B). Since the scattered intensity of heat treated fiber bundles is greater than that of as-spun fiber bundles with similar thickness, this indicates that fibrillation increases the number of voids, but the lateral packing in the fiber is improved, resulting in fewer large voids and a smaller total fiber cross sectional area. That is, the fibrils fill in some of the larger voids. Films extruded from PPA with significantly different SDR (ASR-9,-14 and -15) contain large microvoids which appear to be unaffected by SDR. Heat treatment (consider ASR-14, HTR-13A and 13B) results in microvoids slightly smaller than those in the as-spun ribbons with a slight increase in the scattered intensity. This implies that there is less fibrillation during heat treatment in films from PPA solution.

5.6 Suggestions for Future Experiments

Comparison of the projected void sizes perpendicular to the extrusion direction in PBT films extruded from PPA solutions at similar SDRs but different extrusion temperatures (ASR-9:50°C, ASR-14:20°C) indicates that extrusion temperature does not affect the void size in the small angle region. This implies that the large voids reported in

Chapter IV which increased with extrusion temperature must arise by a different mechanism than the voids observed by SAXS.

In the future, it would be interesting to have a quantitative measure of the volume fraction of microvoids accessable to small angle x-ray scattering. This may be achieved through the SAXS integrated intensity termed the invariant, Q [56]

$$Q \equiv \iiint I_n(\underset{\sim}{s})\, dv_s \tag{5.42}$$

where I_n is the intensity normalized to that of the incident beam. For uniaxial symmetry, I is only a function of s_{r_2} and ϕ_2 and not a function of s_{ψ_2} (see Figure 29).

$$Q = \int_{s_{\phi_2}=0}^{\pi} \int_{s_{\psi_2}=0}^{2\pi} \int_{s_{r_2}=0}^{\infty} I_n(s_{r_2}, s_{\phi_2}) s^2 \sin\phi_2 \, ds_r ds_{\phi_2} ds_{\psi_2} \tag{5.43}$$

$$Q = 2\pi \int_{s_{\phi_2}=0}^{\pi} \int_{s_{r_2}=0}^{\infty} I(s_r, s_\theta)\, s_r^2 \sin\phi_2 \, dr d\phi_2 \,. \tag{5.44}$$

Following the geometry of Crist [73] we make a change of variable:

$$s_1 = s_{r_2}\cos\psi \quad s_2 = s_{r_2}\sin\psi \text{ and } dA = ds_1 ds_2 = s_{r_2} dr_2 dr_\psi$$

Substituting these values into equation 5.44, one obtains

$$Q_{2\text{-}D} = 2\pi \int_{s_1=-\infty}^{\infty} \int_{s_2=-\infty}^{\infty} I_n(s_1, s_2) s_2 ds_1 ds_2 \tag{5.45}$$

or, only using one quadrant of s_1-s_2 space

$$Q_{2\text{-}D} = 4\pi \int_{s_1=0}^{\infty} \int_{s_2=0}^{\infty} I_n(s_1, s_2) s_2 ds_1 ds_2 \tag{5.46}$$

Q may be related to the mean squared electron density fluctuation, $\langle\eta^2\rangle$ [56]

$$Q = \frac{\langle\eta^2\rangle\ i_e N_A d}{4\pi\ a^2} \tag{5.47}$$

where $\langle\eta^2\rangle$ is the mean squared electron density fluctuation (moles^2 electrons $_{cm^{-6}}$)

i_e ≡ Thompson's factor 7.94×10^{-26} cm^2

N_A ≡ Avagadro's Number

d ≡ the sample thickness (cm)

a ≡ the sample-to-detector distance (cm) .

For a two phase system with sharp boundaries, the mean squared electron density fluctuation is given by [56]

$$\langle\eta^2\rangle = \phi_1\phi_2\Delta\rho^2 \tag{5.48}$$

where ϕ_1 and ϕ_2 are the volume fractions of the respective phase and $\Delta\rho^2$ is the square of the difference of the electron density of the two phases.

For a system of voids in PBT, then $\Delta\rho^2$ becomes ρ^2_{PBT} and we obtain an equation for the volume fraction of voids, ϕ_i

$$\phi_i\ (1-\phi_i) = \frac{4\pi a^2 Q}{\rho^2_{PBT} I_e N^2 d} \quad . \tag{5.49}$$

The ρ^2_{PBT} equals 0.71 moles^2 electrons cm^{-6} so equation (59) reduces to

$$\phi_i\ (1-\phi_i) = 6.14 \times 10^{-22}\ a^2\ Q/d\ . \tag{5.50}$$

This would be an excellent area for future work but would require careful determination of sample thickness, necessitating flat fiber bundles such as those used by Heikens et al. [46]. One would also have to subtract the intensity for electron density fluctuations within the PBT phase which occur at high angle. This is termed the liquid-like scatter, and may be obtained from the slope of a Porod plot [74], a plot of $16\pi^4\ Is^4$ and $16\pi^4\ s^4$.

CHAPTER VI

MEASUREMENT OF FINE STRUCTURE BY TRANSMISSION ELECTRON MICROSCOPY

In this chapter the results of transmission electron microscopy (TEM) of PBT fibers and films are presented. The fibers were prepared by Chenevey [12,13] as described in Chapter II. Films were prepared at selected shear rates by the author with the aid of J. Odell using on the apparatus designed by King and Berry [15] also and dry jet wet spun films were supplied by Chenevey [12,13] (see Chapter II). Table III contains a summary of the history of the fibers and films examined. Samples sufficiently thin for TEM were prepared by detachment replication as outlined in Chapter III. Bright field and dark field images and selected area electron diffraction patterns were obtained from the thinnest areas of such samples.The high resistance of PBT to electron beam damage has been measured using selected area diffraction. The extent of order in molecular paching was determined by analysis of dark field and lattice images.

6.1 Measurement of the Electron Irradiation Lifteime of PBT

The resolution attainable for polymer samples is limited by electron beam radiation damage due to crosslinking or chain scission with subsequent loss of mass. Molecules containing aromatic groups have been found to have improved resistance to beam damage (with

respect to aliphatic compounds), presumably due to overall chain rigidity and resonance stabilization of radicals generated by the electron beam. In this section a measurement of the resistance of PBT to electron irradiation damage is reported and its implications for bright field and dark field electron imaging are discussed.

Detachment replication of the surface of an as-spun or heat treated fiber or film extracts thin, fibrillated, sheetlike fragments. Such fragments are sufficiently thin to obtain selected area electron diffraction patterns. The structural interpretation of these electron diffraction patterns will be discussed in depth in Chapter VII. It is sufficient to note here that the reflections decrease in intensity with increasing electron dose.

To quantitatively assess the decay of diffracted intensity with increasing electron dose the desired reflections were selected with an objective aperture while the microscope was operated in the diffraction mode. The intensity (electrons area^{-1} time^{-1}) of these reflections was then proportional to the current collected from the electrically isolated observation screen which was measured with a Keithley electrometer. The electron dose rate was obtained following the method of Grubb [59] where the current collected from the observation screen is measured with the microscope in the imaging mode with the sample removed. The observation screen efficiency, η, was calculated by measuring the current in the sample plane with a Faraday cup and subsequently the current from the observation screen under identical conditions. Thus the dose rate (flux),j, of electrons incident

upon the sample is given by:

$$j_{sample} = \frac{M^2 \, i_{screen}}{\eta_{screen} \, A_{screen}} \tag{6.1}$$

where M is the magnification, i_{screen} is the current from the observation screen, η_{screen} is the screen efficiency (measured to be 0.65 at 100 KeV), and A_{screen} is the area of the observation screen (measured to be 64 cm^2). The dose of electrons, D, is the product of the dose rate and the irradiation time t

$$D = j_{sample} \, t \tag{6.2}$$

Thus, by measuring the screen current arising from an isolated reflection as a function of irradiation time one can obtain the decay in intensity with dose of the particular reflection.

The closely spaced (010), ($\bar{1}$10) and (110) equatorial triplet was isolated with a 5.6 mrad diameter objective aperture and the sample irradiated at a dose rate of 2.8×10^{-3} Amp cm^{-2}. Figure 35 illustrates that the diffracted intensity decayed to a plateau value arising from the damaged polymer and the amorphous carbon support film. A plot of $\ln(i(D) - i(\infty))$ vs dose is linear (see Figure 36), suggesting that the decay is exponential with a charateristic value, $D^* = 1.6$ coul cm^{-2} to decrease to 1/e (37%) of its original value.

The electron irradiation damage of PPTA has been studied by a group at the University of Leeds, but their work contains some inconsistencies. Bennett et al. [60] recorded electron diffraction patterns as a function of dose and measured the area under a microdensitometer trace of the (002) reflection as a function of dose at

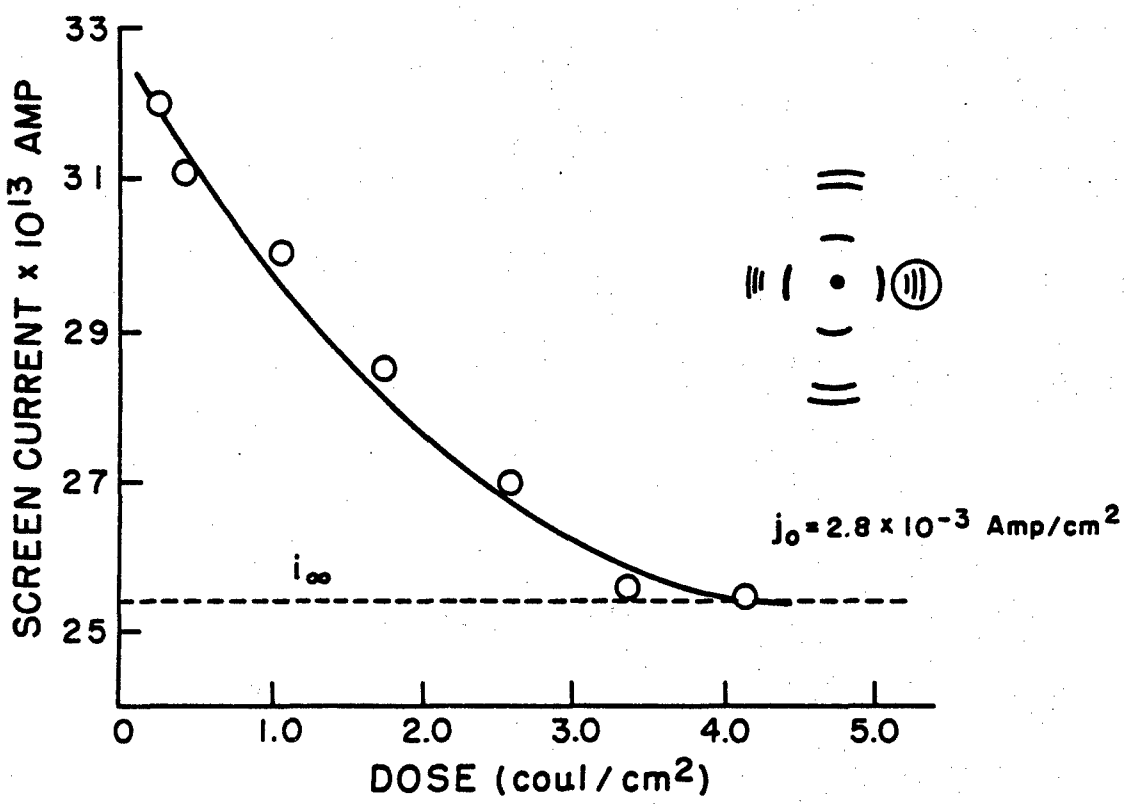

Figure 35. Decrease of scattered intensity from (010),($\bar{1}$10) and (110) reflections from HTR-5.

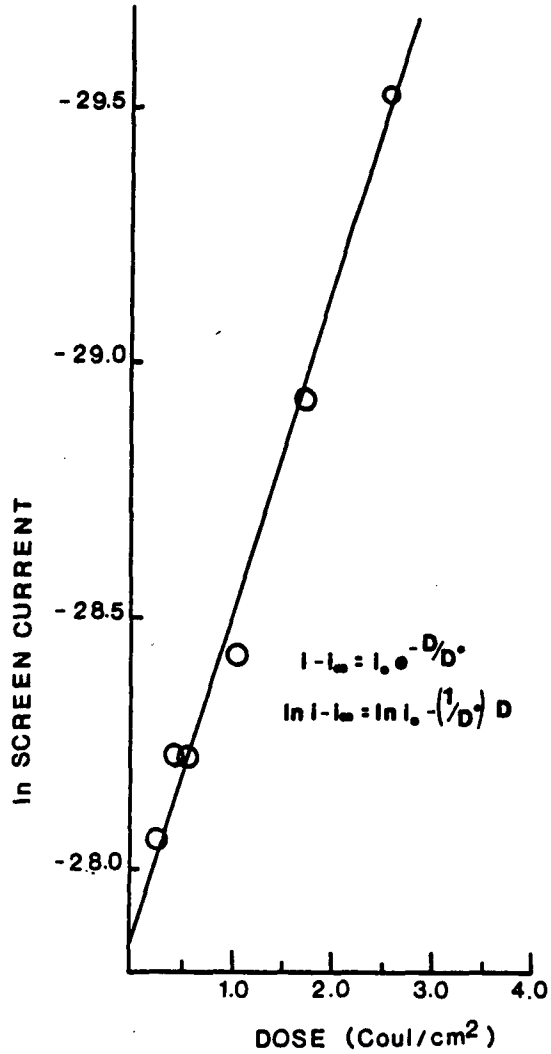

Figure 36. Determination of D^* for HTR-5.

selected dose rates. They observed that at a dose rate of 3.28×10^{-2} Amp cm^{-2} the decrease in area under the (002) trace was exponential with respect to dose and a dose of 1.2 Coul cm^{-2} was required to reduce the area by half. From these data, $D^*(002)$ can be calculated to be 1.7 Coul cm^{-2}. However, Dobb et al. [61] subsequently reported that the (110) reflection was the most stable reflection and did not persist longer than 120 sec at a dose rate of 1.64×10^{-3} Amp cm^{-2}. This corresponds to a dose of 0.19 Coul cm^{-2}, or assuming an exponential decay and that Dobb et al. could only observe decay to 10% of its initial value, would correspond to $D^*(110)$ of 8.3×10^{-2} Coul cm^{-2}. This indicates one of two possibilities:

(1) Dobb et al. [61] meant that the (110) reflection was the most stable equatorial reflection and imply that order perpendicular to the $\underset{\sim}{c}$ axis is destroyed more rapidly than order along $\underset{\sim}{c}$. However, at such low D^* values, the lattice images they have observed would not have been attainable.

(2) Bennett et al. [60] report the correct value and Dobb et al. [61] are in error, perhaps due to a typographical error.

Literature values of 4×10^{-3} Coul cm^{-2} are reported for D^* of polyoxymethylene (POM) and polyethylene (PE) [62]. Thus PPTA and PBT are substantially more resistant to electron irradiation damage than PE and POM, as would be predicted on the basis of their chemical structures.

Thomas and Ast [63] have calculated the maximum magnification for image formation using a reflection ($hl\ell$) at a total electron dose

below D^*. Assuming that focusing is done in bright field ($hk\ell = 000$), $M(hk\ell)$ is given by:

$$M(hk\ell) = \left\{ \frac{D^*}{\frac{D_{focus}\, I_o}{I_{000}} + \frac{D_{record}\, I_o}{I_{hk\ell}}} \right\}^{1/2} \qquad (6.3)$$

where D_{focus} is the dose required for focusing, D_{record} is the dose required for recording an image, and I_o is the incident beam intensity.

The electron speed is defined as the slope of the low optical density portion of the curve of optical density versus electron exposure for a given film processed under specified conditions [64]. Since this curve is linear, the electron speed is normally taken to be the recipocal of the exposure in electrons μm^{-2} required to produce a density of 1.0 above gross fog when the film is processed [64]. For Kodak 4463 film processed in D19 diluted 1:2 with water and developed 4 minutes at 20°C the electron speed is reported to be 0.8 [64]. Therefore, a dose of 1.25×10^8 electrons cm^{-2}, or equivalently, 2.0×10^{-11} coulombs cm^{-2} are required to produce a density of 1.0 above gross fog. This was taken to be the value of D_{record}.

In order to use equation 6.3 to calculate the maximum magnification, one still needs to know the ratio of $I_{hk\ell}/I_o$ and I_{000}/I_o. For typical extracted fragments $I(010)/I_o$ was measured to be 0.02 and I_{000}/I_o was measured to be 0.4. As a first approximation, these values were taken to be independent of dose. If one assumes that focussing is done on an adjacent area so that all electrons are used for recording, the

first term in the denominator of equation 6.3 is zero and the maximum magnification may be easily calculated. The maximum magnification for DF image formation using the (010) reflection was calculated to be 40,000 X while the maximum magnification for bright field imaging with diffraction contrast from (010) was calculated to be 140,000 X. These values are an order of magnitude above the maximum magnifications reported for PE [63]. Thus, the prospects for high resolution imaging of fibers and films from PBT are quite good.

6.2 Dark Field Imaging of PBT Fibers and Films

As pointed out in the previous section, detachment replication of the surface of PBT fibers and films provides thin, fibrillated, sheetlike fragments. Figure 37 shows a typical bright field/dark field pair, the dark field image formed from the (100),(010),($\bar{1}$10) and (110) reflections shown in the inset. In this section we report the extent of order in molecular packing determined by analysis of such dark field images.

Dark field images were formed using the tilted beam technique. The incident electron beam ($\underset{\sim}{s}_0$) was tilted through an angle β, shown in Figure 18, so that the desired diffracted beam $\underset{\sim}{s}_1$ was centered upon the optic axis. Finally $\underset{\sim}{s}_1$ was selected by the appropriate objective aperture, typically 21 or 37 μm in diameter, corresponding to 1.0 and 0.6 nm Airy disc radii, respectively. Focussing was generally performed in bright field on an adjacent area using a beam deflection device [65]. After focussing in bright field, the dark

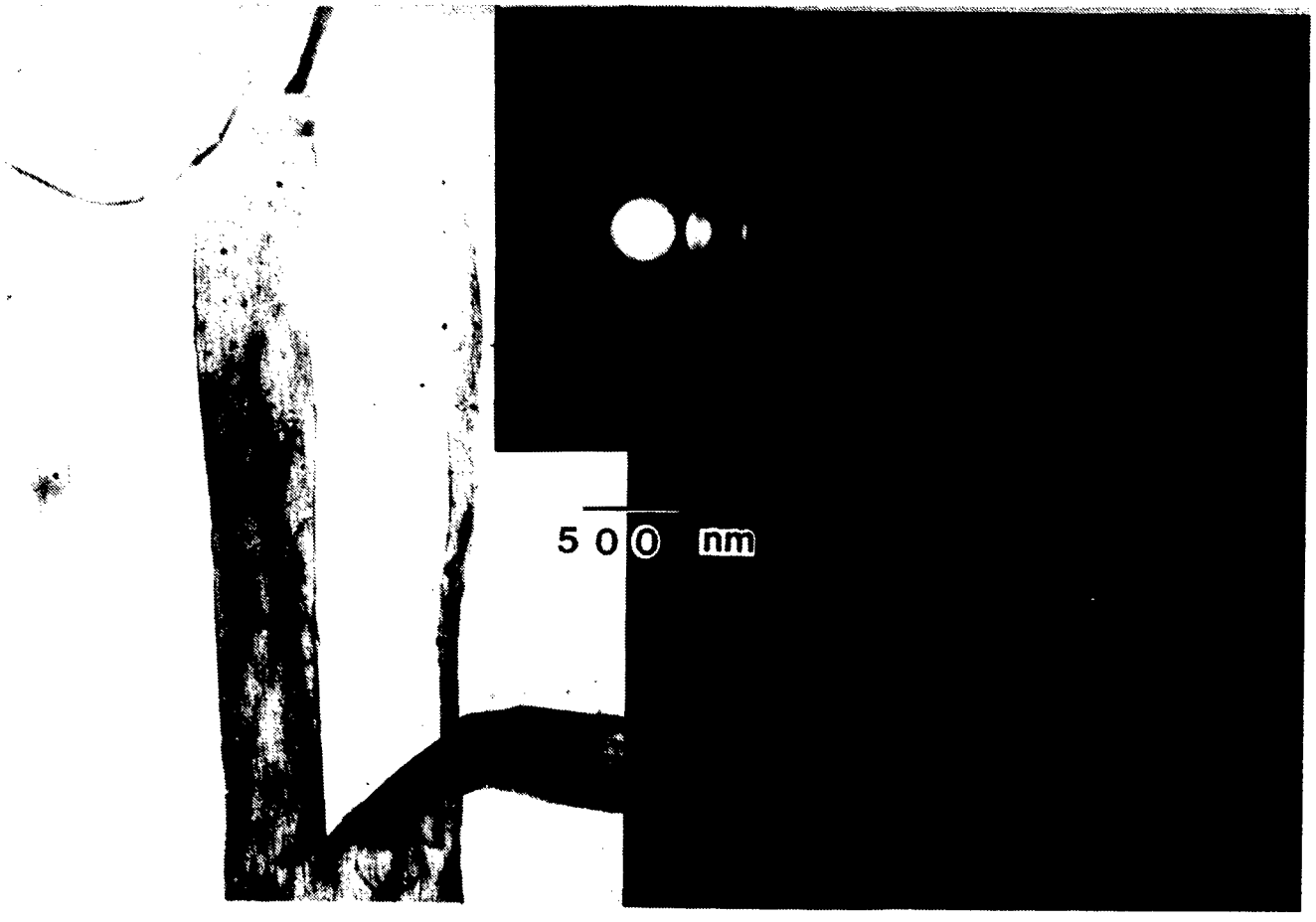

Figure 37. BF/DF pair from HTR-5 (tension-heat treated at 475°C) prepared by detachment replication.

field tilt coils were energized and the incident beam deflected back onto the optic axis and an image recorded. A slight (~ 1 sec) delay in recording the micrograph allowed the sample to adjust to irradiation, reducing the amount of drift and increasing the yield of useful micrographs.

Examination of equatorial dark field images from fragments extracted from all as-spun fibers and films revealed a bright speckle always 2 nm or less in size. Such small scale image detail requires careful work to quantify since the microscope optics strongly influence the image at this level. Furthermore, images must be obtained only from the thinnest areas of the fragments in order to satisfy the requirement that the thickness of the specimens be not much greater than the size of the projected object in order to avoid artefacts arising from a two-dimensional projection of a three-dimensional object. Recognizing these problems, it is estimated that laterally ordered regions in as-spun PBT fibers and ribbons are 2 nm or less in size. This phenomenon may be partially due to the large number of liquid crystalline defects present in the anisotropic solutions these materials are spun from.

Examination of equatorial dark field images of extracted fragments of fibers and films processed from MSA and PPA solutions and heat treated under load at 450°C and above, revealed a much larger scale of diffraction contrast (recall Figure 37). Figure 38 contains two successive dark field images of a HTR-4 (limiting viscosity number = 31) film prepared from a 12% solution in MSA by Celanese. The film was

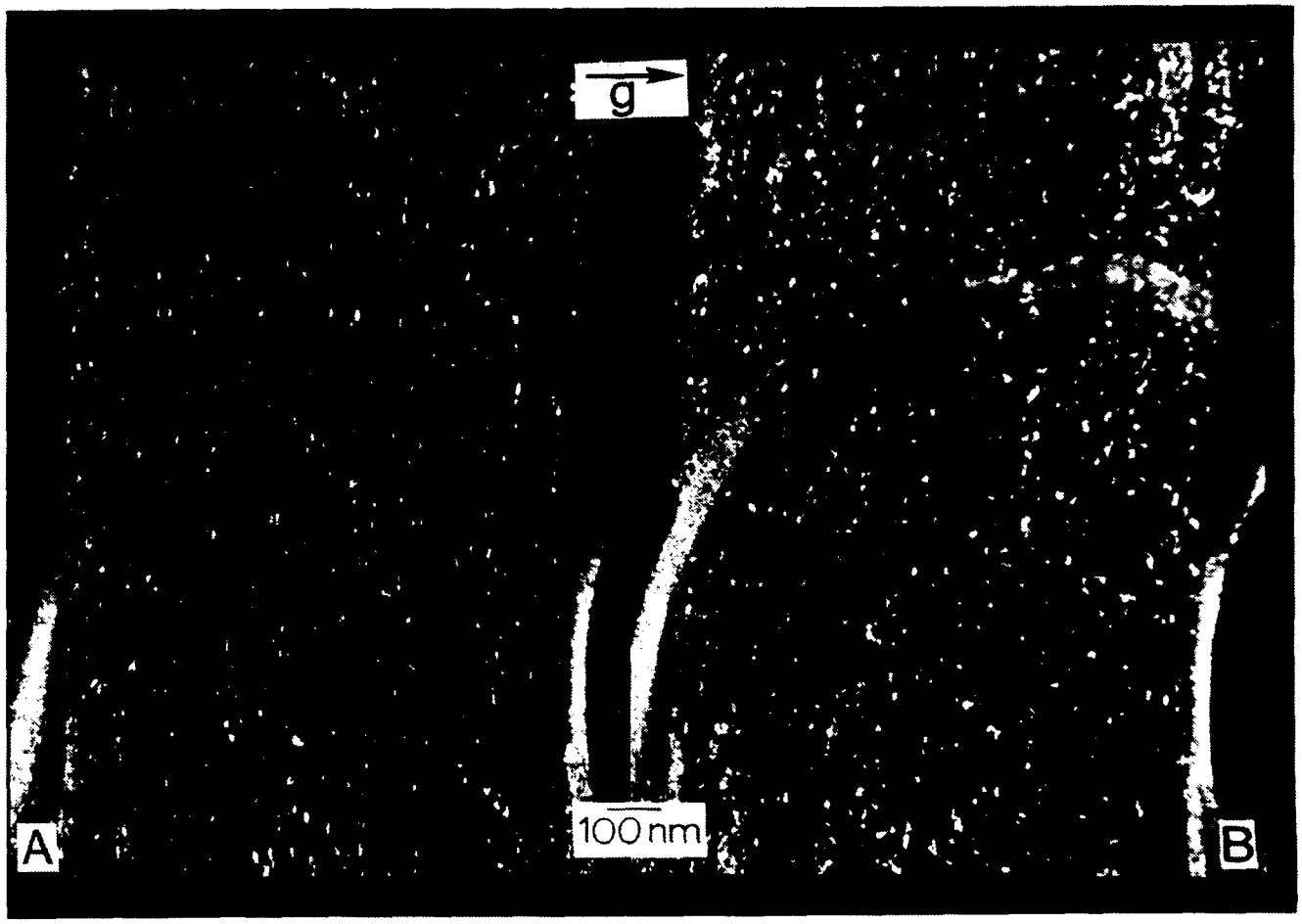

Figure 38. Successive DF images from (110) and the (010),($\bar{1}$10) and (110) reflections DF HTR-4 tension heat treated at 465°C. A. 100 DF; B. (010),($\bar{1}$10) and (110) DF.

extruded with a spin-draw ratio of 1.4 through a 2 mm air gap into a coagulation bath of 50% MSA/50% H_2O. The sample was subsequently heat treated at 465°C under N_2 with a 0.8% stretch and a residence time of 32 seconds. After heat treatment, the modulus was 13 GPa and the strength 0.19 GPa. Successive dark field images were recorded from the (010),($\bar{1}$10), and (110) reflections, respectively. These images were recorded at an instrumental magnification of 10,000 X so that the total electron dose incident on the sample was less than D^* for the two exposures. The projections of the laterally ordered regions were rarely observed to be longer than 40 nm. The micrographs show a relatively uniform spatial distribution of laterally ordered regions within the fragment. When the (100) dark field image is compared by a transparent sheet overlay technique to the (010),($\bar{1}$10),(110) dark field image from the same area, the two images are found to exhibit different arrays of coherently scattering regions of similar size and shape. The size of the coherently scattering regions agrees with the extent of the lattice fringe image observed by Shimamura [66]. When the (010),($\bar{1}$10),(110) triplet is tilted such that only the non-equatorial portion of the intensity falls within the aperture (see Figure 38) and the image is compared to a successive image for which the entire reflection contributes to the image, we find both to have uniform spatial distributions of intensity (see Figure 39).

A similar experiment has been performed on longitudinal thin sections of PPTA fibers by Dobb et al. [67]. Images from selected portions of the (200) reflection in PPTA are shown schematically in

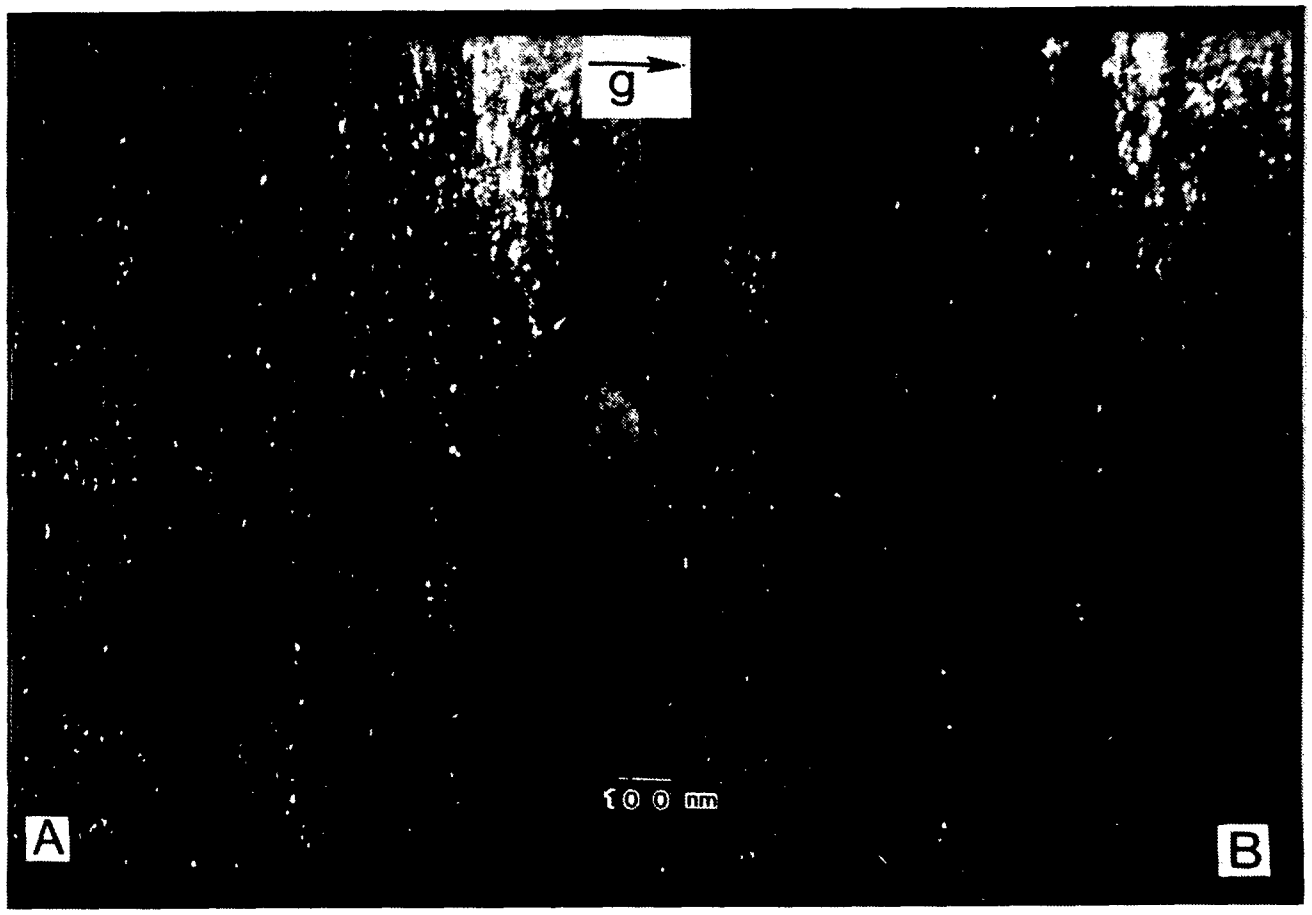

Figure 39. Successive dark field images from the (010), ($\bar{1}$10) and (110) reflections from HTR-4.
A. Objective aperture centered on reflection
B. Objective aperture displaced to accept only the off axis component of reflection.

Figure 40. The periodic banding observed in such images was interpreted as arising from periodic changes in orientation. To account for such observations, Dobb et al. [61,67] have proposed a model for PPTA fibers consisting of "pleated" sheets aranged in a radial array (see Figure 41). Aviakan [68] and Ballou [69] have interpreted the transverse structures observed in plasma etched fibers as arising from these pleated sheets and they claim to have observed a "long" period by soft x-ray scattering at small angles. Their data have, however, not been published and the intense SAXS microvoid scatter and lack of discrete meridional scattering observed from CuKα x-rays by Dobb et al. [47] and this author (Chapter V) is inconsistent with this interpretation and suggests the need for additional work in this

The experimental results rule out such a pleated sheet structure or PBT. Perhaps this is because PBT has no hydrogen bonding to stabilize such a structure.

Figure 42 shows an (010),($\bar{1}$10),(110) dark field micrograph taken at an instrumental magnification of 33,000 X of HTR-13A prepared by Celanese from a PPA solution. The film was extruded from a 12% solution of limiting viscosity number 32 polymer out of a rectangular die through a 1.5 mm air gap, into a water coagulation bath with a spin draw ratio of 1.3. The sample was then heat treated at 475°C with 500 g tension and a 32 sec residence time. The film had a 116 GPa modulus and 1.36 GPa strength. The fragment in the dark field image in Figure 42 was suspended over a gold decorated, perforated carbon support film. The fragment was measured to be approximately 90 nm thick near

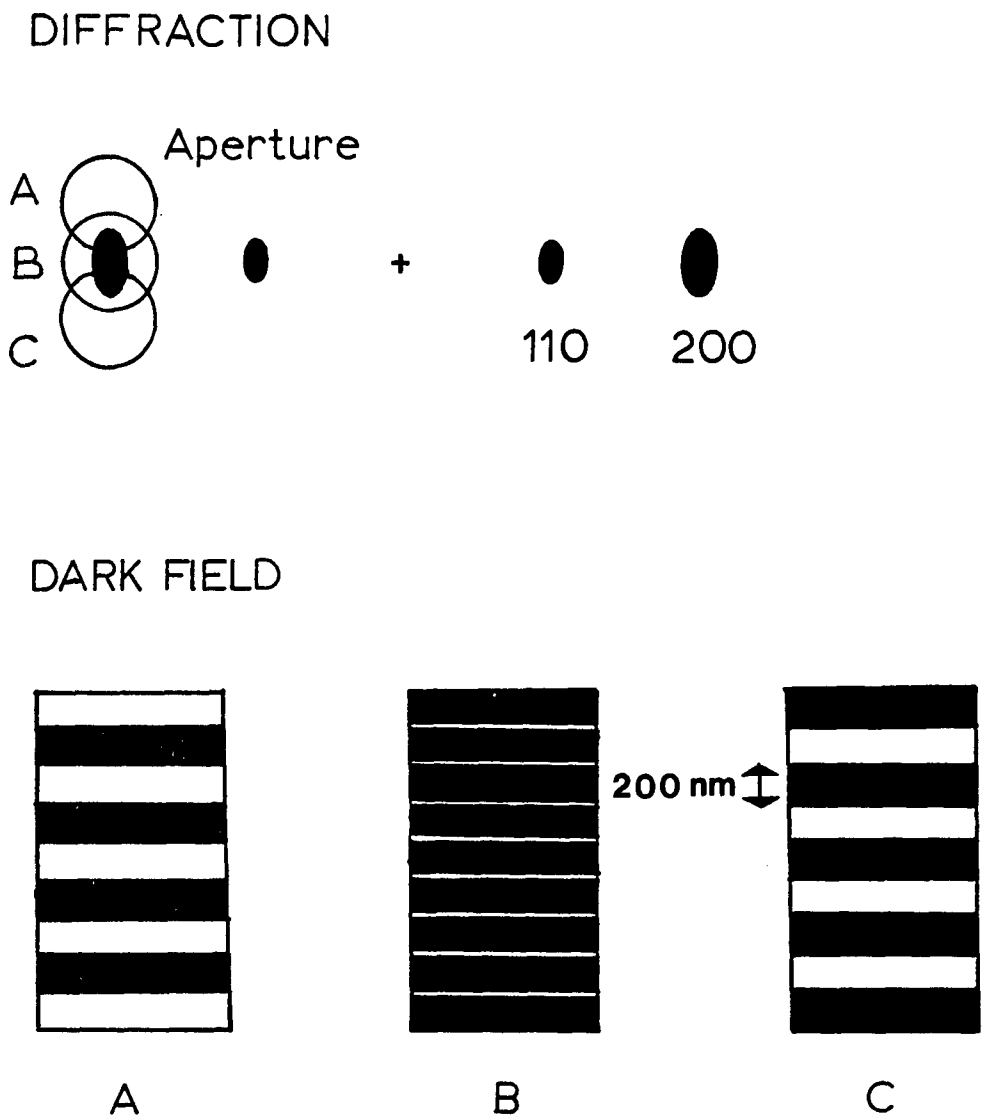

Figure 40. Schematic of experiment similar to that in Figure 38 on PPTA. From Reference [67].

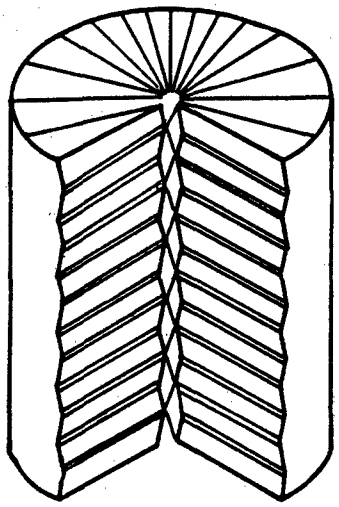

Figure 41. Schematic of pleated sheet model for PPTA fibers. From Reference [67]. The PPTA molecules are assumed to undergo tilt from one pleated region to the next.

the bottom and 45 nm thick near the top by comparison of the optical density in the bright field image with that from a hole assuming only a mass thickness contrast mechanism. The coherently scattered regions in the thinnest areas (~ 45 nm) of the fragment average 10 nm in width and 16 nm in length and are highly aligned in the extrusion direction. The kinked area in the lower right region (marked 'K') shows the effect of tilt about an axis normal to the extrusion direction with a slight twist about the extrusion direction. The nondiffracting region of the kink also shows that the axial orientation is very high and the Bragg condition is only satisfied for normal incidence of the electron beam.

The top of Figure 42 shows an enlargement of the area within the white box. Several bright coherently scattering regions are separated by small, dark, non-coherently scattering regions (marked "B"). These dark regions represent twisted regions or concentrated defects between regions.

Hirsch *et al*. [70] have studied dark field images from bent crystals as well as other imperfect crystals. The problem is formulated in terms of a deviation parameter usually termed $\underset{\sim}{s}$, defined in Figure 43. For this section we will make a change in the diffraction optics nomenclature and consider an incident electron beam $\underset{\sim}{k}$ impinging on a sample and producing a scattered electron beam $\underset{\sim}{k}'$, at an angle 2θ to $\underset{\sim}{k}$. Both $\underset{\sim}{k}$ and $\underset{\sim}{k}'$ have magnitude $1/\lambda$. The locus of all possible $\underset{\sim}{k}'$ defines the Ewald sphere of reflection. The scattering difference vector, $\underset{\sim}{K}'$ in Figure 43, represents the difference between $\underset{\sim}{k}'$ and $\underset{\sim}{k}$ and

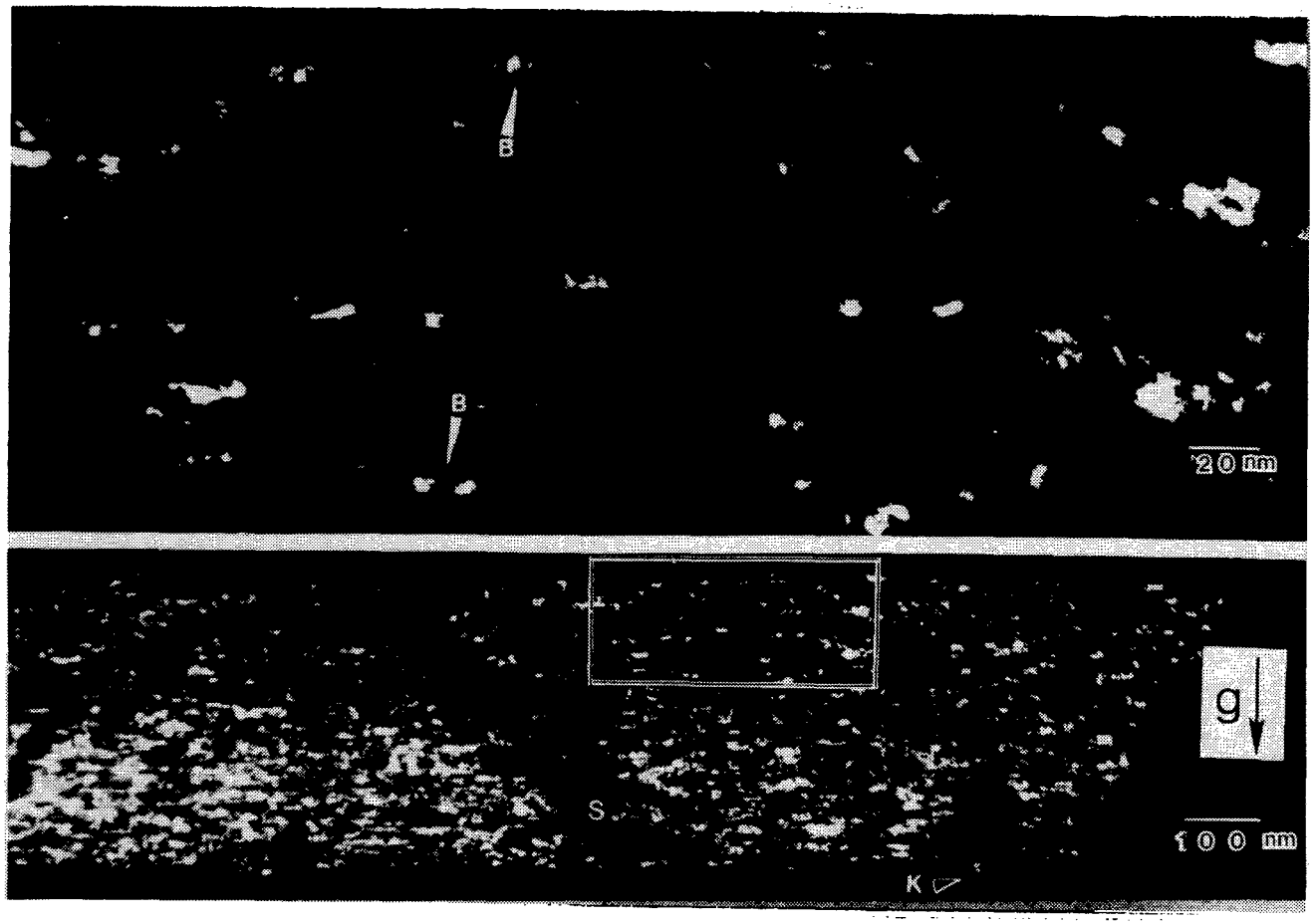

Figure 42. DF micrograph of PBT fragment suspended over a gold decorated, perforated support film (S). "K" denotes tilted area. Extrusion direction is horizontal. Instrumental Magnification = 33,000X. Top: Enlargement of boxed area at bottom. B denotes probable twisted regions.

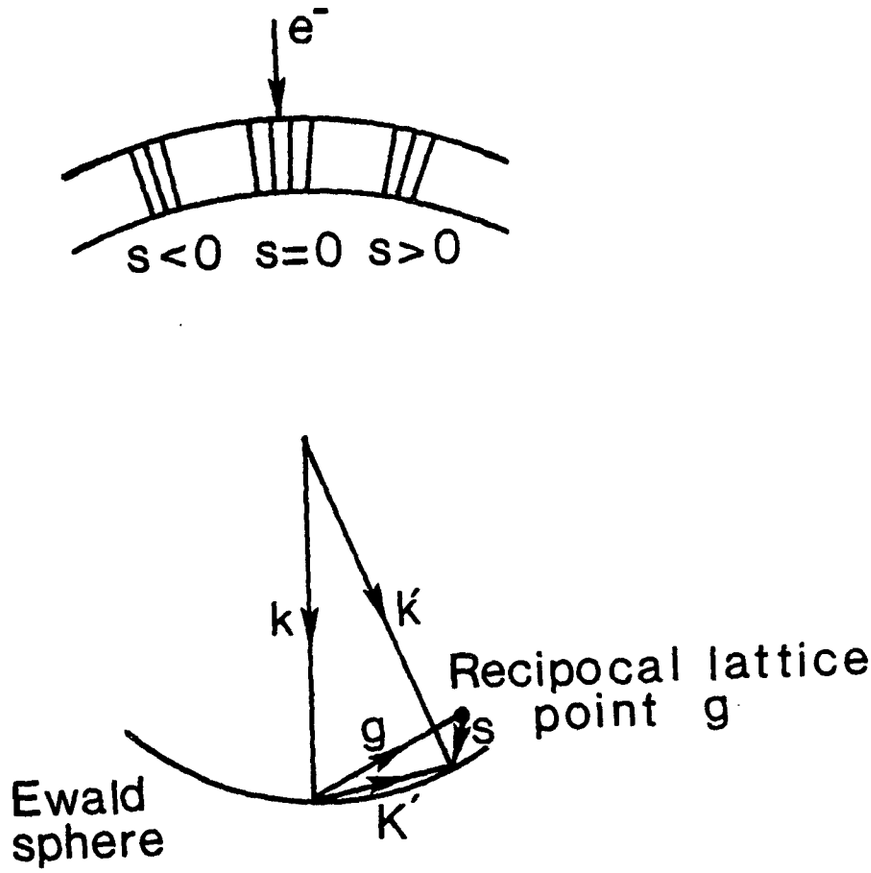

Figure 43. Schematic of scattering from a uniformly bent crystal. s is the deviation parameter.

intersects the Ewald sphere. The deviation parameter, $\underset{\sim}{s}$, is defined as the difference between the recipocal lattice vector $\underset{\sim}{g}$ and the difference scattering vector $\underset{\sim}{K}'$. For the Bragg conditions, $\underset{\sim}{K}' = \underset{\sim}{g}$ and thus, s = 0. We will consider only small deviations arising from misorientation of the crystal shown schematically (Figure 44) and may define a misorientation angle, α, as the angle between $\underset{\sim}{K}'$ and $\underset{\sim}{g}$. For small values of $\underset{\sim}{s}$

$$\alpha \approx \tan \alpha = |\underset{\sim}{s}| / |\underset{\sim}{g}| \tag{6.4}$$

The intensity is then given by

$$I \approx F(hk\ell)^2 \frac{\sin^2 \pi t |\underset{\sim}{s}|}{\pi^2 |\underset{\sim}{s}|^2} \tag{6.5}$$

where t is the crystal thickness. Equation 6.5 is termed the rocking curve. Figures 44 and 45 show the rocking curve for the 1.68 nm^{-1} (100) reflection and the 2.76 nm^{-1} (010) reflection assuming a crystal thickness of 10 nm. In each case, a tilt of less than two degrees is sufficient to decrease the scattered intensity to zero. Thus, a very slight bending of a large crystal would cause a small apparent crystallite size to be determined by dark field.

Meridional DF images obtained from the 1st and 4th layer streaks from annealed PBT fibers and ribbons do <u>not</u> exhibit any prominent diffraction contrast. This indicates that no large scale 3 dimensional crystallites are formed, and is consistent with our assertion in Chapter VII that the intensity along the nonzero layer lines arises

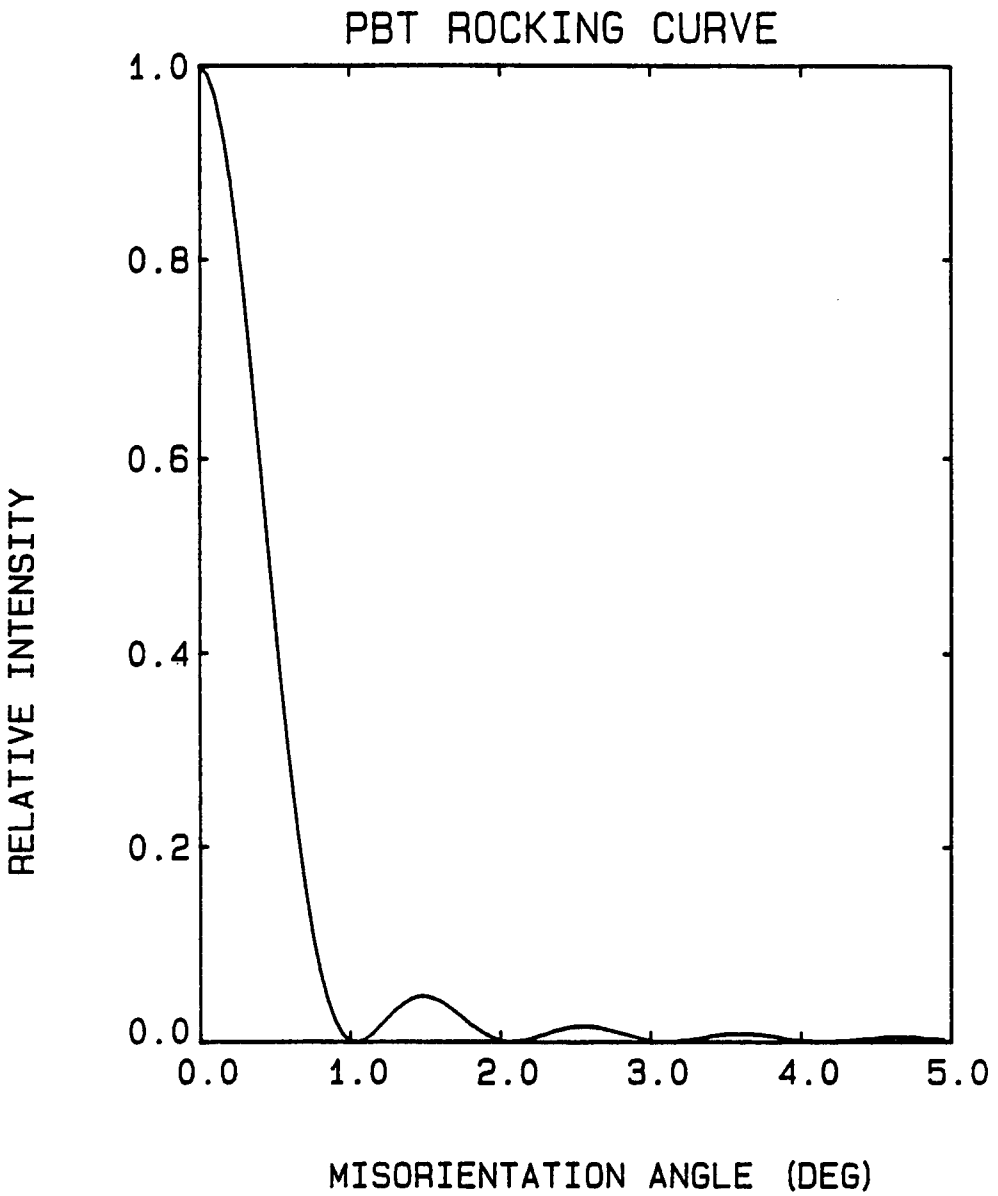

Figure 44. Rocking curve for 1.68 nm^{-1} (100) reflection. Assumed crystal thickness 10 nm.

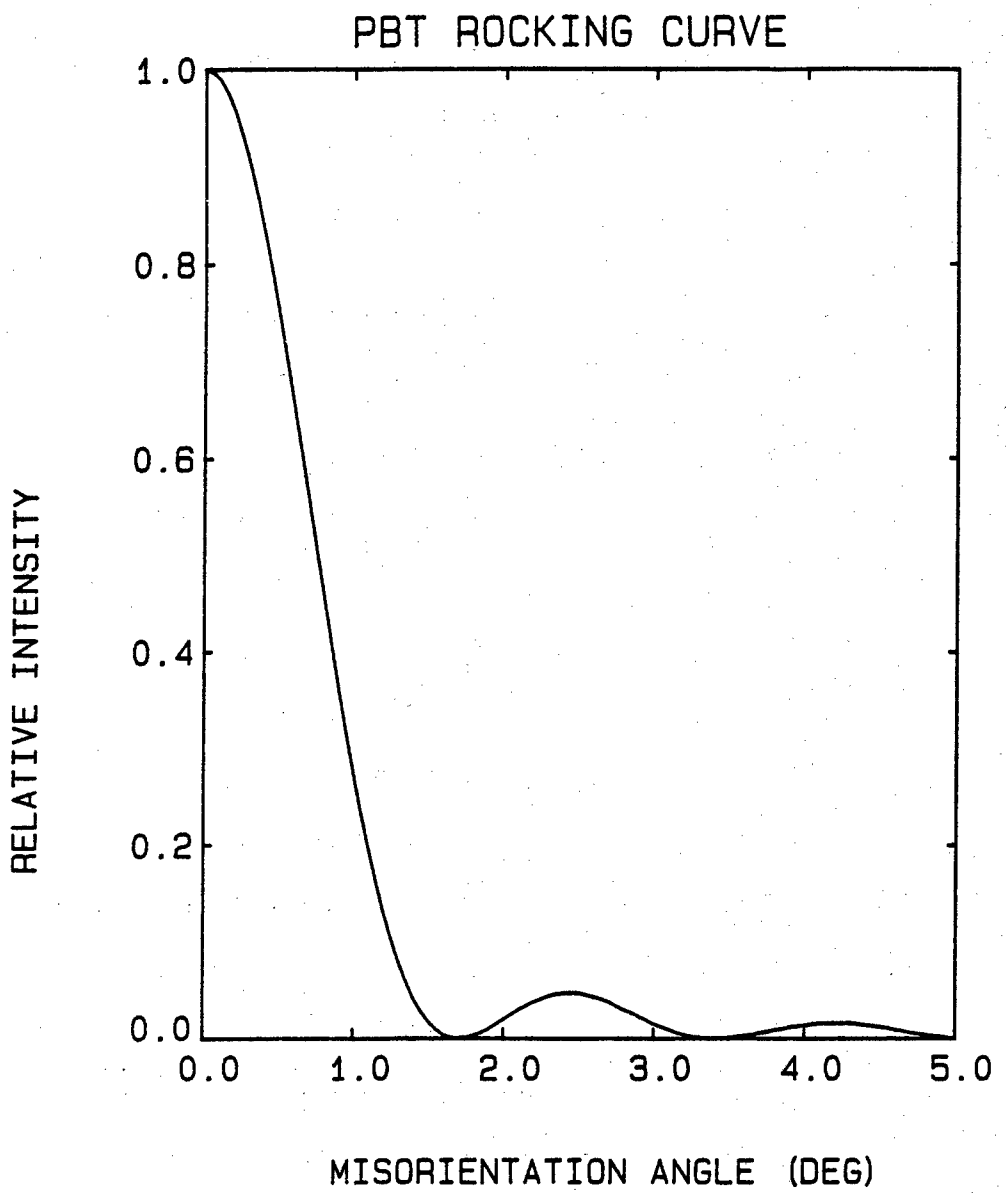

Figure 45. Rocking curve for 2.76 nm^{-1} (010) reflection. Assumed crystal thickness 10 nm.

from incoherent scattering of single chains due to axial translational disorder. The electron density projection of such a model predicts a uniform intensity distribution modulated only by thickness fluctuations.

6.3 PBT Lattice Images

As mentioned earlier, an axial bright field lattice image was obtained by Shimamura [66] of a heat treated PBT fiber from a PPA solution with a spin-draw ratio of 3.7 X. The image was recorded at an instrumental magnification of 100,000 X with an 8 nm^{-1} objective aperture and is shown in Figure 46. The microscope was adjusted to Scherzer defocus (Δf) by minimizing (phase contrast) in the carbon support film ($\Delta f \simeq -170$ nm for our microscope). This value of focus results in good transfer of diffracted beams over the spatial frequency range from about 0.7 to 2 nm^{-1}. Once focus was obtained in a given area, an adjacent unirradiated area was quickly chosen and the photographic exposure made without further adjustment. Distinct fringes (labelled E) are observed parallel to the fiber axis over regions 20 nm wide by 40 nm long with spacing of 0.59 nm corresponding to the first equatorial reflection (100). Less distinct, somewhat meandering fringes are also observed approximately normal to the fiber axis (labelled M). These fringes have a spacing of approximately 1.24 nm corresponding to the first layer line (m_1). They occur in groups of 3-10 fringes with their lateral extent limited to about 5 nm. An optical transform of the bright field micrograph used to print

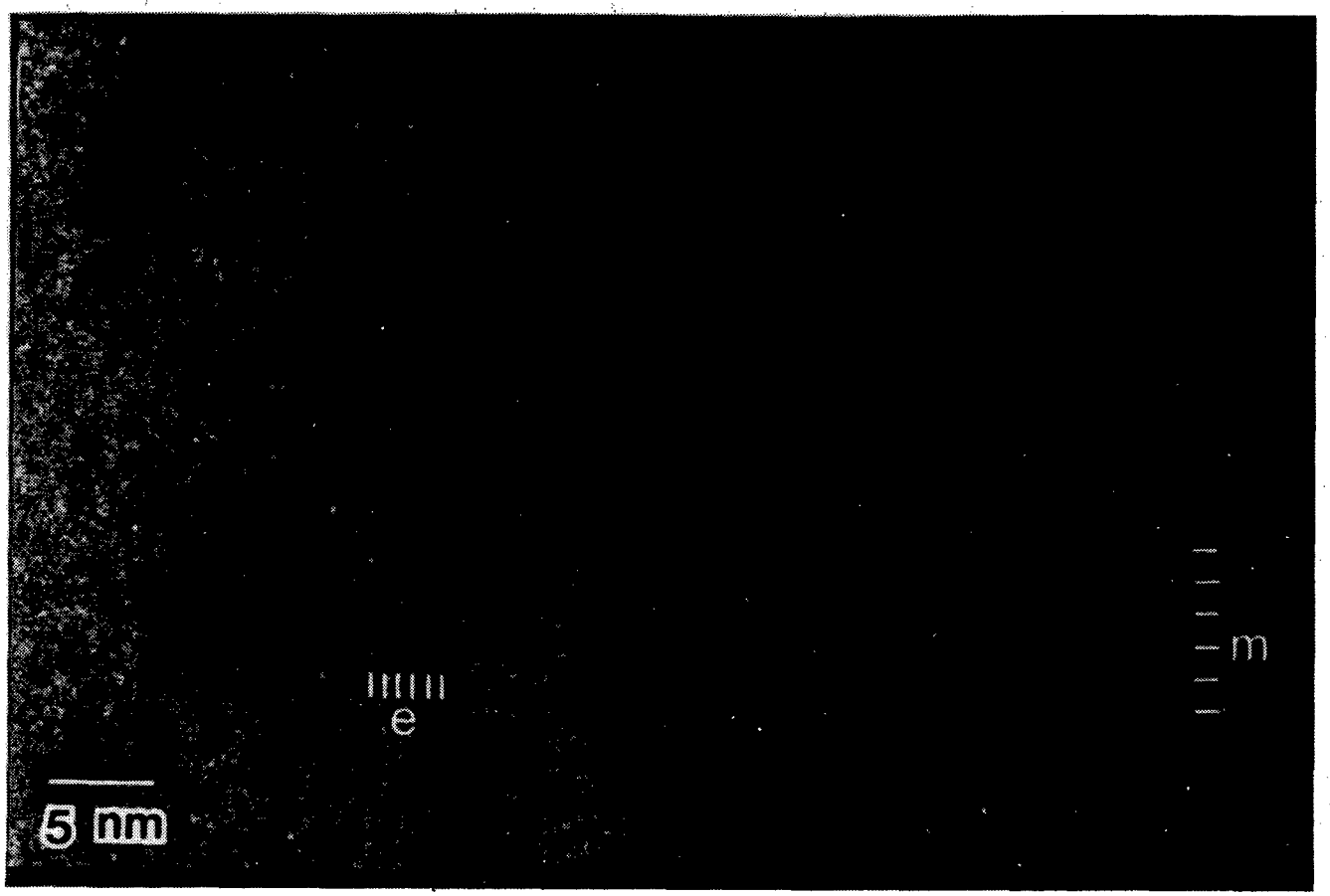

Figure 46. Two regions of an axial bright field lattice image(100,000X instrumental magnification) of a tension heat treated fiber. From Reference [66].

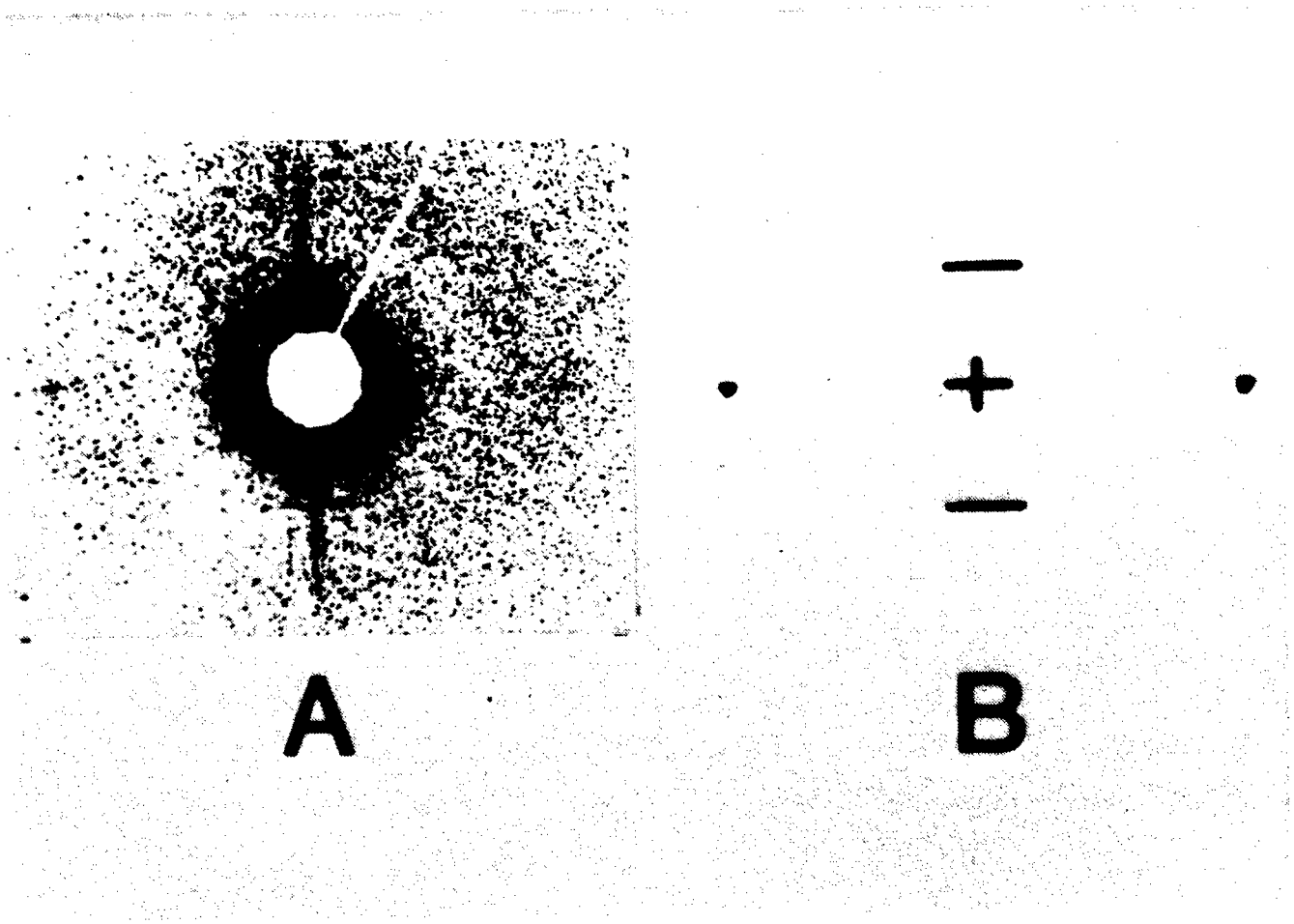

Figure 47. (a) Optical transform of micrograph used to obtain Figure 45.
(b) Schematic of Figure 46a. Sharp spots are due to .59 nm E fringes and diffuse streaks to 1.24 nm M fringes.

Figure 46 is shown in Figure 47a (schematic Figure 47b). A pair of faint spots is seen normal to the fiber axis with a pair of streaks at 90°. The ratio of their reciprocal spacings is 2.13, corresponding well with the ratio m_1/e_1 (i.e. 1.24/.59 = 2.10). The intensity distributions in the optical transform also correspond well with the expected shape forms of the large (E) and small, elongated (M) fringe regions. The 1.24 nm lattice fringes are unequivocal evidence for the occcurence of true three dimensional crystalline order in local regions of the fiber. Only a three-dimensional periodic electron density distribution can produce such fringes. Chains with translational freedom present in most areas of the fibers and films would produce an image with only mass thickness contrast as discussed previously. At present however, these regions with 3-dimensional order are a very minor component of the fibers examined. Because of the relatively small volume fraction, electron diffraction patterns from this sample show no distinct $hl\ell$ reflections and are quite similar to those discussed in Chapter VII. The fringe regions thus far observed while limited in extent, show no evidence of dislocations. This is similar to the perfection of order in lattice images of PPTA fibers [71].

It is interesting to speculate about the cause of the limited size of coherently scattering regions. One possibility is gentle bending with ~ 2° twist. Chain ends are another possibility suggested by Predecki and Statton [72]. A third possibility would be disclinations and inversion wall defects remaining from the liquid crystalline

state.

Predecki and Statton [72] considered the effect of chain ends on packing in flexible semicrystalline polymers. In such cases the stress field around a chain end may be minimized by generating a number of types of line defects. These included edge, screw, coupled-edge, and coupled screw dislocations. Each of these requires bending of the chain axis which may be achieved in flexible polymers by rotating about single covalent bonds. In the case of PBT, such bending of the chain axis could only occur around chemical defects in the chain (unclosed bisthiazole rings) or by breaking of covalent bonds which would be energetically unfeasable and was ruled out in the treatment of Predecki and Statton [72]. One possibility that Predecki and Statton [72] propose that might be feasable in PBT is a low angle tilt boundary formed by condensed chain ends. This is shown schematically in Figure 48. For a PBT of limiting viscosity number of 26 corresponding to an average degree of polymerization of 95 there are approximately 8×10^{19} chain ends per cm^3 or essentially 1 chain end per 50 unit cells. This may be compared to 10^{20} chain ends cm^{-3} for a Nylon 6-6 of molecular weight 15,000 [72]. Because of the extreme chain stiffness of PBT a single chain end may have a much longer range of effect and influence crystal lattice bending.

In conclusion, equatorial dark field images from as-spun PBT fibers and films from MSA and PPA solutions indicate very short range lateral order in molecular packing (2 nm or less). With heat treatment at 475°C or above, this lateral order increases to an average of

10 nm perpendicular to the extrusion direction. The lack of diffraction contrast in meridional dark field images suggests that there is significant translational freedom of the chains along the chain axis, perhaps due to the lack of sharp potential energy minima. However, observation of lattice fringes from meridional reflections suggests that there are some local areas which are more highly ordered than the bulk. It will be interesting to see if optical processing can induce a fully 3-D crystalline structure for PBT. Note also that the increase in local lateral order upon heat treatment observed by dark field is accompanied by fibrillation at the large scale (recall Chapter IV). Further evidence of this was seen by SAXS in Chapter V.

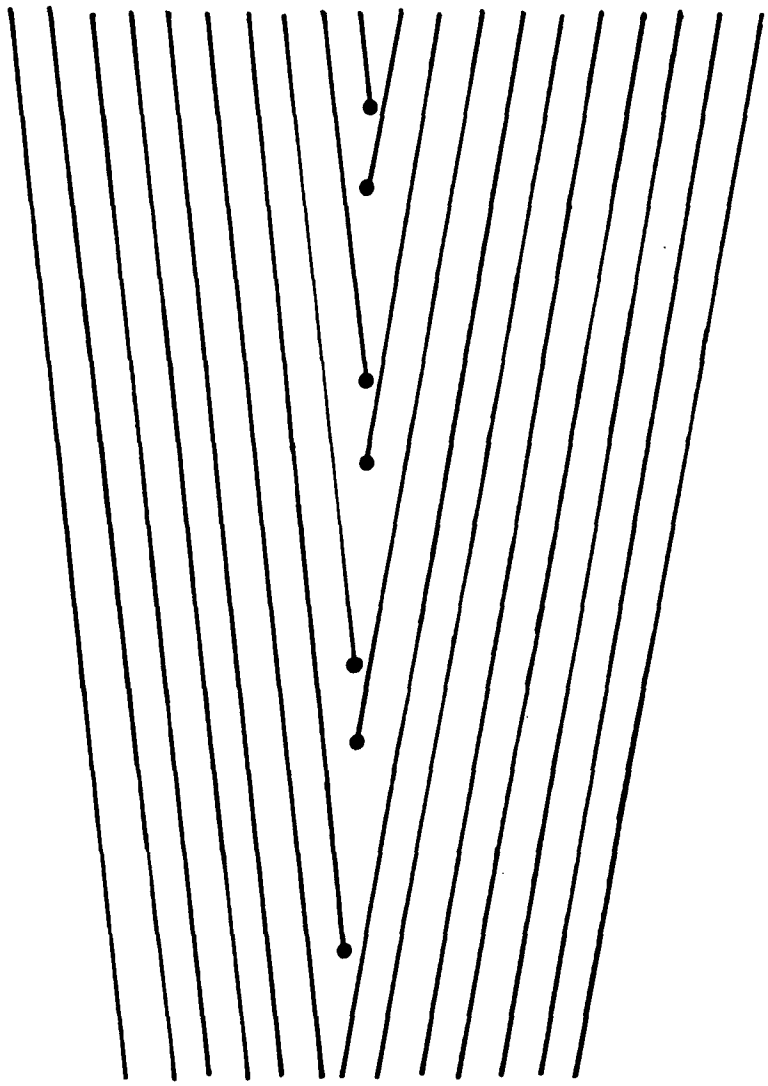

Figure 48. Schematic of model with condensed chain ends. From Reference [72].

CHAPTER VII

STRUCTURAL ANALYSIS BY X-RAY AND ELECTRON DIFFRACTION

7.1 Review of Prior Structure Analysis of PBT and PPTA

7.1.1 PBT. An understanding of the deformation behavior of a material requires a detailed understanding of the structure of the material. Adams *et al.* [73] studied some of the earliest PBT fibers produced by Berry and Wong [10] and interpreted wide angle x-ray and electron diffraction patterns in terms of a model first reported by Oster and Riley [96] consisting of parallel periodic cylinders packed in a hexagonal array. This analysis was based on diffraction patterns consisting of up to 20 diffuse meridional layer lines and two rather broad equatorial maxima. Roche *et al.* [74] studied as-spun fibers produced by Chenevey [12] at higher spin draw ratios which had somewhat improved mechanical properties. Electron diffraction patterns from these fibers also exhibited 20 diffuse meridional layer lines and moreover, contained seven resolvable equatorial reflections. From these patterns a monoclinic net of chains with random translational stagger along the chain axis was proposed. Two possible unit cells were suggested:

Unit Cell I		Unit Cell II	
$a = .583$ nm	$\gamma = 96°$	$a = .710$ nm	$\gamma = 63°$
$b = .354$ nm	$Z = 1$	$b = .665$ nm	$Z = 2$
$c = 1.235$ nm	$\rho = 1.69$ g cm^{-3}	$c = 1.235$	$\rho = 1.69$ g cm^{-3}

More recently, fibers and ribbons annealed at 475°C under load have become available. Electron diffraction patterns now exhibit ten resolved reflections along the equator. The meridional layer lines still consist of diffuse streaks. Analysis of these patterns yields a slightly longer fiber repeat distance, 1.245 ± 0.005 nm. A refinement of unit cell I, is given below. Such a choice of the unit cell corresponds to the first setting of a monoclinic cell [97].

Unit Cell IA

a = .597 nm	γ = 95.2°
b = .362 nm	Z = 1
c = 1.245 nm	ρ = 1.65 gm/cm^3

Unit Cell IA corresponds to the very simple arrangement of parallel chains shown in Figure 49.

Preliminary analysis [74] of the intensities of the equatorial reflections predicts a setting angle ϕ, between the a axis and the phenyl ring of about 35° and an angle, α, between the $\underset{\sim}{a}$ axis and the bisthiazole moiety of -5° (see Figure 49b). For these values, the calculated R factor is 0.096. R is defined as:

$$R = \frac{\Sigma \left| f_o - f_c \right|}{\Sigma f_o} \qquad (7.1)$$

where f_o and f_c are the observed and calculated structure factors, respectively. The observed and calculated structure factors and

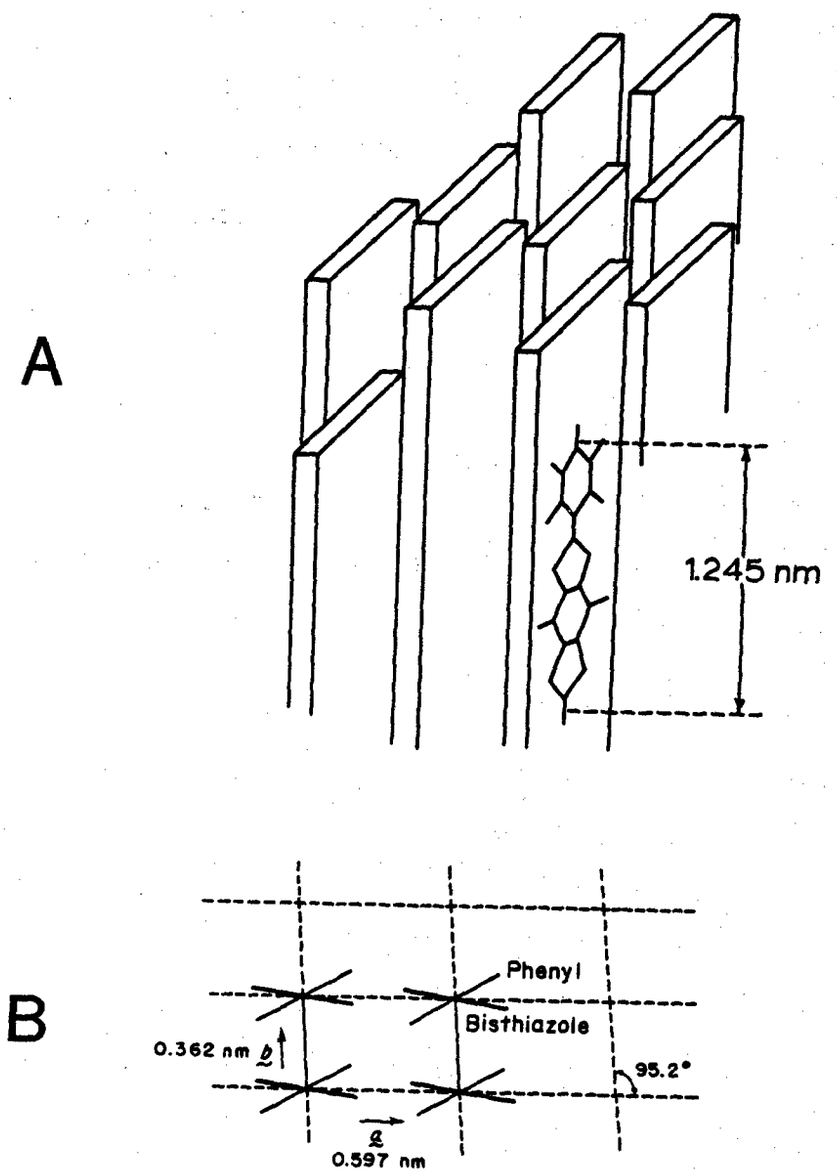

Figure 49. Packing of PBT chains in the solid.

d-spacings [74] for the equatorial reflections are given in Table IX.

The real space lattice is represented by the three basis vectors, $\underset{\sim}{a}$, $\underset{\sim}{b}$, $\underset{\sim}{c}$. Associated with the real space lattice is the reciprocal lattice in scattering space, which may be represented by the three basis vectors, $\underset{\sim}{a}^*$, $\underset{\sim}{b}^*$, $\underset{\sim}{c}^*$. In a monoclinic lattice of the first setting, $\underset{\sim}{c}^*$ is colinear with $\underset{\sim}{c}$ and has a magnitude [97]

$$|\underset{\sim}{c}^*| = \frac{1}{|\underset{\sim}{c}|} \tag{7.2}$$

Both c and c^* are oriented along the extrusion direction in highly oriented PBT fibers and films. The other two reciprocal basis vectors are given by [97]

$$\underset{\sim}{a}^* = \frac{\underset{\sim}{b} \times \underset{\sim}{c}}{\underset{\sim}{a} \cdot \underset{\sim}{b} \times \underset{\sim}{c}} \tag{7.3}$$

$$\underset{\sim}{b}^* = \frac{\underset{\sim}{c} \times \underset{\sim}{a}}{\underset{\sim}{a} \cdot \underset{\sim}{b} \times \underset{\sim}{c}} \tag{7.4}$$

For monoclinic unit cells with the first setting, one obtains the magnitude of $\underset{\sim}{a}^*$ and $\underset{\sim}{b}^*$ from [97]

$$|\underset{\sim}{a}^*| = [\,|\underset{\sim}{a}|\,\sin\gamma]^{-1} \tag{7.5}$$

$$|\underset{\sim}{b}^*| = [\,|\underset{\sim}{b}|\,\sin\gamma\,]^{-1} \tag{7.6}$$

Table IX

Calculated and Observed Equatorial Structure Factors for PBT and d-spacings for Electrons and X-rays

hk	f_c*	$f_{o,x}$	$f_{o,e}$	d_c (nm)	$d_{o,x}$ (nm)	$d_{o,e}$ (nm)
10	58.3	44.4	58.3	.594	.592	.588
01	100.0	100.0	100.0	.360	.354	.355
$1\bar{1}$	46.1	47.6	41.7	.321	.316	.318
20,11	31.9	33.0	29.1	.294	.296	.294
$2\bar{1}$	0.1	---	5.8	.240	---	.234
21	12.2	---	11.7	.220	---	.222
30	1.9	---	5.8	.198	---	.198
31,02	26.5	(40)	29.1	.181	.181	.182
$1\bar{2}$	9.1	w	14.1	.177	.175	.177
31	13.3	w	18.3	.167	.165	.167

R = .096

*temperature factor of .06 nm^2

o,x indicates observed values from x-ray diffraction
o,e indicates observed values from electron diffraction

From Reference [75]

The projection of the $\underset{\sim}{a}^*$ $\underset{\sim}{b}^*$ plane along $\underset{\sim}{c}^*$ and the associated equatorial reflections was constructed from the data in reference [74] and are shown in Figure 50.

In order to model the scattering from a single PBT chain, Odell *et al*. [75] calculated the cylindrically averaged squared Fourier transform, termed the molecular transform, of a single repeat unit in planar conformation based on estimated bond angles and distances obtained from the literature. The results were displayed on a Decwriter III matrix printer and are shown in Figure 51. When 8 such units are joined together to form a single chain, discrete layer lines are obtained in the Fourier transform (Figure 52). The second and seventh layer lines are very weak. As noted by Odell, a comparison of the molecular transform with the electron diffraction patterns from as-spun and heat treated fiber shows remarkable agreement with observed relative intensities of the layer lines (see Figure 53) except on the sixth layer.

Odell *et al*. [75] also proposed two unit cells based on the equatorial reflections:

Odell I		Odell II	
a = .655 nm	γ = 63.62°	a = 1.196 nm	γ = 79.1°
b = .356 nm	Z = 1	b = .356 nm	Z = 1
c = 1.235 nm	ρ = 1.71 g/cm^{-3}	c = 1.235 nm	ρ = 1.71 g/cm^{-3}

As can be seen from Figure 54, these cells are simply different versions of Roche's cell IA. As earlier proposed by Adams [73] and

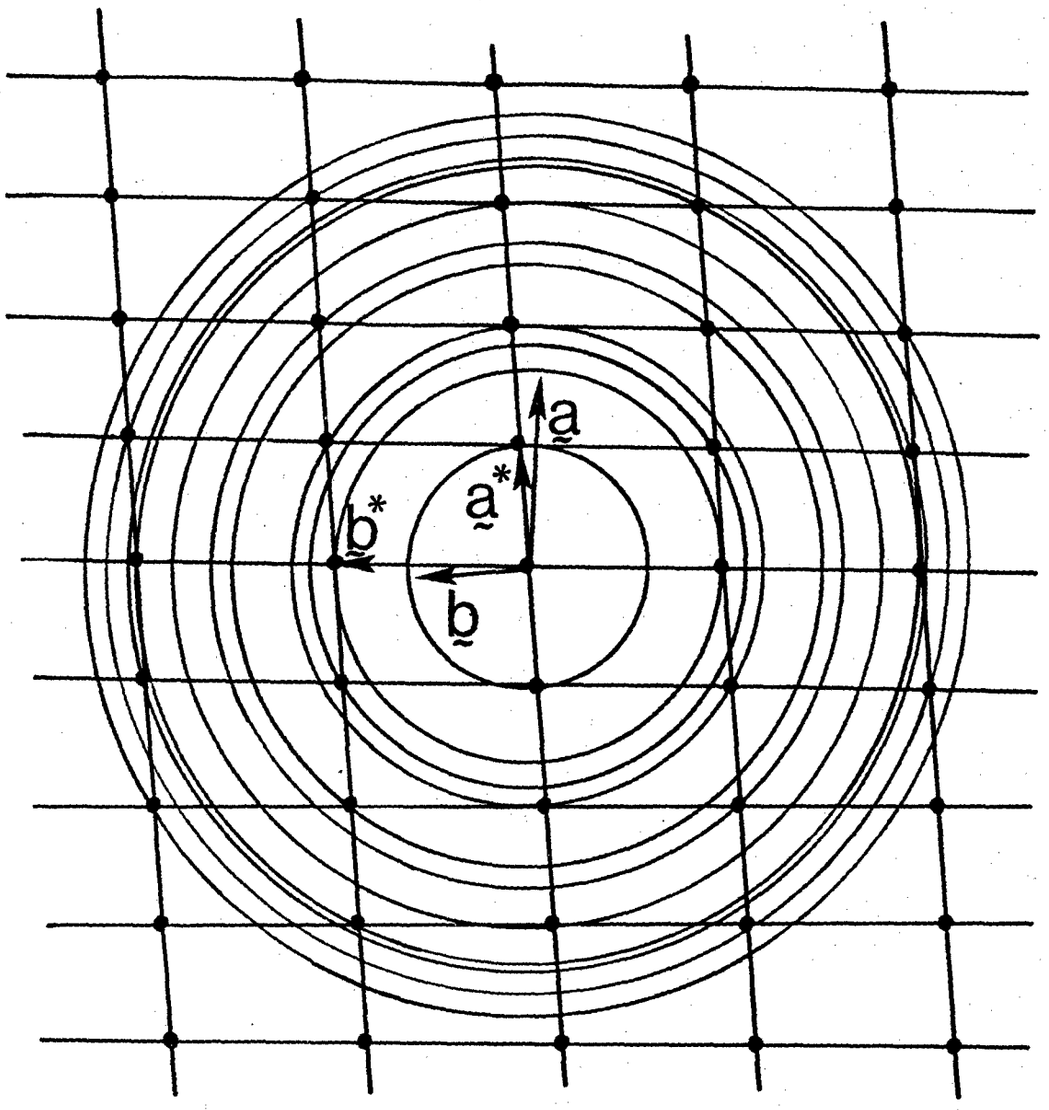

Figure 50. Projection down $\underset{\sim}{c}^*$ of $\underset{\sim}{a}^*$ $\underset{\sim}{b}^*$ plane viewed along c^* in PBT. Circles represent equatorial reflections for uniaxial symmetry.

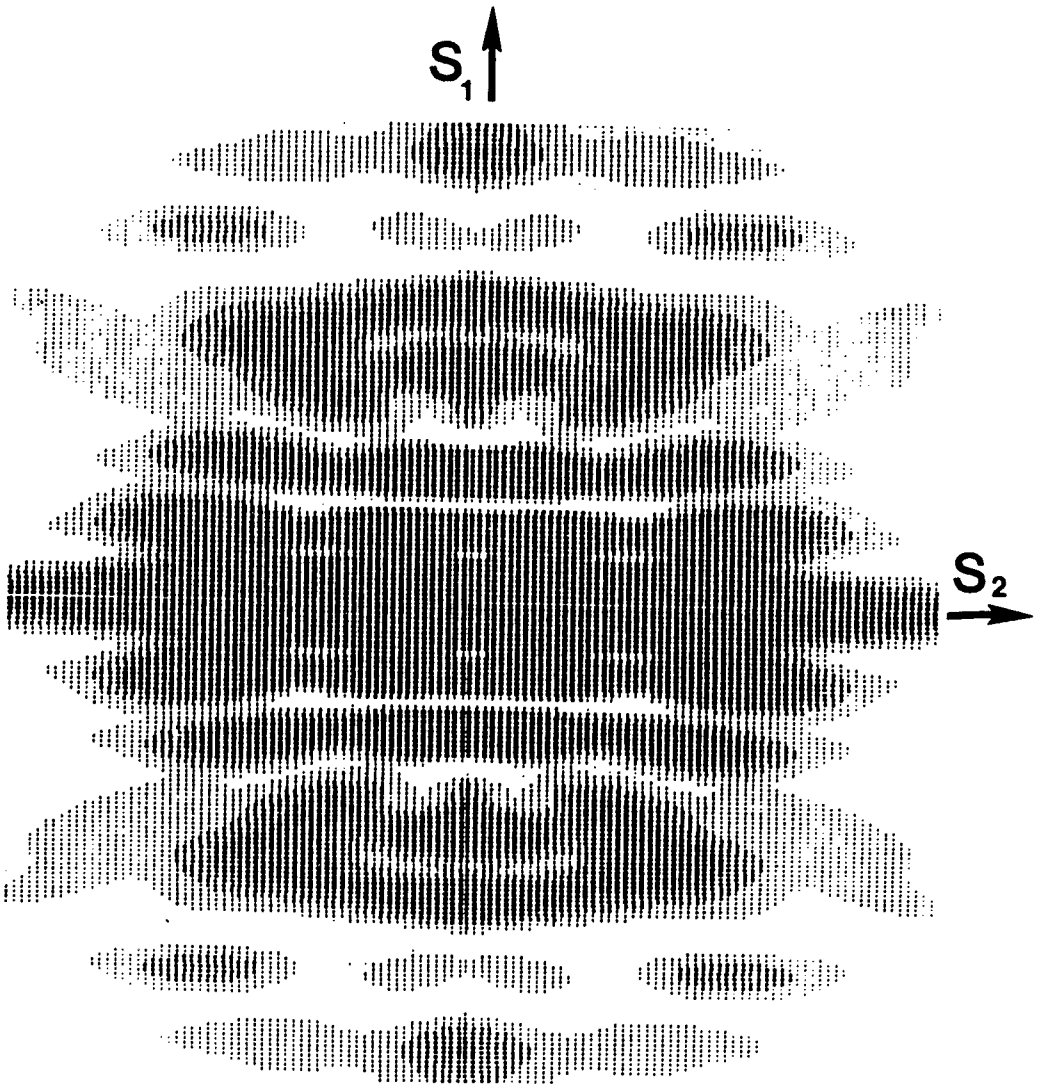

Figure 51. Cylindrically averaged molecular transform of a single PBT repeat unit. From Reference [75].

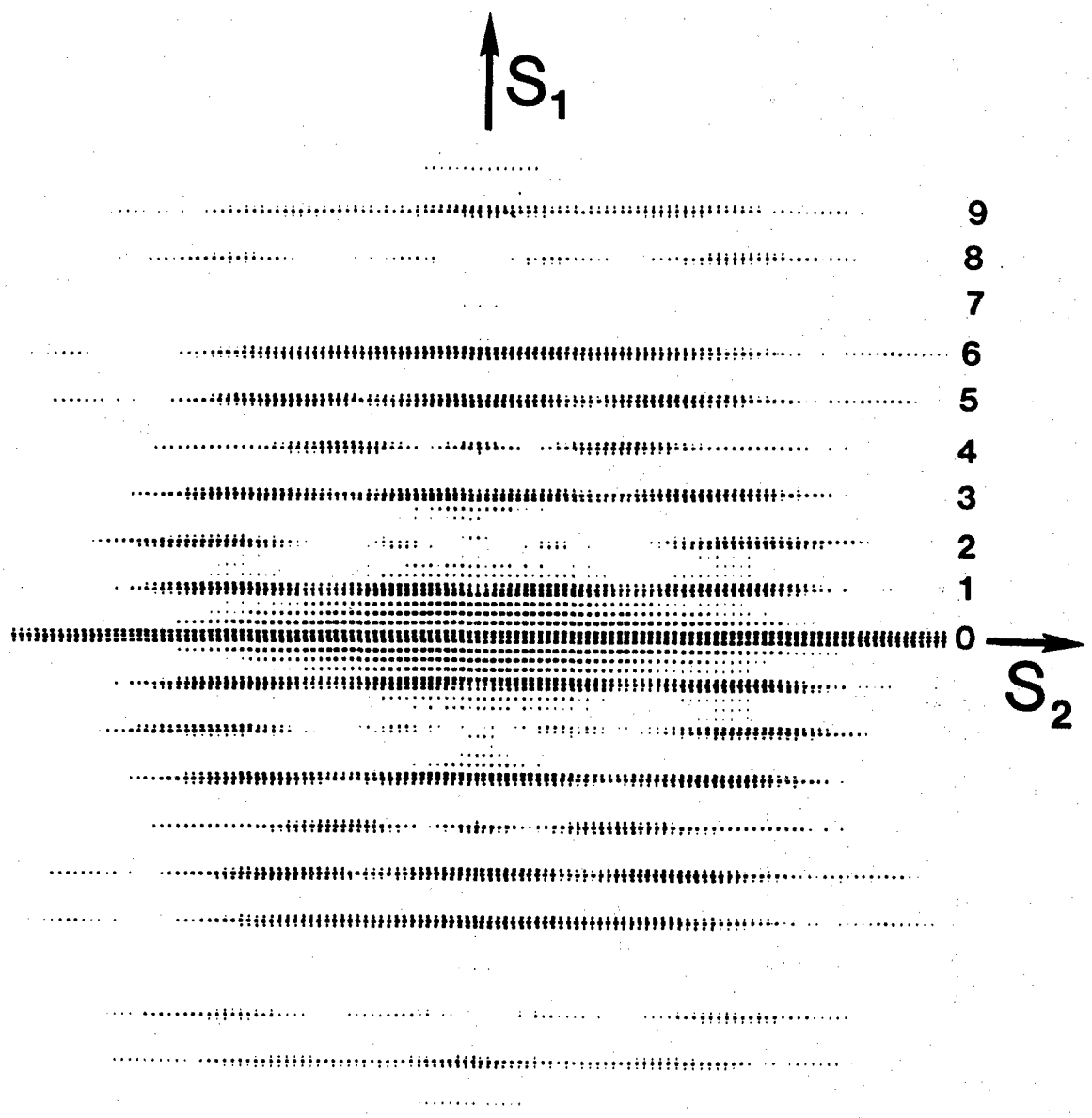

Figure 52. Cylindrically averaged molecular transform of a single PBT chain of 8 repeat units. Numbers on the right side are layer line numbers. From Reference [75].

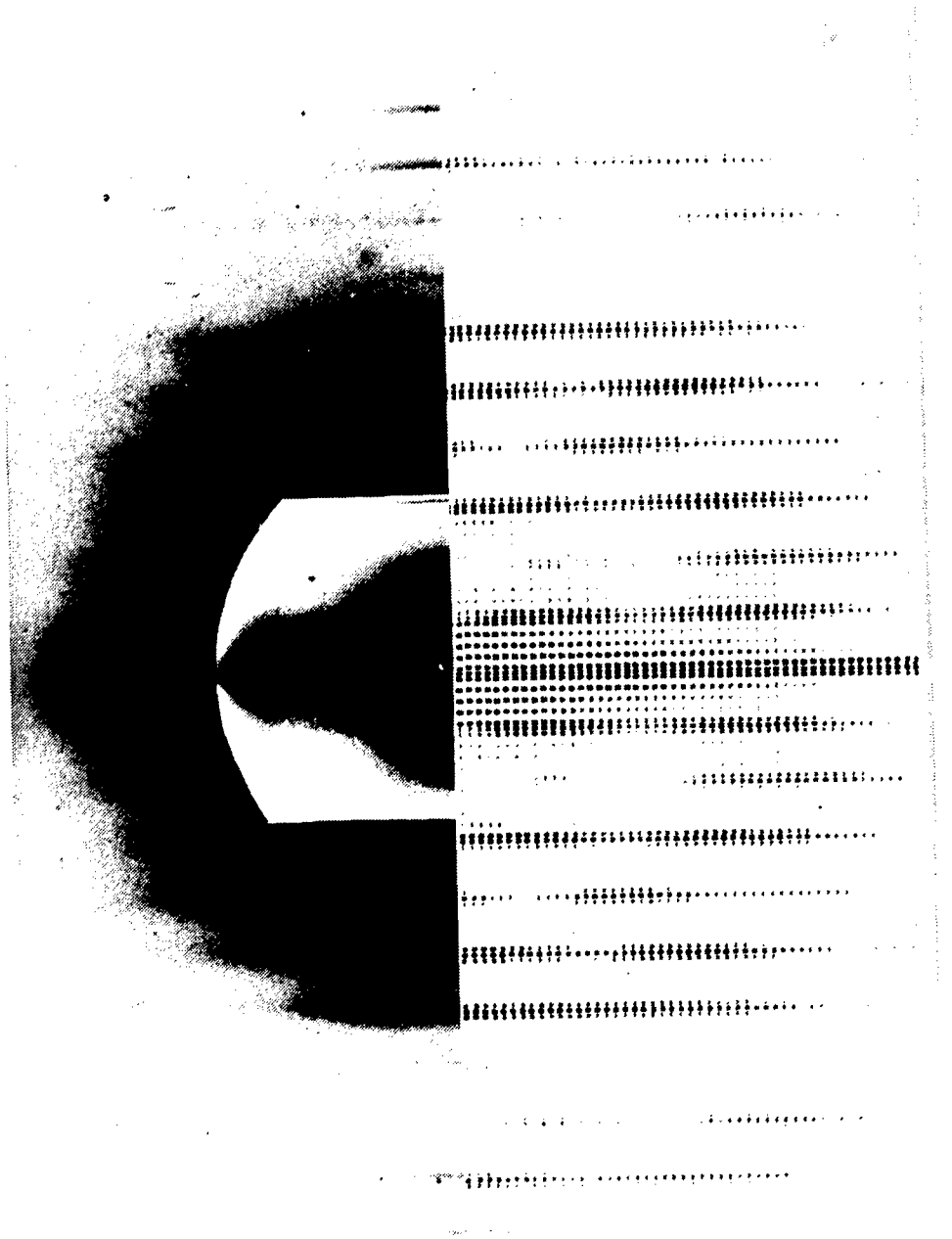

Figure 53. Comparison between the cylindrically averaged molecular transform of 8 repeat units and electron diffration from HTF-23A. Transform from Reference [75], diffraction pattern from this work.

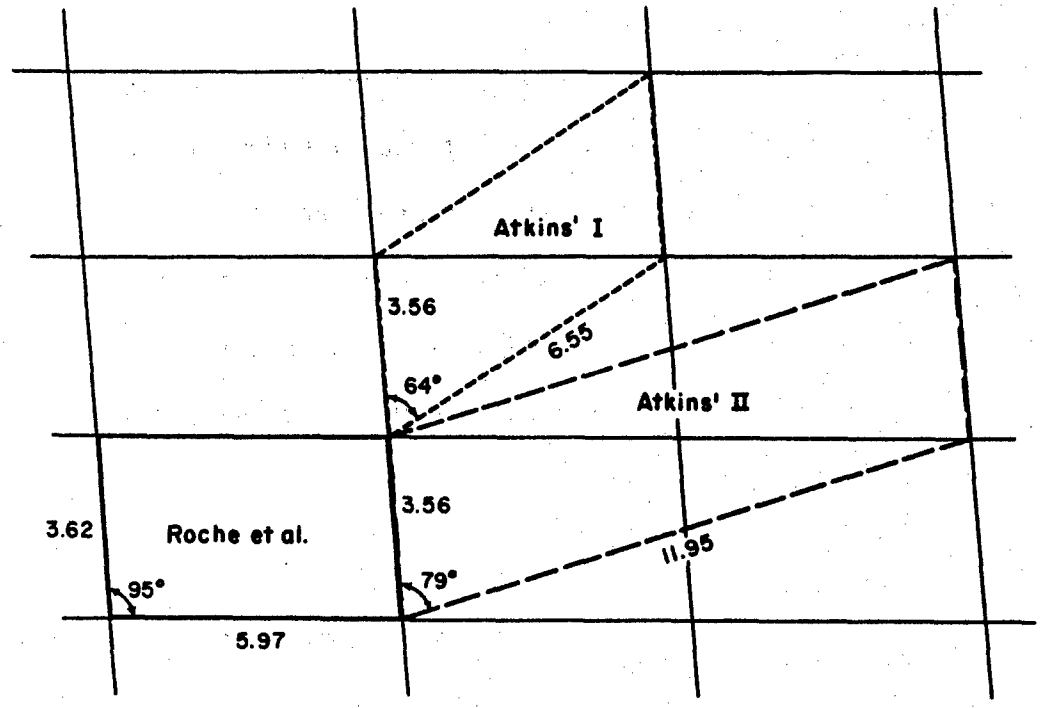

Figure 54. Comparison between PBT and cells proposed by Roche [74] and Odell et al. [75].

Roche [74], the molecular arrangement for the Odell models [75] is also a 2-dimensional net with translational freedom of the chains along the fiber axis and not a three dimensional lattice. This view is further supported in this dissertation by the observation of equatorial lattice images with the lack of coherently diffracting regions in the meridional dark field image, previously discussed in Chapter VI.

7.1.2 PPTA

Structural investigations of PPTA have been reported by several authors and will be briefly reviewed here for comparison to PBT. Northolt [76,77,78] and Tadokoro [82] have reported very similar crystal structures for highly oriented well annealed fibers of PPTA. The basic structure is monoclinic (pseudo-orthorhombic) with $|a| = 0.787$ nm, $|b| = 0.518$ nm, $|c| = 1.29$ nm and close to 90 degrees [78] and is depicted in Figure 55. Northolt remarked that the x-ray patterns were quite similar to those from poly(p-phenylene oxide) (PPO) and poly (p-phenylene sulfide) (PPS). The crystal structural parameters of these polymers are compared to PBT in Table X. Dobb *et al*. [61] reported a diffuse intensity along the layer lines in x-ray diffraction patterns from PPTA fibers. This is most likely due to disordered packing and will be discussed in detail later.

Haraguchi *et al*. [79,80] have studied unoriented thin (3-15 m) films coagulated with selected nonsolvents. In all cases, their films exhibited preferred orientation. Films coagulated with water exhibited

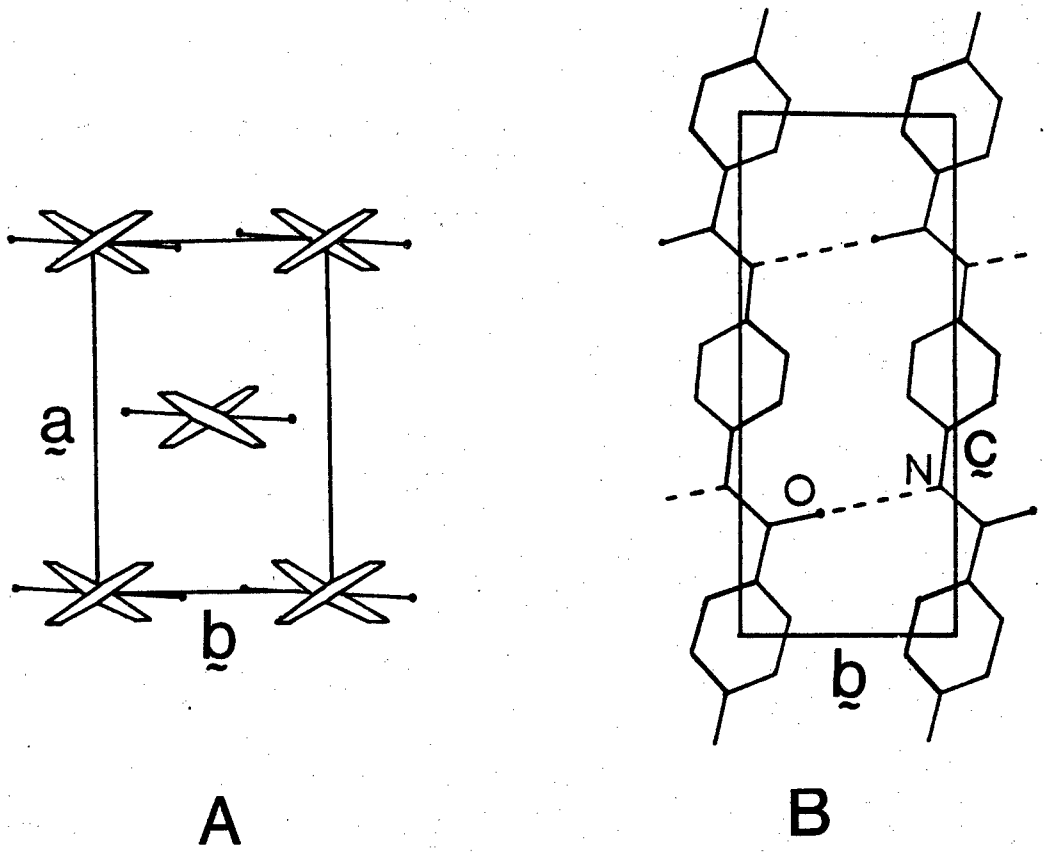

Figure 55. Crystal structure of PPTA proposed by Northolt [76-78].

Table X

Structural Parameters for Selected Aromatic Polymers

Polymer	PBT[1]	PPTA[2]	PPO[2]	PPS[2]
$\lvert \underset{\sim}{a} \rvert$ (nm)	0.597	0.787	0.807	0.867
$\lvert \underset{\sim}{b} \rvert$ (nm)	0.362	0.518	0.554	0.561
$\lvert \underset{\sim}{c} \rvert$ (nm)	1.245	1.29	0.972	1.026
γ (degs)	96.2	~ 90	90	90
z	1	2	2	2
Space Group	?	P_n or $P_{21/n}$	P_{bcn}	P_{bcn}

[1] From Reference [75]

[2] From Reference [78]

a uniplanar orientation with the $\underset{\sim}{b}$ axis parallel to the surface. Haraguchi [79] postulated that water molecules hydrogen bond to the amide groups along the $\underset{\sim}{b}$ direction but that the PPTA molecules pack together along the $\underset{\sim}{a}$ direction due to van der Waals forces. Upon drying and annealing to remove residual water, the hydrogen bond plane becomes perpendicular to the film surface.

However, Haraguchi [79] found that the $\underset{\sim}{a}$ axis of thin PPTA films is preferrentially oriented parallel to the film surface when sulfuric acid PPTA solutions are coagulated with acetone, methanol or ethanol. They attribute this to the lack of competition of methanol, ethanol and acetone for the hydrogen bond sites of the amide group. In these cases, the hydrogen bond planes are parallel to the film surface.

7.2 Calculation of Single Chain Scattering

In order to better understand the distribution of diffuse scattered intensity along nonzero layer lines in the selected area electron diffraction (SAED) and wide angle x-ray diffraction (WAXD) of PBT, we decided to further consider the scattering of a single PBT chain. In this case we used the method of Suehiro, Chatani and Tadokoro [81] and Tadokoro [82] to generate the single chain scattering profile which is the squared Fourier transform of the electron density distribution of the chain and is, therefore, frequently termed the molecular transform. We have specifically considered two sets of atomic coordinates, a set supplied by Odell *et al.* [75] and another set generated by summing bond vectors obtained from bond angles, bond

distances, and internal rotation angles obtained from model compound studies reported by Wellman et al. [83]. The program BONDSUM, which was based on a procedure reported by Yokouchi et al. [84]. The program generated atomic coordinates from bond angles and bond distances, and data are included in Appendix I.A.

Suehiro et al. [81] and Tadokoro [82] have derived the scattered intensity, $I(\underset{\sim}{s})$, for a structure where the molecular chains have a periodic structure and are packed periodically in the lateral directions with respect to the fiber axis while the chains are irregularly positioned along the fiber axis. $I(\underset{\sim}{s})$ is given by

$$I(\underset{\sim}{s}) = [\,|F_m(\underset{\sim}{s})|^2 \frac{\sin^2\pi N_a s_a a \, \sin^2\pi N_b s_b b \, \sin^2\pi N_c s_c c}{\sin^2\pi s_a a \, \sin^2\pi s_b b \, (\pi s_c c)^2}$$

$$+ N_a N_b \sum_m |F_m(\underset{\sim}{s})|^2 \{1 - \frac{\sin^2\pi s_c c}{(\pi s_c c)^2}\}] \frac{\sin^2\pi N s_c c}{\sin^2\pi s_c c} \qquad (7.8)$$

where $F_m(\underset{\sim}{s})$ is the structure factor of the chain in the mth state. N_a, N_b and N_c are the number of repeats along the a, b and c axis, respectively and s_a, s_b, s_c are the components of $\underset{\sim}{s}$ along the $\underset{\sim}{a}^*$, $\underset{\sim}{b}^*$ and $\underset{\sim}{c}^*$ reciprocal lattice vectors. This predicts the diffracted intensity is negligible except when $s_c c = \ell$ (ℓ = any integer) i.e. diffracted intensity only occurs on the layer lines. When $s_a a = h$ and $s_b b = k$ (h and k, integer) and N_a and N_b are large, the scattered intensity distribution is given by:

$$I(s) = N_a^2 N_b^2 N_c \left| \sum_m F_m(h,k,0) \right|^2 \quad \text{for } \ell = 0 \tag{7.9}$$

and

$$I(\underset{\sim}{s}) = N_a N_b N_c \left| \sum_m F_m(h,k,\ell) \right|^2 \quad \text{for } \ell \neq 0 \tag{7.10}$$

This indicates that the equatorial reflections are <u>discrete</u> and the non-zero layer lines are <u>continuous</u>. If one chooses cylindrical coordinates (s_2,α,s_1) in recipocal space such that s_1 is parallel to c^*, s_2 is perpendicular to c^*, and α is the azimuthal angle (see Figure 49), the cylindrically averaged intensity of the layer line ℓ is given by:

$$\langle I(\underset{\sim}{s})\rangle_\alpha = \frac{1}{2\pi} \int_0^{2\pi} \left| F_m(s_2,\alpha,s_1) \right|^2 d\alpha \tag{7.11}$$

Since the integration is independent of m

$$I(\ell/c,s_2) = \sum_{i=j}^{N} \sum_{j=1}^{N} f_j f_j \, J_0(2\pi s_2) r_{ij} \exp\{2\pi i \ell (z_j - z_{j'})/c\} \tag{7.12}$$

where f_i, f_j are the structure factors of the ith and j^{th} atoms, respectively; $r_{ij}^2 = (x_i - x_j)^2 + (y_i = y_j)^2$, where x_i, y_i and z_i are atomic coordinates (<u>not fractional</u>) of the ith atom; c is the fiber repeat distance, and $J_0(x)$ is the zeroth order Bessel function. Since the double sum over $(z_i - z_j)$ has an equal number of positive and negative terms, the exponential in equation 7.12 reduces to a cosine and thus

$$\langle I(s_2,\ell/c)\rangle_\alpha = 2 \left\{ \sum_{i=1}^{N} \sum_{j=i}^{N} f_i f_j J_0(2\pi r_{ij}) \cos(2\pi \ell (z_i - z_j)/c \right\} \tag{7.13}$$

If one does not cylindrically average, one obtains

$$\langle I(s_2,\alpha,\ell/c)\rangle = 8 \{ \sum_{i=1}^{N} \sum_{j=i}^{N} f_i f_j \cos(2\pi s_2(x_i-x_j)\cos\alpha)$$

$$\times \cos(2\pi s_2(y_i-y_j)\sin\alpha)\cos(2\pi\ell(z_i-z_j)/c)\} \qquad (7.14)$$

First, we consider the case of cylindrical symmetry where the scattering is rotationally averaged mathematically (Equation 7.13) using a program CYLTRAN (Appendix I.2) and second, the case of preferred orientation (that is, without the cylindrical average)(Equation 7.14) using a program POTRAN (Appendix I.3). The input files for CYLTRAN or POTRAN are generated using a program DATAGN (Appendix I.4), thereby minimizing the risk of introducing erroneous coordinates by retyping data.

Specifically, calculations have been performed for the 1st - 8th layer lines using a $\underset{\sim}{c}$ axis repeat of 1.245 nm. The scattered intensity along a particular layer line [i.e. at increments of ℓ/c along the $\underset{\sim}{c}^*$ axis (extrusion direction)] was calculated at 0.4 nm^{-1} increments along an axis, labeled s_2, which is normal to $\underset{\sim}{c}^*$.

Following Tadokoro [82] a uniaxial temperature factor was applied to the intensity calculation. Physically the temperature factor accounts for random vibrations of the atoms from their equilibrium positions in the unit cell due to thermal vibrations. In single crystal analysis, a temperature fator is frequently associated with each atom. However, we have applied an average temperature factor to the calculation and accounted for different probabilities of vibration

parallel and perpendicular to the chain axis. The intensity corrected for thermal vibration, $I_{corr}(s_1,s_2)$, is given by [82]:

$$I_{corr}(s_1,s_2) = I_{calc}(s_1,s_2) \exp\{-\frac{1}{2}(B_{\parallel} s_1^2 + B \quad s_2^2)\} \qquad (7.15)$$

where $I_{calc}(s_1,s_2)$ is the intensity calculated without thermal vibrations, $B_{\parallel}$ is the temperature factor parallel to the chain acis, and B is the temperature factor perpendicular to the chain axis. Two cases have been considered, specifically temperature factors of 0.06 and 0.025 nm^2 normal to the chain direction and 0.06 and .005 nm^2 parallel to the chain direction. These values were suggested by E. Roche [85]. In the future these could be experimentally determined from intensity measurements as described by Buerger [86]. In order to test the program CYLTRAN the single chain scattering for poly(β-propiolactone) was calculated using the data of Suehiro et al. [81]. The results obtained from CYLTRAN were identical to those published by Suehiro et al.

7.2.1. Cylindrically Averaged Single Chain Scattering. Figure 56 shows the cylindrically averaged intensity profiles for the first through eighth layer lines calculated assuming the coordinates of Odell et al. [75] where the molecular axis has been rotated by 2.5° to coincide with the fiber axis. This allowed the chain to be easily generated and resulted in an imperceptible effect on the calculated intensity. A temperature factor of (.06, .06 nm^2) (parallel, normal) was used. The variations of intensity along the layer lines are in

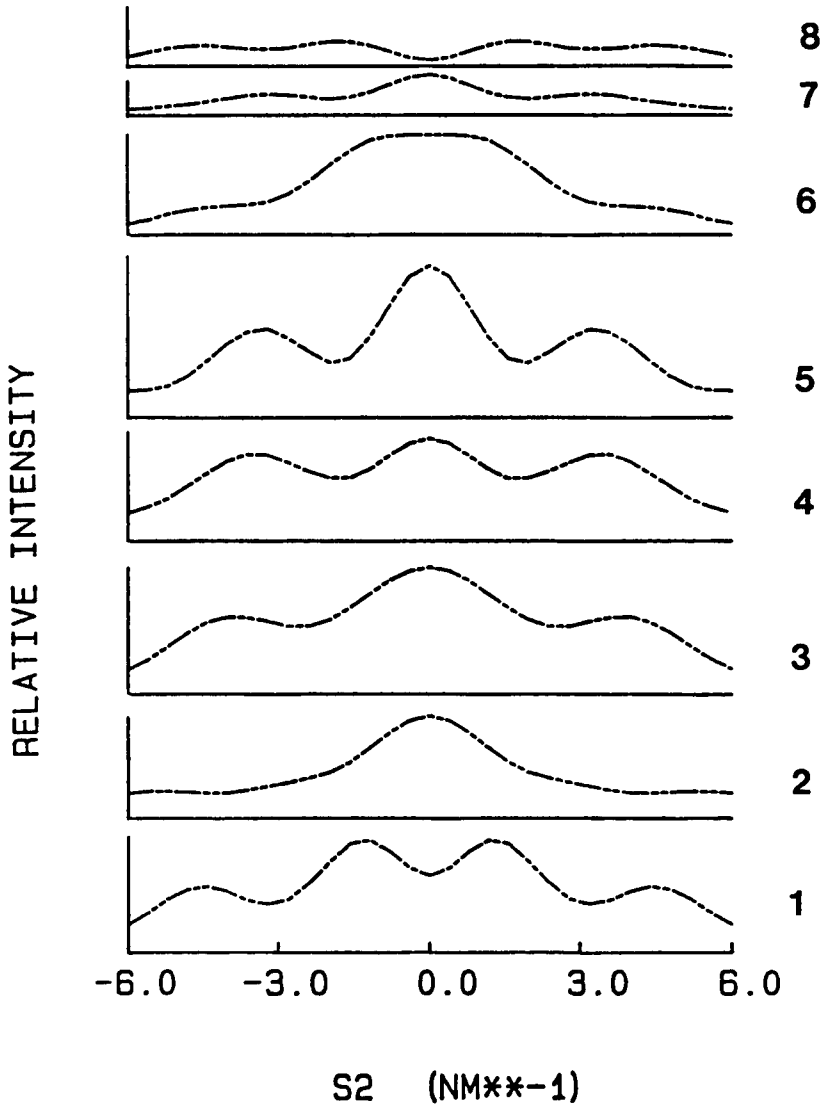

Figure 56. Cylindrically averaged intensity profiles for the first eight layer lines for a PBT chain of 8 units generated assuming the coordinates of Odell et al. [75]. Temperature factor (0.06, 0.06 nm^2) (parallel, perpendicular) to the chain axis. Numbers on the right are the layer line numbers.

qualitative agreement with the matrix printer plots shown by Odell (see Figure 52).

When coordinates generated by BONDSUM were used with a temperature factor of (.005, .025 nm^2) (see Figure 57) a splitting of the sixth layer line is observed. Apparently the slight differences (typically $\pm$ 0.02 nm) in the atomic coordinates are sufficient to cause differences in calculated layer line intensities, particularly in the higher order layer lines which are more sensitive to the local atomic structure. When the temperature factor is increased to (.06, .06 nm^2) (see Figure 58) the intensity decreases faster with increasing (s_1,s_2) on the higher layer lines, but the shapes of the curves are similar. The CYLTRAN program was then used to calculate the distribution of intensity about a given layer line in specified increments of s_1. Figure 59 shows the distribution in intensity about $\ell = 6$ in increments of 2×10^{-2} nm^{-1} along the meridian. The calculated maximum remains at constant S_2 as one moves slightly off the layer line. Therefore splitting will not disappear simply if the Ewald sphere intersects the film slightly away from an integral layer line. It is also important to note that the cylindrical average is insensitive to rotation of the phenyl ring and so <u>cannot</u> be used as evidence to support a model with a particular conformational angle. The relative cylindricaly averaged intensity profile was also found insensitive with respect to including the weak scattering from the six H atoms per repeat unit.

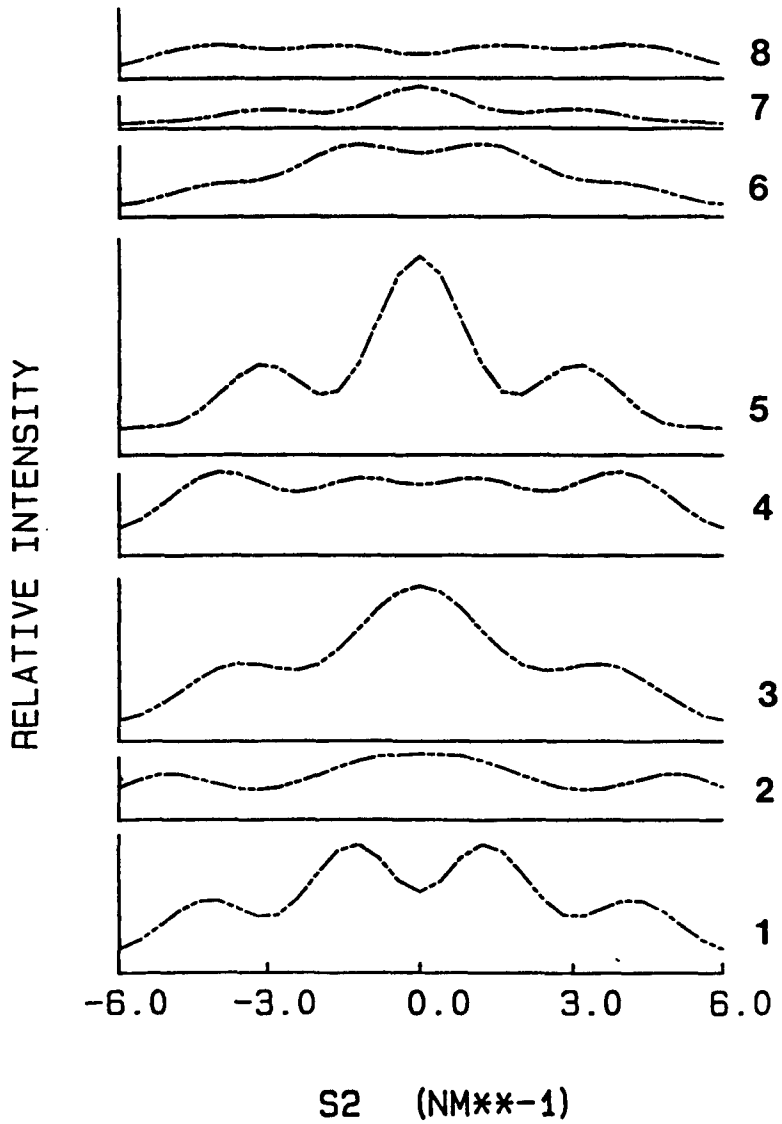

Figure 57. Cylindrically averaged intensity profiles for the first eight layer lines for an H_6PBT chain of 8 units generated assuming the coordinates of Wellman et al. [83]. Temperature factor (0.06, 0.06 nm^2) (parallel, perpendicular) to the chain axis. Numbers on the right are the layer line numbers. Notice splitting of ℓ=6.

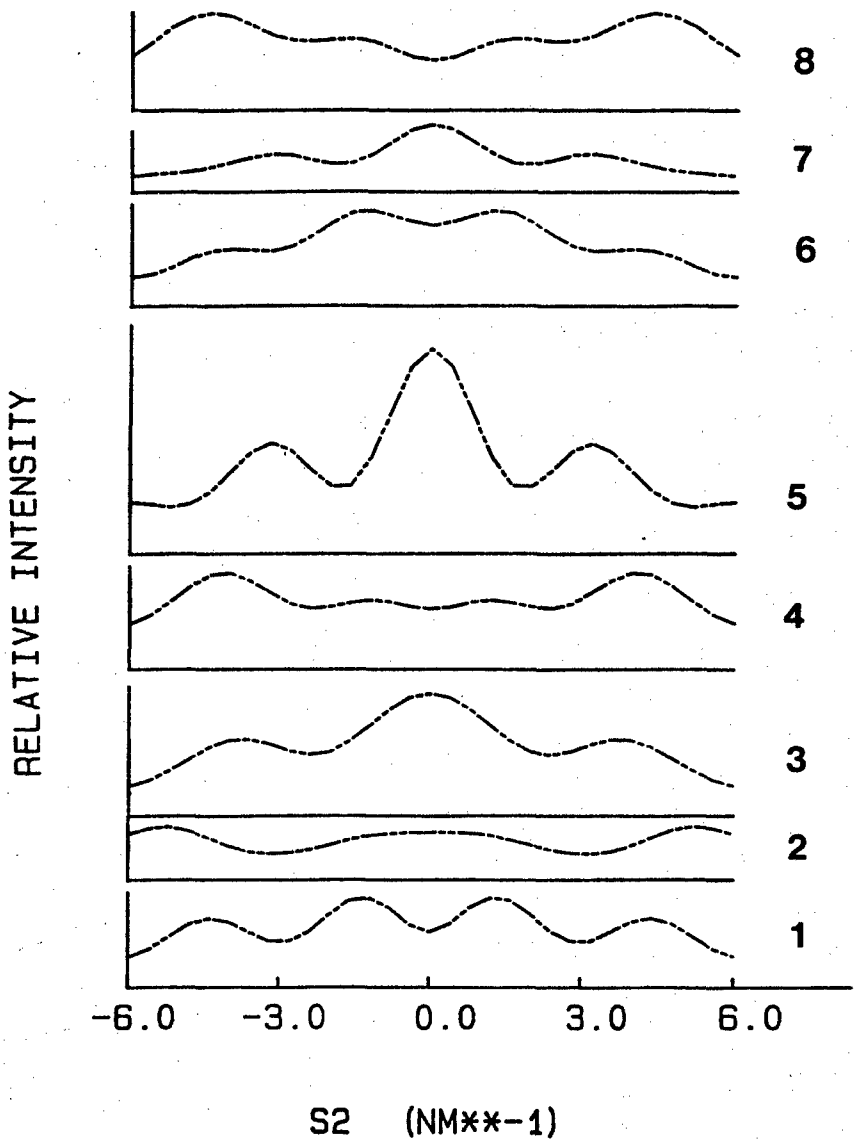

Figure 58. Cylindrically averaged intensity profiles for the first eight layer lines for an H_6PBT chain of 8 units generated assuming the coordinates of Wellman et al. [83]. Temperature factor (0.005, 0.025 nm^2) (parallel, perpendicular) to the chain axis. Numbers on the right are the layer line numbers. Notice splitting of ℓ=6.

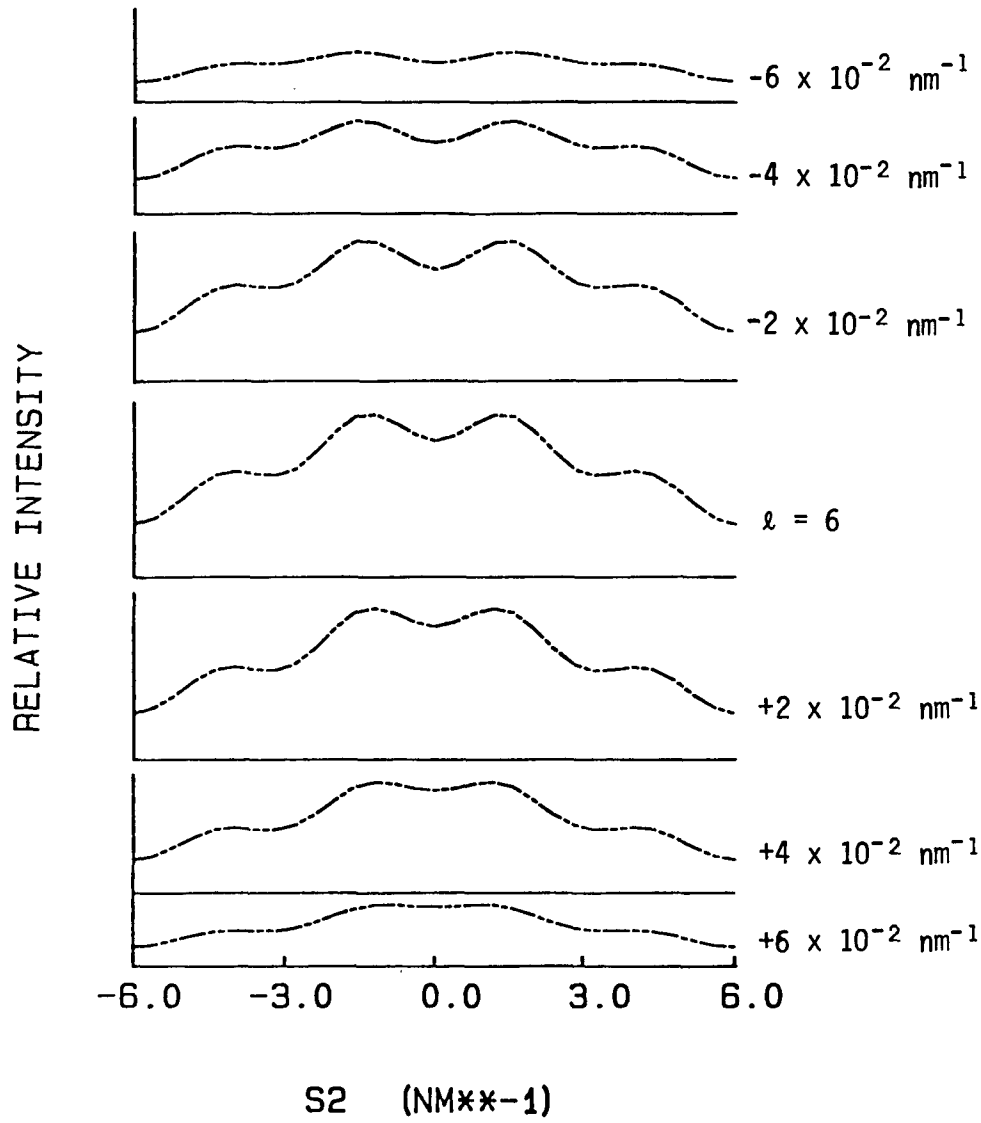

Figure 59. Cylindrically averaged intensity profiles for the first eight layer lines for an H_6PBT chain of 8 units generated assuming the coordinates of Wellman et al. [83]. Center profile is for sixth layer line. Numbers at the right indicate the displacement along s_1 from ℓ=6. Temperature factor (0.005, 0.025 nm^2) (parallel, perpendicular) to the chain axis.

7.2.2. Chains with Preferred Orientation. In order to investigate the effect of preferential orientation we considered two angles: ϕ - the angle of the phenyl ring with respect to the bisthiazole moiety and α, the angle of the bisthiazole moiety with respect to the reciprocal space vector normal to the incident beam direction (taken to be normal to $\underset{\sim}{c}$, see Figures 49 and 66). $I(\underset{\sim}{s})$ is still given by an incoherent sum of single chain scattering.

Figure 60 shows the intensity profiles for a single chain (with $\phi = 35°$) of 8 repeat units as the setting angle, α, is increased from 0° to 90°. Splittings of especially the 5th and 6th layer lines are observed which move to higher s_2 values and decrease in intensity as α increases. Figure 61 shows similar data for $\phi = 0°$, 25°, and 45° for $\alpha = 0°$. These may be compared to Figure 60a. Changing ϕ at constant α results in a change in intensity of the maxima, but not the position.

7.2.3. Comparison with Experiment. The calculated layer line intensity distributions were compared to microdensitometer traces from electron diffraction patterns. A two-dimensional contour plot of the fifth and sixth layer lines is shown in Figure 62. Notice the dramatic splitting of the sixth layer line. This is also observed in the zero layer x-ray precession photograph shown in Figure 63. Figure 64 shows results for the comparison of the calculated intensity distribution for the sixth layer line to the distribution obtained from electron diffraction by microdensitometry. Calc-1 is the cylindrically averaged calculation with the coordinates from Odell *et al*.

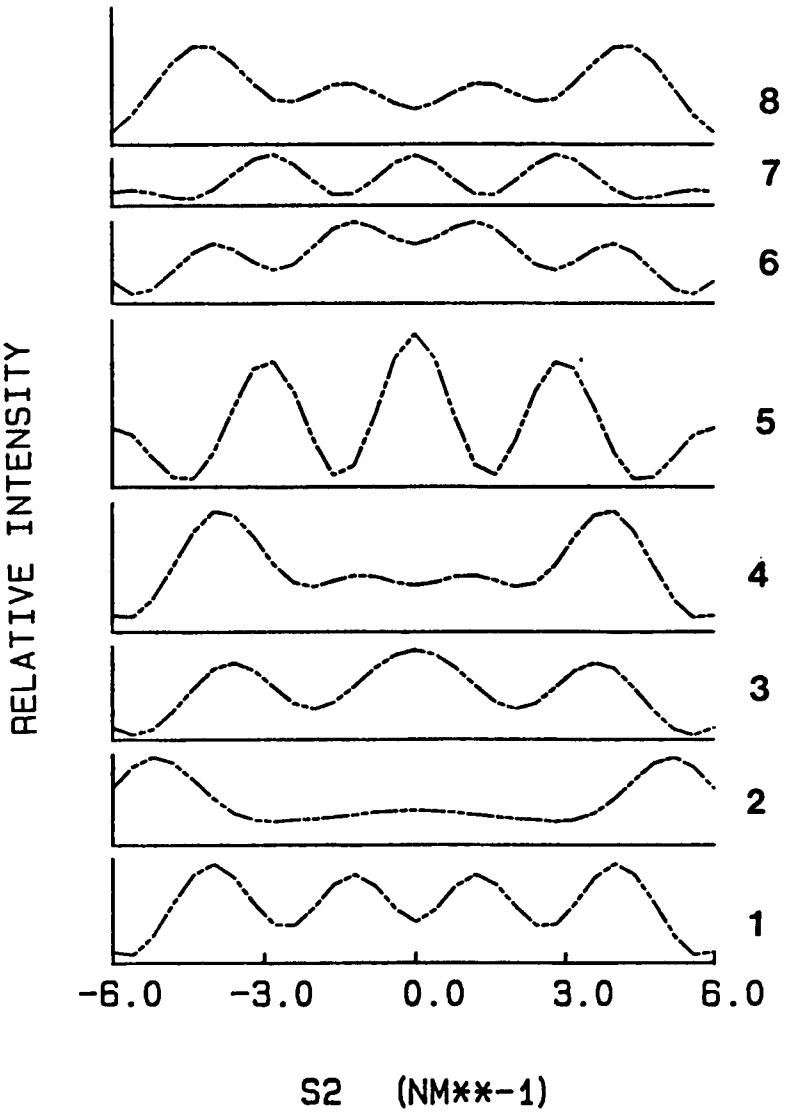

Figure 60a. Intensity profiles for the first eight layer lines for an H_6PBT chain of 8 units generated assuming the coordinates of Wellman et al. [83]. $\phi = 35°$, $\alpha = 0°$. Temperature factor (0.005, 0.025 nm^2) (parallel, perpendicular) to the chain axis. Numbers on the right are layer line numbers.

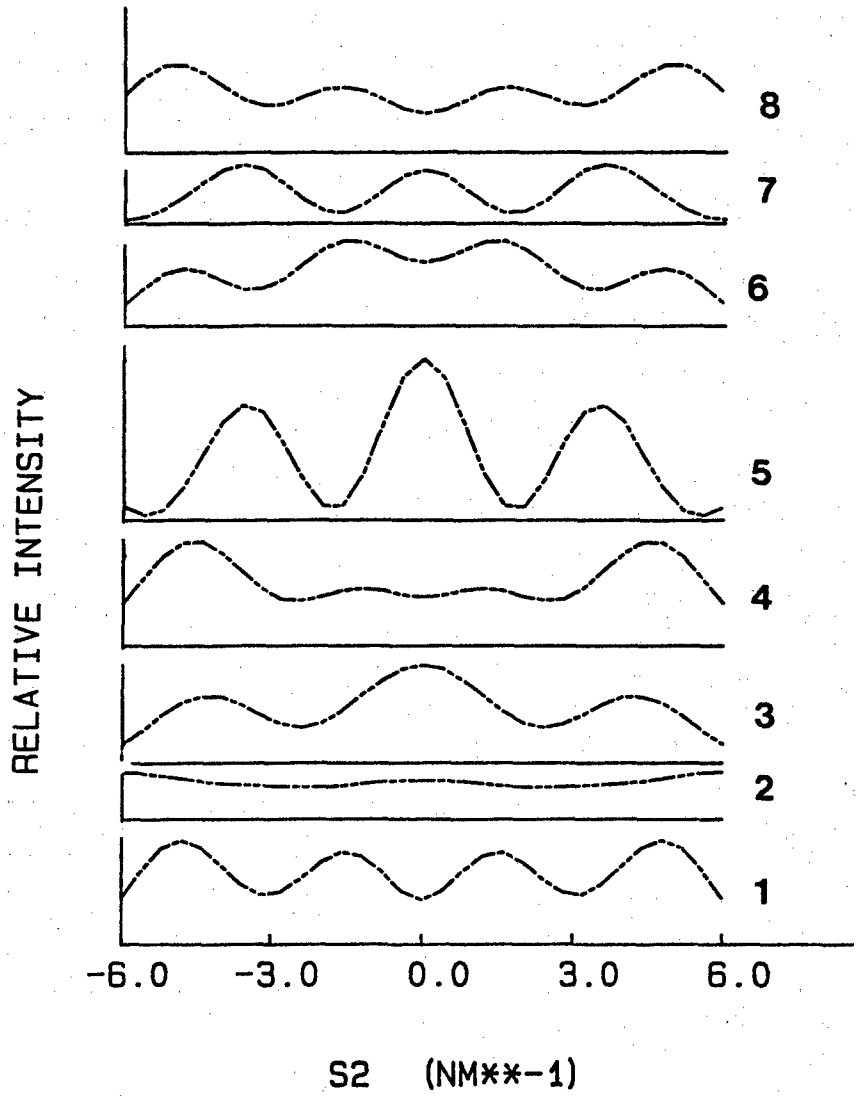

Figure 60b. Intensity profiles for the first eight layer lines for an H_6PBT chain of 8 units generated assuming the coordinates of Wellman et al. [83]. ϕ = 35°, α = 35°. Temperature factor $\overline{(0.005}$, 0.025 nm^2) (parallel, perpendicular) to the chain axis. Numbers on the right are layer line numbers.

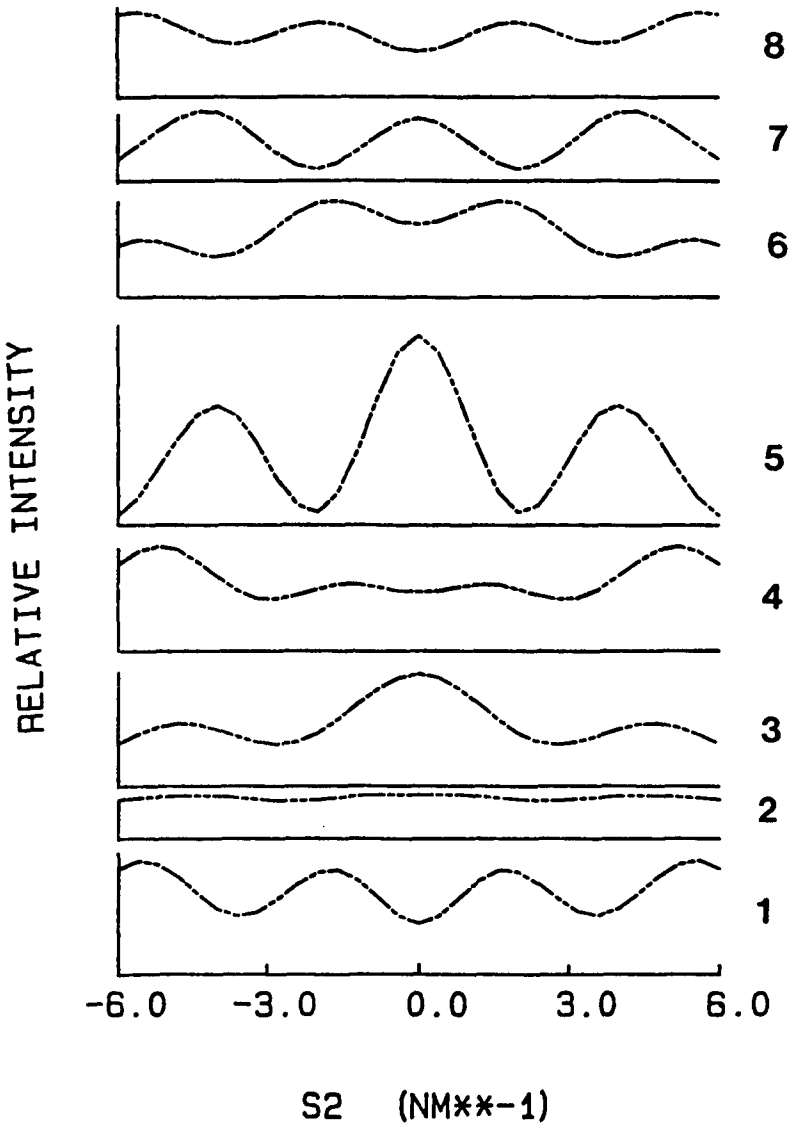

Figure 60c. Intensity profiles for the first eight layer lines for an H_6PBT chain of 8 units generated assuming the coordinates of Wellman et al. [83]. ϕ = 35°, α = 45°. Temperature factor (0.005, 0.025 nm^2) (parallel, perpendicular) to the chain axis. Numbers on the right are layer line numbers.

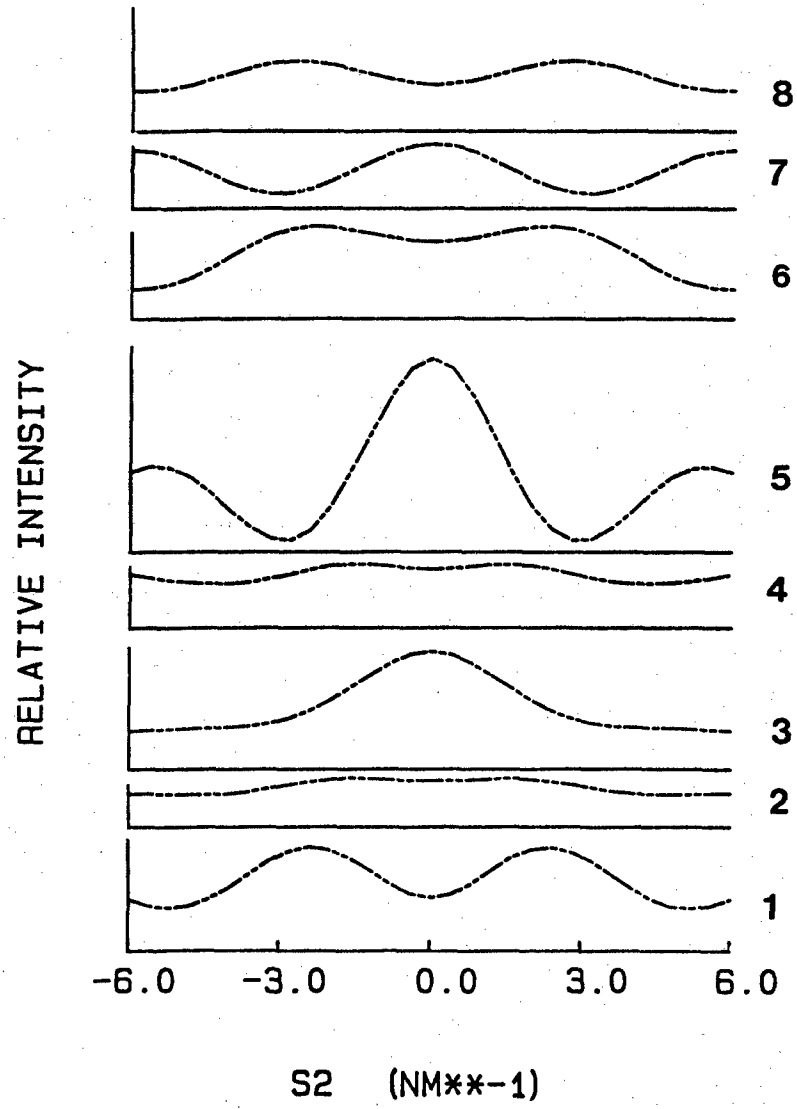

Figure 60d. Intensity profiles for the first eight layer lines for an H_6PBT chain of 8 units generated assuming the coordinates of Wellman et al. [83]. $\phi = 35°$, $\alpha = 60°$. Temperature factor $\overline{(0.005}$, 0.025 nm^2) (parallel, perpendicular) to the chain axis. Numbers on the right are layer line numbers.

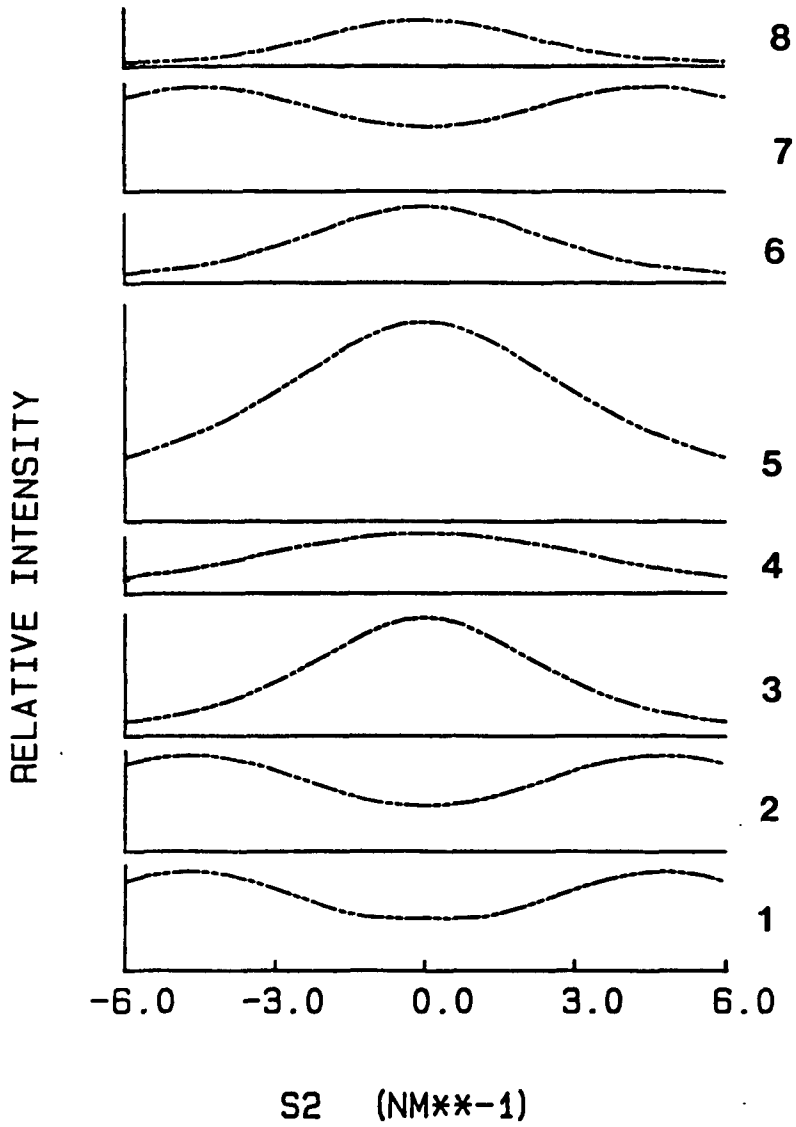

Figure 60e. Intensity profiles for the first eight layer lines for an H_6PBT chain of 8 units generated assuming the coordinates of Wellman et al. [83]. $\phi = 35°$, $\alpha = 90°$. Temperature factor (0.005, 0.025 nm^2) (parallel, perpendicular) to the chain axis. Numbers on the right are layer line numbers.

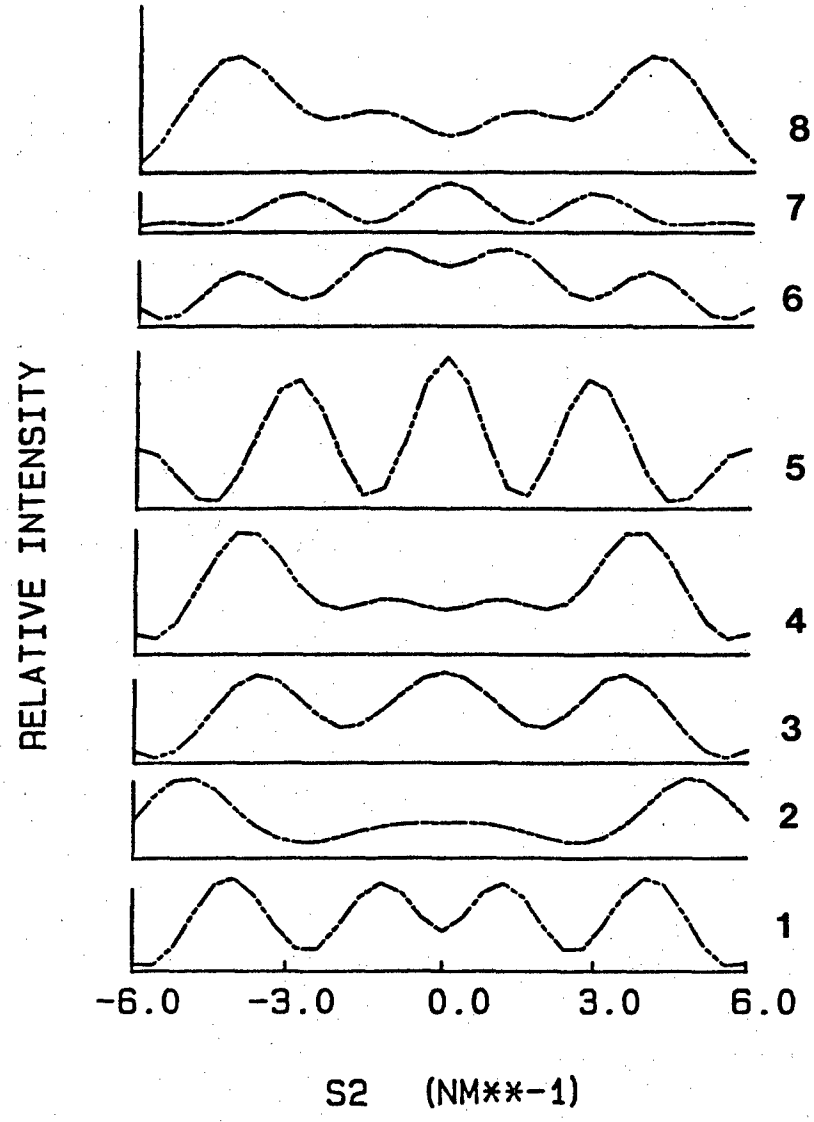

Figure 61a. Intensity profiles for the first eight layer lines for an H_6PBT chain of 8 units generated assuming the coordinates of Wellman et al. [83]. $\phi = 0°$, $\alpha = 0°$. Temperature factor (0.005, 0.025 nm^2) (parallel, perpendicular) to the chain axis. Numbers on the right are layer line numbers.

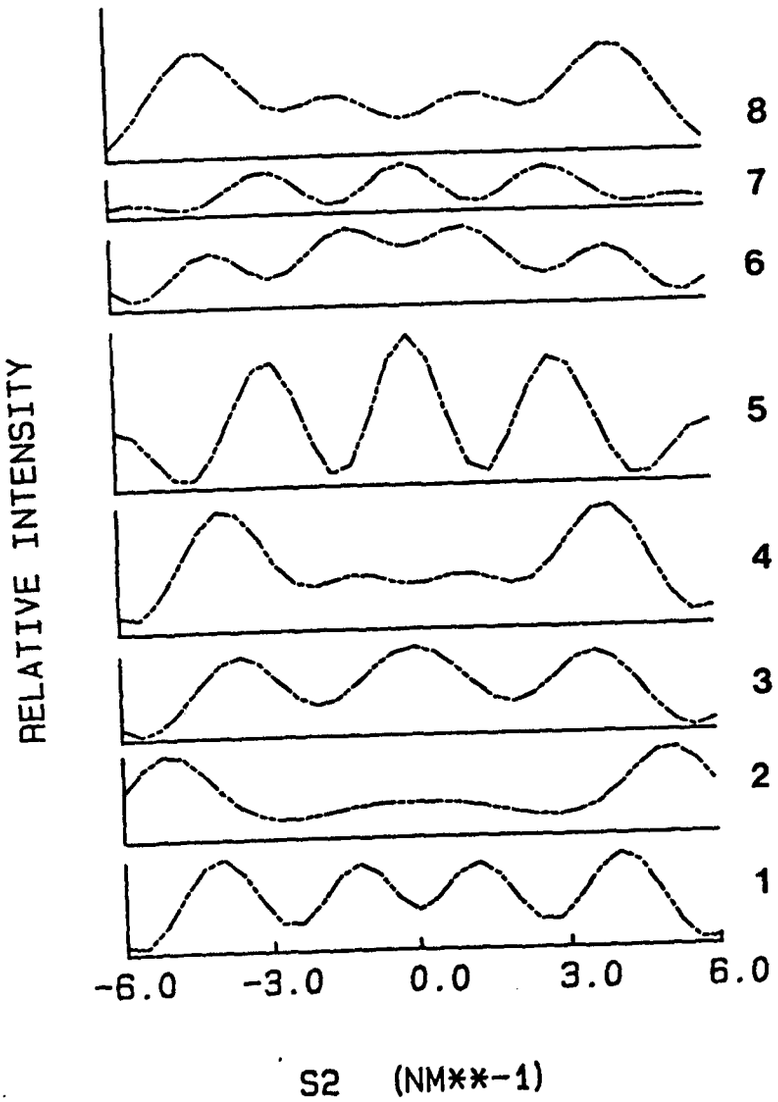

Figure 61b. Intensity profiles for the first eight layer lines for an H_6PBT chain of 8 units generated assuming the coordinates of Wellman et al. [83]. $\phi = 25°$, $\alpha = 0°$. Temperature factor (0.005, 0.025 nm^2) (parallel, perpendicular) to the chain axis. Numbers on the right are layer line numbers.

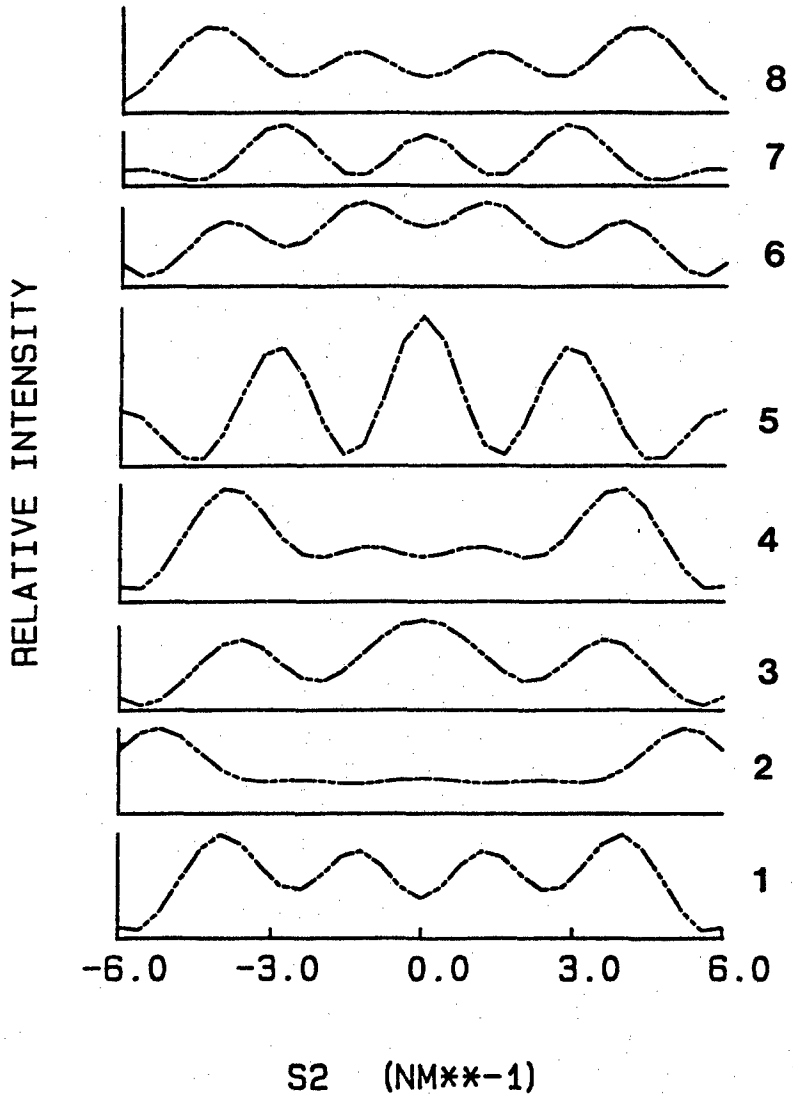

Figure 61c. Intensity profiles for the first eight layer lines for an H_6PBT chain of 8 units generated assuming the coordinates of Wellman et al. [83]. $\phi = 45°$, $\alpha = 0°$. Temperature factor (0.005, 0.025 nm^2) (parallel, perpendicular) to the chain axis. Numbers on the right are layer line numbers.

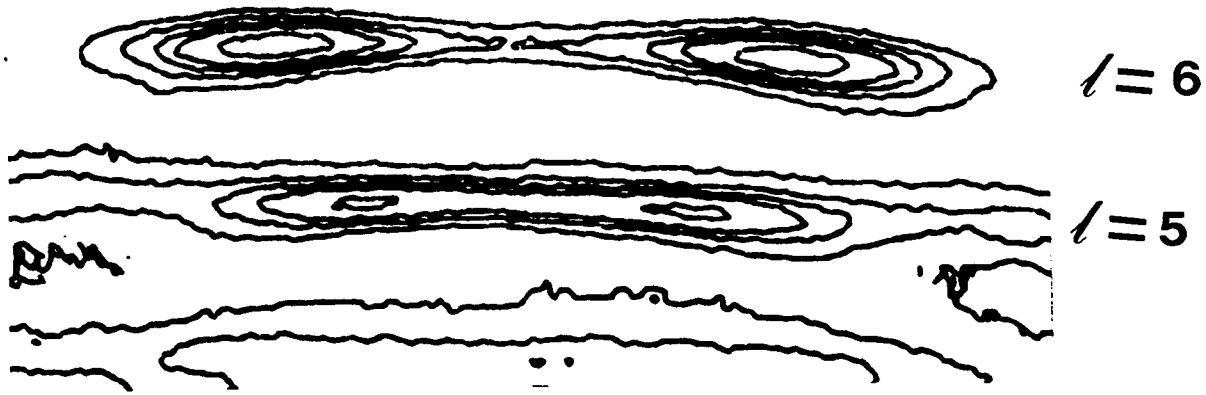

Figure 62. Two-dimensional contour plot of diffracted intensity. Microdensitometry of electron diffraction from HTR.

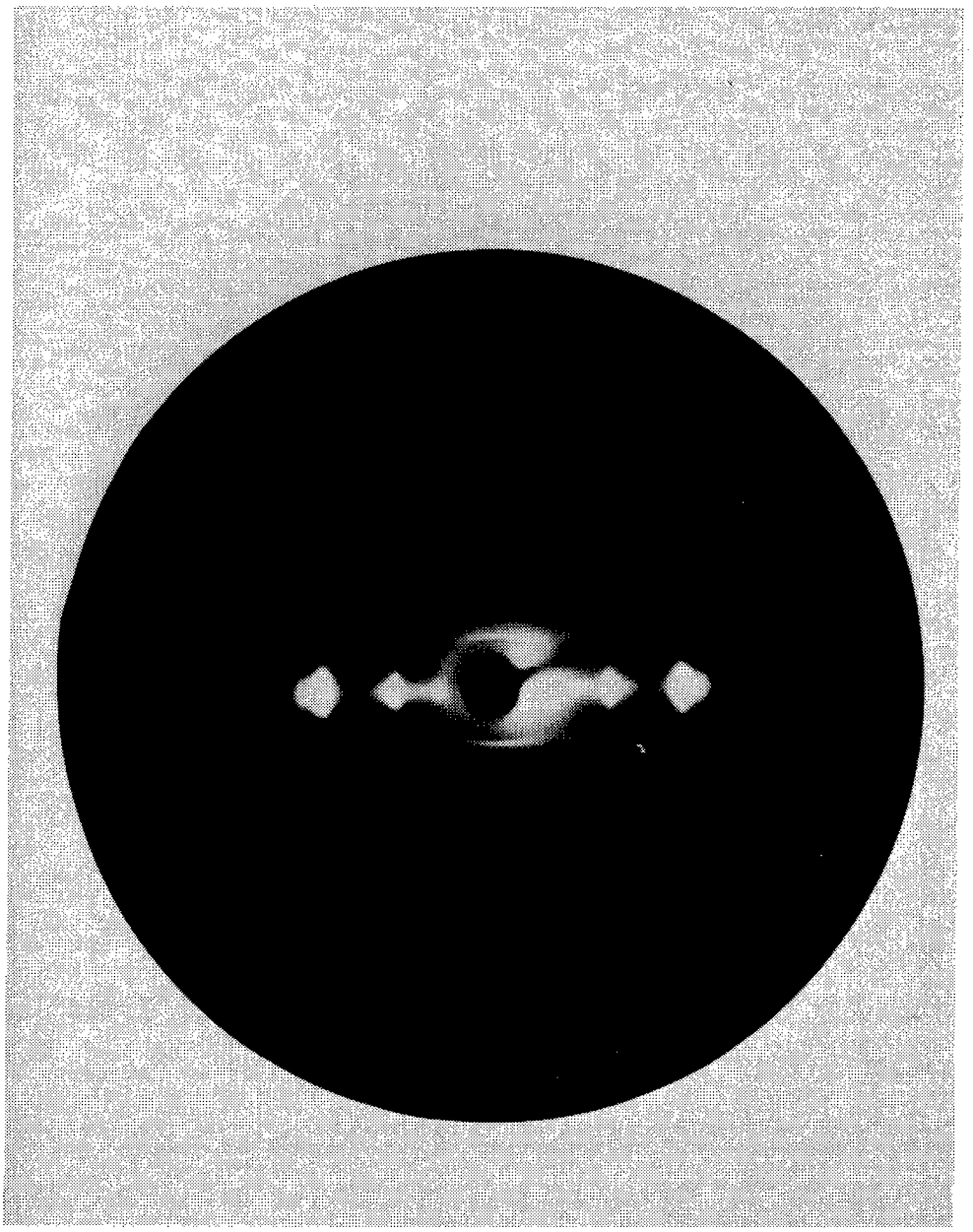

Figure 63. Zero layer precession photograph from HTF-23A. Ni filtered CuKα radiation was used.

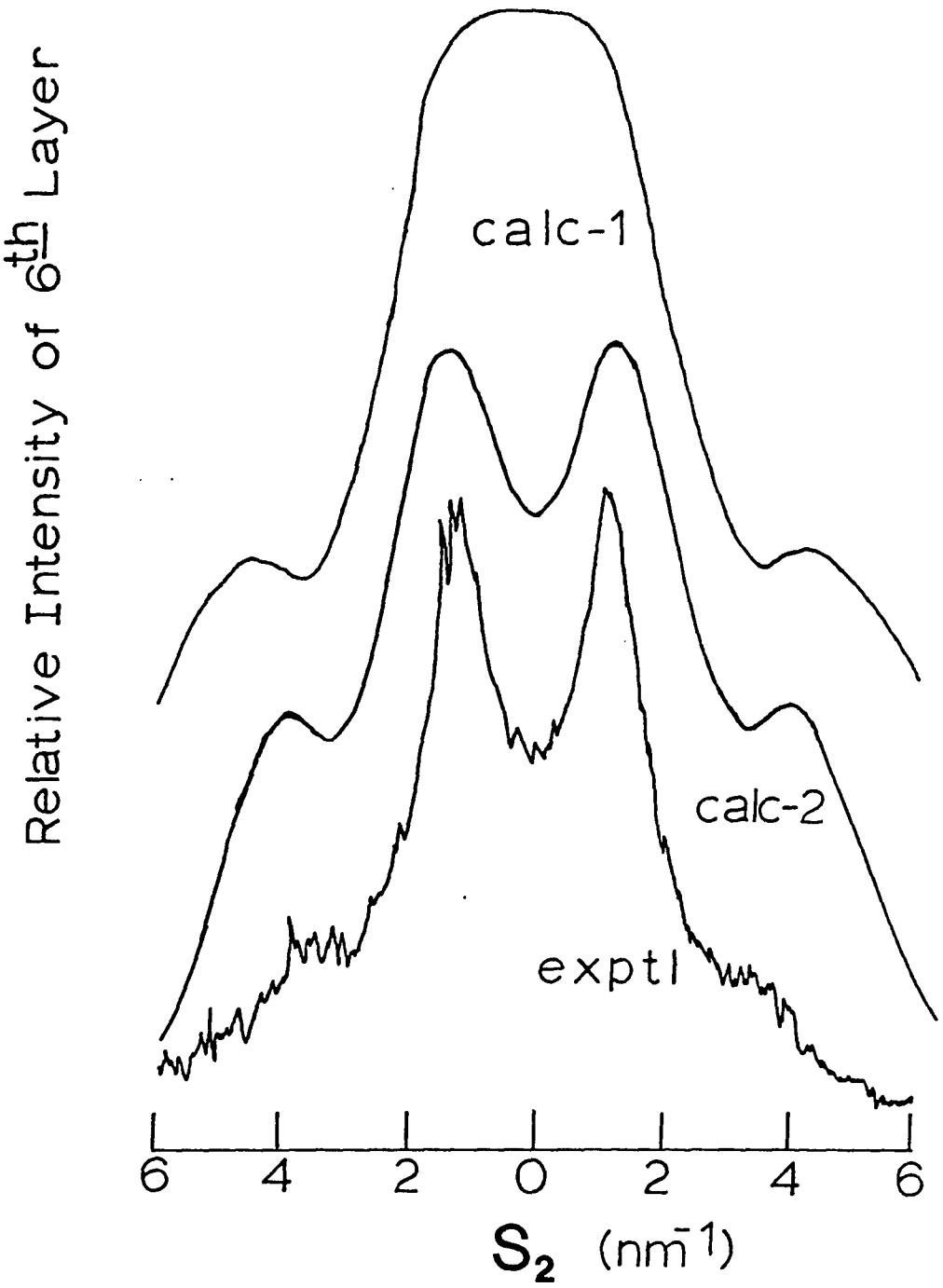

Figure 64. Comparison of the calculated intensity of the sixth layer line (cylindrically averaged) with experimentally determined curve. Calc 1: coordinates from Odell et al. [75] Calc 2: coordinated from Wellman et al. [83].

[84], Calc-2 is our cylindrically averaged calculation using the coordinates from the Wellman et al. [85] model compound study. Notice the remarkable agreement including the secondary maximum near $s_2 = 4$ nm^{-1} in the latter case. For correct comparison to the molecular transform, the diffracting material must have very high axial orientation to prevent smearing out of the intensity due to fibril (and therefore molecular) misorientation.

The molecular transform for a cylindrically averaged PPTA chain was also calculated using the coordinates of Northolt [77]. Figure 65 shows the first eight layer lines. Notice the strong diffuse streak expected for the sixth layer line. This was observed by electron diffraction by Dobb et al. [61] and in this work and suggests that there is some translational disorder in PPTA also.

7.3 Packing Analysis in the PBT Unit Cell

In order to augment our electron diffraction studies we have considered the potential energy of PBT chains packed in a monoclinic net. The potential energy of such an array can be modeled as the sum of the pairwise interactions of a PBT unit with three neighboring chains, each consisting of three units, plus the intrachain potential energy.

The interchain potential energy was calculated from the sum of the pairwise Van der Waals interactions using a Buckingham potential function with parameters supplied by Welsh, Bhaumik and Mark [89]. Following their suggestion "aromatic" Buckingham potential function parameters were used only for 1,3 pairs - that is for interactions

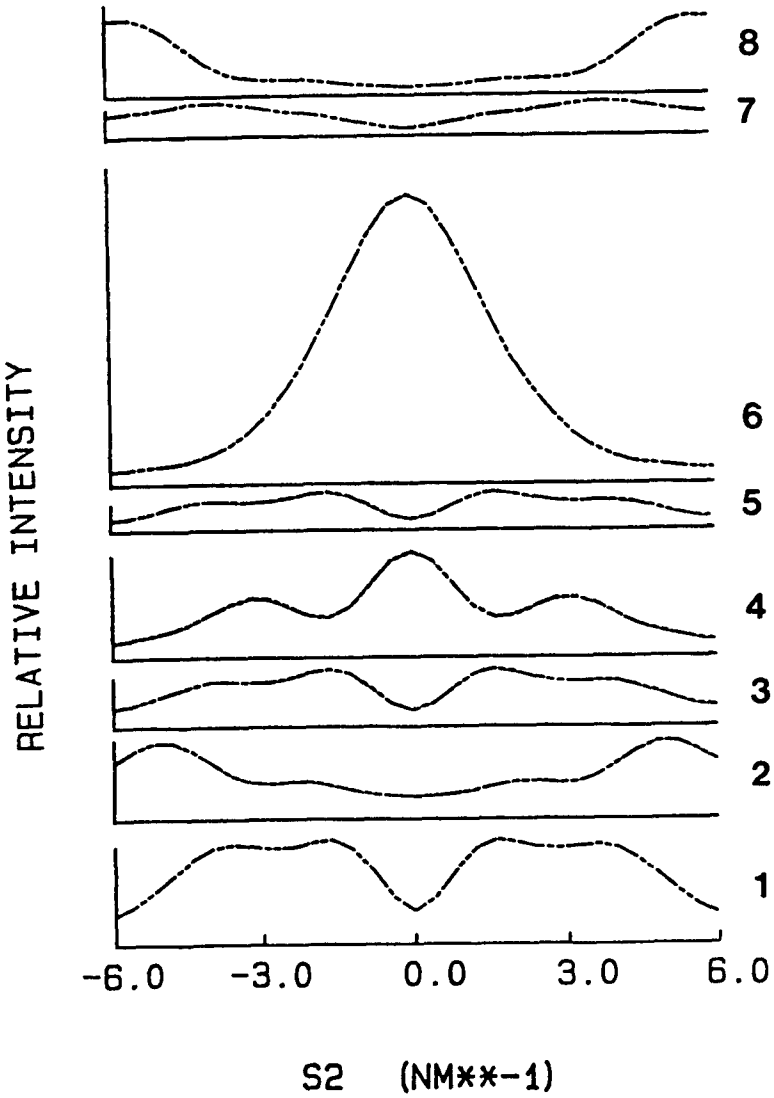

Figure 65. Cylindrically averaged intensity profiles for the first eight units generated assuming the coordinates of Northolt et al. [77]. Temperature factor (0.005, 0.025 nm^2) (parallel, perpendicular) to the chain axis. Numbers on the right are layer line numbers.

roughly perpendicular to the benzene rings. This assumption is only valid for small conformational and setting angles (see below). The parameters used are given in Appendix V, along with the program, PACK, used in the calculation. Program PACK is a corrected version of a program by E. Roche [85] in which several potential energy arrays were improperly dimensioned and, therefore, gave erroneous results. The potential energy of the PBT unit with the ith chain is given by:

$$V_{1-i} = \sum_{j=1}^{N} \sum_{k=1}^{3N} [A_{jk} \exp\{-b_{jk} d_{jk}\} - C_{jk} d_{jk}^{-6}] \qquad (7.16)$$

and

$$E_{TOT} = \sum_{i=2}^{4} V_{1-i} + E_{INTRA} \qquad (7.17)$$

where E_{TOT} = total potential energy

V_{1-i} = potential energy between the PBT segment and the ith chain

N = number of atoms in the segment (24)

d_{jk} = distance between the jth and k^{th} atom

E_{INTRA} = intrachain potential energy

The basic configuration for the calculation is shown in Figure 66 which corresponds to the proposed PBT unit cell (Figure 49). As defined for the single chain scattering calculations the setting (or chain rotation) angle, α, is defined as the angle between the projection of the benzobisthiazole moiety down the $\underset{\sim}{c}$ (chain) axis and the $\underset{\sim}{a}$ axis. The conformational angle, ϕ, is defined as the angle between

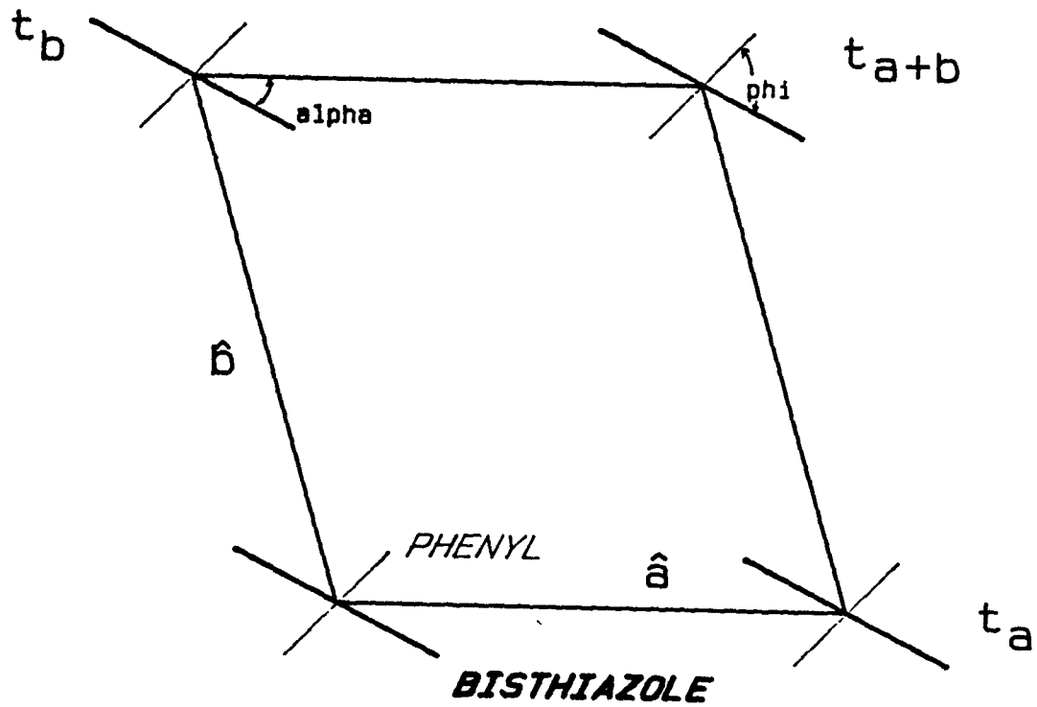

Figure 66. Configuration of packing calculation.

the phenyl ring and the benzobisthiazole moiety when both are projected down the $\underset{\sim}{c}$ axis. Thus, "aromatic" Buckingham parameters were only used for the 1,3 pair.

Intrachain energies in Equation 7.17 were obtained by interpolating values obtained by Welsh et al., [87] which were obtained by summing Van der Waals, torsional, and coulombic terms.

The chain at (o,a) was translated along the $\underset{\sim}{c}$ axis from -0.4 nm to 0.3 nm in increments of 0.1 nm (the value specified by "T"), with all other chains fixed with their origin at c=0. The setting angle α was varied from -40° to +50° and chain conformational angle ϕ was varied from -90° to +90°. Results revealed two broad energy minima in (α,ϕ) space. The first occurs at (-15, +40) and is the "global minimum" at T = 0.0 nm. The second occurs at (20, -5)and is a local minimum at T = 0.0 nm. To pass from one conformation to the other would require crossing about a 15 Kcal/mol barrier (see the energy contour plot in Figure 67). However, calculation of the structure factors for equatorial reflections for each of these conformations showed poor agreement with the experimentally observed values, which suggests that our violation of the assumption of small α,ϕ significantly affected the results. Thus the energy minima lie outside the range of validity of our assumption of small α and ϕ. However, the slow change of potential energy within the range of validity of our assumption supports the case for axial translational disorder of the molecule.

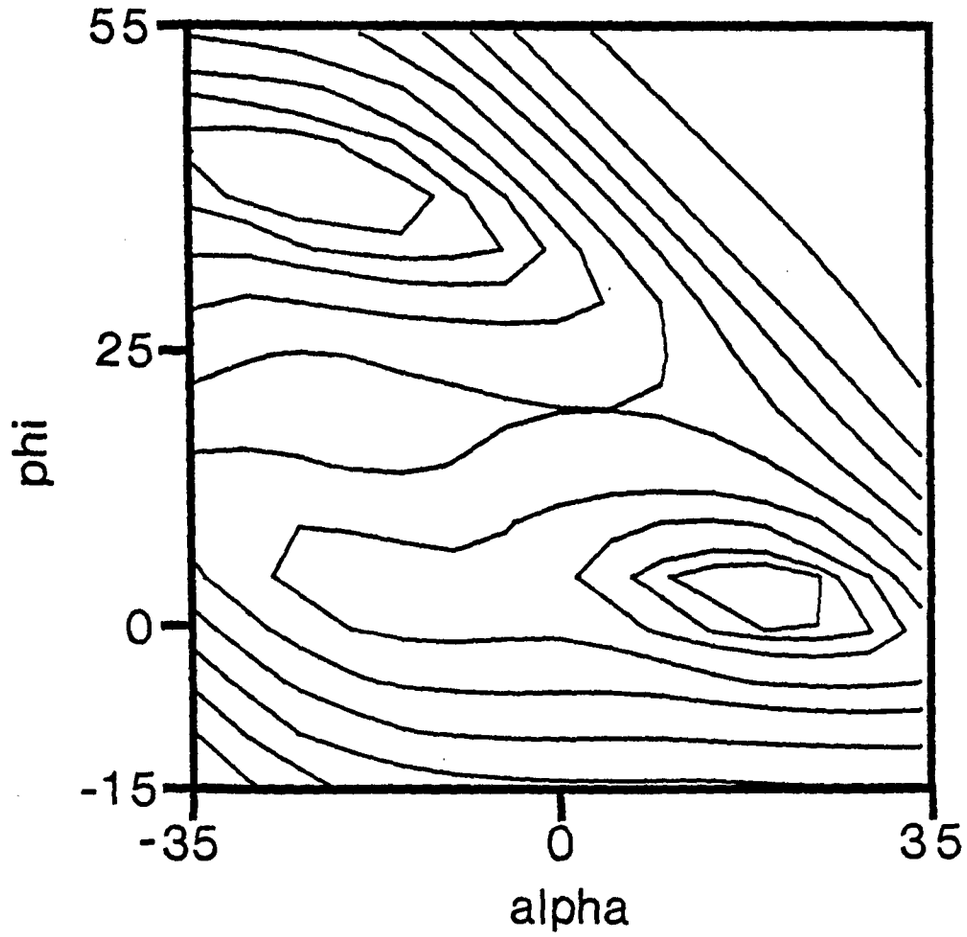

Figure 67. Potential energy surface of the H_6PBT unit cell. Contours represent 0.5, 1, 2, 4, 8, 16, 32, 54, 128 Kcal/9 monomer units from the minimum.

7.4 Diffraction Line Broadening: A Preliminary Study

The breadth of a diffraction line is dependent upon the size of the scattering regions [88], strain in the crystals [89], random displacement of the scatterers from the crystal lattice ("thermal distortion") [90], lattice distortion within the crystal [91] (paracrystalline type II distortions) and instrumental broadening [92]. Given a suitable instrumental standard and several orders of a given reflection, each of these effects may be distinguished. However, in the case of PBT there are only a limited number of equatorial reflections with sufficient intensity and so as a first approximation, we only considered broadening due to the size of the scattering regions. In the case of electron diffraction patterns, only patterns obtained with the second condenser lens fully overfocused were employed and so the instrumental broadening could be neglected. X-ray diffraction line profiles were corrected for instumental broadening by using a hexamethyltetraamine standard, assuming the profiles to be Gaussian. Thus, the observed breadth of a reflection $\Delta\beta_{ob}$ is related to the true breadth $\Delta\beta_t$ by [92]:

$$\Delta\beta_{ob} = \Delta\beta_t^2 + \Delta\beta_i^2 \tag{7.18}$$

where $\Delta\beta_i$ is the instrumental broadening. $\Delta\beta_t$ may be related to the apparent crystallite size $\bar{L}_{ap}$ by the Scherrer equation [88,93]

$$\bar{L}_{ap} = K/\Delta\beta$$

where $\Delta\beta_t$ is in $\underset{\sim}{s}$ space ($|\underset{\sim}{s}| = 2 \sin\theta/\lambda$) and K is termed the Scherrer constant, and is best defined as the ratio of the true to apparent crystal size [93]. K is generally taken as 1.0 for integral breadth and 0.89 for full width at half-maxima, but it has been shown to also be a function of crystal shape and disorder [93], and can vary from 0.5 to 2.1. Recognizing these limitations, we have assumed K to be 1 and calculated the apparent crystal size by electron diffraction and x-ray diffraction. The results are given in Table XI. A typical diffractometer scan for an as-spun and heat treated PBT film sample is given in Figure 68. Samples where both x-ray and electron diffraction analyses were performed exhibited similar values for $\overline{L}_{ap}$. Generally the extent of lateral order from e_1 planes was greater than that from (010) planes by up to 50%. It is significant to note that the values for $\overline{L}_{ap}$ for heat treated samples are roughly 33 - 50% of the values observed by dark field. This may arise for a number of reasons

(a) errors due to choice of K

(b) increased broadening due to overlapping peaks (true for the (010),($\bar{1}$10) and (110) triplet)

(c) dark field may only average those regions larger than about 2 nm

Thus, there is a need for more detailed study including resolution of overlapping peaks to obtain more realistic values for $\Delta\beta$ and careful choice of K by following the suggestions of Hindeleh and Johnson [93], where K is chosen as a function of the apparent size and the disorder of the coherently scattering regions.

Table XI

Apparent "Crystal Size" by Line Broadening

Sample	$\overline{L}_{(100)}$(nm)		$\overline{L}_{(010)}$(nm)	
	x-rays	electrons	x-rays	electrons
ASR-7	---		---	4.7 ± .4
HTR-5	---	6.7	---	
ASR-13	---	---	---	4.5
HTR-13A	5.3	---	4.7	---
HTR-13B	5.3	5.1	4.7	3.6
HTR-9	---	7.6	---	5.3
ASF-39	1.6	---	1.6	---
ASF-38	2.3	---	1.9	---
HTF-38	8.6	---	4.7	---
HTF-42	---	4.3	---	---
HTF-41B	4.7		4.7	

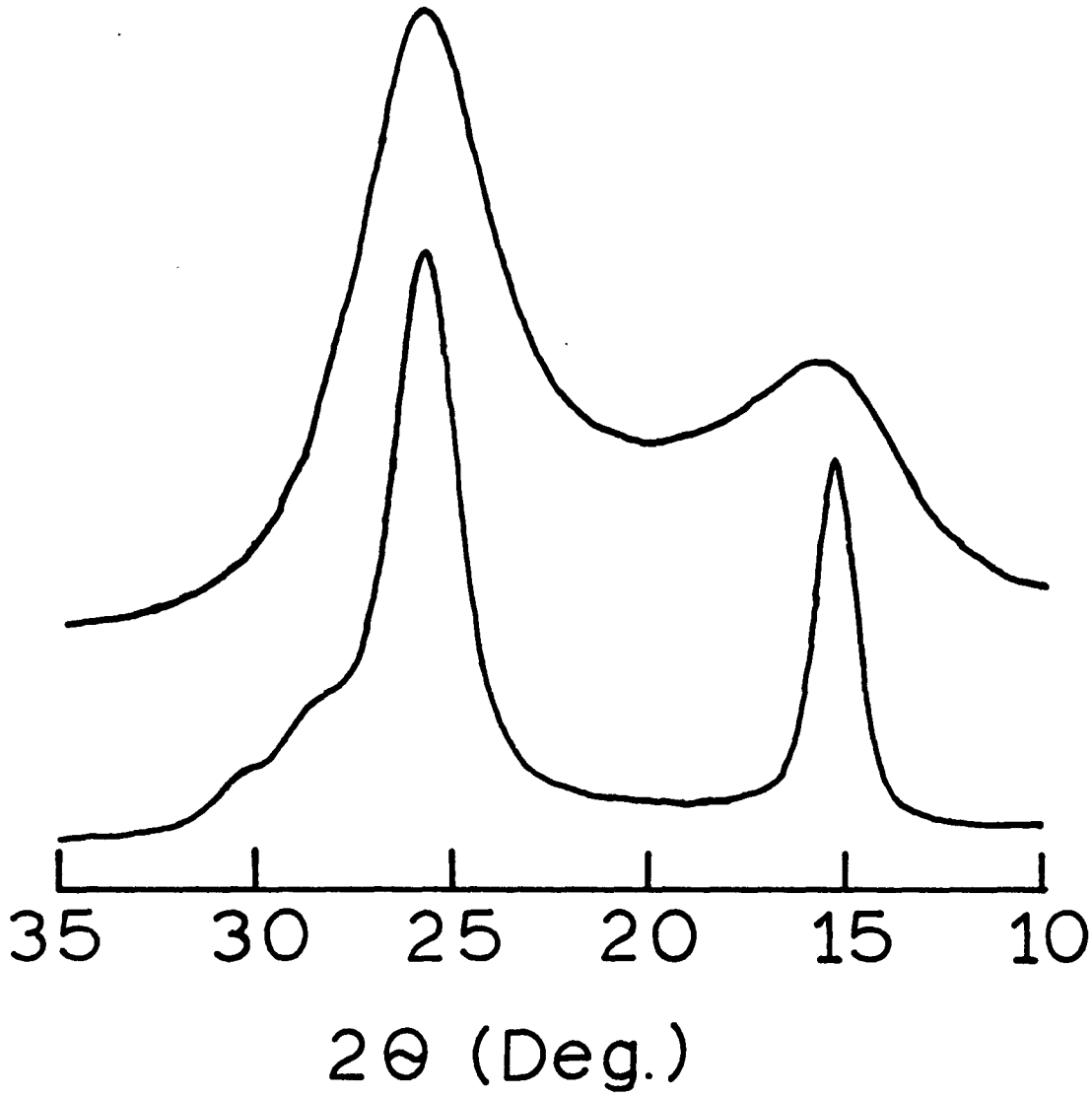

Figure 68. Typical diffracometer traces of as-spun and heat-treated fibers: (a) ASF-39 (b) HTF-39.

7.5 Orientation: A Preliminary Study

In order to study the orientation of PBT films, small cubes were prepared by stacking 15 layers. First, these were examined by photographic WAXS on a Statton Camera. Figure 69 shows the x-ray patterns obtained in 3 orthogonal directions for an 'as-spun' PBT film from MSA solution. The 0.597 nm (100) reflection is preferentially oriented in the surface of the film. The molecular orientation in the extrusion direction appears to be poor - a full width at half maximum of about 40 degrees. When the x-rays are incident along the normal direction (ND) and about 50 when the x-rays are incident along the transverse direction (TD).

Figure 70 shows a similar scattering arrangement for an as-spun film from PPA. Here, the film appears to be oriented normal to the extrusion direction but randomly oriented along the extrusion direction.

To obtain a quantitative measure of this orientation, a preliminary pole figure analysis was performed on these samples. Because of the cubical nature of the specimen, data could be collected over most of recipocal space using nominal reflection geometry of the diffractometer. The sample was aligned such that the diffractometer axis and the extrusion direction were colinear. Intensity was measured at the maximum 2θ value for the (100) and (010),($\bar{1}$10) and (110) reflections as a function of sample rotation angle about the extrusion direction ("machine direction", MD) and the normal direction

Texture

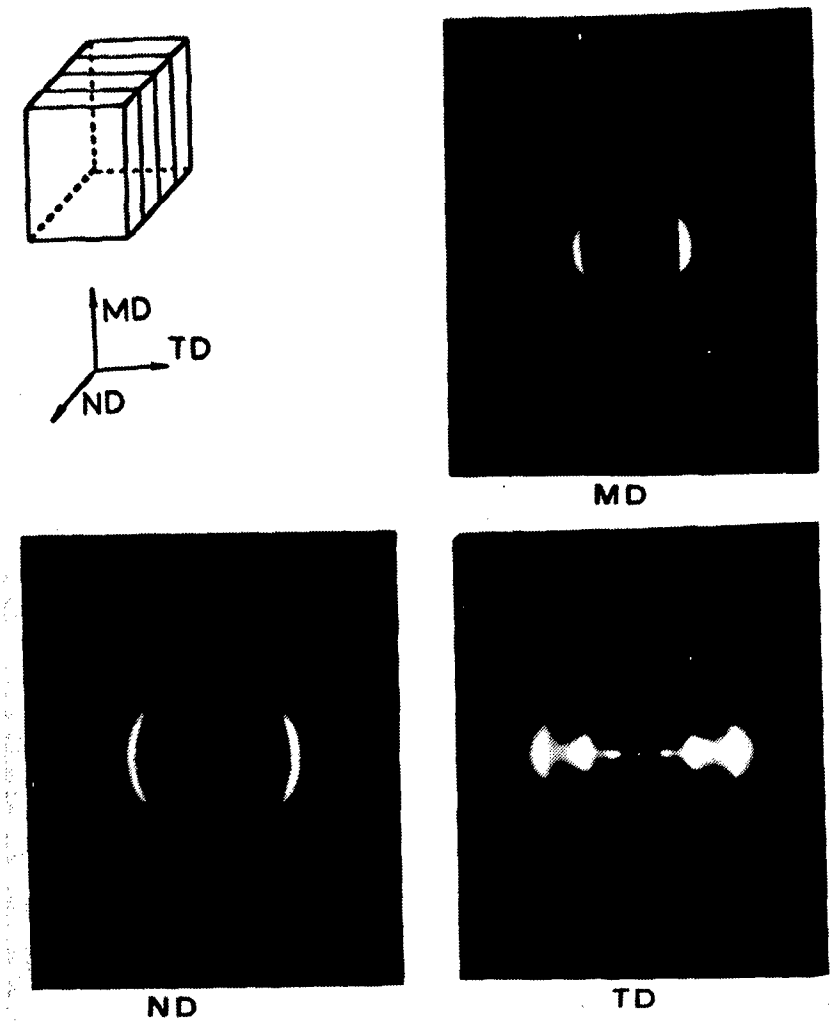

Figure 69. Wide angle x-ray diffraction from PBT film from MSA solution along 3-directions.

fiber symmetry

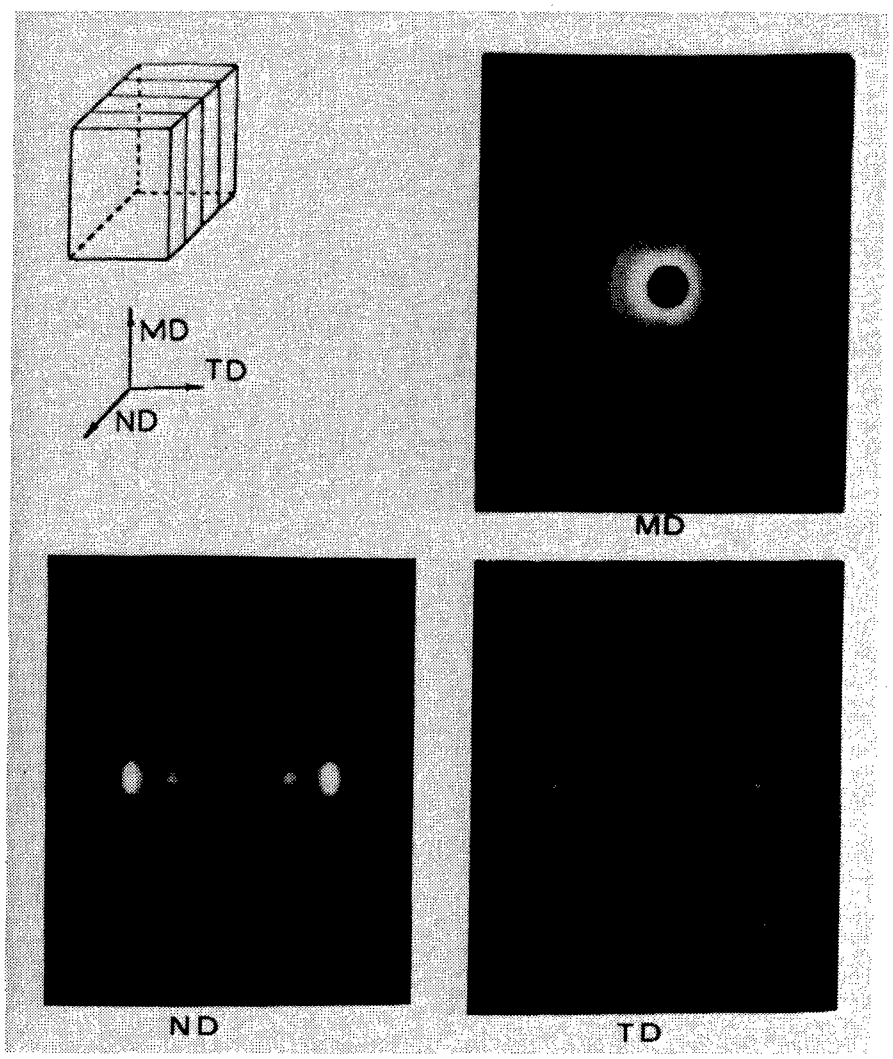

Figure 70. Wide angle x-ray diffraction from a PBT film from PPA solution along 3-direction.

(ND) as depicted in Figure 71. No corrections were made for background, instrumental broadening, or overlapping peaks. Orientation was expressed in terms of the average cosine squared of the angle, between the normal for the plane of reflection and the MD. This may be related to the Hermans-Stein orientation function

$$f_{hk\ell} = \frac{3 \langle\cos^2\phi\rangle_{hk\ell} - 1}{2} \qquad (7.20)$$

where ϕ is the angle between the normal to the $hk\ell$ plane and the MD. f_{hk} yields a value of -0.5 for a reflection perfectly oriented on the equator. The values of the average cosine are given in Figure ~~68~~ 71. In the case of the PPA film, the orientation may be classified as uniaxial in Sisson's nomenclature or axial in Heffelfinger and Burton's nomenclature [56]. The MSA film is slightly uniplanar axial in Heffelfinger and Burton's nomenclature or selective uniaxial in the nomenclature of Sisson. That is, in the as-spun film from MSA, (100) is preferentially oriented in the MD-ND plane.

Orientation in the machine direction is slightly higher in PPA than MSA ($f_{(010)}$ = -0.335 compared to -0.230 for MSA). Correction for background would probably increase the orientation slightly. Electron diffraction from local areas of PBT films revealed much higher values of orientation. This may be seen in Figure 72. Fibrillation of the bulk sample, or a more highly oriented surface of the film which is relatively sampled by the detachment replication procedure used for e^- diffraction specimens would account for this observation. However, repeated replication of film surfaces produced highly oriented

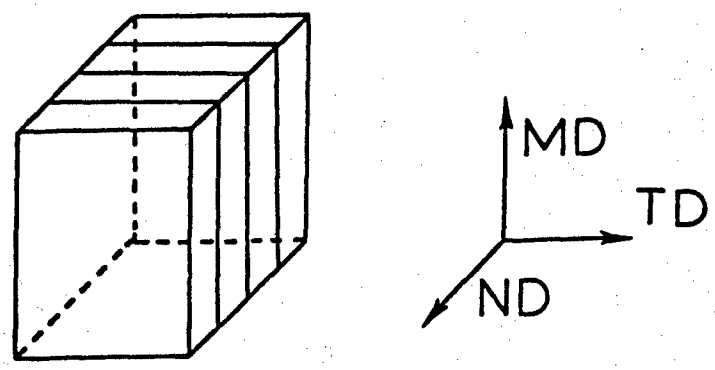

Film	Direction	$f_{(100)}$	$\langle\cos^2\phi\rangle_{(100)}$	$f_{(010)}$	$\langle\cos^2\phi\rangle_{(010)}$
ASR-5	TD	0.01	0.34	0.13	0.42
(MSA)	ND	0.20	0.47	0.08	0.39
	MD	-0.22	0.19	-0.23	0.18
ASR-9	TD	0.12	0.41	0.18	0.45
(PPA)	ND	0.13	0.42	0.16	0.44
	MD	-0.25	0.17	-0.34	0.11

Figure 71. Hermans-Stein orientation factors, f, and average square direction cosines, $\langle\cos^2\phi\rangle$, for the (100) and (010) reflections with respect to the three film axes.

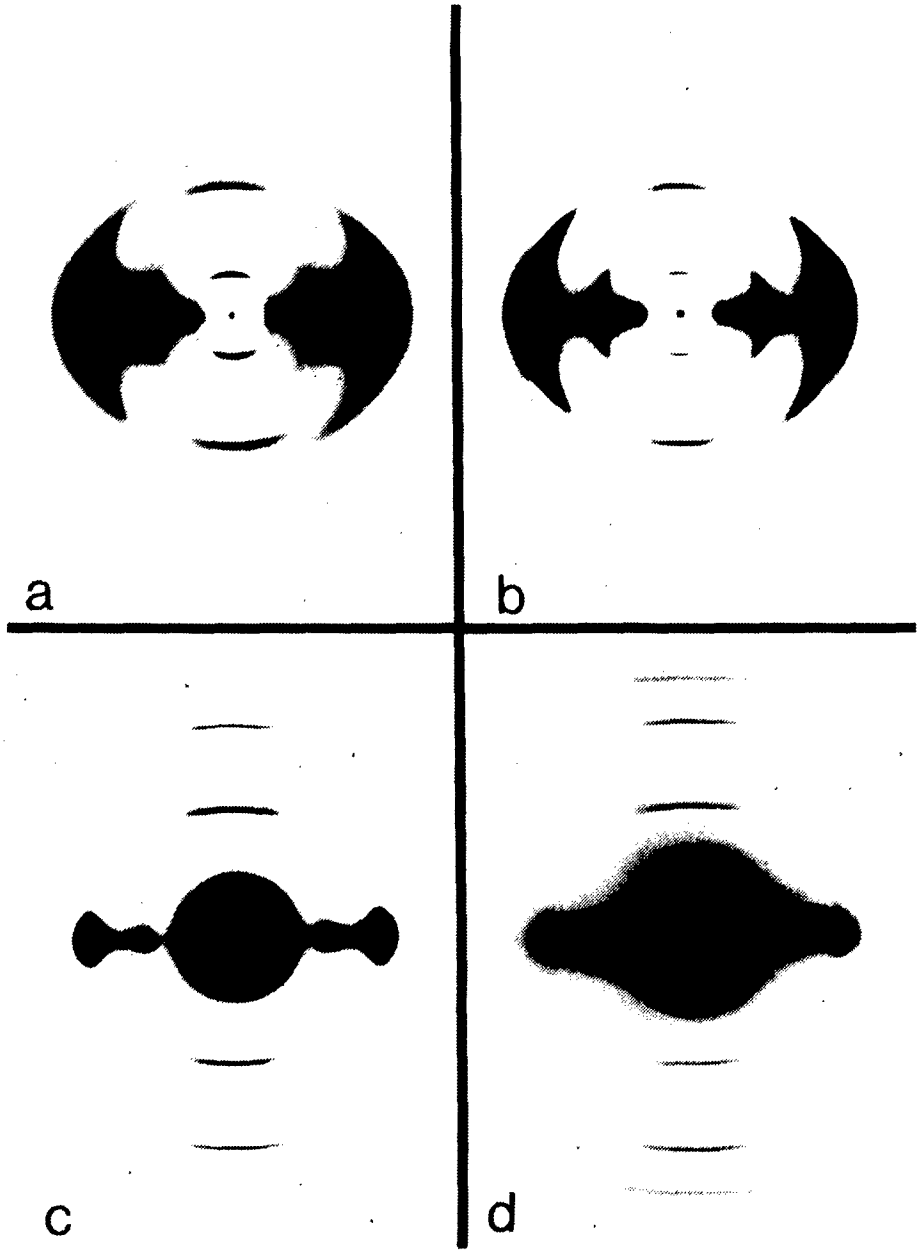

Figure 72. Comparison between WAXS and SAED in PBT films.
(a) WAXS: ASR-5 (b) WAXS: HTR-5
(b) SAED: ASR-5 (d) SAED: HTR-5

fragments from the interior of the film, indicating that the improved orientation is not just a surface effect. The orientation measured by electron diffraction is probably a better indication than that measured by x-ray diffraction when fibrillated samples are used.

Microdensitometer traces of equatorial reflections in electron diffraction patterns were obtained on a Joyce Loebl scanning microdensitometer as described in Chapter III. As a first approximation, the effects of thermal vibrations were ignored and the structure fators were assumed to be equal to the square root of the relative intensity of the particular reflection. No precautions were taken to separate overlapping peaks. The observed structure factors for the (100),(010) and $(2\bar{1}0)$ reflections obtained by electron diffraction are given in Table XII. This seems to suggest that the (100) planes orient normal to the extrusion direction when the MSA films are heat treated. However, since optical microscopy of these films revealed them to be highly blistered, this probably indicates that the detachment replication is essentially looking at a section of the film which is closer to the edge than the flat surface.

In summary, large scale three dimensional crystalline order has not yet been achieved in PBT ribbons or fibers. Current samples consist of coherently scattering regions with molecules laterally well packed in a two dimensional net with irregular translations of chains along the fiber axis. Comparison of electron diffraction patterns from films prepared from PPA solution with the cylindrically averaged molecular transform generated using coordinates of Wellman _et al_. [83]

Table XII

Observed Structure Factors by Electron Diffraction

Sample	F_o (100)	F_o (010)	F_o ($2\bar{1}0$)
ASR-7	66.1	100.0	---
HTR-4	100.0	69.1	19.5
HTR-5	100.0	66.1	---
ASR-13	75.3	100.0	22.6
HTR-13B	91.6 ± 0.3	100.0	29.0 ± 0.9
ASR-9	67.0	100.0	---
HTR-9	85.0	100.0	25.3

reveals remarkable agreement. It remains for future optimization of processing and heat treatment conditions to achieve full three dimensional crystalline order in PBT. PBT films from MSA exhibit preferential orientation, with the 0.597 nm (100) reflection preferentially in the surface of the film, while PBT films prepared from MSA solution possess uniaxial symmetry.

CHAPTER VIII

SMALL ANGLE NEUTRON SCATTERING

The objective of this work is to study the configuration of PBT molecules in dilute isotropic solution, concentrated nematic solutions and in the bulk, i.e. oriented and unoriented PBT films. The difference in neutron scattering cross section of hydrogen and deuterium provides scattering contrast when a mixture of deuterium labeled PBT in a solvent or in a hydrogenated PBT matrix is used.

In small angle scattering, the problem may be formulated as scattering from monomer units. Following the development of Cotton et al. [98], the total coherent, elastic scattering length, B, for a monomer containing n atoms may be written as:

$$B = \sum_{i=1}^{n} b_i \qquad (8.1)$$

where b_i is the coherent, elastic scattering length for the ith atom. The coherent, elastic scattering cross-section is $4\pi B^2$. The incoherent, elastic scattering cross-section for the monomer is obtained by summing the incoherent scattering cross-sections for the individual atoms:

$$\sigma_{inc}^{TOT} = \sum_{i=1}^{n} \sigma^{EL} - 4\pi b_i^2 \qquad (8.2)$$

where σ^{EL} is the total elastic scattering cross-section for the ith atom. Values of σ^{EL} and b_i have been tabulated by Bacon [99] and Cotton et al. [98]. These are summarized for atoms of interest in Table XIII.

TABLE XIII

Scattering Parameters of Atoms Useful for PBT SANS

Atom	b_i (10^{-12}cm)	$\sigma_i^{el,coh}$ (10^{-24}cm^2)	σ_i^{EL} (10^{-24}cm^2)	$\sigma_i^{el,inc}$ (10^{-24}cm^2)
C	0.661	5.49	5.51	0.02
N	0.949	11.10	11.4	0.3
S	0.31	1.2	1.2	0.0
D+	0.65	5.4	7.6	2.2
D++	0.667	5.59	(12.8)	7.2
H	-0.378	1.8	81.5	79.7
O	0.577	4.2	4.24	0.04
P	0.53	3.53	3.6	0.07

+Bacon [99] ++Cotton et al. [98]

Bacon's [99] value for the incoherent scattering cross-section for deuterium differs substantially from that used by Cotton et al. [98]. Other literature surveyed revealed that about half of the authors used each value. The original sources appear to be about the same age (1962-1965) and it is not clear which value is correct. For this reason, calculations were done using each value. More recently (1972, 1977), Bacon [100,101] confirmed the coherent scattering length of deuterium of 0.667 x 10^{-12} cm, but still reports the incoherent cross-section as 2.0 x 10^{-24} cm^2.

The appropriate scattering parameters were calculated for selected

molecules of interest and are displayed in Table XIV. Molar volumes were calculated for PBT chains based on the structural model of Roche et al. [102] using a density of 1.69. Polyphosphoric acid (PPA) was assumed to be $(PO_3)_n$ with n sufficiently large to make end group contributions negligible. PPA was also assumed to have a density equal to that of H_3PO_4.

TABLE XIV

Parameters for Contrast Factor and Signal to Noise Calculations for SANS

Species	B (10^{-12}cm)	Source	σ_{inc}^{TOT} ($10^{-24}cm^2$)	Molar Volume (cm^3/mole)	Density (g/cm^3)	Monomer M. Wt. (gmole)
D_4H_2PBT	13.60	Bacon	169.0	152.68	1.69	270.3
D_4H_2PBT	13.67	Cotton	188.0	152.68	1.69	270.3
D_6PBT	15.65	Bacon	13.0	152.68	1.69	272.3
D_6PBT	15.76	Cotton	44.0	152.68	1.69	272.3
H_6PBT	9.49	Bacon	478.0	152.68	1.69	266.3
MSA	4.21	Bacon	319.0	64.89	1.481	96.1
PPA	1.88	Bacon	79.7	43.6	1.834	80.0
D_4MSA	5.30	Bacon	8.0	67.56	1.481	100.1
D_4MSA	5.37	Cotton	32.0	67.56	1.481	100.1
D_1PPA	2.91	Bacon	5.2	44.15	1.834	81.0
D_1PPA	2.93	Cotton	7.4	44.15	1.834	81.0

The scattered intensity was calculated for a dilute mixture of a polymer of molecular weight M (monomer molecular weight m_1) in a matrix of species 2 of molecular weight m_2. If species 2 is a polymer, we assume that the polymer molecular weight is the same as species 1, and m_2 is the monomer molecular weight. For a dilute mixture, the intensity of elastically-scattered neutrons, I, as a function of the

scattering vector $q = \frac{4\pi}{\lambda} \sin \frac{\theta}{2}$ is given by equation (8.3):

$$I(q) = N_A V \phi_o \, tT[K^2 \frac{c_1}{m_1} \frac{M}{m_1} S_o(q) + \frac{c_1}{m_1} B_{I_1}^2 + \frac{c_2}{m_2} B_{I_1}^2] + \int_o^t N(q,t)dt \qquad (8.3)$$

N_A	=	Avagadro's Number
V	=	scattering volume (cm^3)
ϕ_o	=	incident neutron flux ($cm^{-2}sec^{-1}$)
t	=	counting time (sec)
c_1 and c_2	=	concentration (g/cm^3) of species 1 and 2
K^2	=	square of the contrast factor (given by equation (11))
$S_o(q)$	=	scattering function
T	=	specimen transmittance (given by equation (12))
$N(q,t)$	=	electronic noise from the detector - e.g. the dark current

The first term of equation (8.3) is the coherent scattering, the second and third terms are due to incoherent scattering of the polymer and solvent and the fourth term is due to system noise.

The square of the contrast factor is defined as

$$K^2 = [B_1 - (\frac{V_1}{V_2}) B_2]^2 \qquad (8.4)$$

where V_1 and V_2 are the molar volumes of species 1 and 2. The transmittance, T, is given by

$$T \equiv \frac{I}{I_0} = \exp\{-\eta\sigma^{EL}x\} \tag{8.5}$$

where η is the number of scatterers per unit volume, σ^{EL} is the total elastic scattering cross-section for neutrons, and x is the sample thickness. The optimum sample thickness occurs for a value of the transmittance of $\frac{1}{e}$, i.e. $x = \frac{1}{\eta\sigma^{EL}}$ (see Table XV).

TABLE XV

Optimum Matrix Thickness for SANS of PBT

Species	Xoptimum (cm)
D_4H_2PBT	.10
D_6PBT	.08
H_6PBT	.16
MSA	.20
PPA	.58
D_1PPA	.66
D_4MSA	.31
H_8 Polystyrene+	.27
D_8 Polystyrene+	.14

+Values of Polystyrene are given for comparison

SANS samples much larger than the thickness of normal PBT ribbons are therefore necessary. Processing single films 1 mm thick is impractical, so one must stack multiple films and optimize signal/noise by the proper choice of label species and matrix.

The scattering function $S_0(q)$ is given by

$$S_o(q) = \frac{1}{n_1^2} \sum_i^{n_1} \sum_j^{n_1} e^{iq \cdot r_{ij}} \tag{8.6}$$

where the double sum is over all monomer units in a single polymer molecule. $S_o(q)$ as defined is normalized to unity for q = 0 and falls off with scattering angle depending on the molecular configuration. For randomly oriented rods of length 2L [95]:

$$S_o(q) = \frac{Si(qL)}{qL} + \frac{\sin^2(qL)}{(qL)^2} \tag{8.7}$$

where $$Si(qL) = \int_o^{qL} \frac{\sin u}{u} du \tag{8.8}$$

A plot of $S_o(q)$ for an anisotropic solution of rods is shown in Figure 73. The larger the rod length the faster the decrease of $S_o(q)$ with scattering angle. Guinier and Fournet [95] have shown that for $R_g q \ll 1$

$$S_o(q) \simeq 1 - \frac{R^2_g q^2}{3} \tag{8.9}$$

where R_g is the radius of gyration and is for a rod of length 2L:

$$R^2 = \frac{4L^2}{12} \tag{8.10}$$

Using the approximation $e^{-x} \simeq 1-x$, equation (8,9) becomes

$$S_o(q) = e^{-Rg^2 q^2/3} \tag{8.11}$$

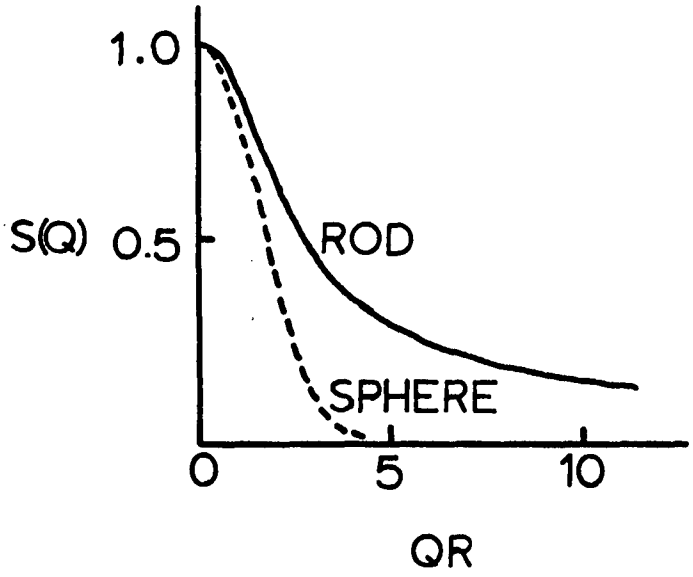

Figure 73. Single chain scattering function, S(q), for a rod and a sphere. R is the radius of the sphere and 1/2 the length of the rod. From Reference [95].

and thus a plot of log $S_0(q)$ versus q^2 yields the radius of gyration and hence the rod length.

If one neglects the dark current of the detector, the signal/noise ratio may be calculated as the ratio of coherent to incoherent scattering. This is given by equation (8.12) below:

$$S/N = \frac{k^2 DP}{B^2_{I_i} + \frac{c_2 m_1}{c_1 m_2} B^2_{I_2}} S_0(q) \qquad (8.12)$$

where DP is the degree of polymerization and the B_{Ii} are the incoherent scattering cross-sections. Calculated values of K^2 and S/N for various polymers and matrixes are given in Table XIII. Representative combinations are given in Table XVI.

For a mixture of species 1 (weight fraction, w_1) in a matrix of species 2 (weight fraction, w_2), the concentration in g/cm^3 of solution is given by:

$$c_1 = w_1^2 (\rho_1 - \rho_2) + w_1 \rho_2 \qquad (8.13)$$

analagously for c_2

$$c_2 = w_2^2 (\rho_2 - \rho_1) + w_2 \rho_1 \qquad (8.14)$$

where ρ_1 and ρ_2 are the densities of the pure components 1 and 2. The degree of polymerization of species 1 (typically for PBT: 20, 50 and 100) and weight fractions (typically 0.01 and .05) were used to calculated the signal to noise ratio.

TABLE XVI

Contrast Factor and Signal to Noise Ratio for Selected Pairs of Species 1 (LABEL) in Species 2 (MATRIX) for Small Angle Neutron Scattering Assuming $W_1 = 0.01$ and $DP_1 = 50$

Species 1	D_4H_2PBT			H_6PBT			D_6PBT		
Species 2	K^2	S/N^+	S/N^{++}	K^2	S/N^+	S/N^{++}	K^2	S/N^+	S/N^{++}
D_4H_2PBT				17.47	0.65	0.58	4.37	0.16	0.15
H_6PBT	17.47	0.23	0.23				39.31	0.51	0.51
D_6PBT	4.37	1.90	0.61	39.31	14.22	5.21			
MSA	14.17	0.10	0.10	0.17	0.00	0.00	34.27	0.24	0.24
PPA	50.22	1.18	1.18	8.45	0.20	0.20	84.21	1.97	1.97
D_4MSA	2.35	0.64	0.17	7.00	1.70	0.49	13.14	3.81	0.95
D_1PPA	12.51	4.17	2.99	0.41	0.12	0.09	31.67	11.41	7.94

$^+$ S/N times $S_0(q)$, data from Bacon [42]
$^{++}$S/N times $S_0(q)$, data from Cotton [38]

Since $0.1 \leq 1$, a S/N^+ ratio of at least 10 is desired. The best candidates are thus seen to be D_6PBT and H_6PBT (bulk), D_6PBT and D_1PPA, and D_4H_2PBT and D_1PPA (solution).

Equation (17) shows the signal to noise ratio is directly proportional to the degree of polymerization. Therefore DP should be as high as possible, e.g. a DP of 500 would increase all S/N ratios in Table 7 by a factor of 10.

SANS experiments have been performed at Oak Ridge National Laboratory on isotropic solutions of 1 wt% D_4H_2 PBT in MSA, nematic 10% polymer (10% D_4H_{2PBT} + 90% H_6PBT) in MSA, and bulk 50% D_4H_2PBT/50% H_6PBT extruded ribbons and relaxed, precipitated films. The experimental signal to noise ratio for the isotropic and nematic colutions was too low for meaningful analysis and in addition problems were encountered with the beam monochromator.

The bulk precipitated films showed an unexpectedly strong scattered intensity. This scattering is likely due to voids caused by the coagulation (precipitation) process. A plot of the log of radially averaged intensity vs q^2 for an isotropic precipitated film sample is shown in Figure 74. From the limiting slope at zero angle we calculate a radius of gyration of 22 nm for the voids. As expected this is between the values obtained along s_1 and s_2 by SAXS in Chapter V.

Future SANS experiments on PBT must be carefully designed. If synthetically feasible, a substantial increase in S/N would be obtained using D_6PBT and higher molecular weight PBT. However, because PBT is a rod-like molecule, Rg increases linearly with MW, so

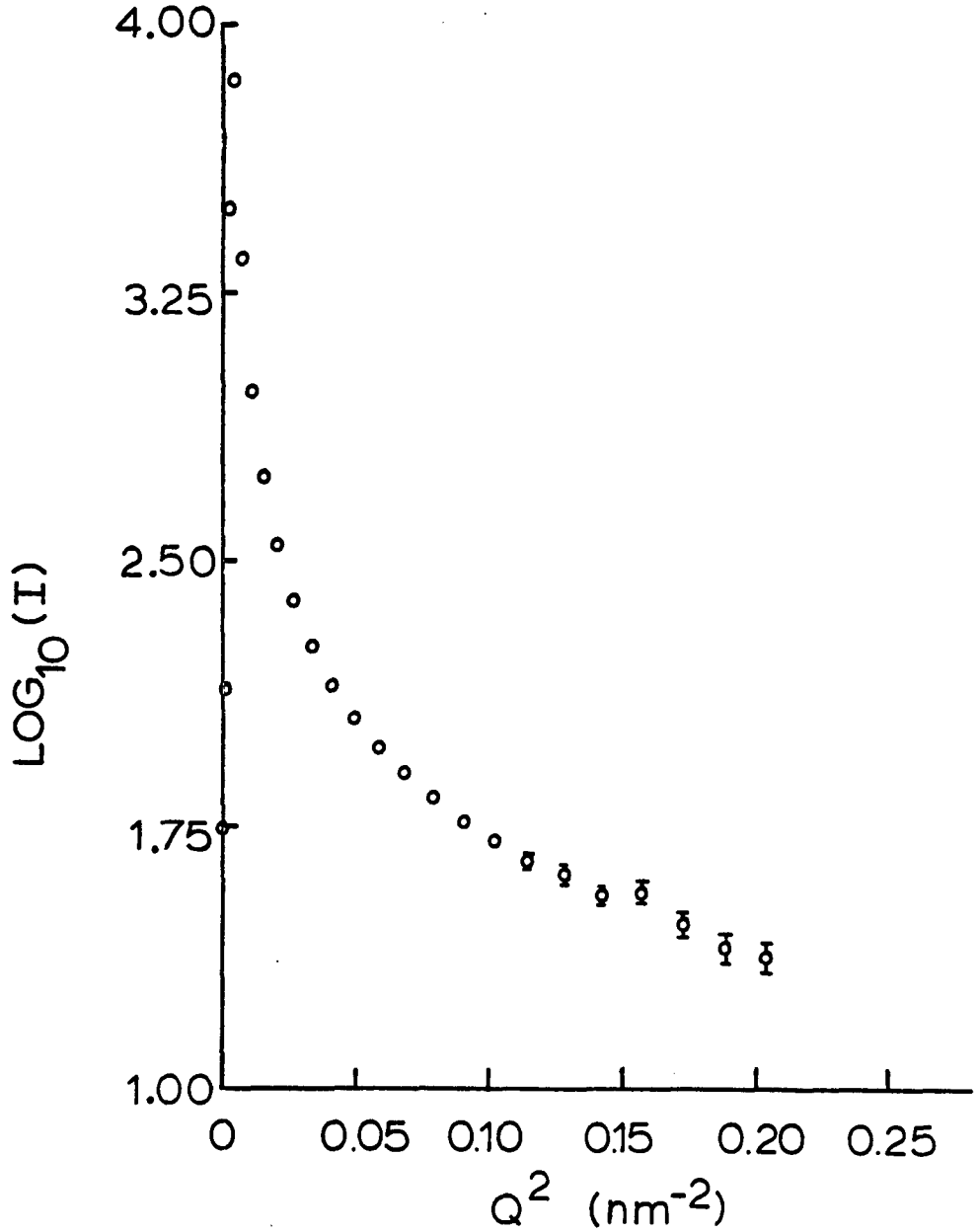

Figure 74. Guinier plot for SANS intensity from precipitated PBT. 10% D_4H_2PBT, 90% H_6PBT.

that a degree of polymerization of 120 (corresponding to a Rg of 150 nm) is about the largest size rod-like molecule which the present 30-m SANS apparatus can measure. For bulk studies, void content must be minimal, indicating the need for slower coagulation of the polymer from the solvent. Finally, instead of using a dilute label, recent work [102,103] has shown that the single chain form factor of the polymer in bulk can be obtained from a single concentration measurement for <u>any</u> concentration of labelled molecules, providing the molecular weights of the matrix and labelled molecules are the same and the molecular weight distributions are narrow. Thus 50/50 blends could be used to improve S/N.

CHAPTER IX

CONCLUSIONS AND POSSIBLE EXTENSIONS

9.1 Recapitulation

Dry-jet-wet spun PBT fibers and films with well characterized processing histories were studied using complementary microscopic and scattering techniques to determine how wholly aromatic PBT molecules are arranged in the solid state and how this arrangement is affected by changes in processing variables.

9.1.1 Observation of PBT Fine Structure by High Resolution Transmission Electron Microscopy.

Extraction of thin fragments from the surface of PBT fibers and films using collodion (nitrocellulose) or polyacrylic acid provided thin samples with a minimum number of artefacts induced during sample preparation. This was a more reliable method of sample preparation than either sonication [25] or ultramicrotomy [26]. Unlike most polymer samples, PBT fragments are quite resistant to irradiation damage by the electron beam. At room temperature and 100 KV, a dose of 1.6 Coul cm^{-2} is required to decrease the diffracted intensity from the (010) reflection of 1/e of its original value and is a characteristic dose for the material. Since $I_{(010)}/I_0$ was measured to be approximately 0.02 and I_{000}/I_0 was measured to be approximately 0.4 for a typical heat treated fragment, the maximum magnification to obtain nearly undamaged dark field

micrographs was calculated to be 40,000x. Accordingly, the maximum magnification to obtain bright field images with (010) diffraction contrast was calculated to be 140,000x. These values are an order of magnitude greater than the values for polyethylene.

High resolution (010) DF images were obtained up to an instrumental magnification of 33,000x suggesting that the calculated value of 40,000x was reasonable. Analysis of these images revealed the coherently scattering regions in as-processed fibers and films to be 2 nm and below in size. With tension heat treatment at 475°C and above, the average size of the coherently scattering regions increased to 10 nm perpendicular to the extrusion direction and 15 nm parallel to the extrusion direction. Regions longer than 40 nm were rarely observed. Successive (100) and (010) DF images revealed the coherently scattering regions containing these planes to be of similar size and shape. Thus, the crystallite shape is described as elongate-prismatic. The average size of the coherently scattering regions in heat treated fibers and films was independent of heat treatment time, temperature, and load within the limits of experimental error. However, only a limited range of variation of these parameters was represented in the available samples.

Coherently scattering regions containing bands of intensity perpendicular to the extrusion direction were interpreted as twisted crystals. Calculation of the rocking curve for the (010) reflection indicated that a tilt about an axis parallel to the extrusion direction of less than 2° is sufficient to decrease the diffracted

intensity to zero. These observations are consistent with a model of slightly twisted crystals.

High resolution DF images formed with the meridional component of the third and sixth layer lines exhibited only mass-thickness contrast. The lack of prominent diffraction contrast in these images indicates that the meridional reflections arise essentially from intrachain scattering. The projected electron density distribution of the chains along the extrusion direction in a 30 - 90 nm thick film is smoothly averaged by the other translationally disordered chains around it and therefore cannot be resolved.

The interpretation of DF images is in agreement with the axial bright lattice images of a heat treated PBT fiber recently obtained by Shimamura [66]. Fringes parallel to the molecular axis persist over an average of 10 nm in a direction perpendicular to the molecular axis and over an average of 15 nm in a direction parallel to the molecular axis. These fringes arise from interference between the (100) diffracted beam and the transmitted electron beam. In a few small areas, a second set of faint meandering fringes approximately normal to the first set with a 1.2 nm spacing were observed and attributed to local periodic alignment of the chains along the chain axis, and therefore, small scale 3-dimensional ordering. It is important to emphasize that this arrangment represents an extremely small fraction of the material.

9.1.2 Structural Analysis by Diffraction Methods. Electron and x-ray

diffraction patterns are explained by a model first reported by Suehiro et al. [81] for poly(β-propiolactone) in which the polymer chains are packed in a two-dimensional net perpendicular to the extrusion direction and possess random axial translational disorder. This model predicts a continuous distribution of intensity along the nonzero layer lines and discrete interferences along the zero layer line (equator). This behavior is observed in PBT diffraction patterns. The intensity distribution along the nonzero layer lines was calculated for a single chain of eight repeat units. The effects of slight variations in atomic coodinates, temperature factor, cylindrical averaging, preferred chain orientation, and conformational angle between the phenyl and benzobisthiazole moieties have been systematically studied. The most reliable atomic coordinates were obtained from the bond angles and bond distances in the model compound study of Wellman et al. [83]. Small changes in these coordinates resulted in intensity variations in the higher order layer lines. The calculation was relatively insensitive to conformational angle in the region investigated (0 - 45°). Rotation of the chain from normal incidence of the incident radiation to the bisthiazole plane (corresponding to the setting angle, α) resulted in a decrease of scattered intensity and a shift in the maxima on the nonzero layer lines to higher angles. Comparison of the calculated intensity profiles with those measured by microdensitometry of electron diffraction patterns shows remarkable agreement, predicting the maxima on $\ell=6$ at $s_2=1.2$ nm^{-1} and the second order maxima at $s_2=3.5$ nm^{-1} where previous calculations [25] failed.

Potential energy calculations predicted fascile translation of the chains, supporting the model with translational disorder along the chain axis.

The apparent size of the coherently scattering regions predicted from the breadth of x-ray and electron diffraction line profiles was consistently lower than observed by dark field. However, the apparent crystallite size in tension heat treated samples was observed to be greater than the as-spun precursors. This indicates a need for further work to obtain the correct Scherer parameter.

X-ray orientation measurements on as-spun films processed form MSA and PPA solutions indicate that the chain axis is moderately well oriented in the extrusion direction. Hermans-Stein orientation factors for the (010) reflection were measured to be -0.23 for the MSA film and -0.34 for the PPA film compared to -0.5 for perfect orientation. Electron diffraction, however, indicated that local areas of the films are more highly oriented than the bulk. This was attributed to fibrillation of the bulk samples. As-spun films from PPA solutions were found to possess uniaxial symmetry whereas similar films from MSA possess selective uniaxial symmetry [44] with the $\underset{\sim}{a}$ axis preferentially oriented in the film plane.

9.1.3 Void Analysis in PBT. PBT fibers and films contain voids ranging in size from several nanometers to several microns. Voids 2 μm and above are termed 'macrovoids' and were studied by light microscopy. Voids 200 nm and below are termed 'microvoids' and were

studied by small angle x-ray scattering (SAXS).

Fibers and films processed from MSA solutions at room temperature contain macrovoids due to inhomogeneous coagulation. The linear number density of voids increases rapidly with increasing concentration of nonsolvent in the coagulation bath and less rapidly with increasing coagulation bath temperature. These data were interpreted to support a model in which coagulation occurs by deprotonation of the polymer.

Fibers and films processed form PPA solutions contain few macrovoids, perhaps due to the high viscosity of the fluid. When PPA solutions were extruded at higher temperature, the films frequently had a grainy appearance prior to coagulation. When examined by light microscopy, large voids were observed; the size and number density of which increase with increasing extrusion temperature. These have been attributed either to insufficient degassing of the solution prior to extrusion or to evolution of water by further condensation of PPA.

Microvoids in PBT fibers and films were investigated by analysis of the diffuse SAXS intensity measured on the 10 m SAXS apparatus with a 2-dimensional position sensitive detector at ORNL. Four models were considered for data analysis: direct Fourier inversion to obtain the projected correlation function, anisotropic Debye analysis based on the work of Summerfield and Mildner [51], anisotropic Guinier analysis based on the work of Stein [53], and finally analysis based on various assumed exponential density fluctuation correlation functions. The first of these methods is most general, but it is difficult to obtain

a characteristic void length. Anisotropic Guinier analysis and anisotropic Debye analysis proved to be most useful and provided characteristic void sizes. The average microvoid size perpendicular to the extrusion direction was insensitive to processing history except fo rheat treatment at 475°C which resulted in a decrease in microvoid size but an increase in scattered intensity and therefore microvoid fraction. This indicated that fibrillation and lateral contraction filled in some of the larger microvoids.

9.2 Generalizations and Suggestions for Future Work

9.2.1 The Molecular Transform. Preliminary investigations indicate that there is a significant amount of disorder in wide angle diffraction patterns from PPTA. Calculation of the molecular transform shows the regions of reciprocal space where strong intrachain scattering maxima are located and would provide useful insight into analysis of these patterns. Work by other investigators has generally involved commerical Kevlar® samples with ill defined processing histories. It would be interesting to investigate the effect of processing conditions on molecular order in fibers before and after heat treatment to see if as-spun Kevlar® forms a two-dimensional structure. The effect of single chain scattering (molecular transform) on fiber diffraction patterns raises a question of the validity of using (00ℓ) line broadening to measure apparent crystallite size as, for example, the work of Hindeleh and Dobb [93]. With a significant amount of translational disorder, the breadth of the (ooℓ) "reflections" should

yield a measure of chain length, not crystal size. Translational disorder has been postulated in polyacrylonitrile and other fibers [107] and the molecular transform could be used to quantitatively confirm this.

9.2.2 Structural Analysis of PBT. If improved processing induces large scale true three-dimensional order into PBT, the linked atom least squared refinement technique [108] would be usedful to determine the structure. Bascially this technique simultaneously minimizes the conformational energy and the difference between the observed and calculated structure factors. This program has been quite useful for biological macromolecules.

High resolution dark field and lattice imaging of a highly ordered PBT sample could be used to measure the size and size distribution of coherently scattering regions. These measurements, coupled with careful equatorial line broadening analysis would be useful for evaluation of the Scherrer parameter for the system.

9.2.3 Microvoid Analysis. As developed in Section 5.6, the ORNL 10-m SAXS could be used to determine the volume fraction of microvoids in PBT and other films. This would require the use of carefully prepared sample wound on a frame to give a flat bundle in order that thickness could be accurately determined. If fiber density were measured, this could be accurately calculated from the sample frame size and the fiber weight.

9.2.4 Study of Lyotropic Helical Polypeptides. Although PBT is of industrial importance, it is a very complicated system due to protonation in the strong acid solvents and ill defined phase equilbria. The helical polypeptide, poly(γ-benzyl glutamate) forms lyotropic mesophases in organic solvents and has been extensively studied, notably by G. Kiss of this laboratory [109].

PBG is polymerized from an N-carboxy anhydride by primary anionic initiators to form samples with a narrow molecular weight distribution [110,111] in contrast to PBT. The average molecular weight is easily determined [112] from the intrinsic viscosity since the polymer does not protonate in solution. The Mark-Howink constants for PBG are given in Table XVII.

Table XVII

Mark-Howink Constants for PBG in Selected Solvents [113]

Solvent	Temp. (°C)	K x 10^3 ml/g	a	Enantiomer
DCA	25	2.78	0.87	L
DMF	25	0.00029	1.70	L
DCA	25	2.85	0.85	D+L
DMF	25	37.7	0.55	D+L

DMF: dimethylformamide DCA: dichloroacetic acid

These data suggest that PBG exists as a helical rod in DMF and meta-cresol (m-C), and undergoes a helix-coil transition upon addition

of DCA [114]. The L enantiomer alone (PBLG) forms a cholesteric mesophase, and when mixed with an equimolar amount of the D enantiomer (PBDG) to give PBG, a nematic mesophase results [115]. The ternary phase equilibria of PBLG/DMFH_2O and PBLG/DMF/CH_3OH have been well studied [116,117] and are in qualitative agreement with Flory's theory [118] of rigid rod phase equilibria.

Thus, well characterized samples of PBG could be studied as a model system in which samples of similar molecular weight spun from cholesteric and nematic mesophases and as a flexible chain by judicious choice of the enantiomer(s) and solvent used. Use of well characterized samples of PBG will eliminate many of the unavoidable uncertainties encountered with PBT and PTA.

PBLG has been spun into fibers but has not been of commerical interrest since it did not become as highly ordered on drawing as other polypeptides such as poly(γ-methyl-L-glutamate) [116]. However, the effect of porcessing variables has not been examined.

In summary, helical polypeptides such as PBLG would provide excellent model systems for other lyotropic liquid crystals such as PBT and PPTA. These model systems would be much easier to characterize and provide more insight into the fiber spinning process and its affect on sample microstructure.

REFERENCES

1. T.E. Helminiak, "The Air Force Ordered Polymers Research Program: An Overview." A.C.S. Org. Coat. and Plast. Preprints, 4, 475-479 (1979).
2. S.R. Allen, A.G. Filippov, R.J. Farris, E.L. Thomas, C.-P. Wong, G.C. Berry, and E.C. Chenevey, "Mechanical Studies of High-Strength, High-Modulus Poly(p-phenylene benzobisthiazole) Fibers." Macromolecules, 14, 1135-1138 (1981).
3. J.F. Wolfe, B.H. Loo, and F.E. Arnold, "Rigid Rod Polymers. 2. Synthesis and Thermal Properties of Para-Armomatic Polyamides with 2,6 Benzobisthiazole Units in the Main Chain." Macromolecules, 14, 915-920 (1981).
4. J.F. Wolfe and F.E. Arnold, "Rigid Rod Polymers. 1. Synthesis and Thermal Properties of Para-Aromatic Polymers with 2,6 Benzobioxazole Units in the Main Chain." Macromolecules, 14, 909-915 (1981).
5. D.B. Cotts and G.C. Berry, "Polymerization Kinetics of Rigid Rodlike Macromolecules: Polycondensation of Poly([benzo(1,2-d:5,4d')bisoxazole-2,6 diyl]1,4 phenylene)." Macromolecules, 14, 930-934 (1981).
6. E.W. Choe and S.N. Kim, "Synthesis, Spinning, and Fiber Mechanical Properties of Poly(p-phenylene benzobisoxazole)." Macromolecules, 14, 920-924 (1981).
7. D.Y. Shen, G.M. Venkatesh, D.J. Burchell, P.H.C. Shu, and S.L. Hsu, "Spectroscopic Studiey of Rigid-Rod Polymers. II. Protonation Effect." J. Polym. Sci.: Polym. Phys. Ed., 20, 0000-0000 (1982).

8. G.C. Berry, P.C. Metzger, S. Venkatraman, and D.B. Cotts, "Properties of Rodlike Polymers in Solution." A.C.S. Polym. Preprints, 20(1), 42-44 (1979).

9. C.-P. Wong, H. Ohnuma, and G.C. Berry, "Properties of Some Rodlike Molecules in Solution." J. Polym. Sci.: Polym. Symp., 65, 173-192 (1978).

10. G.C. Berry, "Physical Chemical Properties of Aromatic Heterocyclic Polymers, Part VII." AFML-TR-71-Part VII (1977).

11. J.R. Schaefgen, V.S. Foldi, F.M. Logullo, V.H. Good, L.W. Gulrich, and F.L. Killian, "Viscosity-Molecular Weight Relationships in Stiff Chain Aromatic Polyamides." A.C.S. Polym. Preprints, 17(1), 69-74 (1976).

12. E.C. Chenevey and E.W. Choe, "Processing of Rodlike Polymers." AFWAL-TR-80-4142 (1980).

13. E.C. Chenevey, "Processing of Rodlike Polymers." Part II, AFWAL-TR-80-4142.

14. H. Aoki, Y. Onogi, J.L. White, and J.F. Fellers, "Characterization and Continuous Extrusionof Iotropic and Aniostropic Poly(p-Phenylene Terephthalamide)/Sulfuric Acid Solutions to Form Ribbons and Blown Film." Polym. Eng. and Sci., 20(3), 221-229 (1980).

15. G.C. Berry, E.F. Cassassa, C.C. Lee, R. Furukawa, R.S. King, S. Venkatraman, "Physical Chemical Studies of Polymers with Rod-like Backbone Elements." AFWAL-TR-80-4099 (1980).

16. R.B. Bird, M.W. Johnson, Jr., and J.F. Stevenson, "Molecular Theories of Elongational Viscosity." Proc. Fifth Int. Cong. Rheol., 4, 159-168 (1970).

17. S.R. Allen, A.G. Filippov, R.J. Farris, and E.L. Thomas, "Macrostructure and Mechanical Behavior of Fibers of Poly-p-Phenylene Benzobisthiazole." J. Appl. Polym. Sci., 26, 291-301 (1981).

18. S.R. Allen, A.G. Filippov, R.J. Farris, E.L. Thomas, C.-P. Wong, G.C. Berry and E.C. Chenevey, "Mechanical Studies of High-Strength, High-Modulus Poly(p-phenylene-benzobisthiazole) Fibers." Macromolecules, 14, 1135-1138 (1981).

19. D.D. Perrin, W.L.F. Armstrong, and D.R. Perrin, Purification of Laboratory Chemicals. New York: Pergamon Press, 1966, p. 199.

20. W.J. Patzelt, Polarized-Light Microscopy. Principles, Instruments, Applications. 2nd ed., W. Germany: Leitz, 1974, p. 74.

21. R.D. Allen, G.B. David, G. Nomarski, "The Zeiss-Nomarski differential interference equipment for transmitted-light microscopy." Z. für Wissenschaftliche Mikroskopie und Mikroskopische Technik, 4(69), 193-221 (1969).

22. W. Lang, Nomarski Differential Interference-Contrast Microscopy, W. Germany: Zeiss, (1969).

23. D. Thompson, personal communication (1979).

24. Eastman Kodak Company, Kodak Technical Pan Film (ESTAR-AH Base) SO-115, USA: Kodak Pamphlet No. P-255 (1977).

25. E.J. Roche, T. Takahashi, and E.L. Thomas, "Structure of High Modulus Fibers of Poly(p-phenylene benzbisthiazole)." Fiber Diffraction Methods, ACS Symposium Series 141, Ed. A.D. French and K.H. Gardner, 303-313 (1980).

26. E.L. Thomas, R.J. Farris, S.L. Hsu, S. Allen, A. Filippov, J. Minter, E. Roche, K. Shimamura, T. Takahashi and G. Venkatesch, "Mechanical Properties vs. Morphology of Ordered Polymers." AFWAL-TR-80-4045, Vol. 2 (1981).

27. M.C. Dobb, D.J. Johnson and B.P. Saville, "Macromolecular Structure of a Poly p-Phenylene Terephthalamide Fibre." Inst. Phys. Conf. Ser., 36, 403-406 (1977).

28. P.H. Geil, Polymer Single Crystals, Huntington, NY: R.B. Krieger, (1973), pp. 69-70.

29. K. Shimamura, personal communication.

30. J. Dubochet, "High Resolution Darkfield Electron Microscopy." Principles and Techniques of Electron Microscopy. Biological Applications, vol. 3, Ed M. Hayat, NY: Van Nostrand/Reinhold, (1973), pp. 144-146.

31. W. Baumeister and M. Hahn, "Specimen Supports." Principles and Techniques of Electron Microscopy, vol. 8, Ed. M. Hayat, NY: Van Nostrand/Reinhold, (1973), pp. 1-112.

32. W. Adams, personal communication.

33. R.W. Hendricks, "The ORNL 10-M Small Angle X-Ray Scattering Camera." Oak Ridge National Laboratory TM-6342.

34. S. Chandrasekhar, Liquid Crystals, Cambridge: Cambridge University Press, (1977).

35. F.C. Frank, "I. Liquid Crystals. On the Theory of Liquid Crystals." Disc. Faraday Soc., 25, 19-28 (1958).

36. H. Benoit and A. Straizielle, personal communication (1980).

37. P.W. Morgan, "Synthesis and Properties of Aromatic and Extended Chain Polyamides." Macromolecules, 10, 1381-1390 (1977).

38. Y. Onogi, J.L. White and J.F. Fellers, "Structural Investigations of Polymer Liquid-Crystalline Solutions: Aromatic Polyamides, Hydroxy Propyl Cellulose, and Poly(γ-Benzyl-L-Glutamate)." J. Polym. Sci., Polym. Phys. Ed., 18, 663-682 (1980).

39. C.H. Kao and J.M. Ottino, personal communication.

40. G.C. Berry, C.-P. Wong, S. Venkatramen, S.-G. Chu, "Solution Processing - Rodlike Polymers." AFML-TR-79-4115 (1979).

41. S. Allen, E.L. Thomas, R.J. Farris, and S.L. Hsu, "Mechanical Properties vs. Morphology of Ordered Polymers." AFWAL-TR-80-4045, (1980).

42. M.E. Epstein and A.J. Rosenthal, "Spinning of Polyamides from Sulfuric Acid Solution. Polymer Solubility and Coagulation Mechanisms." Text. Res. J., 36(9), 54-56 (1966).

43. J.P. Knudsen, "The Influence of Coagulation Variables on the Structure and Physical Properties of an Acrylic Fiber." Text. Res. J., 33, 13-20 (1963).

44. L.E. Alexander, X-Ray Diffraction Methods in Polymer Science, NY: Krieger Publishing Co., (1979).

45. W.O. Statton, VI. Small-Angle X-Ray Studies of Polymers." Newer Methods of Polymer Characterization, Ed. B. Ke, USA: Interscience, (1964), pp. 231-278.

46. P.H. Hermans, D. Heikens, and A. Weidinger, "A Quantitative Investigation on the X-Ray Small Angle Scattering of Cellulose Fibers. Part II. The Scattering Power of Various Cellulose Fibers." J. Polym. Sci., 35, 145-165 (1959).

47. M.G. Dobb, D.J. Johnson, A. Majeed, B.P. Saville, "Microvoids in aramid-type fibrous polymers." Polymer, 20, 1284-1288 (1979).

48. P. Debye and A.M. Bueche, "Scattering by an inhomogeneous solid." J. Appl. Phys., 20, 518-525 (1949).

49. P.F. Van Hutten, "Small-Angle X-Ray Scattering Studies of Macromolecular and Colloidal Systems." Ph.D. dissertation, University of Groningen, 1981.

50. R.S. Stein and T. Hotta, "Light Scattering from Oriented Polymer Films." J. Appl. Phys., 35(7), 2237-2242 (1964).

51. G.C. Summerfield and F.R. Mildner, "Small Angle Scattering with Azimuthal Symmetry." J. Appl. Cryst., in press.

52. E.O. Brigham, "The Discrete Fourier Transform." The Fast Fourier Transform, Englewood Cliffs, NJ: Prentice Hall, (1974).

53. R.S. Stein, personal communication.

54. MH. Jellinek, E. Solomon, and I. Fankuchen, "Measurement and Analysis of Small-Angle X-Ray Scattering." Ind. Eng. Chem., 18(3), 172-175 (1946).

55. R. Hosemann and S.N. Bagchi, Direct Analysis of Diffraction by Matter, New York: North-Holland Pub. Co./Interscience, (1962).

56. L.E. Alexander, op. cit., pp. 291-293.

57. B. Crist, "Microfibril Dimensions from Small-Angle X-ray Scattering." J. Appl. Cryst., 12, 27 (1979).

58. J.T. Koberstein, B. Morra, and R.S. Stein, "The Determination of Diffuse-Boundary Thicknesses of Polymers by Small-Angle X-Ray Scattering." J. Appl. Cryst., 13, 34-45 (1980).

59. D.T. Grubb, "The calibration of beam measurement devices in various electron microscopes, using an efficient Faraday cup." J. Scient. Instrum., 4, 222 (1971).

60. S.C. Bennett, M.G. Dobb, D.J. Johnson, R. Murray, and B.P. Saville, "High-Resolution Studies of Electron-Beam Sensitive Polymers." EMAG Proceedings, (1975).

61. M.G. Dobb, D.J. Johnson, and B.P. Saville, "Direct Observation of Structure in High-Modulus Aromatic Fibers," J. Polym. Sci.: Polym. Symp., 58, 237-251 (1977).

62. D.T. Grubb and G.W. Groves, "Rate of Damage of Polymer Crystals in the Electron Microscope: Dependence on Temperature and Beam Voltage." Phil. Mag., 24, 815-828 (1971).

63. E.L. Thomas and D.G. Ast, "Image intensification and the electron microscopy of radiation sensitive polymers." Polymer, 15, 37-41 (1974).

64. Eastman Kodak Company, "Kodak Electron Image Film SO-163, USA: Kodak Pamphlet No. P-252, (1981).

65. Y. Harada, Y. Ishida, Y. Fujiyoshi, T. Kobayashi, and N. Uyeda, "High Resolution Observation of Beam Sensitive Specimens - Minimum Dose System and its Application." JEOL News, 19E(2), 1-5 (1981).

66. K. Shimamura, J.R. Minter, and E.L. Thomas, "Poly-p-Phenylene Benzobisthiazole (PBT) Lattice Imaging." Polymer Preprints, Japan, 31(4), (1982).

67. M.G. Dobb, D.J. Johnson, and B.P. Savile, "Structural Aspects of High Modulus Aromatic Polyamide Fibres." Phil. Trans. R. Soc. Lond. A., 294, 483-485 (1979).

68. P. Aviakan, R.C. Blume, T.D. Gierke, H.H. Yang, and M. Panan, "Poly(p-phenylene terephthalamide) Morphology." A.C.S. Polym. Preprints, 21(1), 8-9 (1980).

69. J.W. Ballou, "The Structure of Fibers from p-Oriented Aromatic Polyamides." Polymer Preprints, April 1976, 75-78.

70. P. Hirsch, A. Howie, R.B. Nicholson, D.W. Pashley, M.J. Whelan, Electron Microscopy of Thin Crystals, NY: Krieger Pub. Co., (1977).

71. S.C. Bennett and D.J. Johnson, "Electron-Microscope Studies of Structural Heterogeneity in PAN-Based Carbon Fibres." Carbon, 17, 25-39 (1979).

72. P. Predecki and W.O. Statton, "A Dislocation Mechanism for Deformation in Polyethylene." J. Appl. Phys., 38(11), 4140-4144 (1967); J. Appl. Phys., 37(11), 4053-4059 (1966).

73. W.W. Adams, L.V. Azaroff, and A.K. Kulshreshtha, "X-ray diffraction by a nematic polybenzothiazole fiber." Z. für Krist., 150, 321-326 (1976).

74. E. Roche, personal communication.

75. J.A. Odell, A. Keller, E.D.T. Atkins, and M.J. Miles, "Preparation, properties and structure of poly(p-phenylene benzbisthiazole) films." J. Mat. Sci., 16, 3309-3318 (1981).

76. M.G. Northolt and J.J. van Aartsen, "Chain Orientation Distribution and Elastic Properties of Poly(p-Phenylene Terephthalamide), a 'Rigid Rod' Polymer." J. Polym. Sci.: Polym. Symp., 58, 283-296 (1977).

77. M.G. Northolt, "X-Ray Diffraction Study of Poly(p-phenylene terephthalamide) Fibres." Eur. Polym. J., 10, 799-804 (1974).

78. M.G. Northolt and J.J. van Aartsen, "On the Crystal and Molecular Structure of Poly-(p-Phenylene Terephthalamide)." J. Polym. Sci.: Polym. Lett. Ed., 11, 333-337 (1973).

79. K. Haraguchi, T. Kajiyama, and M. Takayanagi, "Uniplanar Orientation of Poly(p-phenylene Terephthalamide) Crystal in Thin Film and Its Effect on Mechanical Properties." J. Appl. Polym. Sci., 23, 903-914 (1979).

80. K. Haraguchi, T. Kajiyama, and M. Takayanagi, "Effect of Coagulation Conditions on Crystal Modification of Poly(p-phenylene terephthalamide)." J. Appl. Polym. Sci., 23, 915-926 (1979).

81. K. Suehiro, Y. Chatani, and H. Tadokoro, "Structural Studies of Polyesters. VI. Disordered Crystal Structure (Form II) of Poly(β-Propiolactone)." Polymer J. (Japan), 7(3), 352-358 (1975).

82. H. Tadokoro, Structure of Crystalline Polymers, USA: John Wiley and Sons, Inc., (1979).

83. M.W. Wellman, W.W. Adams, R.A. Wolff, D.S. Dudis, D.R. Wiff, and A.V. Fratini, "Model Compounds for Rigid-Rod Aromatic Heterocyclic Polymers. 1. X-Ray Structures of 2-6 Diphenylbenzo[1,2d:4,5d']bisthiazole and 2-6 Diphenylbenzo[1,2-d:5,4-d']bisthiazole." Macromolecules, 14, 935-939 (1981).

84. M. Yokouchi, H. Tadokoro, Y. Chatani, "Conformational and Packing Stability of Crystalline Polymers. V. A Method for Calculating Conformational Parameters of Polymer Chains with Glide, Helical and Translational Symmetries." Macromolecules, 7(6), 769-776 (1974).

85. E. Roche, private communication.

86. M.J. Buerger, "Some Physical Factors Affecting Intensities." Crystal Structure Analysis, NY: Wiley (1960), pp. 195-241.

87. W.J. Welsh, D. Bhaumik, and J.E. Mark, "Phenylene Group Rotations and Nonplanar Conformations in Some cis- and trans-Poly(benzobisoxazoles) and Poly(benzobisthiazoles)." Macromolecules, 14, 947-950 (1981).

88. P. Scherrer, "Evaluation of size and internal structure of colloidal particles by means of Roentgen rays." Gottinger Nachr., 2, 98 (1918).

89. R. Hosemann and D.N. Bagchi, op. cit., pp. 294-299.

90. ibid, pp. 247, 271-277.

91. ibid, pp. 302-331.

92. A.R. Stokes, "A Numerical Fourier-Analysis Method for the Correction of Widths and Shapes of Lines on X-Ray Powder Photographs." Proc. Phys. Soc. (London) A61, 382 (1948).

93. A.M. Hindeleh and D.J. Johnson, "An empirical estimation of Scherrer parameters for the evaluation of true crystallite size in fibrous polymers." Polymer, 21, 929-935 (1980).

94. C.R. Desper and R.S. Stein, "Measurement of Pole Figures and Orientation Functions for Polyethylene Films Prepared by Unidirectional and Oriented Crystallization." J. Appl. Phys., 37(11), 3990-4002 (1966).

95. A. Guinier and G. Fournet, Small Angle Scattering of X-Rays, New York: John Wiley and Sons., Inc., (1965).

96. G. Oster and D.P. Riley, "Scattering from Cylindrically Symmetric Systems." Acta Cryst., 5, 272-276 (1952).

97. N.F.M. Henry and K. Lonsdale, Eds., International Tables for X-Ray Crystallography, Vol. I. Symmetry Groups, 2nd ed., Kynoch Press, Birmingham, England (1965).

98. J.P. Cotton, D. Decker, H. Benoit, B. Tarnoun, J. Higgins, G. Jannick, R. Ober, C. Picot, and J. des Cloiseaux, "Conformation of Polymer Chain in the Bulk." Macromolecules, 7, 863-872 (1974).

99. G.E. Bacon, Neutron Diffraction, 2nd ed., Clarendon Press, Oxford, 1962.

100. G.E. Bacon,"Coherent Neutron Scattering Amplitudes." Acta Cryst., A28, 357-358 (1972).

101. G.E. Bacon, Neutron Scattering in Chemistry, Butterworths, London (1977).

102. A.Z. Akcasu, G.C. Summerfield, S.N. Tahshan, C.C. Hur, C.Y. Kim, and H. Yu, "Measurement of Single Chain Neutron Scattering in Concentrated Polymer Solutions." J. Polym. Sci.: Polym. Phys. Ed., 18, 863-869 (1980).

103. G.D. Wignall, R.W. Hendricks, W.C. Koehler, J.S. Cin, M.P. Wai, E.L. Thomas, and R.S. Stein, "Measurements of Single Chain Form Factors by Small Angle Neutron Scattering from Polystyrene Blends Containing High Concentrations of Labeled Molecules." Polymer, 22, 886-889 (1981).

104. C.R. Crosby, III, N.C. Ford, Jr., F.E. Karasz, and K.H. Langley, "Depolarized light scattering of a rigid macromolecule poly(p-phenylene benzbisthiazole." J. Chem.. Phys., 75, 4298-4306 (1981).

105. A. Guinier "Diffraction of X-rays at Small Angles - Application to the Study of Ultramicroscopic Phenomena" Ann. Physique, 12, 161-237 (1939).

106. H. Yamakawa, Modern Theory of Polymer Solutions, Harper and Row, New York (1971).

107. C.R. Bohn, J.R. Schaefhen and W.O. Statton, "Laterally Ordered Polymers: Polyacrylonitrile and Poly(vinyl trifluoro acetate)" J. Polym. Sci., 55, 531-549 (1961).

108. P.J. Campbell-Smith and S. Arnott, "LALS: A. Linked Atom Least-Squares Reciprocal Space Refinement System Incorporating Stereochemical Restraints to Supplement Sparse Diffraction Data" Acta. Cryst., A34, 3-11 (1978).

109. G. Kiss, "Rheology and Rheo-optics of Concentrated Solutions of Helical Polypeptides," Ph.D. Dissertation, University of Massachusetts, Amherst (1979).

110. E.R. Blout and R.H. Karlson, "Polypeptides.III. The Synthesis of High Molecular Weight Poly(γ-benzyl-L-glutamate)," J. Am. Chem. Soc., 78, 941-946 (1956).

111. D.G.H. Ballard, "Synthetic POlypeptides," Man Made Fibers: Science and Technology, Vol. 2, ed. H.F. Mark, S.M. Atlas and E. Cernia, Interscience, N.Y., 401-433 (1968).

112. P. Doty, J.H. Bradbury and A.M. Holtzer, "Polypeptides. IV. The Molecular Weight, Configuration and Association of Poly-γ-benzyl-L-glutamate in Various Solvents," J. Am. Chem. Soc., 78, 947-954 (1956).

113. J. Brandrup and E.H. Immergut, Polymer Handbook, second ed. Interscience, NY (1975).

114. A. Cifferi, "Ultra-high Modulus Fibers From Solution Spinning," Polym. Eng. and Sci., 15, 191-198 (1975).

115. C. Robinson and J.C. Ward, "Liquid Crystalline Structure in Polypeptides," Nature, 180, 1183-1184 (1957).

116. A. Nakajima, F. Hayashi and M. Ohmori, "Phase Equilbria of Rodlike Molecules in Binary Solvent Systems," Biopolymers, 6, 937-982 (1968).

117. E.L. Wise and W.G. Miller, "Liquid Crystal-Isotropic Phase Equilibria in the System Poly(γ-benzyl-L-glutamate)-Dimethylformamide," J. Phys. Chem., 75, 1446- 1452 (1971).

118. P.J. Flory, "Phase Equilibria in Solutions of Rod-like Particles," Proc. Roy. Soc. A., 234, 73-89 (1956).

119. H. Blades, "High Modulus High Tenacity Poly(p-phenylene terephthalamide) Fiber" U.S. Patent, 3,869,430 (1975).

120. A. Ziabicki, Fundamentals of Fibre Formation, New York: Wiley-Interscience (1970).